Science Requirement Document for the proposal Critical Velocities in Open Capillary Channel Flows (CCF)

Uwe Rosendahl, Michael E. Dreyer, Aleksander Grah, Jörg Klatte

Center of Applied Space Technology and Microgravity,

University of Bremen, Am Fallturm, D-28359 Bremen, Germany

Mark Weislogel

Department of Mechanical and Materials Engineering

Portland State University, Portland, Oregon 97207, United States

Version 1.1

January 2007

Preface

The present document is the first update of the original version of the Science Requirement Document for the CCF-project (SRD CCF Version 1.0) written in 2002. Based on SRD CCF Version 1.0 the Science Concept Review has been passed and the feasibility studies Phase A (Baumbach *et al.*, 2003), Phase B_0 (Rosendahl *et al.*, 2004*a*) and Phase B (EADS Space Transportation, 2005) have been performed.

Deviating from the original planings, the experiment is now limited to two experiment units. EU#1 is foreseen for the investigation of the parallel plate and groove channel, while EU#2 is concerned with the wedge-shaped channel. The document has been updated concerning the latest experimental and theoretical findings of the parallel plate channel and a new theoretical approach and experiment strategy for the wedge. If possible the actual design status and in particular the current system specification were incorporated into this document.

Contents

Nomenclature

In the following often used symbols are listed. Double-meaning of the symbols are possible.

a	gap distance
a_0	acceleration
A	cross section of flow path
A_0	cross section at the inlet
A_{min}	minimal cross section
b	plate breadth, H_2/H_1 for wedge flow
c_s	speed of sound
c_{ch}	wave speed of a compressible fluid in an open channel
c_{sw}	shallow water wave speed
D	distensibility
D_b	bubble diameter
D_h	hydraulic diameter
f	dimensionless geometric cross flow interface curvature function
F_A	dimensionless cross flow area function
F_i	dimensionless geometric flow resistance function
G	gap distance of the wedge according to Fig. 2.2
g	gravitational or residual acceleration
g_0	gravitational acceleration on earth
$h = 2H$	twice the mean surface curvature
h	surface profile (wedge-shaped channel)
H	mean surface curvature (parallel plate channel)
H	characteristic height (wedge-shaped channel)
H_b	position of bubble injection
H_1, H_2	interface elevations at wedge inlet and outlet, respectively
H_0	mean curvature at the channel inlet
k	surface profile (parallel plate channel)
K_{pf}	friction factor of the fully developed flow
K_{pe}	friction factor of the entrance flow
$K_{1,2}$	pressure loss constants

l	channel length
L	characteristic channel length (wedge-shaped channel)
l_e	entrance length
p	fluid pressure
p_0	channel inlet pressure
p_a	ambient pressure
p_b	back pressure
p_e	entrance pressure
Q	volume flux
Q_{crit}	critical volume flux
Q_{max}^{st}	maximal stable volume flux from the experiment
$Q_{\min}^{unst}$	minimal unstable volume flux from the experiment
Q_1	volume flux of the supply pump
R	radius of curvature
R_1, R_2	principle radii of curvature
R_c	radius of compensation tube
S	speed index, 3-D surface elevation for wedge flow
S_R	approximated speed index
t	time
t_0	start time of the microgravity phase in the drop tower
t_c	time of contact between the liquid and the suction device
t_r	rise time of the liquid in the capillary channel
T	liquid temperature
U	x-component velocity scale for wedge flow
u, v, w	velocity components along the axis x, y, z (wedge-shaped channel)
v	mean liquid velocity (parallel plate channel)
v_c	longitudinal wave speed in a capillary channel
v_{cR}	approximated longitudinal wave speed in a capillary channel
v_f	liquid velocity in a channel under $1g$
v_g	gas velocity
v_w	relative wave speed
w	mass flow per unit area
w_f	friction work

x	flow coordinate
x_e	entrance length
x_s	Sparrow length
y	flow coordinate
z	flow coordinate

α	wedge angle
$\Gamma = 2l/a$	length ratio
θ	slenderness ratio for wedge flow
θ	wetting angle
κ	adiabatic coefficient
$\Lambda = b/a$	gap ratio
μ	dynamic viscosity
ν	kinematic viscosity
ν_b	bubble injection frequency
Π	aspect ratio
ϕ	tilt angle
ρ	density
σ	surface tension
τ_w	wall shear stress

Bo	Bond number
Ca	Capillary number
Fr	Froude number
Ma	Mach number
Oh	Ohnesorge number
Re_h	Reynolds number based on hydraulic diameter
Re_0	Reynolds number based on v_0

$\mathcal{L}$	Dimensionless channel length

1 Executive Summary

We propose the investigation of liquid flows in open capillary channels. An open capillary channel is a structure that establishes a liquid flow path at low BOND numbers, i.e. when the capillary pressure caused by the surface tension force dominates in comparison to the hydrostatic pressure induced by gravitational or residual accelerations. The cross section of the flow path is partly confined by free surfaces.

As an example the capillary channel consisting of two parallel plates is shown in Figure 1.1. The liquid flows along the x-axis from the inlet to the outlet and forms free surfaces at the sides between the plates. The flow is maintained by external pumps and the free surface deforms according to the pressure along the flow path.

The aim of the experiment is to determine the shape of the free surface and to find the maximum flow rate which may be achieved in the channel without a collapse of the free surface. Due to convective and viscous momentum transport the pressure along the flow path decreases and forces the free surface to bend inwards. The maximum flow rate is achieved when the free surface collapses and gas ingestion occurs at the outlet. This critical flow rate depends on the geometry of the channel and the properties of the liquid. A secondary objective of the experiment is to determine the ability of such constructs to adapt to bubbly flows and to passively separate fluid phases for a variety of applications in spacecraft propellants, cryogenics and other fluids management.

Similarities exist to compressible gas flows in ducts and open channel flows under terrestrial conditions. Each of these flows is governed by similar equations. The flow rate of these flows is limited due to choking. The theory of choked flow predicts a limiting velocity corresponding to a characteristic signal velocity of the flow. Once this critical velocity is reached the mass flow is maximal and cannot be increased further. In compressible gas duct flows the limiting speed is defined by the speed of sound. The characteristic number is the MACH number (Ma) and the maximal flow passes through the duct when $\mathrm{Ma} = 1$ is reached Shapiro (1953). In open channel flows the speed of shallow water waves define the limiting velocity (FROUDE number problem) Faber (1995). For the open capillary channel flows to be investigated in our experiment a limiting speed defined by the capillary waves of long wavelength is expected. This velocity is derived from the capillary pressure and requires a measurement of the contour of the free surface.

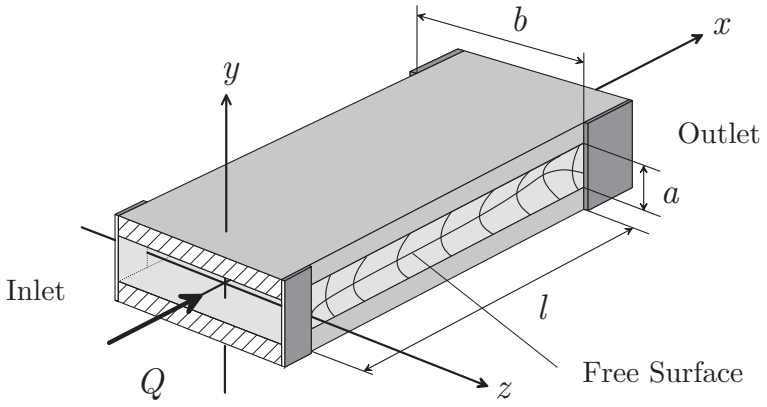

Figure 1.1: Schematic drawing of the parallel plate channel. The liquid flows parallel to the x-axis from the inlet to the outlet of the channel.

We propose to study four different geometries: channels consisting of parallel plates, grooves, wedges, and wedges with gaps. For each geometry a test matrix is defined to vary specific dimensions, such as the aspect ratio of the cross sections, the lengths of the channel, the angle of the wedge, the flow rate, etc. The capillary channels are implemented in a fluid circulation system to establish a continuous flow with variable velocity. It is intended to investigate three approaches to the critical velocity: quasi-steady increase of the flow rate, transient increase of the flow rate, and oscillatory changes of the flow rate. The contour of the free surface will be observed by high speed video cameras and evaluated by image processing. Starting with a steady flow at a low flow rate, the flow rate will be increased in small steps up to the critical value. When gas ingestion occurs, the flow rate will be reduced to subcritical flow conditions to reproduce the cycle. The data obtained for each parameter in the test matrix are the contours of the free surface and the critical flow rate.

Experiment objectives

The experiment objectives are to test the theoretical predictions for the free surface shapes and the critical flow velocities and to validate the assumptions central to the derivation of the governing equations. Four different geometries requiring two experiment units (EU#1 parallel plate, groove, and EU#2 wedge and gapped wedge) are considered to investigate a significant range of the dimensionless parameters. Each geometry has its specific properties that give rise to different effects.

We developed a steady, one dimensional mathematical model from the mass and momentum conservation equations to predict the free surface shape for each geometry and flow rate. Furthermore we are able to anticipate the critical flow rate for each geometry. The model contains the pressure gradient caused by the shape of the free surface taking into account both radii of curvature, the convective acceleration due to the change in cross section

and the friction losses in the channel. For most of the channel lengths to be investigated we must address an entrance flow problem. Thus, the velocity distribution does not obey a simple parabolic HAGEN-POISEUILLE type law. The boundary conditions at the inlet in terms of velocity distribution and pressure can only be determined with the help of fully 3D computation using commercial CFD packages such as FIDAP or FLOW-3D.

The determination of the limiting capillary wave speed for the choking problem requires the knowledge of the free surface shape. The theory compares the signal velocity (capillary waves) with the fluid velocity at the smallest cross section of the flow paths. The flow is classified as choked in the sense of the classical theory if both velocities approach each other.

The motivation for this investigation stems from a noted shortfall in theoretical and experimental work. Very few papers are available that provide engineering solutions for applications in surface tension tanks. No experimental validation is known. The theory for choked flows due to the limiting capillary wave velocity was only recently developed by the authors and awaits flight experiment validation.

An extensive database is necessary before the theory can be validated and thus reliably applied to the design and analysis process for current and advanced spacecraft propellant management systems. Open capillary channels (i.e. vanes) are used in surface tension tank technology for the highly controlled distribution of fuel within the tank as well as the transport of liquid to a reservoir or directly to an outlet. The limiting flow rate for such constructs is a fundamental performance limiter for gas-free liquid supply to the engine and serves as a critical design guide for optimal tank geometry.

2 Introduction and Background

2.1 Brief Overview of Scientific Topic

We consider a liquid flow path as a capillary channel whose perimeter is partially confined by free surfaces. A constant volumetric flow rate Q is established by a withdrawal pump at the outlet of the channel. Liquid is provided at the inlet by a reservoir. Fluctuations of the liquid volume in the system due to gas ingestion are accommodated by a compensation tube. The liquid surfaces of the open channel and the compensation tube are exposed to the ambient gas at pressure p_a. Both p_a and the temperature of the liquid T are held constant.

The liquid pressure inside the channel decreases in the flow direction due to convective and viscous flow losses. The mean curvature of the free surface adjusts to the pressure inside the channel in the case of a subcritical flow condition. The maximum flow rate is achieved when the free surface collapses and gas ingestion occurs.

We have chosen four different geometries for our investigation: (1) parallel plate, (2) groove, (3) wedge, and (4) gapped wedge. Two Experiment Units (EUs) are required to meet the test geometry requirements: EU#1 focuses on the parallel plate and the groove geometry and precisely and deeply probes the fundamentals of the choking phenomena to be described in greater detail herein. EU#2 relaxes precision requirements for greater flexibilty in test cell geometry. EU#2 tests the limits of performance of the wedge and gapped wedge geometries. Schematic drawings of the geometries 1 to 4 are given in Fig. 2.1 and Fig. 2.2, respectively. All channels have length l.

The parallel plate channel consists of two plates of breadth b and separation distance a. It was chosen as a fundamental representative of capillary vanes used in surface tension tank technology. This channel has been investigated soundly by the authors and the theory is well developed. The flow in this channel has a convective and a viscous dominated regime with an intermediate region between. The theory is corroborated by experiments. The choking phenomenon is found to limit the flow rate.

The groove-shaped channel is accomplished from the parallel plate channel by closing one open side. It has width b and gap distance a. Although this channel is widely used in heat pipes, experimental and theoretical data in particular for the convective dominated regime are rare.

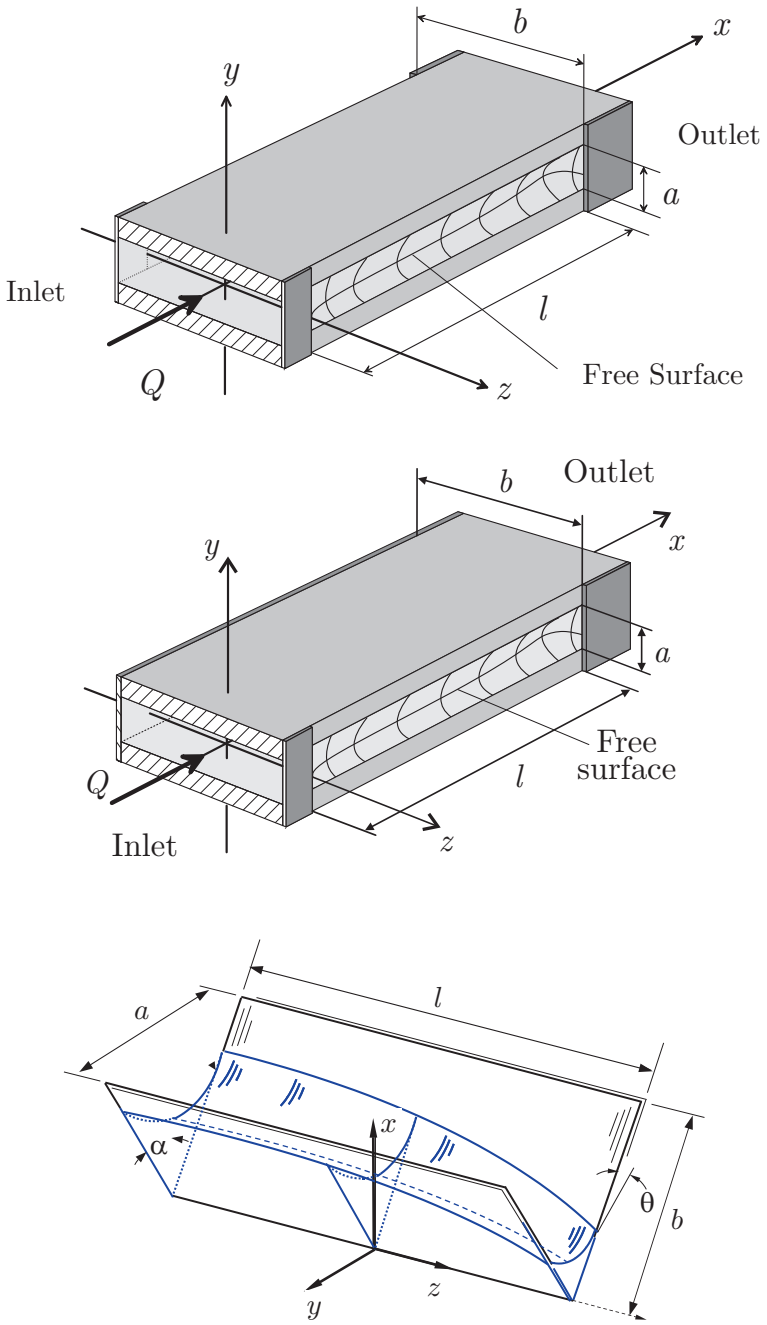

Figure 2.1: Schematic of the channel geometries. (Top) parallel plate channel. (Middle) groove channel. (Bottom) wedge.

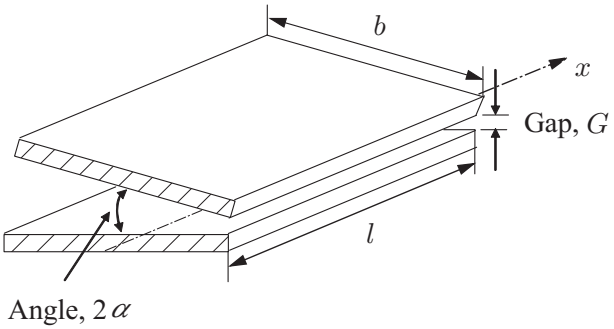

Figure 2.2: Schematic of the gapped wedge geometry.

The wedge is characterized by the plate breath b and the wedge half-angle α. It represents a universal flow path with variable angle from a narrow slit to a wide gap. No experimental data are available for inertially-dominated flow through the wedge though capillary-driven flows have been investigated extensively by the authors. 'Gapped wedge' flows are characterized by wedge half-angle α and gap G (Fig. 2.2).

The mathematical modelling shows that for each geometry the non-dimensional critical flow rate is given by a function

$$Q'_{crit} = f(\mathrm{Oh}, \Pi, \mathcal{L}) \tag{2.1}$$

with the non-dimensional flow rate Q', the aspect ratio Π and the non-dimensional flow length $\mathcal{L}$. Note that for the viscous limit, when the governing equations are scaled using the capillary velocity, $Q'_{crit} \simeq const. = f(F_i/3)$. The corresponding numbers for each geometry are given in Table 2.1.

	D_h	Oh	Π	$\mathcal{L}$	v_0	A_0
plates	$2a$	$\sqrt{\rho\nu^2/(\sigma D_h)}$	$\Lambda = b/a$	Oh $l/(2D_h)$	$\sqrt{4\sigma/(\rho D_h)}$	ab
groove	$4b/(2\Lambda+1)$	$\sqrt{\rho\nu^2/(\sigma D_h)}$	$\Lambda = b/a$	Oh $l/(2D_h)$	$\sqrt{4\sigma/(\rho D_h)}$	ab
wedge	$a\cos\alpha$	$\sqrt{\rho\nu^2/(\sigma D_h)}$	α	Oh $l/(2D_h)$	$\sqrt{4\sigma/(\rho D_h)}$	$a^2\cot\alpha/4$

Table 2.1: Corresponding numbers for parallel plate channel and wedge-shaped channel.

The hydraulic diameter is defined as

$$D_h = \frac{4A_0}{L_w} \tag{2.2}$$

with the wetted perimeter L_w of the cross section and the initial cross section A_0. This concept is widely used in non-circular duct flow and helps to organize the friction factors for different geometries. Errors in the use of D_h for laminar flows are acknowledged (White, 1991; Ransohoff & Radke, 1988) and more precise length scales for the cross flows are employed where merited. The Ohnesorge number Oh in our case is the reciprocal value of the

REYNOLDS number with v_0 as the characteristic velocity:

$$\mathrm{Oh} = \sqrt{\frac{\rho\nu^2}{\sigma D_h}} = \frac{2\nu}{D_h v_0} = \frac{2}{\mathrm{Re}_0} \quad \text{with} \quad \mathrm{Re}_0 = \frac{D_h v_0}{\nu} \tag{2.3}$$

The characteristic velocity v_0 can be seen as a wave speed of the system and it also scales the maximum velocity of spontaneous, or capillary-driven flows, see Dreyer *et al.* (1994). The dimensionsless flow length for the parallel plates, wedge and gapped wedge corresponds to the length introduced in entrance flow problems (see Sparrow & Lin, 1964, among others):

$$\mathcal{L} = \frac{Oh}{2D_h} l = \frac{l}{\mathrm{Re}_0 \mathrm{D_h}} \tag{2.4}$$

The dimensionless flow rate is defined for all three cases:

$$Q' = \frac{Q}{A_0 v_0}. \tag{2.5}$$

Due to the fact that the flows along the tilted plate accelerate or decelerate depending on the sign of the tilt angle, the entrance lengths for this channel geometry requires alternate expressions.

The solution of Eq. (2.1) is achieved by numerical treatment of the governing equations which will be derived in section 2.4. It gives the limiting flow rate in a numerical sense, i.e. the algorithm does not converge due to the occurance of a singularity at the critical flow rate. The critical flow rate in the experiment is realized when the free surface becomes unstable and gas ingestion occurs at the outlet. In our theory and in experiments we performed so far we only considered quasi stationary increases of the flow rate. Transient or oscillatory changes are planned for this experiment but theory is under development. The proof to be given by the proposed experiment is the validity of the theoretical approach and the application of our assumptions. In part, the proof will be given in terms of the free surface shape and the value of the critical flow rate. This requires the measurement of the free surface position and the flow rate with high accuracy.

2.2 Application for Liquid Management in Space

Open capillary channels are used in space technology to transport and position liquids. An open capillary channel is a structure of arbitrary geometry which establishes a liquid flow path at low BOND number. The free surface of the liquid is always exposed to the ambient pressure and the liquid is fixed inside the channel due to capillary forces. Prominent applications are heat pipes and surface tension tanks for satellites. In the latter case, open capillary channels, so called vanes, provide a flow path from the bulk of propellant to the tank outlet. Ordinary vanes consist of a thin metal sheet mounted parallel or perpendicularly

to the tank shell. Whenever the vane is in contact (or in 'near proximity' in the case of the gapped wedge) with the propellant the vane fills itself due to the capillary forces. Driven by a gradient of the capillary pressure between the liquid head in the vane and the bulk liquid, the propellant flows to the tank outlet. Thus, vanes are simple and elegant devices for the direct supply of fuel to the tank outlet independent of where the bulk propellant is located in the tank.

In addition to the physical constraint of the system geometry and fluid properties, capillary flows along vanes are limited by spacecraft acceleration levels that can increase the BOND number, destabilize the interface, and interrupt the flow. If either limit is exceeded the flow collapses and gas will be ingested into the engine. Depending on the specific system requirements, two technical solutions are currently used to avoid gas ingestion. In cases of low flow rate and low acceleration, the vanes are used for direct supply and maximal flow rate are crudely estimated requiring high safety factors. For much higher flow rates and higher BOND numbers the propellant is buffered in a refillable liquid reservoir that feeds the engine during the maneuver. After the maneuver the reservoir is refilled by means of the vanes.

2.3 Brief Literature Survey

In spite of the high number of applications the effects of flow-rate limitation in open capillary channel flows have not been throughly investigated. As far as the literature shows, theoretical work is rare and just a few publications dealing with numerical model computations are available. Experimental investigations have not been performed, except for the experiments presented in this proposal.

Focussing on a particular PMD-design, Jaekle (1991) performed numerical model computation of a liquid flow through two communicating T-shaped capillary channels ('simple vane'). Neglecting the surface curvature in the flow direction, the one-dimensional momentum equation was solved numerically yielding the radius of curvature in the cross-sectional plane and the corresponding flow rates of steady and time-dependent flows. For this model, solutions for interface shapes could not be computed for all flow rates. Jaekle attributed this phenomenon to a 'choking-effect', i.e. a general flow rate limitation. However, the proof of this effect as well as the the discussion of its physical origin were not given. Experimental investigations of forced flow through an open capillary parallel-plate channel were performed in a 4.74 s drop tower. An upper bound was found for the steady volumetric flow rate. Above that limit, the free surfaces collapsed and gas ingestion occurred at the channel outlet (Dreyer *et al.*, 1998; Rosendahl *et al.*, 2001, 2002). The experiments were based on the work of Dreyer (1994) who investigated the rise of liquid between two parallel plates after a

step reduction of gravity in a drop tower. It was shown that the velocity of the rising liquid cannot exceed a certain critical value. Likewise, motivated by challenges in low-gravity propellant management, Srinivasan (2003) computed the flow rates of capillary self-driven liquid flows in open parallel-plate channels. A semi-analytical method for the solution of the steady three-dimensional Stokes equations was proposed that assumes extremely small flow rates. For two data sets, the computations were compared to the experimental results from (Rosendahl *et al.*, 2002). The computed flow rate was approximately three times lower than the experimental measurement which the author attributes to the inertia in the experiment. Experimental, numerical and theoretical investigations of open parallel-plate channels were performed by Rosendahl *et al.* (2004*b*). The experiment was operated under microgravity conditions aboard the sounding rocket TEXUS-37. In this experiment the flow limit was approached by a stepwise increase of the volumetric flow rate. For the flow prediction a theoretical one-dimensional flow model was developed. Its numerical solutions for the profiles of the free liquid surfaces are in good agreement with the experimental results. Furthermore, theory and experiment confirm that limitations of the flow rate occur due to a choking effect, analogous to the well known phenomena for compressible flow in ducts.

Der (1991) analysed the propagation of small disturbances in simple vanes theoretically. Motivated by the technical application in PMDs, the work poses the question of which speed and in which direction waves propagate along the vane if the fluid is at rest. Neglecting the radius of curvature in the flow direction as well as the viscosity, a linear wave equation, analogous to the acoustic wave equation, is derived. Thus, the considered waves are of the longitudinal type. Der shows that the wave speed depends on the liquid volume attached to the vane. In the case that the corresponding radius of curvature is smaller than the vane height the wave speed depends on the fluid properties and the radius of curvature. This speed can also be derived from the general from Eq. (9.22) presented in appendix C. In the case of a radius of curvature larger than the vane height the speed additionally depends on the vane height itself.

To our knowledge, no significant body of research exists for other conduit geometries addressing phenomena specific to the inertial-capillary regime such as wave propagation phenomena and choking. (Note: the work of Quéré (1997); de Ryck & Quéré (1996) is acknowledged relevant to inertial-capillary phenomena, but is not sufficiently applicable here.) However, a significant effort has been made to understand related phenomena such as capillary-driven flows along interior corners, grooves, wedges, rounded corners, and vane gaps. The wide majority of such studies have focused on viscous dominated flows with only glimpses into the inertial regime (Weislogel & Lichter, 1998; Chen & Collicott, 2004). It is only necessary to mention several papers in connection with this research. For example, Romero & Yost (1996) consider the spreading of a liquid wetting front in a V-shaped surface groove (wedge). The position of the wetting front is proportional to $\sqrt{Dt}$. D is the diffusion

coefficient which depends on the fluid properties, the contact angle and the groove angle. Weislogel & Lichter (1998); Weislogel (2001*a*); Weislogel & Collicott (2004) investigate the flow along the interior corners of polygonal cylinders and models of heavily-vaned spacecraft fuel tanks after sudden reductions of 'gravitational' forces. The theoretical predictions of the liquid flow follow from a nonlinear one-dimensional diffusion equation in a similar manner as previous authors, but uniquely without the strong dependence on numerical data (i.e. Ransohoff & Radke (1988) and Ayyaswamy *et al.* (1974)). The theoretical results are compared with the experimental data collected using 2.2 s drop tower, low-g aircraft, and certain space flight experiments. Flows in infinite corners, damped waves, spreading drops, steady flows, as well as flows in irregular polygonal vessels were recently reviewed Weislogel (2003*a*), and several articles are forthcoming (i.e. Weislogel (2006)). In such investigations, maximum flow rates are predicted for viscous-dominated flows only and efforts to include inertia as a small parameter have proven difficult.

The theory of choking in compressible gas flow is discussed in several textbooks, e.g. Faber (1995), Landau & Lifschitz (1991), White (1991), and Shapiro (1953). The last mentioned publication is emphasized since it gives an substantial explanation of the choking phenomena and detailed derivation of all relevant equations. An explanation and theoretical derivation of choking in an open channel flow under normal gravity is given in Smits (2000). Here the considered choking effect occurs since the liquid flows through a smooth constriction.

2.4 Current Status of Understanding

In this section a brief overview of the mathematical approaches for the geometries shown in Fig. 2.1 is given. The specific equations for each geometry and detailed derivations are described in the appendices (i.e. Appendix A for parallel plates). The tilted plate and gapped wedge channel geometries are analyzed using similar methods. The appendices contain all the relevant coefficients to use the general equations and are considered to be confidential (partly unpublished data).

2.4.1 Parallel plate and groove-shaped channel

To provide some insight into our analytical method, we consider a capillary liquid flow in a channel of two parallel plates. The other channel geometries are analyzed using similar methods. The flow enters the channel via the inlet and leaves through the outlet. The flow is created by an external pump at the outlet. The inlet is connected to a reservoir which provides the necessary liquid volume. Along the open sides of the channel liquid surfaces are formed. A steady flow is obtained only for a flow rate below a critical value ($Q < Q_{crit}$). For $Q > Q_{crit}$ the liquid surfaces collapse at the channel outlet, and the flow changes from

steady single phase flow to unsteady two-phase flow.

Mathematical Approach

For the analysis we follow the steady state approach introduced by Jaekle (1991) for the flow rate limitation in different capillary vanes. We assume a one-dimensional, isothermal flow along the channel axis x characterized by the mean velocity v and the liquid pressure p. The basic equations to be solved are the momentum equation

$$\underbrace{v\frac{\mathrm{d}v}{\mathrm{d}x}}_{\mathrm{I}} = \underbrace{-\frac{1}{\rho}\frac{\mathrm{d}p}{\mathrm{d}x}}_{\mathrm{II}} - \underbrace{\frac{4\tau_w}{\rho D_h}}_{\mathrm{III}} \tag{2.6}$$

and the equation of continuity

$$\frac{\mathrm{d}Q}{Q} = \frac{\mathrm{d}A}{A} + \frac{\mathrm{d}v}{v} = 0. \tag{2.7}$$

Here $Q = Av$ is the constant volumetric flow rate passing the cross sectional area A of the flow in the planes $x = \text{const}$. The terms in the momentum equation result from the convective momentum transport (I), the gradient of the static pressure (II) and the viscous or molecular momentum transport (III). The irreversible pressure gradient due to viscous forces,

$$\frac{\mathrm{d}p_v}{\mathrm{d}x} = -\frac{4\tau_w}{D_h}, \tag{2.8}$$

is approached by the generalized form for non-circular cross sections based on the mean wall shear stress τ_w and the hydraulic diameter

$$D_h = \frac{4A_0}{U} \tag{2.9}$$

according to White (1991). Herein $A_0 = ab$ is the cross section area of the channel and U its wetted perimeter. The hydrostatic pressure is neglected due to the vanishing body force under microgravity conditions. The criterion for this neglect is that the Bond numbers along the three coordinate directions are smaller than 1%, i.e.

$$\mathrm{Bo}_x = \frac{\rho g_x l a}{2\sigma} < 0.01 \tag{2.10}$$

$$\mathrm{Bo}_y = \frac{\rho g_y a^2}{2\sigma} < 0.01 \tag{2.11}$$

$$\mathrm{Bo}_z = \frac{\rho g_z b a}{2\sigma} < 0.01. \tag{2.12}$$

Under isothermal conditions and for negligible small shear stress at the gas-liquid interface, the static pressure p is related to the curvature of the liquid surface by the Gauss-Laplace equation (see Antar & Nuotio-Antar (1993))

$$\frac{p - p_a}{\sigma} = -2H = -\left(\frac{1}{R_1} + \frac{1}{R_2}\right). \tag{2.13}$$

Here H is the mean curvature of the surface, R_1 and R_2 are the principal radii of curvature. We follow the mathematical convention that R_1 and R_2 have a positive sign if the normal vector on the liquid surface points towards the concave side of the free surface (see Bronstein & Semendjajew, 1987). Since the ambient pressure p_a is constant the pressure gradient becomes

$$\mathrm{d}p = -2\sigma \mathrm{d}H. \tag{2.14}$$

Due to the low lateral Bond numbers Bo_y and Bo_z and the one-dimensional character of the flow, symmetries of the liquid surface with respect to the planes $y = 0$ and $z = 0$ exist. Therefore the consideration of the surface can be reduced to the consideration of the surface profile k. The profile is defined by the intersection line of the liquid and the plane $y = 0$ and corresponds to the innermost position of the surface (see Fig. 7.3a for the parallel plates and in Fig. 8.2 for the groove in appendix A and B, respectively). Using the profile the general form of the surface curvature may be simplified by the approximation

$$2H(x, y = 0) = \frac{1}{R_1} + \underbrace{\frac{\mathrm{d}_{xx}k}{(1 + (\mathrm{d}_x k)^2)^{3/2}}}_{R_2^{-1}} \tag{2.15}$$

with the derivatives $\mathrm{d}_x k = \mathrm{d}k/\mathrm{d}x$ and $\mathrm{d}_{xx}k = \mathrm{d}^2k/\mathrm{d}x^2$. Herein the second term defines the portion of the curvature in flow direction, determined by the inverse principal radius of curvature $1/R_2$. The first term gives the portion of the curvature transversal to the flow, determined by the inverse principal radius of curvature $1/R_1$. Note that the radius R_1 as well as the cross section area A are only function of the profile, $R_1 = R_1(k)$ and $A = A(k)$.

The gradient of the irreversible pressure loss due to viscous forces $4\tau_w/D_h$ consists of two parts, the laminar viscous pressure loss $4\tau_{wl}/D_h$ and the additional entrance pressure loss $4\tau_{we}/D_h$, which is a result of the change of the velocity field from the entrance profile to the fully developed velocity distribution (Poiseuille flow in case of the parallel plates channel). For the fully developed laminar liquid flow between two infinite wide parallel plates an analytic solution of the two-dimensional Navier-Stokes exists. From this solution the wall shear stress

$$\tau_{wl} = \frac{K_{pl}}{\mathrm{Re}_h} \frac{\rho v^2}{8} \quad \text{with} \quad \mathrm{Re}_h = \frac{D_h v}{\nu} \tag{2.16}$$

may be derived (see White, 1991), where K_{pl} is a friction constant and Re_h the Reynolds number based on the hydraulic diameter D_h. Since the flow velocity varies along the flow path due to the changing cross section area, Eq. (2.16) is applied locally (vgl. Spurk, 1992), so that

$$\tau_{wl}(x) = \frac{\mu K_{pl}}{8 D_h} v(x) = \frac{\mu K_{pl}}{8 D_h} \frac{Q}{A(x)} \tag{2.17}$$

is achieved. Here $\mu = \nu\rho$ is the dynamic viscosity. For the parallel plates channel $K_{pl} = 96$ applies, for the groove the friction constant needs to be adapted according to the aspect

ratio, $K_{pl} = K_{pl}(\Lambda)$ (interpolation of the values given by White, 1991, Table 6.4). The determination of the additional pressure loss due to the inlet flow is based on the work of Sparrow & Lin (1964). The authors provide an analytic relation for the pressure loss factor K from which the wall shear stress may by calculated by

$$\tau_{wl}(x) = \frac{2\mu K_{pe}}{D_h} v(x) = \frac{2\mu K_{pe}}{D_h} \frac{Q}{A(x)} \tag{2.18}$$

with

$$K_{pe}(\check{x}) = \frac{\mathrm{d}K(\check{x})}{\mathrm{d}\check{x}}. \tag{2.19}$$

Herein $\check{x}$ is an internal flow coordinate, which has to be transformed if velocity distribution of the considered flow at the channel inlet deviates from the underlaying homogenous distribution. The pressure loss factor K is derived for flow between parallel plates but it might also be applicable for grooves. With Eq. (2.17) and Eq. (2.18) the gradient of the total frictional pressure loss reads

$$\frac{4\tau_w}{D_h} = \frac{4(\tau_{wl} + \tau_{we})}{D_h} = \frac{\mu(K_{pl} + 16K_{pe})}{4D_h^2} \frac{Q}{A(x)}. \tag{2.20}$$

Using the definition of the flow rate $Q = Av$, the second term of Eq. (2.6) can be rewritten as

$$\rho v \frac{\mathrm{d}v}{\mathrm{d}x} = -\rho \frac{Q^2}{A^3} \frac{\mathrm{d}A}{\mathrm{d}x}. \tag{2.21}$$

With Eq. (2.14), Eq. (2.20) and Eq. (2.21) the momentum equation (2.6) reads

$$\sigma \frac{\mathrm{d}(2H)}{\mathrm{d}x} + \rho \frac{Q^2}{A^3} \frac{\mathrm{d}A}{\mathrm{d}x} - \frac{\mu(K_{pl} + 16K_{pe})}{4D_h^2} \frac{Q}{A} = 0. \tag{2.22}$$

The reformulation of Eq. (2.15) yields

$$\frac{\mathrm{d}^2 k}{\mathrm{d}x^2} + \left(\frac{1}{R_1} - 2H\right) \left[1 + \left(\frac{\mathrm{d}k}{\mathrm{d}x}\right)^2\right]^{3/2} = 0. \tag{2.23}$$

These model equations are coupled ordinary differential equations of first order in H and second order in k and require three boundary conditions. They are given by the fixed liquid surface at the channel inlet and outlet

$$k(x = 0) = k(x = l) = k_0 \tag{2.24}$$

where $k_0 = b/2$, and the surface curvature at the channel inlet

$$2H_0 = 2H(x = 0). \tag{2.25}$$

Eq. (2.25) depends on the flow path before the channel inlet, but due to the complex geometry of the experiment setup analytical relations are generally not available. For this

reason three-dimensional numerical computations of the flow in the geometry before the inlet are required. The pressure loss may be approximated by

$$2H_0 = \Big(K_1 + \frac{K_2}{Re_{h_0}}\Big)\frac{\rho v_0^2}{2\sigma} + \frac{p_a - p_1}{\sigma} \tag{2.26}$$

where K_1 and K_2 are constants and $p_a - p_1$ is the capillary pressure at a reference liquid surface (e.g. the liquid surfaces of the liquid reservoir or the compensation tube in the experiments, see §3.1).

Non-dimensional Equation

For the non-dimensionalisation of Eq. (2.22) and Eq. (2.23) all length perpendicular to the flow direction are scaled by $a/2$. The cross sectional area is non-dimensionalized with $A_0 = ab$ and the x-axis with the channel length l. From the scaling of the GAUSS-LAPLACE equation (Eq. (2.13)) the characteristic pressure $\tilde{p} = 2\sigma/a$ is achieved which yields the characteristic velocity $\tilde{v}_c = \sqrt{\tilde{p}/\rho} = \sqrt{4\sigma/\rho D_h}$. This velocity is already known as characteristic property from experiments of the capillary rise of liquids between parallel plates (see Dreyer, 1994). For the wall shear stress we find $\tilde{\tau_w} = 4\mu\tilde{v}_c/D_h$.

With this scaling the dimensionless form of Eq. (2.22)

$$\frac{\mathrm{d}h'}{\mathrm{d}x'} + \frac{Q'^2}{A'^3}\frac{\mathrm{d}A'}{\mathrm{d}k'}\frac{\mathrm{d}k'}{\mathrm{d}x'} - \Big[K_{pl} + 16K_{pe}(\check{x}_S)\Big]\frac{\mathcal{L}Q'}{2A'} = 0. \tag{2.27}$$

is obtained, whereas the primes denote dimensionless variables. Note the for numerical reasons a new variable $2H' = h$ was introduced. The curvature term reads in dimensionless form:

$$\Gamma^{-2}\frac{\mathrm{d}^2k'}{\mathrm{d}x'^2} + \left(\frac{1}{R_1'} - h'\right)\left[1 + \Gamma^{-2}\left(\frac{\mathrm{d}k'}{\mathrm{d}x'}\right)^2\right]^{3/2} = 0. \tag{2.28}$$

The Eq. (2.27) has to be integrated numerically together with Eq. (2.28) and the boundary conditions which are (i) the position of the surface at the inlet and outlet of the channel and (ii) the surface curvature at the channel inlet. The numerical solution yields the dimensionless position $k'(x')$ of the liquid surface in terms of

$$k'(x') = f(\Lambda, \mathrm{Oh}, \mathcal{L}, Q'). \tag{2.29}$$

For each set of Λ, Oh, and $\mathcal{L}$ several computations with different Q' have to be performed. We assume that the critical flow rate is reached when the numerical integration does not converge. As the maximum theoretical flow rate Q'_{crit} we define the maximum flow rate Q' leading to the convergence of the numerical algorithm. Thus for each set of Λ, Oh and $\mathcal{L}$ the critical flow rate $Q'_{crit} = f(\Lambda, \mathrm{Oh}, \mathcal{L})$ is the result of an iteration within a given numerical accuracy. The parameter ranges for which numerical calculations were performed are given in Table 2.2.

	Oh	Π	$\mathcal{L}$
parallel plates	$10^{-5} \leq \text{Oh} \leq 10^{-2}$	$\Lambda = 1; 2; 5; 50$	$10^{-5} \leq \mathcal{L} \leq 10$
groove	$10^{-5} \geq \text{Oh} \geq 10^{-2}$	$\Lambda = 0.7; 1; 2; 5; 50$	$10^{-5} \geq \mathcal{L} \geq 10$

Table 2.2: Parameter space for the computation of the critical flow rate.

Cause of the flow rate limitation

We discovered two effects as cause of the flow rate limitation in open capillary channels. These effects occur in different parameter ranges, and according to the limiting mechanism they are denoted as 'viscous limitation' and 'waves speed limitation (choking)' (Rosendahl, 2006).

For very large $\mathcal{L}$ the convective term in Eq. (2.27) is negligible small compared to the viscous term. Under these conditions the flow reduces to a pure STOKES flow, and the increase of the capillary pressure along the flow path (increasing $H(x)$) is caused only by viscous forces. The maximum flow rate is achieved when differential pressure between the liquid and gas phase is identical to the maximal capillary pressure of the the surface due to its maximum curvature. For larger flow rates the flow becomes unstable since the liquid surface cannot withstand the low pressure. These flows can be investigated on ground, and are not subject of the proposed investigations.

For small and moderate $\mathcal{L}$ the flow is determined more or less by both, the convective and the viscous term in Eq. (2.27). The limitation of the flow rate occurs then due to a choking effect, analogous to the well known phenomena for compressible flow in ducts. Choking denotes the effect that the mass flux of a flow becomes maximum if the flow velocity v locally reaches a certain limiting wave speed. In compressible gas duct flows, the characteristic limiting wave speed is defined by the speed of sound v_s. The characteristic number is the MACH number ($\text{Ma} = v/v_s$), and the maximum flow passes through a duct when $\text{Ma} = 1$. In gravity dominated open channel flows, the speed of shallow-water waves v_{sw} corresponds to the limiting velocity. The flow is characterized by the FROUDE number ($\text{Fr} = v/v_{sw}$), and choking occurs for $\text{Fr} = 1$. Both wave speeds are derived from the general form

$$v_l = \sqrt{A \frac{\mathrm{d}p}{\mathrm{d}(\rho A)}}. \tag{2.30}$$

Eq. (2.30) is the wave speed of longitudinal waves in flows in which the density and the cross section are related to the fluid pressure (Lighthill, 1978). This wave speed is valid in compressible flows in ducts, with constant cross section as well as in free surface flows in open channel with uniform walls, or flows in flexible tubes. A close analogy exists between these flow types and the open capillary flows investigated in the present work. To show that

the flow rate limitation is caused by choking, we introduce the capillary speed index

$$S = \frac{v}{v_c} \tag{2.31}$$

analogous to the Mach number and the Froude number. Herein

$$v_c = \sqrt{-\frac{2\sigma A}{\rho}\frac{\mathrm{d}H}{\mathrm{d}A}} \tag{2.32}$$

is the speed at which longitudinal small-amplitude waves in open capillary channels propagate which we achieve by applying Eq. (2.13) to Eq. (2.30). In case of choking the liquid velocity and Eq. (2.32) are identical, and $S = 1$.

Using the definition of the speed index, Eq. (2.27) can be rewritten, and the following dimensional formulas are achieved:

$$\frac{\mathrm{d}p}{\mathrm{d}x} = -\frac{\nu\rho A[K_{pl} + 16K_{pe}(\check{x}_S)]}{2D_h(1-S^2)}, \tag{2.33}$$

$$\frac{\mathrm{d}A}{\mathrm{d}x} = -\frac{\nu A^2 S^2[K_{pl} + 16K_{pe}(\check{x}_S)]}{2D_h Q(1-S^2)} = -\frac{\mathrm{d}v}{\mathrm{d}x} \tag{2.34}$$

and

$$\frac{\mathrm{d}S^2}{\mathrm{d}x} = \frac{\nu A S^4(2+M)[K_{pl} + 16K_{pe}(\check{x}_S)]}{2D_h Q(1-S^2)} \tag{2.35}$$

with

$$M = 1 + A\frac{\mathrm{d}^2h/\mathrm{d}A^2}{\mathrm{d}h/\mathrm{d}A}. \tag{2.36}$$

Eq. (2.33) through Eq. (2.35) define the gradient of the properties p, A, v and S along the flow path. The sign of the gradient depends on whether the speed index is larger or smaller than unity, since the term $(1 - S^2)$ appears in the denominator. Note that the structure of the equations is analogous to the well-known equations for compressible gas flows (see Shapiro, 1953). From the model assumptions it is known that both the cross section A as well as the pressure p decrease along the channel axis since the liquid accelerates. Therefore it follows from Eq. (2.33) and Eq. (2.34) that the investigated flow must be subcritical ($S < 1$). Accordingly, the speed index given by Eq. (2.35) increases in flow direction. For the supercritical flow ($S > 1$) the opposite behavior occurs. Since p, A increases along the flow path, the speed index decreases. On both flow branches $S = 1$ defines the flow limit, since for this value a singularity occurs in Eq. (2.33) through Eq. (2.35). At that state choking is present, and the flow rate is maximum. A flow rate above this critical value leads to collapse of the liquid surface, and the time dependent form of Eq. (7.41) must be solved to predict the flow.

2.4.2 Wedge-shaped channel

Inertially-dominated corner flows are most readily analyzed using the general approach outlined above for parallel channel flow. In such cases, the viscous resistance term requires $K_{pf} = 8/F_i$, where $1/8 \leq F_i(\alpha, \theta) \leq 1/6$. θ is the contact angle.

The viscous limit ($Re_h(D_h/4L) << 1$) provides an analytic benchmark for the otherwise numerical solutions in both overlap and fully inertial regimes. The Navier-Stokes equation for this limit is

$$\frac{F_G}{\mathrm{Oh}^2}\frac{DU}{Dt} = \nabla P + \nabla^2 U \tag{2.37}$$

where F_G is a system-dependent geometric function. When $F_G/\mathrm{Oh}^2 << 1$, the flow is either slow, parallel, or both (i.e. inertia is small). Under the constraint of a parallel flow, the free surface may be expressed as a construct of circular arcs in the y-z-plane satisfying the contact angle condition at the wall. The Navier-Stokes equation reduces to the x-component equation at leading order, which when integrated numerically can be used to determine the x-component velocity distribution $u(y, z, x, t)$. Numerically integrating this velocity over the cross-flow section yields the average velocity (and F_i), which when substituted into the global mass balance equation in the x-direction yields a governing nonlinear PDE for a variety of flows differing only by respective boundary conditions. The proper scaling of the governing equations significantly reduces the reliance on numerical data for the many closed form expressions that result.

The governing partial differential equation resulting from the global x-component mass balance is akin to the foam drainage equation (Verbist *et al.*, 1996) and a most simplified version is given by

$$k_t = 2k_x^2 + kk_{xx} \tag{2.38}$$

This equation is applicable for all values of contact angle and corner half-angle satisfying the critical wetting condition studied mathematically by Concus & Finn (1969), where $\theta < \pi/2 - \alpha$ in order to achieve the capillary flow condition studied here. Many solutions to Eq. (2.38) are possible using a variety of analytic and numerical techniques depending on the boundary conditions for the particular problem. Such solutions provide practical results for use in low-g fluids system design.

2.5 Key Issues where Knowledge is Still Lacking

As mentioned, the flow rate limitation in open capillary channels has not been discussed significantly in the literature. Experimental work is rare, and only a few publications dealing with numerical model computations are available. Experimental investigations have not been performed except for the experiments presented in this document. In addition, open capillary

channels are part of technical applications in heat pipes or in surface tension tanks. Since experimental data concerning the maximal flow rate is lacking the design is performed by using large safety factors. From this background we propose to investigate open capillary channel flows both from the applied and fundamental points of view. In section 3.1 we show results for the maximal flow rate and the corresponding critical velocity in a capillary channel. We demonstrate that our calculations are in good agreement with experiments performed in the drop tower and the TEXUS sounding rocket. Furthermore, the experiment on board the sounding rocket confirmed the influence of the speed index. All recent knowledge is limited to a quasi steady increase of the flow rate. The experiment objectives are to test the theoretical predictions for the free surface shapes and the critical flow velocities, and to validate the assumptions put in the derivation of the governing equations. The experiments are designed to investigate a parameter space in which the flow is dominated by convection. In addition to the steady increase of the flow rate, transient and oscillatory changes of the flow velocity will be investigated. Since an analogy to FROUDE and MACH number problems is expected, the experiments shall answer the question whether the speed index is the relevant parameter to characterize the liquid flow in the capillary channel.

For the wedge flow scenario, significant challenges remain in the analytical treatment of flows with leading order and first order inertia. An experimental database is nonexistent. For the large length scale capillary flows to be addressed in this research Re $\sim$ O(1000) is routine, a value many times larger than possible for terrestrial flows. But inertia remains a second order quantity in ground studies due to the parallel nature of the flows addressed. This should not be the case for flows aboard spacecraft where rapid changes in the flow direction or interface curvature necessitate the inclusion of inertial terms in the governing system of equations – a non-trivial task. Inertia in corner flows has been observed and reported (Weislogel & Lichter (1998) and Allen (2003)), but not sufficiently analyzed.

3 PI's Related Research and Proposed Space Experiment

3.1 Parallel plate and groove-shaped channel

Capillary flows in open channels consisting of two parallel plates have been investigated in this research project with a large number of experiments using the drop tower, parabolic aircraft and sounding rocket. The first experiments were carried out in the Bremen drop tower and were based on the experiments of capillary liquid rise between two parallel plates performed by Dreyer *et al.* (1994); Dreyer (1994). Dreyer et al. investigated the capillary rise of various liquids in channels of different geometries and predicted theoretically the time-dependance of the liquid rise.

For the first generation of drop tower experiments, the set up used by Dreyer (1994) was modified. A withdrawal device was mounted at the end of the parallel plates which stood upright in a container of liquid. During the experiments the capillary liquid rise was used to fill the channel before the withdrawal device was started to establish a liquid flow between the parallel plates. Several experiments with various liquids and different channel properties were performed[1]. The maximal flow rate determined from the experiments showed good agreement with the theoretical prediction presented in appendix A. Nevertheless the flow conditions provided by the set up were not satisfying. Due to the transition from the self-driven capillary flow to the forced flow, inertia effects occurred which made a controlled approach of the critical value impossible. Furthermore the established flow rate had to be kept constant since the short experimental time did not allow an increase of the flow rate.

To operate under longer μg-time an experiment module flown on the sounding rocket TEXUS-37[2] was developed. The preparations for TEXUS lead to a new experimental concept. The set-up allows an increase of the flow rate in fine steps up to the critical value. To keep the inertia effects small the flow is established by two synchronized pumps. Three-dimensional model computations were performed to optimize the flow conditions in the experiment cell and to define the boundary conditions of the flow precisely. At the same

[1] The drop tower experiments were funded by the European Space Agency (ESA).

[2] The sounding rocket experiment was performed with funds of the European Space Agency (ESA) (hardware and the flight opportunity) and the German Aerospace Center (DLR) (research project).

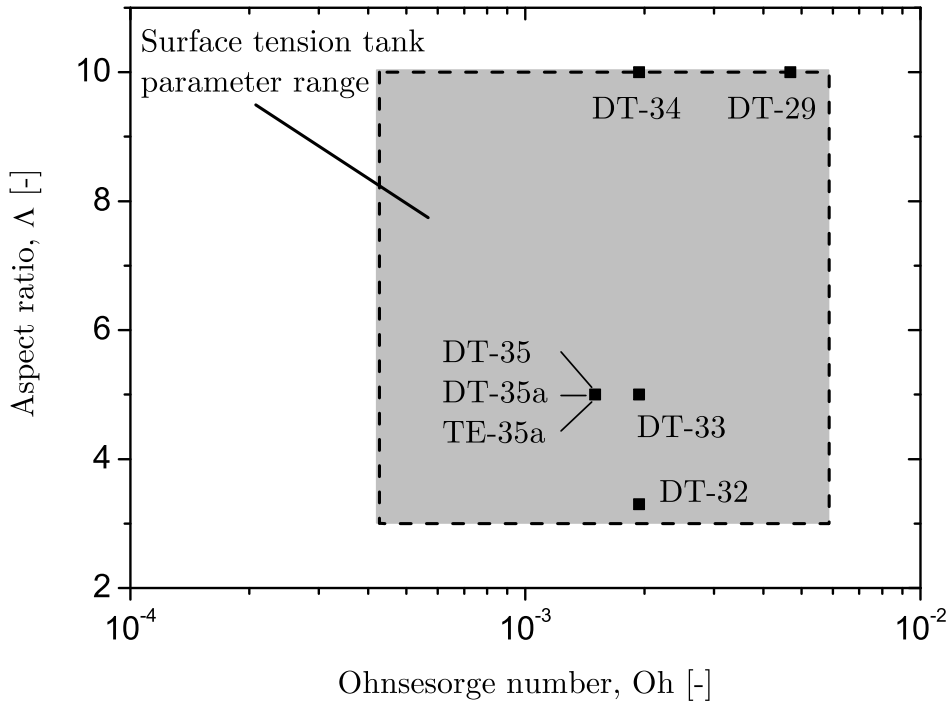

Figure 3.1: Typical parameter space of Oh and Λ for surface tension tanks in satellites (dashed frame). The black squares denote experiments performed in the drop tower. The parameter set TE-35a was chosen for the experiment on board the sounding rocket TEXUS.

time a new experiment module for use in the drop tower and parabolic flights was built. It is based on the TEXUS concept and its operation is analogous to that of the TEXUS experiment. Thus, the concept of the TEXUS experiment module could be tested in advance. The parabolic flights were necessary to get practical experience for the experiment control under the longer microgravity conditions of the TEXUS flight.

The following sections give a brief overview of the different experiments performed in the drop tower and on board the sounding rocket TEXUS-37. The experiment set-up and the main results are discussed as well as the choice of parameters on which the experiments are based. Since the idea of these experiments was motivated by the application of capillary channels (vanes) in surface tension tanks, the experimental parameters were chosen with respect to propellant data (N_2O_4 and mono-methyl-hydrazine, MMH) and tank geometries. Satellite tanks usually operate in the temperature range $0 \leq T \leq 40$ °C and typical geometries are: gap distances $1 \leq a \leq 10$ mm, plate breadths $10 \leq b \leq 30$ mm. This leads to the parameter space given by the combination $4.27 \cdot 10^{-4} \leq \mathrm{Oh} \leq 5.881 \cdot 10^{-3}$ and $3.3 \leq \Lambda \leq 10$ shown in Fig. 3.1. The numbered black dots denote experiments performed in the drop

tower. As Fig. 3.1 shows, not all desired combinations of Oh and Λ can be obtained in the drop tower experiments. The choice of parameters is restricted essentially by two factors, the capillary rise time and the optical resolution. The rise time is required to fill the channel before the actual experiment can be started. It has to be kept small to get maximal observation time of the channel flow. For the evaluation of the free surface a minimum resolution of the video pictures is necessary. To operate with a resolution of 0.1 mm/pixel the breadth and the length of the plates are limited to $b = 30$ mm and $l = 100$ mm, respectively. Based on a defined set of Oh and Λ the length of the channel has to be chosen with respect to the rise time. Using a low viscosity silicone oil (Silicone Fluid 200 DOW Corning 0.65 cSt) the minimal value of Oh $= 1.52 \cdot 10^{-3}$ leading to an appropriate rise time was attained. The parameter set #35 was chosen for the experiment on board the sounding rocket.

3.1.1 Experiments in Drop Tower

The experiment was developed to operate within a drop capsule of the Bremen drop tower. With the 110 m long drop tube evacuated to approximately 10 Pa the drop tower provides a free fall of 4.74 s. The residual acceleration measured in the capsule is less than 10^{-5} g_0. Fig. 3.2 shows the schematic drawing of the experimental set up. The capillary channel (1) stands upright in a liquid container (2). Both the channel and the container are manufactured from acrylic glass (PMMA, perspex, plexiglass). On the top of the channel a suction head (3) is mounted. It is connected to a syringe (9) which is mounted to a linear drive (10).

To avoid liquid rise outside the channel during the experiments, circular pinning (5) lips are mounted at a certain height inside the liquid container and outside the channel. The container is filled with the test liquid up to the bottom edges of the lips. Since both plates are dipped into the liquid, the channel is filled up to the wetting lips under 1g-conditions. In order to operate the experiment under a defined liquid temperature, the temperature of the container is controllable. The tempering is achieved by a flexible tube coil which may be supplied by an external tempering unit (7). The channel is observed by two CCD cameras (11) located outside the liquid container. Their optical axes are aligned perpendicular to the front plate of the channel. Both sections of the camera have an overlap in the middle of the channel. Markings on the outside of the channel define the orientation and the resolution of the picture for the digital image processing. The obtained resolution is approximately 0.1 mm/pixel at a frame rate of 25 fps. For a homogeneous background illumination (8) fluorescent light and a Teflon® diffuser were installed. A front view normal to the plates is shown in figure 3.3(a). Due to total reflection of the background light, the profiles of the liquid surfaces appear as dark zones on the video images. Referring to figure 3.3(b) the profiles are defined by the distance $b/2-k$, where the position k correspond to the innermost position of the liquid in the plane $y = 0$.

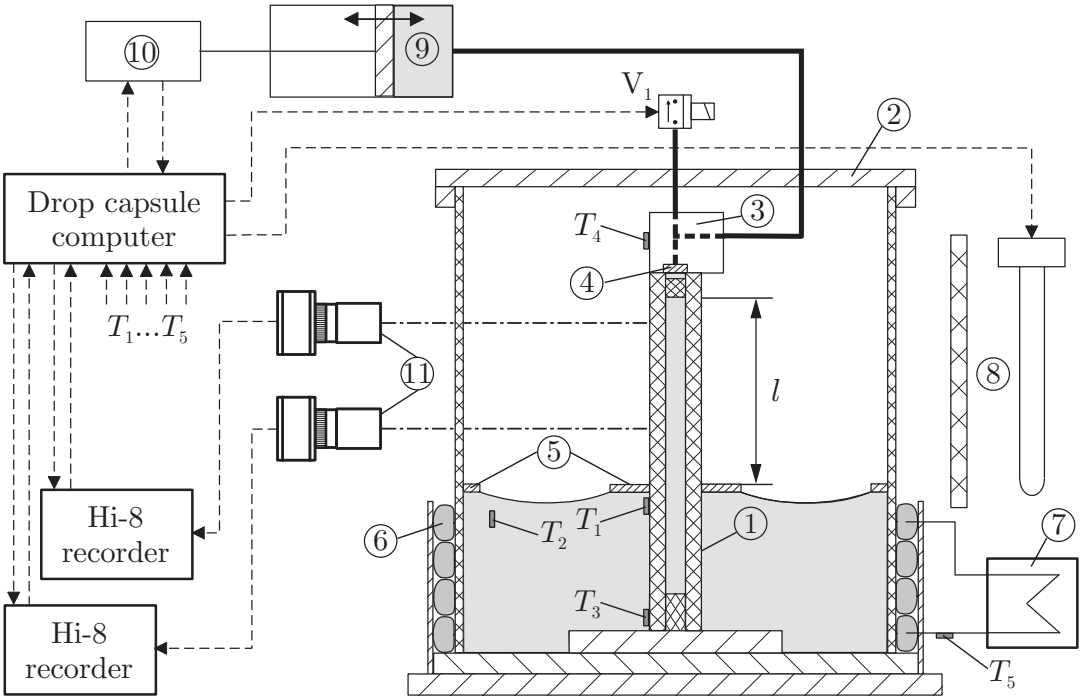

Figure 3.2: Schematic drawing of the experiment set-up for the drop tower. Capillary channel (1), liquid container (2), suction head (3), screen (4), pinning lips (5), flexible tube coil (6), tempering unit (7), background illumination (8), glass syringe (9), linear drive (10), CCD-cameras (11).

During the 90-minute long evacuation of the drop tube, the temperature of the liquid is kept constant at $T = 20°$ C. Before the drop the suction side is filled up to the screen (4) located at the inlet of the suction head. Gas bubbles are removed by the degassing valve (V_1). With the release of the capsule at time t_0, the liquid starts to rise between the plates. The liquid movement is caused by the capillary pressure gradient between the liquid surface in the container and the liquid surface in the gap of the plates. When the liquid meniscus contacts the suction device at t_c, the linear drive is started, and a defined constant volume rate Q is withdrawn from the channel by the syringe. The rise time $t_r = t_c - t_0$ can be predicted numerically from the meniscus acceleration derived by Dreyer (1994).

The parameter space of the experiments is listed in Table 3.1. All fluids show perfect wetting behavior at the capillary walls, thus the static contact angle is zero. The properties of the test liquids are given in Table 3.2. The choice of parameters is limited essentially by the rise time t_r and the resolution of the pictures. The lowest Ohnesorge numbers can be achieved with the fluid of the lowest viscosity, HMDS, and the widest gap distance of $a = 5$ mm (DT-35). Larger gap distances lead to longer rise times for the capillary to be

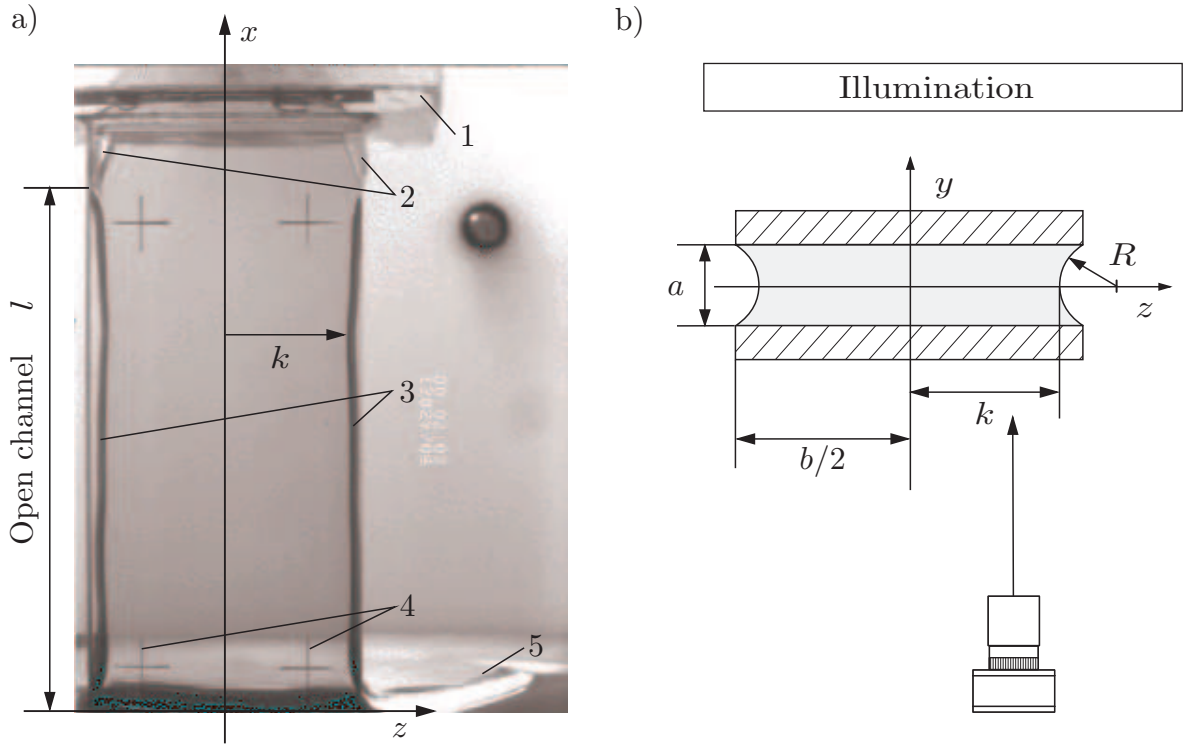

Figure 3.3: (a) Camera view of the channel in the drop tower experiment (parameter set DT-35a). Suction head (1), guiding wedges (2), surface profiles (3), calibration markings (4), pinning lip (5). Due to total reflection the surface profiles appear dark. (b) Orientation of the camera (schematically). The width of the profile corresponds to the distance $b/2 - k$.

filled before the suction starts and thus to shorter observation times of the flow through the capillary itself. To obtain a resolution of 0.1 mm/pixel the channel length is restricted to 100 mm.

A total of 40 experiments were performed with an average of 5 drops for each parameter set. The first drop serves to determine the exact rise time t_r of the liquid. This time has to be estimated within ± 0.05 s. If the withdrawal device starts too early, gas is ingested at the beginning of the suction. If the withdrawal device starts too late, the inertia of the rising meniscus tends to form convex menisci at the sides of the capillary. The additional volume contained in this overshoot must be withdrawn and reduces the observation time of the experiment. The following experiments for each parameter set were aimed to determine the critical flow rate. Due to the good agreement of the theory with the experiment the critical flow rate could be predicted with good accuracy and the number of drops could be minimized. For each parameter set one stable and one unstable flow rate with gas ingestion could be achieved. The highest stable flow rate was reproduced to minimize experiment

No.	Liquid	a [mm]	b [mm]	l [mm]	t_r [s]	Oh [-]	Λ [-]	$\mathcal{L}$ [-]
DT-29	FC-77	2	20	74.9	1.7	$4.57 \cdot 10^{-3}$	10.0	$4.3 \cdot 10^{-2}$
DT-32	HMDS	3	10	94.2	1.3	$1.96 \cdot 10^{-3}$	3.3	$1.54 \cdot 10^{-2}$
DT-33	HMDS	3	15	96.3	1.2	$1.96 \cdot 10^{-3}$	5.0	$1.57 \cdot 10^{-2}$
DT-34	HMDS	3	30	94.6	1.2	$1.96 \cdot 10^{-3}$	10.0	$1.55 \cdot 10^{-2}$
DT-35	HMDS	5	25	93.4	1.5	$1.52 \cdot 10^{-3}$	5.0	$7 \cdot 10^{-3}$
DT-35a	HMDS	5	25	48.4	0.7	$1.52 \cdot 10^{-3}$	5.0	$4 \cdot 10^{-3}$
TE-35a	HMDS	5	25	46.6	-	$1.52 \cdot 10^{-3}$	5.0	$4 \cdot 10^{-3}$

Table 3.1: Experiment parameters for the experiments in the drop tower (DT) and aboard of TEXUS-37 (TE) with the plate distance a, the plate breath b, the channel length l, the rise time of the liquid meniscus t_r, the Ohnesorge number Oh, the aspect ratio Λ and the dimensionless channel length $\mathcal{L}$.

Liquid	ρ [kg m^{-3}]	ν [10^{-6}m^2 s^{-1}]	σ [N m^{-1}]
HMDS	766 ± 0.2%	0.69 ± 2%	0.0158 ± 2%
FC-77	1773 ± 0.2%	0.85 ± 3%	0.0153 ± 3%

Table 3.2: Test liquids and properties at $T = 20°$C. Hexamethyldisiloxane (HMDS, silicone oil) provided by Dow Corning, Fluorinert liquid FC-77 provided by 3M. The static contact angle is $\Theta_{stat} = 0$ on perspex and glass. The density, kinematic viscosity and surface tension are denoted by ρ, ν and σ, respectively.

errors.

The capillary rise necessary to fill the channel is shown in Fig. 3.4. The images show how the liquid meniscus moves into the channel until the meniscus contacts the suction device. Note that the driving pressure gradient is determined by the concave radius of curvature in the gap between the plates (visible as bright are at the edges of the liquid meniscus (2)). After the forced flow is established, two typical observations depending on the adjusted Q are made. Up to a certain flow rate Q_{max}^{stable} the flow in the channel is stable. Merely slight oscillations of the liquid surfaces are observed so that the flow may be considered as quasi-steady. The free surface is stable and the corresponding apex point of the surface is constant in time, $k = k(x)$. For $Q > Q_{max}^{stable}$ the surface collapses and gas ingestion occurs. The free surface becomes time-dependent, $k = k(x, t)$. The withdrawn total flux now is a superposition of the maximal liquid flow rate and an additional flow rate of gas. Fig. 3.5

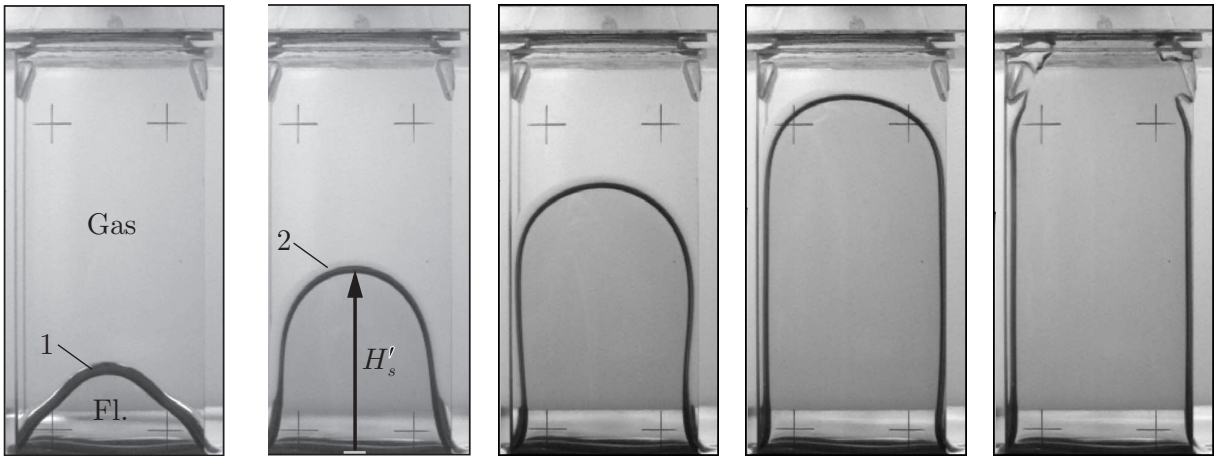

Figure 3.4: Spontaneous or self-driven capillary rise in the channel after the release of the drop capsule (parameter set DT-35a). The liquid is driven by a capillary pressure difference between the meniscus (1) and the liquid surface in the liquid container. The bright ares (2) at the upper edge of the profile allude to a concave surface curvature.

shows a stable flow at $Q = 8.75$ ml/s. After the channel was filled by the capillary rise of the liquid the syringe was started at $t = 0.78$ s. Surface waves caused by the start of the syringe travel upstream ($t = 0.86$ s). When the waves are damped out a slight oscillation of the surface can be observed. These oscillations are induced by pressure fluctuations occurring due to the reorientation of the liquid surface in the container under microgravity conditions. The oscillation decays at the end of the experimental time and the surface reaches its final position.

Increasing the flow rate about 3% to $Q = 9.04$ ml/s yields an unstable flow as shown in Fig. 3.6. The surface becomes unstable at the left side of the channel ($t = 1.75$ s), and a gas bubble is ingested into the suction head ($t = 2.03$ s, $t = 2.27$ s). The surface stabilizes ($t = 2.37$ s) and the process starts again ($t = 2.85$ s).

For the determination of the critical flow rate of the channel, several drop experiments are necessary. By adjusting the flow rate alternating above and below the critical value, the upper limit of a stable flow is iterated. All other parameters are kept constant. The critical flow rate is defined as

$$Q_{crit}^{\exp} = \frac{1}{2}(Q_{\max}^{st} + Q_{\min}^{unst})$$

where Q_{max}^{st} is the maximum stable flow rate and $Q_{\min}^{unstable}$ is the minimum flow rate leading to gas breakthroughs. The results of the experiments and the numerical prediction of the critical flow rate are listed in Table 3.3. The data is given in the dimensionless form $Q' = Q/(\tilde{v}_c \tilde{A})$,

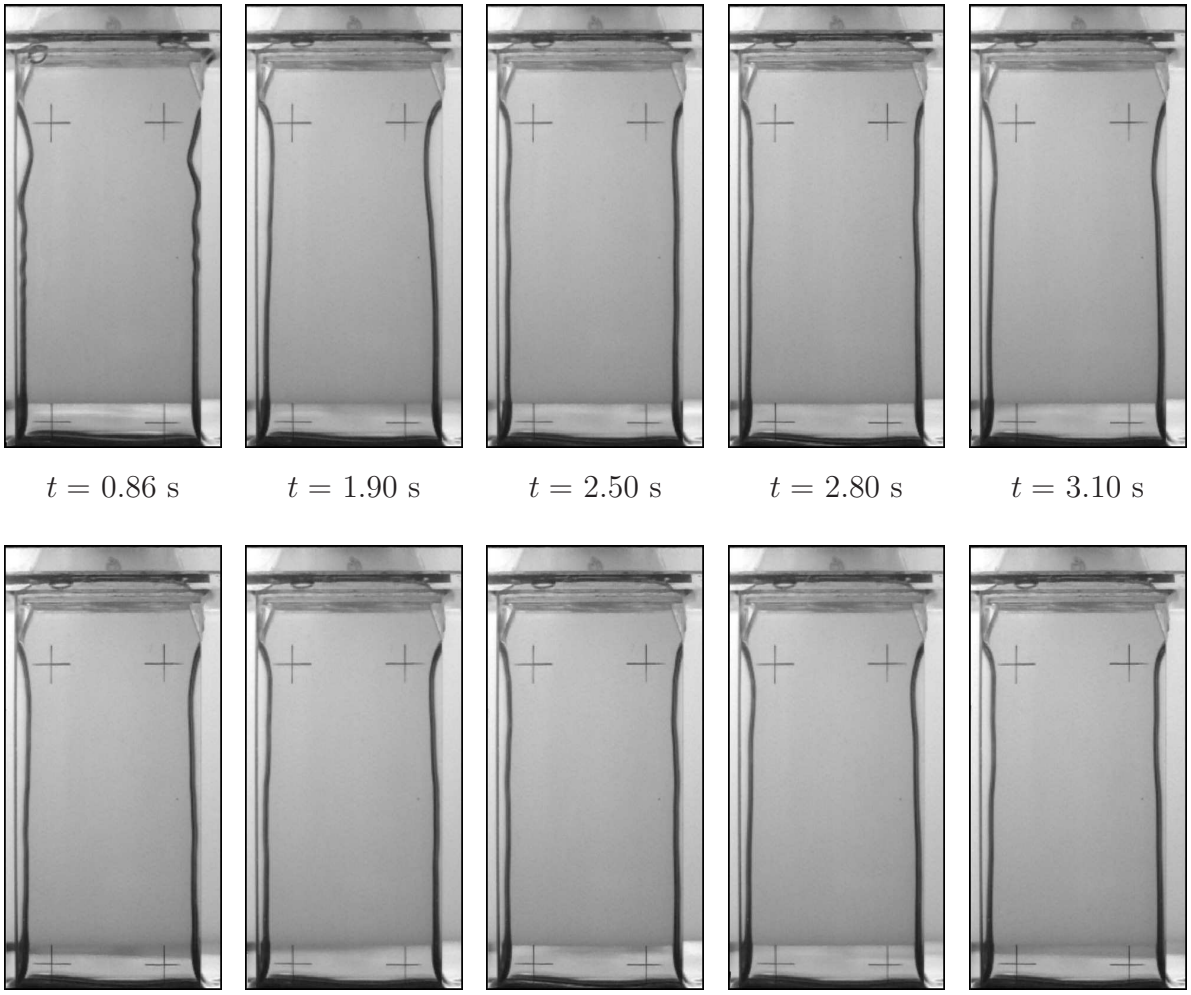

Figure 3.5: Stable flow in the capillary channel in the drop tower experiment (parameter set DT-35a), $Q = 8.75$ cm^3/s. The flow direction is from the bottom to the top. The withdrawal of liquid is started at $t = 0.78$ s. Surface waves initiated at the channel outlet propagate upstream ($t = 0.86$ s). After that the flow is quasi-steady.

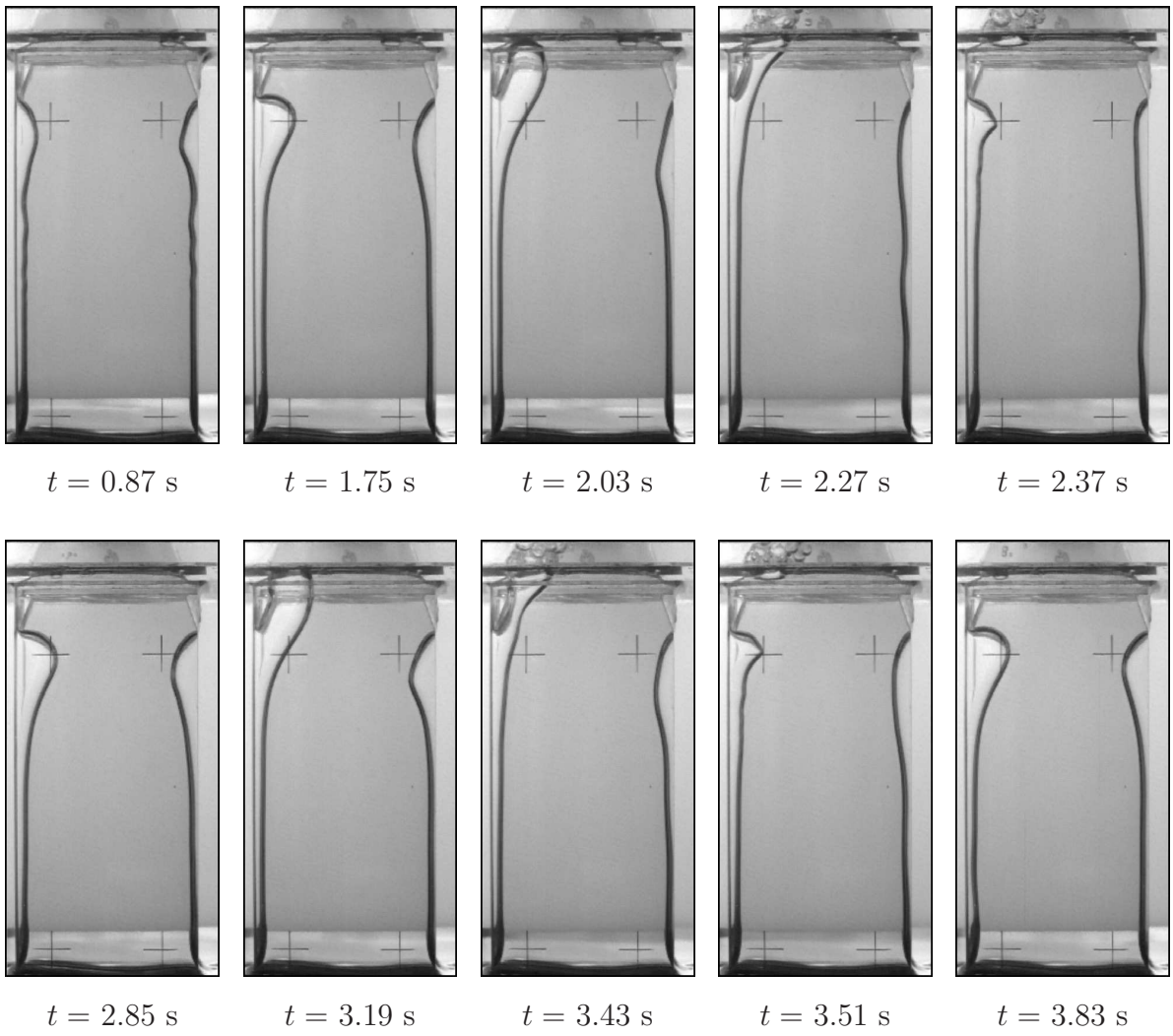

Figure 3.6: Unstable flow with gas breakthroughs in the drop tower experiment (parameter set DT-35a), $Q = 9.04$ cm^3/s. The surface stabilizes ($t = 2.37$ s), and the cycle starts again ($t = 2.85$ s).

with $\tilde{v}_c = \sqrt{2\sigma/(\rho a)}$ and $\tilde{A} = ab$. The calculation were performed with Eq. (7.41) given in the Appendix A. The Reynolds number for the critical velocity $\mathrm{Re}_{h,crit} = Q_{crit} D_h/(\tilde{A}\nu)$, is well below the transition value for turbulent flow, thus laminar flow conditions are expected. The entrance pressure drop for each parameter set was calculated using the commercial CFD code FIDAP (see page 125) et seqq. in Appendix 7. The table demonstrates that the flow model can predicted the critical flow rate well. The deviation between the experiment data and the numerical prediction , $\Delta Q = |Q^{exp}_{crit} - Q^{num}_{crit}|/Q^{exp}_{crit}$, varies in the range of $2\% \leq \Delta Q \leq 14\%$. Note that due to inherent transient effects of the experiment the determined Q^{exp}_{crit} is generally slightly below the real critical value.

The comparison between the experimental and numerical surface profiles $k(x)$ is shown

No.	Q'^{st}_{max}	Q'^{unst}_{min}	Q'^{exp}_{crit}	Q'^{num}_{crit}	k'^{*}	S^{*}_{R}	S^{*}
DT-29	0.380	0.392	0.386 ± 0.006	0.391	9.05 ± 0.12	0.20 ± 0.07	0.23
DT-32	0.498	0.529	0.515 ± 0.017	0.588	2.95 ± 0.08	0.23 ± 0.03	0.25
DT-33	0.527	0.555	0.542 ± 0.015	0.603	9.38 ± 0.09	0.22 ± 0.05	0.23
DT-34	0.578	0.591	0.585 ± 0.007	0.616	9.38 ± 0.09	0.22 ± 0.05	0.24
DT-35	0.655	0.702	0.679 ± 0.024	0.730	4.49 ± 0.13	0.30 ± 0.07	0.29
DT-35a	0.771	0.796	0.784 ± 0.013	0.800	4.36 ± 0.07	0.47 ± 0.09	0.45
TE-35a	0.738	-	-	0.776	4.35 ± 0.04	0.46 ± 0.05	0.43

Table 3.3: Results of the drop tower (DT) and the TEXUS-37 (TE) experiments. Maximum steady flow rate Q'^{st}_{max}, minimum unsteady flow rate Q'^{unst}_{min}, experimental and numerical critical flow rate Q'^{exp}_{crit} and Q'^{num}_{crit}, minimum surface position k'^{*}, experimental speed index S'^{*}_{R} and numerical speed index S'^{*} at the smallest cross section for Q'^{st}_{max}.

in Fig. 3.7 for parameter sets DT-35a an DT-29. The solid line is the solution of Eq. (2.22) and Eq. (2.23) with the boundary conditions from Eq. (2.24) and (2.25). The dashed line represents the averaged profile from the experiment. To achieve it, the analog video is digitized and the single video frames are exported to Bitmap images. After that the edges of the profiles are detected by digital image processing and averaged. The error of the processing is given by the dotted line. In general a good agreement between both profiles is achieved. The strong constriction close to the channel inlet in Fig. 3.7a results from lateral inflow which was not considered for the theoretical flow model. This effect is negligible small in strong viscous flows (Fig. 3.7b). For the numerical calculation of DT-29 the Ohnesorge number was decreased by 2% within the experiment error. These results are representative for all investigated parameter set from Table 3.1.

In order to proof the choking effect as cause for the flow limitation the speed index from Eq. (2.31) need to be determined at the location of the smallest cross sectional area of the flow. With $v = Q/A$ it follows from Eq. (2.31) and (2.32) that for a given Q the speed index depends on the relation between the cross section area and the surface curvature, $A = A(H)$. This relation is a priori unknown and needs to be determined. While the numerical solutions of the flow model enable a very precise determination, only an approximation is possible for the experiments. This approximation considers the surface curvature transversal to the flow but neglects the curvature in flow direction (for more details see section "Modelling of the free liquid surface" on page 116 et seqq. in Appendix A). With this approximation Eq. (2.31) reduces to

$$S^{*}_{R} = \frac{Q}{A}\sqrt{\frac{\rho}{\sigma}\frac{R^2}{A}\frac{\mathrm{d}A}{\mathrm{d}R}} \tag{3.1}$$

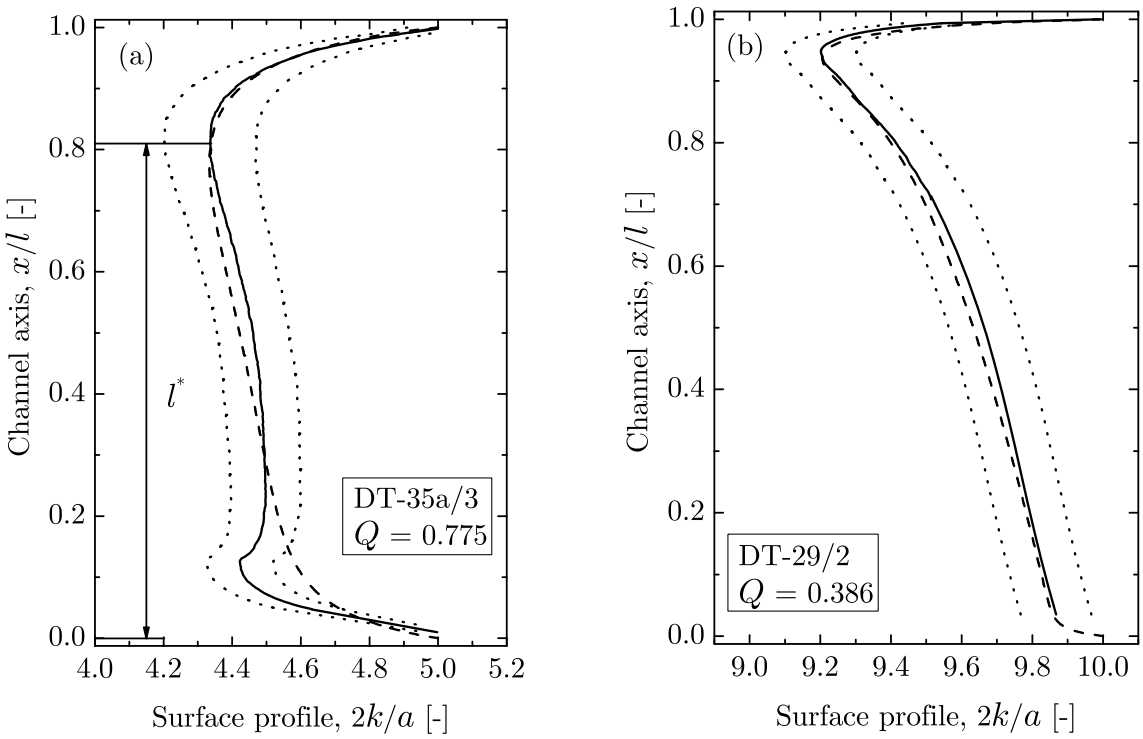

Figure 3.7: Surface profiles of the drop tower experiments, —— experimental data, - - - - numerical data, ⋯ experiment error. $\Lambda = 5$, Oh $= 1{,}5{\cdot}10^{-3}$, $\mathcal{L} = 3{,}63{\cdot}10^{-3}$. (a) DT-35a/3, $Q = 0.775$, (b) DT-29/2, $Q = 0.386$.

where R is the radius of curvature in the cross section plane $y = 0$ (see Fig. 3.3b). The star indicates that the property is determined at the location of the narrowest flow path. Note that the radius of curvature as well as the cross section plane are functions of the profile, $R = R(k)$ and $A = A(k)$, respectively (see also Eq. (7.15) and Eq. (7.16) in Appendix A). In contrast to Eq. (3.1), the speed index achieved from the numerics contains the full information about the surface curvature, and it reads

$$S^* = \frac{Q}{A}\sqrt{-\frac{\rho}{\sigma A}\frac{\mathrm{d}A}{\mathrm{d}(2H)}}. \tag{3.2}$$

For the parameter sets DT-35a and DT-33 the speed index is plotted as function of the dimensionless flow rate Q' in Fig. 3.8. The dashed and the solid lines denote the numerical solutions of the Eq. (3.1) and Eq. (3.2), respectively. The experimental data for Eq. (3.1) is given by the single squares, the triangles indicate the number of gas breakthroughs during the unstable flow. As the numerics show, S^* increases with increasing Q' and reaches $S^* = 1$ for the critical flow rate Q'_{crit}. For $Q' > Q'_{crit}$ no solutions of the model equations are possible, and we conclude that the flow rate limitation is caused by an choking-effect. The

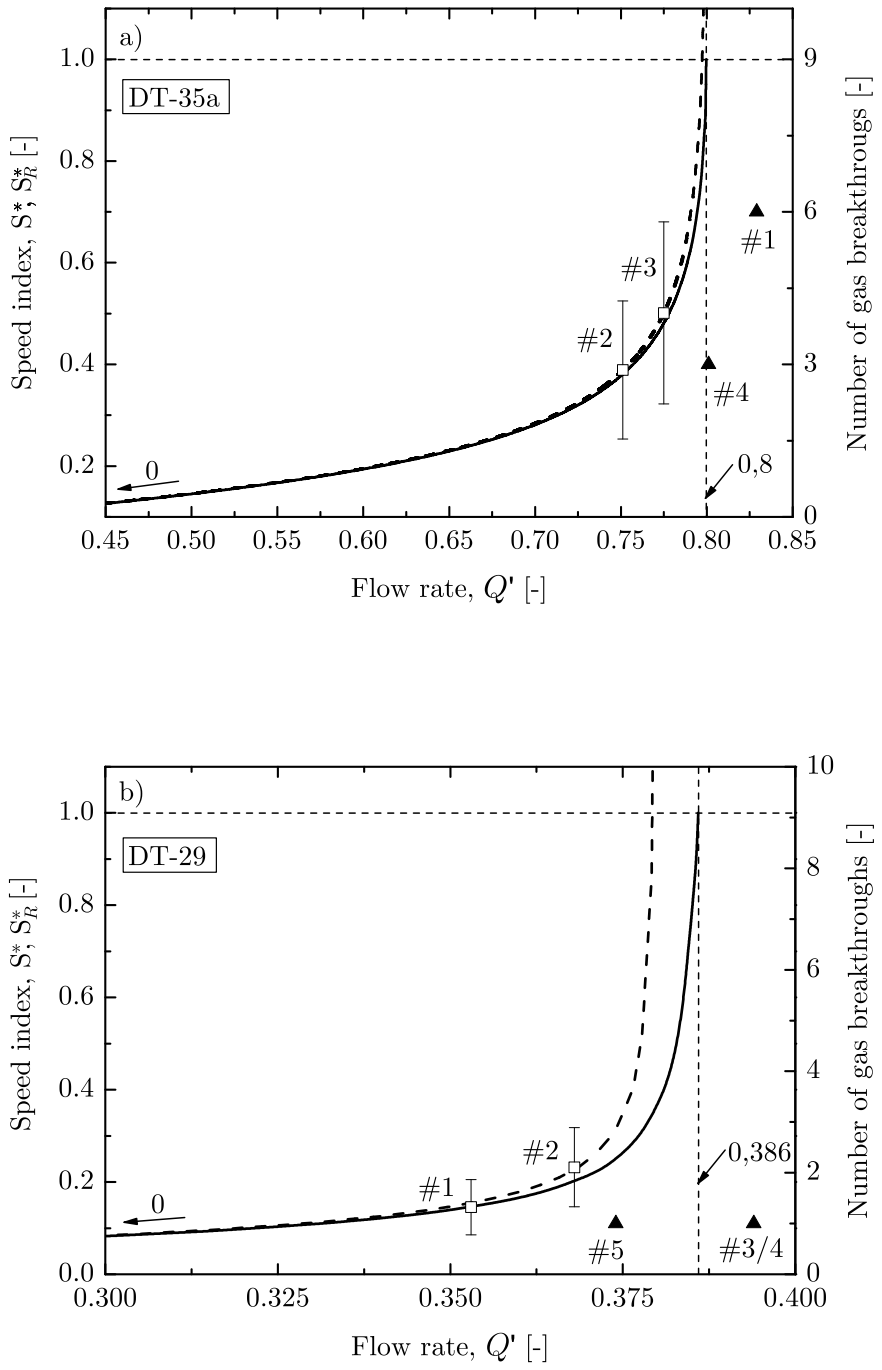

Figure 3.8: Speed index at the narrowest flow path versus the flow rate (drop tower experiments). □ S^*_R experimental, ■ S^*_R experimental, unstable start-up, ---- S^*_R numerical, —— S^* numerical, ▲ number of gas breakthroughs. (a) DT-35a, $\Lambda = 5$, $\mathrm{Oh} = 1.50{\cdot}10^{-3}$, $\mathcal{L} = 3.63{\cdot}10^{-3}$. (b) DT-35, $\Lambda = 5$, $\mathrm{Oh} = 1.50{\cdot}10^{-3}$, $\mathcal{L} = 7.00{\cdot}10^{-3}$.

experimental data show the same tendency but due to the approximation of the surface curvature the speed index S_R^* deviates from S^*, especially for flow rates close to the critical one. As the triangle demonstrate flow rates larger than Q'_{crit} causes an unstable flow with several gas breakthroughs. Nevertheless, the surface collapse may also occur for $Q' < Q'_{crit}$ (see data point # 6 in 3.8b). As mentioned above, this behavior is due to inherent transient effects and cannot be avoided with this set-up. In general these flows stabilize and yield utilizable results (black square).

3.1.2 Experiment on a Sounding Rocket (TEXUS-37)

In order to investigate the channel flow under a longer duration of microgravity an experiment for the sounding rocket TEXUS was developed. The rockets of the TEXUS-program (**T**echnologische **Ex**perimente **u**nter **S**chwerelosigkeit) are equipped with a two-stage solid rocket motor (Skylark-7, VSB-30 from 2005 on) which lifts the payload on a parabolic trajectory to an apogee of up to 270 km height. During the ballistic flight phase the experiment is exposed to a compensated-gravity environment of 10^{-4} g_0 (g_0 is the acceleration due to gravity) in all axes for approximately 6 minutes. Via the service module of the rocket a communication with the payload including the downlink of data and several S-VHS videos channels is enabled. After the reentry into the atmosphere the payload is decelerated by a parachute and brought back to the ground.

The experiment was flown in March 2000. A schematic of the experiment setup is shown in Fig 3.9. The core element of the setup consists of a cylindrical liquid reservoir (1) with a compensation tube (8) and an observation chamber (2) with the open channel (3). The channel is connected to the liquid reservoir via a nozzle (4). The compensation tube as well as the nozzle can be closed pneumatically by a gate valve (S_1) and a stemple (5). The liquid reservoir was especially designed to enable a controlled filling of the channel at the beginning of the microgravity phase and provides defined boundary conditions at the channel inlet. The flow through the channel is established by two gear pumps. One pump (PU_1) supplies the reservoir through a circular gap on the bottom of the reservoir at flow rate Q_s. The flow enters through a screen-controlled rectifier (6) to ensure a homogenous velocity distribution. The second pump (PU_2) withdraws the liquid via the channel and the nozzle from the reservoir at flow rate Q. The unavoidable flow rate differences between both pumps are accommodated by the perspex compensation tube (8) (inner diameter 45 mm). Furthermore the liquid meniscus in the tube sets the pressure in the reservoir and defines the boundary condition needed to solve Eq. (2.22) and Eq. (2.23). To prevent the meniscus from disappearing into the reservoir the supply pump was adjusted to pump a 3% higher flow rate than the suction pump. With this adjustment the liquid rises continuously in the compensation tube. Each pump is connected to a separate reservoir for the supply with test

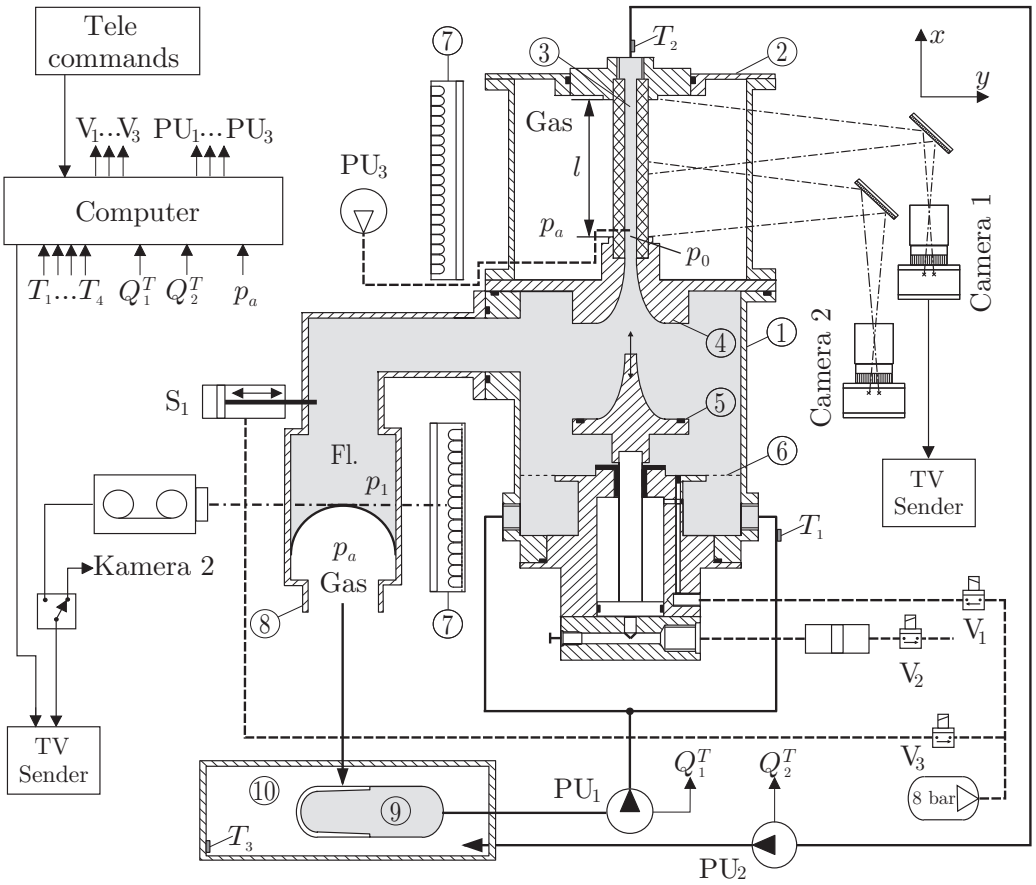

Figure 3.9: Schematic of the experimental setup to investigate an open capillary channel flow aboard the sounding rocket TEXUS-37. Liquid reservoir (1), observation chamber (2), open channel (3), nozzle (4), stemple (5), screen (6), illumination (7), compensation tube (8), supply membrane tank (9), disposal tank (10). The flow is established by the supply pump PU_1 and the withdrawal pump PU_2. p_a is the ambient pressure, p_0 the pressure at the channel inlet and p_1 the pressure inside the compensation tube.

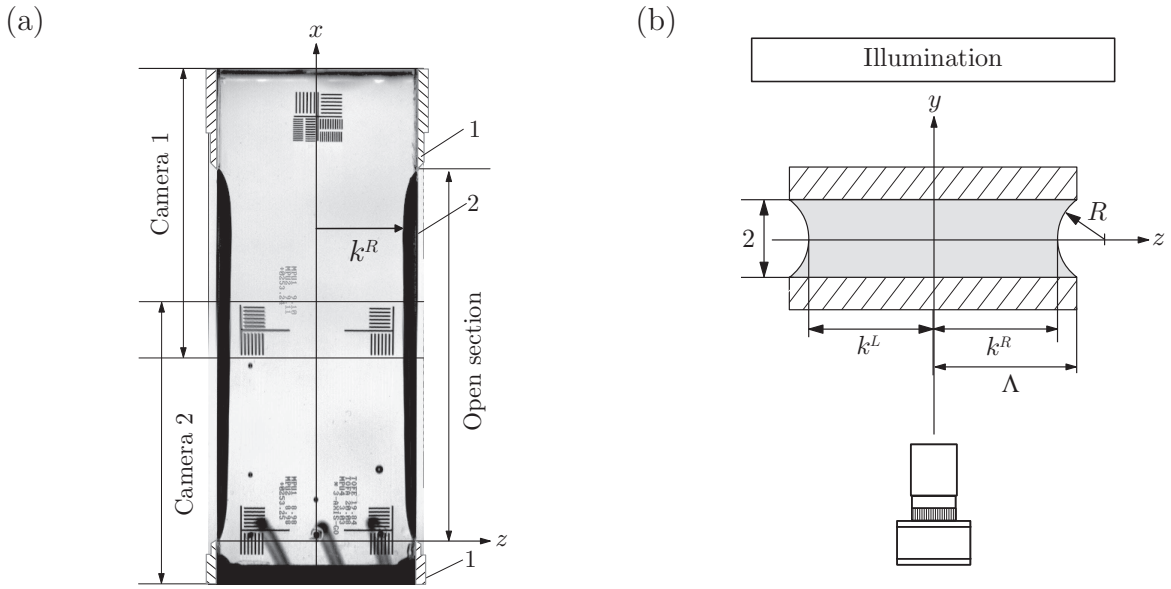

Figure 3.10: (a) Front view of the channel. The optical axes of the cameras are aligned normal to the top plate. The inlet and outlet are covered by thin FC-725 coated metal plates at the sides (1). Due to total reflection the liquid interfaces appear dark (2). (b) The profiles correspond to the distances k^L and k^R.

liquid and the storage of withdrawn liquid.

The capillary channel consists of two parallel quartz plates with breadth $b = 25$ mm, gap $a = 5$ mm and length $l = 46.6$ mm. With the properties of the applied liquid HMDS from Table 3.2 the governing parameter $\Lambda = 5.0$, $\mathrm{Oh} = 1.52 \cdot 10^{-3}$ and $\mathcal{L} = 4 \cdot 10^{-3}$ (parameter set TE-35a in Table 3.1) are obtained. To prevent the spreading of liquid away from the channel, the inlet and outlet are covered by thin metal plates at the sides. A front view normal to the plates is shown in figure 3.10(a). The channel has precise markings for the calibration and evaluation of the video images. Two CCD cameras were used. The camera fields of view overlapp by approximately 10 mm, and the image resolution is 47 μm/pixel. A homogenous illumination is achieved by an LED panel with a Teflon diffusor (7). Just like in the drop tower experiments, the profiles of the surface appear as dark zones on the video images due to the total reflection at the gas-liquid interfaces. Referring to figure 3.10(b) the profiles are defined by the distances $b/2 - k^L$ and $b/2 - k^R$, where the positions $k^L(x)$ and $k^R(x)$ correspond to the left and right hand side profiles of the surface shape in the plane $y = 0$, respectively. During the experiment the video signals were downlinked to the ground and recorded on VCR (S-VHS quality).

The experiment was controlled manually during the flight of the sounding rocket. All hand-controlled procedures necessary for the TEXUS experiment control had been practiced during two parabolic flight campaigns in October and December 1999. In the initial con-

figuration before the lift off, the compensation tube and the nozzle were each closed. Both pumps were stopped. Under microgravity conditions the capillary channel had to be filled. To avoid wetting outside the channel, caused by an uncontrollable liquid jet, the channel was not filled directly by the pressure pump but by the self-driven capillary rise well-known from the drop tower experiments. For that reason the compensation tube was filled at first. After removing the stemple out of the nozzle, the liquid rise occurred, and the channel filled itself. When the liquid reached the channel outlet, it was withdrawn by the withdrawal pump which was already running. By starting the supply pump, the continuous flow was established.

The filling procedure took approximately 30 s. In the remaining experimental time the flow rate was increased up to the critical value. In contrast to the drop tower experiment the change of flow rate by each step is small. Since the channel is supplied by two synchronized pumps, the inertia effects are sufficiently smaller than in the previous drop tower experiments. The experiment provided the options to change the flow rate in 0.46 ml/s or 0.04 ml/s increments. At first the large increment for a coarse approach was chosen to save time. After the first gas breakthrough was observed, the flow rate was decreased, and a second approach with the small increment was performed. With this procedure the maximal flow rate was determined as $Q_{max}^{exp} = 8.38\,\mathrm{ml/s}$. The typical observations at flow rates below the critical value are shown in Fig. 3.11. The surface profiles are symmetrical with respect to the plane $z = 0$. They broaden along the flow path and with increasing flow rate. For $Q > Q_{crit}$ the surfaces collapse (Figure 3.12). A periodic ingestion of gas bubbles (gas breakthroughs) is observed leading to a two-phase flow downstream the channel outlet. During the bubble formation the surfaces stay pinned at the side walls of the outlet.

For the evaluation of the flow the video images are digitalized. After that the surface profiles are detected and averaged. A detailed description of the image processing can be found in Rosendahl *et al.* (2004*a*). Fig. 3.13(a) shows the average profile k along the channel axis x as a function of the adjusted flow rates Q. The labels refer to the evaluated sequences of constant flow rate. For characterization we introduce the lengths l_1 and l^*, where l_1 defines the inlet region, in which the surface curvature in flow direction is larger that 10% of the total curvature, and l^* the location of the smallest cross section. With increasing flow rate, l^* decreases and the location of the minimum cross section shifts towards the inlet. Along $0 \leq x \leq l_1$ the curvature of the surfaces essentially adapts to the inlet pressure p_0 defined by $2H_0$ from Eq. (2.26). Since $p_0 < p_a$ the surfaces bend inwards. The widening at the outlet is forced by the pinned surfaces at the side walls of the channel outlet. The labels in the figure indicate the chronological order in which the flow rates were adjusted during the experiment. The comparison of the sequences S-04 and S-07 (both at $Q = 7.82$ ml/s ($Q^{'} = 0.689$)), as well as S-05, S-06 and S-12 (all at $Q = 8.29$ ml/s ($Q^{'} = 0.730$)) shows the high degree of reproducibility. The sequences S-05 and S-06 are evaluated before

$Q = 0.489$ $Q = 0.572$ $Q = 0.653$ $Q = 0.735$

Figure 3.11: Stable flow through the open capillary channel at various flow rates. The flow direction is from bottom to top. The profiles broaden along the flow path and with increasing flow rate.

and after the compensation tube was emptied which illustrates the reproducibility of the pressure boundary condition inside the compensation tube. Note that due to insufficient contrast the profile points near the inlet and outlet could not be detected. The solutions of Eq. (7.41) and Eq. (7.42) (dimensionless form of Eq. (2.22) and Eq. (2.23)) with the boundary conditions $\Lambda(x = 0) = 5.076$ and $\Lambda(x = 1) = 5.11$ (considering the metal plates from figure 3.3(a)) and Eq. (7.48) with $K_1 = 1.4$, $K_2 = 374$ and $K_3 = 0.222$ are displayed in figure 3.13(b). The surface profiles for the different flow rates are in good agreement with the experimental data.

For a detailed comparison between experiment and theory the lowest and the highest realized flow rate are depicted in Fig. 3.14. The experimental profiles (solid lines) are well reproduced by the numerical calculations (dashed lines). This level of agreement is achieved for all profiles shown in Fig. 3.13. All numerical profiles are located within the experimental error bars (dashed lines). Note that no flow constriction occur at the inlet since – different from the drop tower experiments – due to the nozzle no transversal components of the flow exist.

In Fig. 3.15 the experimental speed index S_R^* according to Eq. (3.1) (squares) and

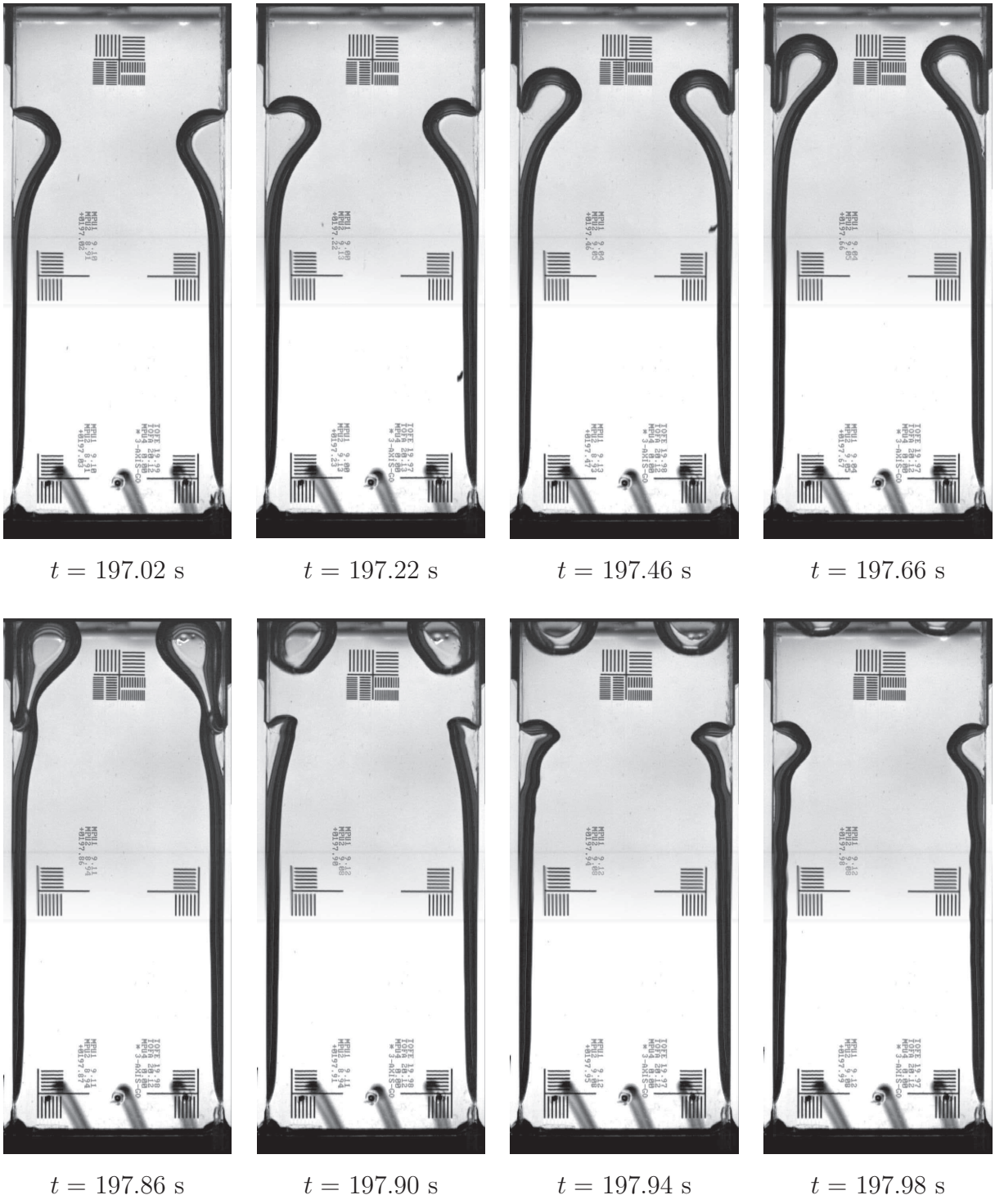

$t = 197.02$ s $t = 197.22$ s $t = 197.46$ s $t = 197.66$ s

$t = 197.86$ s $t = 197.90$ s $t = 197.94$ s $t = 197.98$ s

Figure 3.12: Unstable flow through the open capillary channel in the TEXUS-experiment at a flow rate above the critical value, $Q > Q_{crit}$. Periodic gas breakthroughs occur via both surfaces.

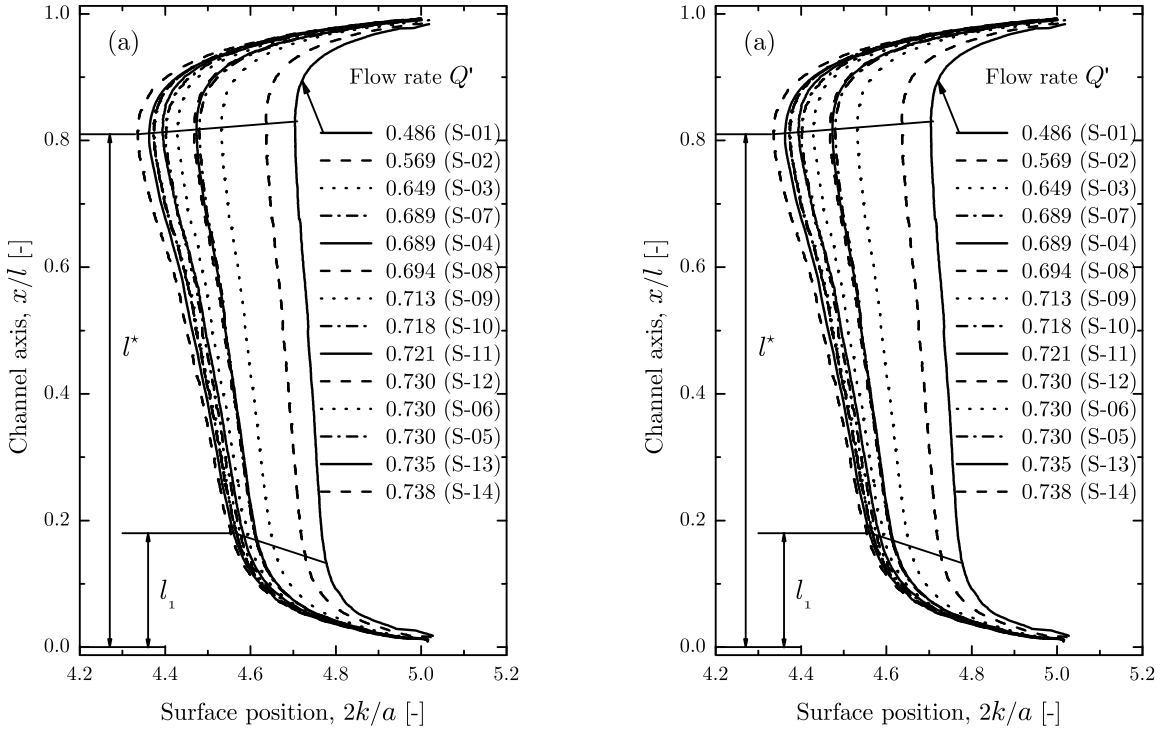

Figure 3.13: Profiles $k'(x')$ of the TEXUS experiment in dependency of the dimensionless flow rate $Q' = Q/\tilde{Q}$. (a) Experimental values. (b) Numerical solution.

the numerical speed index S* according to Eq. (3.2) (solid line) are plotted versus the dimensionless flow rate Q'. The plot shows that S* increases with increasing flow rate tends towards unity for the critical flow rate $Q_{crit}^{num'} = 0.778$. For $Q' >_{crit}^{num'}$ no solutions for the model equations Eq. (7.41) and Eq. (7.42) exist. A steady flow in the channel above the critical flow rate is therefor not possible, whereas the limit of the liquid transport is obviously determined by the speed index and therefor – as predicted theoretically – by the choking effect. The experimental speed index S_R^* follows this trend but deviates increasingly from the reals value. Moreover merely the value $S_R^* = 0.47$ was reached since the experiment had to be stopped ahead of schedule when the end on microgravity was reached. From the basis of numerically determined stability limit, the this corresponds to a flow rate of approximately 0.95 Q_{crit}. According to this the experimental flow was close to the critical even if S* has reached at this value less than the half of its maximum value. Note that the good agreement between the experimental data with the numerically determined values for S_R^* (dashed line) results from the general good agreement between the experimental and numerical surface profiles. More details concerning the choking mechanism are given in Rosendahl *et al.* (2004*a*); Rosendahl (2006).

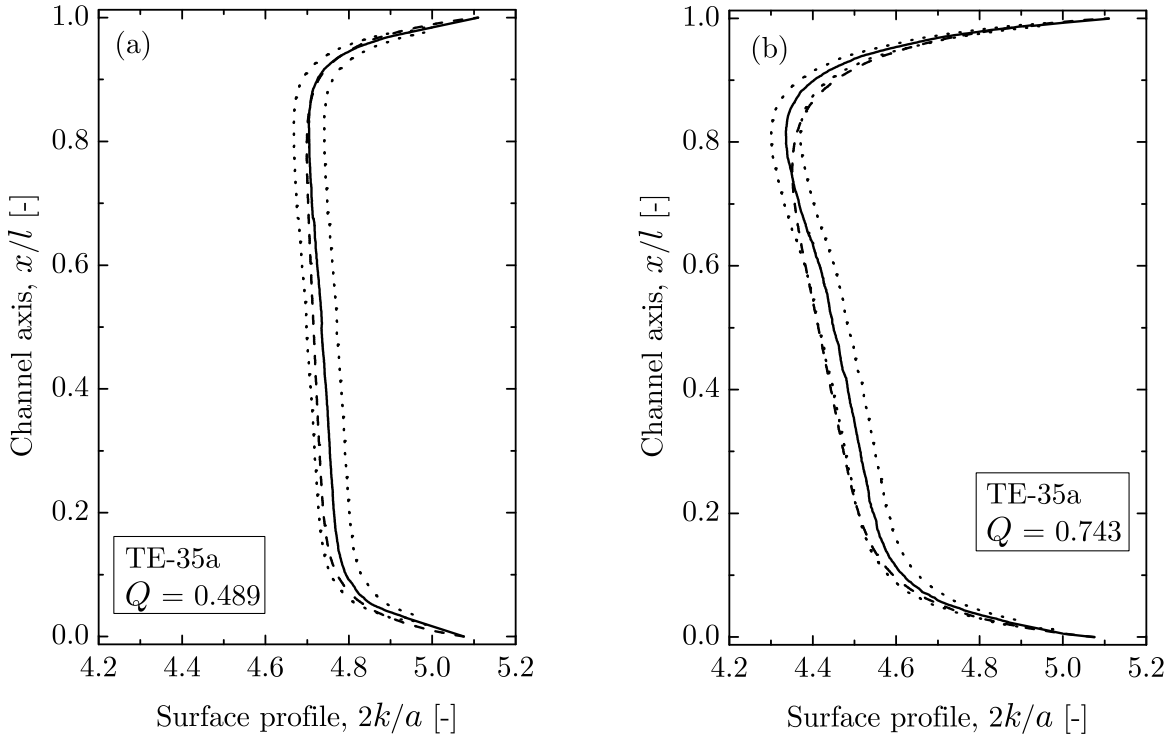

Figure 3.14: Profiles from the TEXUS experiment (solid lines), error of the profile data (dotted line) and numerical prediction (dashed line) for the lowest and the highest flow rate. (a) Q =5.52 ml/s (S-01). (b) Q =8.38 ml/s (S-14).

3.2 Wedge-shaped channel

3.2.1 Wedge viscous limit analysis background section

Numerous authors have outlined problem formulations for incompressible viscous dominated capillary driven flows in interior corners (Lenormand & Zarcone, 1984; Dong & Chatzis, 1995; Ransohoff *et al.*, 1987; Romero & Yost, 1996; Langbein & Weislogel, 1998, to name several). A scant review of the basic formulation is provided here following Weislogel & Lichter (1998), which culminates in the transient nonlinear diffusion equation governing such flows. The formulation is identical in principal to that of others, but subtleties in geometric scaling yield perhaps the most compact analytic form for solutions, relying the least on accurate though broadly varying numerically determined coefficients (Ayyaswamy *et al.*, 1974; Ransohoff & Radke, 1988) or analytically fit numerical coefficients (Romero & Yost, 1996). For the discussion to follow, a sketch of a liquid column in an interior corner is

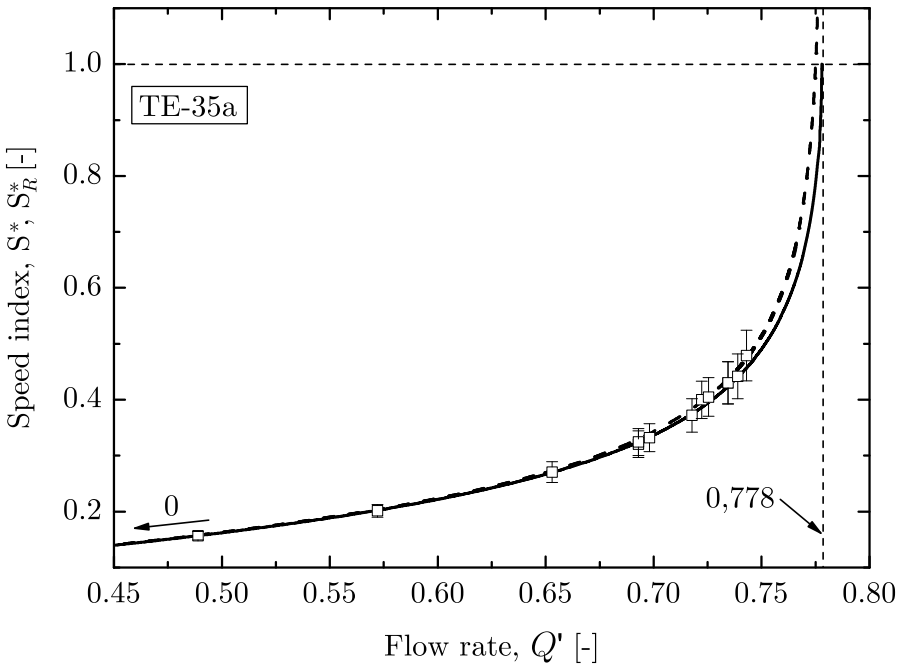

Figure 3.15: Speed index as the smallest cross section as function of the dimensionless flow rate Q'. □ S^*_R experimental, ---- S^*_R numerical, —— S^* numerical.

provided in Fig. 3.16. The cross-flow section cross-hatched in Fig. 3.16 is sketched in Fig. 3.17, where the notation $h(x,t)$ replaces $k(x,t)$ for previous developments. For systems where the Bond number is much less than unity, $\text{Bo} \equiv \rho g r^2/\sigma \ll O(1)$, capillary forces dominate the flow – ρ is the density difference across the fluid interface, g is the acceleration field strength (i.e. gravity), r is a characteristic length for the system (i.e. container size), and σ is the surface tension. This 'viscous limit' formulation is presented since it is expected to serve as a base state for CCF wedge flows from which inertia is introduced and systematically increased until it becomes itself the dominating force.

In general, the solution begins with the requirement that the Concus-Finn corner (Concus & Finn, 1969) wetting condition is satisfied; namely, $\theta < \pi/2 - \alpha$, where θ is the wetting or contact angle of the system as measured in the wetting fluid phase and α is half the vertex angle of the interior corner. If the Concus-Finn condition is not satisfied and the fluid column is sufficiently slender the fluid will not spontaneously wet the corner and will either spontaneously recede or break-up due to the Rayleigh instability (Langbein, 1990). Provided the Concus-Finn condition is satisfied, and $\text{Bo} \ll 1$, the primary assumption of locally parallel flow along the corner axis coordinate $\varepsilon^2 \equiv (H/L)^2 \ll 1$ results in significant

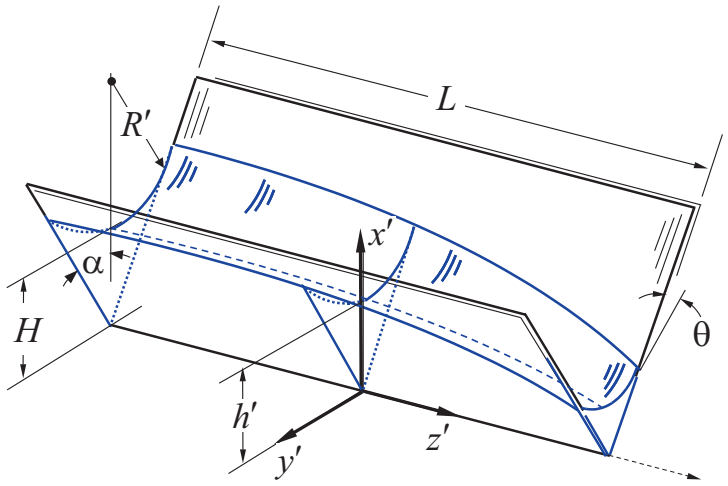

Figure 3.16: Fluid column in an isolated corner, angle $2a$. The 3-D surface profile is $S(y, z, t)$ with characteristic height and length, H and L, respectively.

simplification of the governing equations; ε is the slenderness ratio, H is the characteristic height of the interface, and L is the characteristic length of the liquid column. Solutions under such constraints constitute the 'viscous limit'. The flows may be fast (i.e. high Reynolds number), but their parallel nature renders inertia a secondary contributor. However, solutions obtained in this limit may be used in a perturbation analysis to assess the magnitude of the inertia neglected as well as to determine the flow conditions and parameters where inertia is expected to play an increasing and eventually dominating role.

Under the slender column constraint, the normal stress balance at the free surface may be solved for the pressure in the liquid independently from the momentum equation, revealing that the dynamic capillary surface is a construct of circular arcs in the cross-flow plane satisfying the static contact angle θ condition at the wall (see Fig. 3.17). To leading order the capillary pressure in the fluid is only a function of the cross-stream surface curvature and may be expressed as $P' = -\sigma/R' = -\sigma/fh'$, where f is a dimensionless geometric function given by

$$f = \frac{\sin\alpha}{\cos\theta - \sin\alpha}. \tag{3.3}$$

The condition $\varepsilon^2 f << 1$ is required to neglect streamwise interface curvature at leading order and is often satisfied naturally by the slender column assumption $\varepsilon^2 << 1$. Choosing scales $z' \sim h' \sim H$, $y' \sim H\tan\alpha$, $x' \sim L$, $P' \sim \sigma/fH$, and z-component velocity scale

$$u' \sim \frac{H\sigma\sin^2\alpha}{\mu f L}, \tag{3.4}$$

where μ is the dynamic viscosity of the liquid, the locally parallel flow assumption $\varepsilon^2 \ll 1$

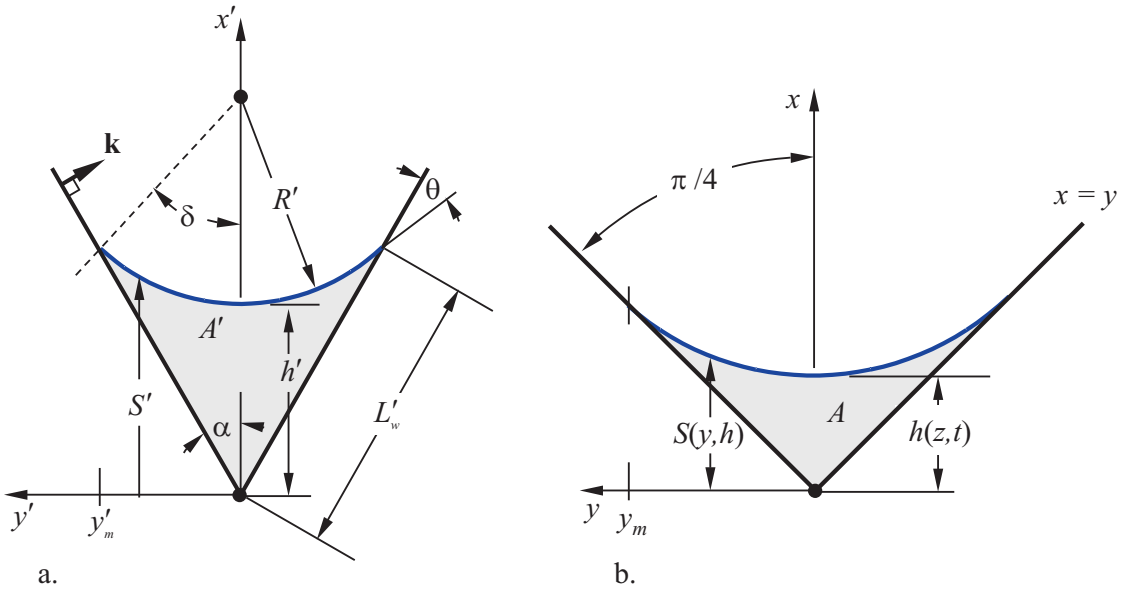

Figure 3.17: Cross-flow notation: a) dimensional (primes dropped), b) nondimensional. Note that $h(z,t) = S(0,z,t)$.

reduces the Navier Stokes equation to the zeroth order x-component equation

$$\mathrm{Re}\frac{Du}{Dt} = -P_x + \nabla^2 u, \tag{3.5}$$

where $D/Dt = u\partial/\partial x + v\partial/\partial y + w\partial/\partial z$ and $\nabla^2 = \sin^2\alpha\partial^2/\partial y^2 + \cos^2\alpha\partial^2/\partial z^2$. Re is the parameter that captures the strength of inertia in the flow and is defined by

$$\mathrm{Re} = \frac{\varepsilon^2 \sin^4\alpha}{f\mathrm{Oh}^2} \tag{3.6}$$

where $\mathrm{Oh} = \mu/(p\sigma H)^{1/2}$. In addition to the slender column assumption $\varepsilon^2 \ll 1$ the further constraints of small streamwise curvature $\varepsilon^2 f << 1$ and small inertia $\mathrm{Re} \ll 1$ reduce the dimensionless Navier-Stokes equation further to Poison's equation for the leading order z-component velocity distribution $u(z,y,t)$,

$$P_x = h^{-2}h_x = u_{zz}\sin^2\alpha + u_{yy}\cos^2\alpha, \tag{3.7}$$

subject to the no slip boundary condition at the wall, the no shear stress condition on the free surface, and the symmetry condition along $y = 0$, respectively:

$$u = 0 \qquad \text{on} \quad y = z, \tag{3.8}$$

$$u_z\sin^2\alpha - S_y u_y\cos^2\alpha = 0 \quad \text{on} \quad z = S, \tag{3.9}$$

$$u_y = 0 \qquad \text{on} \quad y = 0. \tag{3.10}$$

The dimensionless cross flow section is sketched in Fig. 3.17b. Eq. (3.7) when integrated over the cross-flow section subject to the boundary conditions (3.8)–(3.10) yields the dimensionless average velocity

$$\langle u \rangle = -F_i h_x, \tag{3.11}$$

where $F_i \equiv F_i(\alpha, \theta)$ is a weak geometric function of the integration and is narrowly confined such that $1/8 \leq F_i \leq 1/6$, or correlation $F_i = \frac{1}{b}\left(1 - \frac{\sin 2\alpha}{5}\right)$, and may be treated as a constant, say $F_i \approx 1/7$, and if greater accuracy is necessary Weislogel (1996) should be consulted where the numerical computations of Ayyaswamy *et al.* (1974); Ransohoff & Radke (1988), and most recently Nardin & Weislogel (2005) are used to compute precise values of $F_i(\alpha, \theta)$. The appearance of F_i in the governing equations can be prevented by introducing the more correct z-component velocity scale U

$$U \sim \frac{H F_i \sigma \sin^2 \alpha}{\mu f L} \equiv \varepsilon G, \tag{3.12}$$

From this velocity scale capillary driving forces are characterized by $\sigma H/f$, while viscous resistance is characterized by $\mu L/F_i \sin^2 \alpha$. With knowledge of $\langle u \rangle$ from Eq. (3.11) a mass balance equation may be written for the cross flow plane of dimensional area $A' = F_A h'^2$, where

$$F_A = f^2 \left(\frac{\cos\theta \sin\delta}{\sin\alpha} - \delta \right) \tag{3.13}$$

and $\delta \equiv \pi/2 - \alpha - \theta$. Choosing scales for cross-flow area $A' \sim F_A H^2$, time $t' \sim L F_i/\varepsilon G$, and volumetric flow rate $\dot{Q}' \sim \varepsilon G F_A H^2$ the dimensionless mass balance becomes

$$A_t = -\dot{Q}_x. \tag{3.14}$$

And since

$$\dot{Q} = A\langle u \rangle = -F_i h^2 h_x, \tag{3.15}$$

substitution of (3.15) into (3.14) produces the governing equation

$$(h^2)_t = F_i (h^2 h_x)_x. \tag{3.16}$$

Any solution for h from (3.16) may be used to construct the entire three-dimensional surface $S(y, x, t)$ through

$$S = h(1 + f) + (h^2 f^2 - y^2 \tan^2 \alpha)^{1/2}, \tag{3.17}$$

where $|y| \leq hf \sin\delta / \tan\alpha \equiv y_m$ (see Fig. 3.17b). Eq. (3.16) is a transient nonlinear diffusion equation and has been derived and solved in general in a variety of forms by a number of researchers for a variety of problems (i.e. boundary conditions). A partial list of works is cited here as recently reviewed by Weislogel (2003*b*) that correspond to studies particularly relevant to low-g fluids management-studies that include low-g experimental results are

noted:

Flows in Isolated Interior Corners:

- Constant volume drop spreading (Weislogel & Lichter, 1996, – aircraft data).
- Similiarity solutions for prescribed inlet flow conditions: constant height (Dong & Chatzis, 1995; Romero & Yost, 1996), constant, parabolic and exponential flow (Mayer *et al.*, 1983; Weislogel & Lichter, 1998, – drop tower data).
- Mixed contact line conditions (J. A. Mann *et al.*, 1995; Romero & Yost, 1996).
- Perturbed infinite column with gravitational effects, steady base state flow, and slightly nonplanar walls (Weislogel, 2001*b*).
- Steady flow (Weislogel, 1996; Dreyer, 2006).

Flows in Containers with Corners:

- Square capillary tubes with and without rounded corners (Ransohoff *et al.*, 1987; Dong & Chatzis, 1995)
- Rhombic containers (de Lazzer *et al.*, 1996, – sounding rocket data), (Langbein & Weislogel, 1998, – drop tower data)
- Cylinders of various section (drop tower data): equilateral triangles, squares, rectangles rounded rectangles (Weislogel & Lichter, 1998), irregular triangles (Weislogel, 2001*a*), symmetric containers with vanes (Weislogel & Collicott, 2002), containers with rounded corners (Chen *et al.*, 2006),
- Complex vaned tanks (Chato & Martin, 1997, – space flight data), (Weislogel & Collicott, 2002),
- Asymmetric tanks with vanes and vane gaps (Chen & Collicott, 2002, – drop tower data)).

3.2.2 Zero-g Isothermal Steady Flow Solution and Verification

The steady solution to Eq. (3.16) is trivial, but is not frequently used because terrestrial capillary flows of interest are often time-dependent or have a significant dependence on a component of gravity acting in the x-direction, the latter which can be insignificant in low-g environments. Steady corner flows do arise in passive thermal cycles, such as heat pipes with

microgrooves, and have been analyzed in this context in works for example by Peterson & Ha (1998) and others. However, the objective of the present effort is to benchmark the large length scale steady isothermal solution in order to extend its use to systems of increased complexity in the low-g environment.

Introducing Bo $\equiv H_2/H_1$, and nondimensionalizing h by H_1, the steady solution to Eq. (3.16) for specified interface heights and is $h(0) = 1$ and $h(1) = h_2$ is

$$h = \left(1 - \left(1 - h_2^3\right) x\right)^{1/3}, \tag{3.18}$$

from which the dimensionless flow rate using Eq. (3.15) yields $\dot{Q} = (1 - h_2^3)/3$ with the dimensional result

$$\dot{Q}' = \frac{H_1^3 F_A G}{3L}\left(1 - h_2^3\right), \tag{3.19}$$

where

$$G \equiv \frac{\sigma F_i \sin^2 \alpha}{\mu f}. \tag{3.20}$$

The flow rate is seen to increase as h_2 decreases; however the streamwise curvature of the interface is unbounded as $x \to 1/(1 - h_2^3)$ in violation of the assumption of dominant cross stream curvature. (Note: inertia in the flow also grows unbounded as $x \to 1/(1 - x)$ for $h_2^3 \ll 1$ as will be discussed shortly in connection with the CCF experiments.) The viscous limit solution given by Eq. (3.18) is constrained by local slope conditions and x-coordinate curvature conditions $h_x^2 \ll 1$ and $fhh_{xx} \ll 1$, or $\varepsilon^2(1 - h_2^3)^2/9h^4 \ll 1$ and $2f\varepsilon^2(1 - h_2^3)^2/9h^4 \ll 1$, respectively – both criteria of which are violated in cases where $h \to 0$. The dimensionless solution (3.18) is shown schematically in Fig. 3.18.

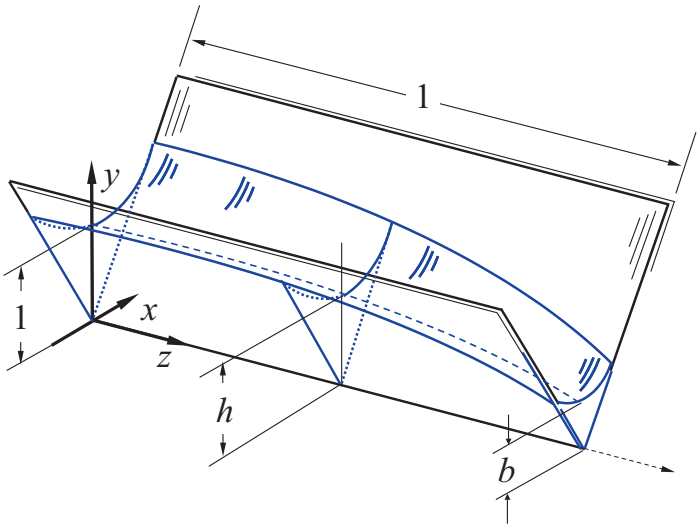

Figure 3.18: Steady corner flow profile and notation.

half angle	D	L_c
5	20	70
20	20	70

Table 3.4: Test cell material: acrylic plastic

ν	ρ	σ
$[10^{-6}\text{m}^2\ \text{s}^{-1}]$	$[\text{kg m}^{-3}]$	$[10^{-3}\text{N m}^{-1}]$
0.2	872	18.7
0.5	913	19.7
1.0	935	20.1

Table 3.5: Silicone oil fluid properties ($\theta = 0°$)

Simple experiments to confirm eqs. (3.18) and (3.20) are conducted aboard NASA's KC-135 low-g aircraft flying parabolic trajectories. The aircraft is capable of producing brief periods $\sim$ 20-25 s of reduced gravity levels $\sim \pm 10^{-2} g_0$ approximately 50 times per flight, $g_0 = 9.8$ m/s^2. A schematic of the experimental apparatus is shown in Fig. 3.19. A typical transparent test cell shown in Fig. 3.20 is backlit by a diffuse light source and photographed

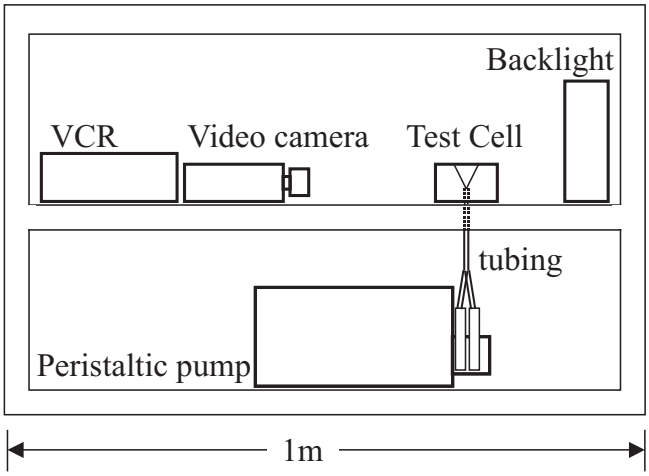

Figure 3.19: Schematic of low-g experimental apparatus.

orthogonally to the $x - z$ plane at a long working distance by video camera as depicted in Fig. 3.19. Important test cell and silicone oil fluid properties are listed in Tables 3.4 and 3.5 for the experiments performed and reported here. Other test using more complex geometries and wetting conditions will be reported in a subsequent publication.

The test fluid is introduced and removed through vertical ports at left and right ends of

the test cell (flow is left to right in Fig. 3.20). The entrance and exit regions of the flow field do not satisfy the parallel flow conditions assumed by the analysis, but the central region of the flow does, where $\varepsilon^2 \ll 1$. Thus, a preliminary step in the data reduction procedure is necessary to determine the correct x-coordinate origin for the flow as will be discussed shortly.

A 6-roller MasterFlex® peristaltic pump is used to provide the required steady flow rates in the appropriate range 1-100 ml/min predicted by Eq. (3.20) for the test cells fabricated. Average flow rate measurements from pump rotation rates are repeatable to at worst ±5%, which includes uncertainties due to pump head/tube tension, temperature, cycle life, and fluid viscosity. The pump is calibrated before and after the experiments with spot checks performed at random and various points during the overall test sequence. The presence of pulsations in the flows due to the peristaltic pump are minimized using two reversed pump head cartridges sketched in Fig. 3.19 and by operating the pump at high rotation rates. Pulsations could not be observed by eye in the test cells during normal operation.

The test cells are designed to be as large as possible, without being so large that the interface is destabilized by the variable g-environment of the aircraft. For a given fluid and test cell, a typical test requires only selection of test cell fill level $H_0(\dot{Q}' = 0)$ and flow rate $\dot{Q}'$. The former is varied using a syringe plumbed into the loop upstream of the pump and isolated during the flow process by a valve. The latter is achieved simply by varying the pump rotation rate. The initial tests are performed at low values for H_0 and $\dot{Q}'$, both of which are gradually increased during subsequent tests to levels where disturbances from the aircraft are significant or air is ingested at the test cell exit port. H_0 and/or $\dot{Q}'$ are then slightly reduced, and multiple measurements are made at these 'maximum,' though reduced, levels. In a strict sense, the g-environment of the aircraft is neither steady nor repeatable, being dependent on atmospheric winds at elevation, pilot skill, and location of the experiment aboard the aircraft. However, from both video images as well as estimations of the Bond number, $\mathrm{Bo} \ll 1$, it is possible to achieve the steady flow condition.

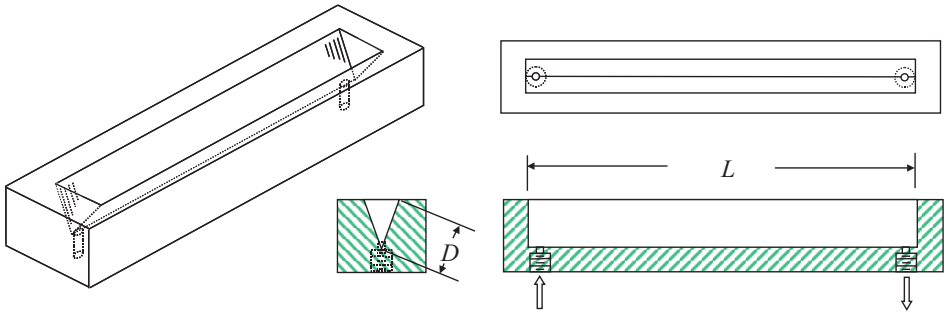

Figure 3.20: Views of transparent test cell: arrows indicate introduction and removal of fluid. Capillary driven flow is left to right.

As a condition to the parabolic reduced gravity trajectories of the aircraft, a brief period of 'elevated-g' occurs prior to each low-g period. The acceleration during this 'pull-up' phase is approximately 2-g_0 and lasts approximately 25 s. Video images of a typical in-flight steady flow test at $\sim$ 2-g_0 and during the $\sim$25 s period of reduced gravity are shown in Fig. 3.21. The distinction between the predominantly flat 2-g_0 surface of uniform height H_0 and

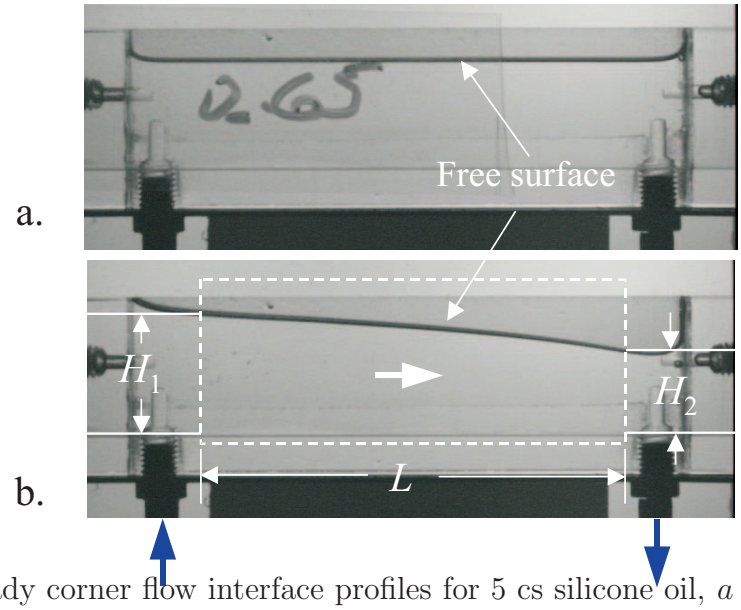

Figure 3.21: Steady corner flow interface profiles for 5 cs silicone oil, $a = 5°$, and fixed flow rate 0.0338 ml/s with pump setting of 0.65: a) 2-go and b) low-g (dashed region is field of interest).

the curved low-g surface at identical flow rates is obvious. The central parallel flow region identified by the dashed region in Fig. 3.21b is the focus of the investigation. This region satisfies the $\varepsilon^2 \ll 1$ condition, and is away from the entrance and exit regions where inertial 3-dimensional flows and surfaces are present. The surface profiles within this region may be directly compared to theory.

For the various experiments conducted, the video images are digitized using the Spotlight image analysis software developed by NASA Glenn Research Center (Klimek *et al.*, 1996; Klimek & Wright, 2006). The dynamic interface profiles are determined by an automated and highly repeatable routine that includes: a smoothing filter, simple thresholding, and a morphological outline of the interface. With this procedure, the interface is reduced to a pixelized line, which is then corrected for slight optical distortion due to the mismatched refractive index between test cell and test fluid. The location of the corner vertex is used as the reference from which to determine $h(z,t)$ from the pixelized interface profile.

Fig. 3.22(left) shows select interface profiles during the overdamped transition between high-g/low-g/high-g states for a test where $\alpha = 5°$, $H_0 = 12$ mm, $\dot{Q}' = 0.129$ ml/s for 5 cs Silicone oil. The curve identified at time $t = 0$ is the interface profile shortly after the entrance of the aircraft into the low-g period of the trajectory and is arbitrarily selected as the

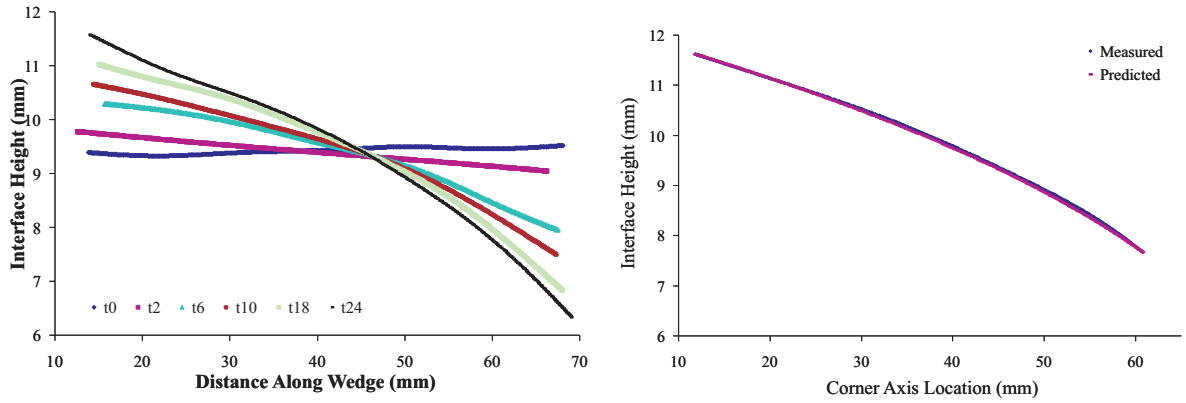

Figure 3.22: (Left) establishment of steady flow interface profile during transition to low-g. (Right) comparison of established steady profile to theoretical prediction.

time origin. The curves nearly overlap at times between 4s and 18s after which disturbances caused by the aircraft are observed. The central portion of the interface during this presumed quasi-steady flow period identified by the dashed rectangular region sketched in Fig. 3.22(left) is presented in Fig. 3.22(right) at time around t=24 s. Slightly downstream of the inlet begins the section of the flow that is parallel and modeled by Eq. (3.18). The parallel flow region ends near the exit port where 3-dimensional flows and surfaces are present. The length of this region is determined by the quality of fit between the measurements and predictions based on Eq. (3.18).

The height of the interface at a given 'entrance' and 'exit' of the presumed parallel flow region, H_1 and H_2, respectively, are taken directly from the data and used in Eq. (3.18) to compute the steady interface profile, which is also presented in Fig. 3.22(right). The agreement is excellent $\pm$ 1% for this case and better than $\pm$ 2% for all of the surfaces digitized. Eq. (3.20) is used to compute flow rate based on the measured values of H_1 and H_2 and L for the test. For the case of Fig. 3.22(right), values for $\dot{Q}'$(0.135 ml/s) reveal an over-prediction of the experimentally measured flow rate (0.129 ml/s) by $< 5\%$, which is typical for tests where a quasi-steady condition as argued by Fig. 3.22(left) is achieved. At low flow rates interface curvature is small and image resolution limits can contribute up to $\pm$10% errors in $\dot{Q}'$ computed from Eq. (3.20) using the measured values of H1 and H2.

3.2.3 1-g Steady Flow Solution and Verification

The formulation for the 1-g$_0$ low Bond number horizontal corner flow problem is altered by the presence of gravity and by writing $P' = -\sigma/fh' + pgh'$ the identical steps performed above for the 0-g case produce the dimensionless governing equation

$$(h^2)_t = (h^2(1 + h^2 \mathrm{Bo}_H)h_x)_x, \tag{3.21}$$

where $\mathrm{Bo}_H \equiv pg_z f H_1^2/\sigma$. This equation is valid for capillary flow for positive and negative values of Bo_H when $|\mathrm{Bo}_H| \ll 1$. It is important to note that Eq. (3.21) is also valid for gravity dominated θ-independent flow when $\mathrm{Bo}_H \gg 1$ using only α and $\delta = 0$ (or $\theta = \pi/2 - \alpha$) when determining f, F_A, and F_i.

The dimensionless steady solution to (3.21) is implicit for $h(x)$; namely,

$$z = \frac{1 - h^3 + \frac{3\mathrm{Bo}_H}{5}(1 - h^5)}{1 - b^3 + \frac{3\mathrm{Bo}_H}{5}(1 - b^5)}. \tag{3.22}$$

The explicit form of $h(z)$, Eq. (3.18), is recovered when $\mathrm{Bo}_H = 0$, and for gravity-dominated flow, $\mathrm{Bo}_H \gg 1$, the zeroth order explicit form of $h(z)$ is $h = (1 - (1 - h_2^5)x)^{1/5}$. For the case $|\mathrm{Bo}_H| \ll 1$, Eq. (3.22) is constrained by unbounded streamwise curvature in a similar manner as Eq. (3.20) only as $x \to 1/(1 - h_2^3 + 3B_H(1 - h_2^5)/5)$. The liquid column is unstable when $\mathrm{Bo}_H \leq -5(1 - h_2^3)/3(1 - b^5)$ and the dimensional flow rate is determined from Eq. (**??**) and (3.22),

$$\dot{Q}' = \frac{H_1^3 F_A G}{3L}\left[1 - h_2^3 + \frac{3B_H}{5}\left(1 - h_2^5\right)\right]. \tag{3.23}$$

The low-g tests are easily repeated at normal-gravity conditions using the experimental apparatus. Steady digitized surface profiles accompanied by the profiles predicted by (3.22) are conducted for a variety of $\dot{Q}'$ with $\alpha = 5°$, and 5cs Silicone oil. Maximum and average deviations of the predicted and measured interface profiles are shown to reveal a slight but certain over-prediction of the surface elevation. Flow rates calculate using (3.23) compared with experimental values also indicate a systematic over-prediction for the range of $\dot{Q}'$ tested. The analytically determined flow rates are susceptible to increased uncertainty due to pixel resolution limits on the empirically determined values of H_1 and H_2 that are used as inputs.

Solutions for flows along curved corners, flow with heat transfer, flows with free surface shear, and a variety of planar and 3-dimensional corner networks have also been solved and are to be reported in the literature shortly.

3.2.4 Assessment of Inertia in the Zero-Gravity Steady Flow Solution

With the steady solution $h(x)$ from Eq. (3.18), the average x-component of velocity $\langle u \rangle = -F_i h_x$ from Eq. (3.11) may be used to evaluate the order of magnitude of inertial terms neglected in the analysis. Noting that y- and z-component velocities are small, $v \ll 1$ and $w \ll 1$, the scale version of Eq. (3.5) yields

$$\mathrm{Re}\langle u \rangle \langle u \rangle_x \sim -P_x, \nabla^2 u \tag{3.24}$$

Substituting for $\langle u \rangle$, inertia may be neglected when small compared to the pressure gradient ($P = h^{-1}$), namely;

$$\frac{\mathrm{Re}\langle u \rangle \langle u \rangle_x}{-P_x} = F_i^2 \mathrm{Re} h^2 h_{xx} = \frac{2F_i^2 \mathrm{Re}(1-h_2^3)^2}{9(1-(1-h_2^3)x)} \ll 1 \tag{3.25}$$

At the exit $x = 1$ and

$$\frac{\mathrm{Re}\langle u \rangle \langle u \rangle_x}{-P_x} = \frac{2}{9}\frac{F_i^2 \mathrm{Re}(1-h_2^3)^2}{h_2^3} \ll 1, \tag{3.26}$$

or, substituting for Re,

$$\frac{\mathrm{Re}\langle u \rangle \langle u \rangle_x}{-P_x} = \frac{2}{9}\frac{F_i^2 \varepsilon^2 \sin^4\alpha (1-h_2^3)^2}{f\mathrm{Oh}^2 h_2^3} \ll 1 \tag{3.27}$$

It is clear that the low inertia limit is readily exceeded for $b^3 \ll 1$ as x approaches unity where inertial forces grow with relative strength as $\sim (1-x)^{-1}$. Streamwise curvature, assumed small in the viscous limit analysis, also becomes significant in this limit, but at a different rate, namely

$$fhh_{xx} = \frac{2}{9}\varepsilon^2 f(1-h_2^3)^2(1-(1-h_2^3)x)^{-4/3} \ll 1, \tag{3.28}$$

where at the exit $x = 1$ and

$$\frac{2}{9}\varepsilon^2 f\frac{(1-h_2^3)^2}{h_2^4} \ll 1. \tag{3.29}$$

This latter condition is also violated for $h_2^3 \ll 1$ as x approaches unity and grows at a rate $\sim (1-x)^{-4/3}$. It is thus possible to identify flow regimes where inertia and not streamwise curvature limit the applicability of the viscous limit solution. This range of parameters may be shown to satisfy

$$N = \frac{f^2\mathrm{Oh}^2}{F_i^2 b \sin^4\alpha} \ll 1. \tag{3.30}$$

Tests performed also satisfying this criterion can investigate the impact of inertia without introducing the complications of an additional surface curvature dimension that adds numerous nonlinear terms to the free surface boundary condition. Along with Re, N is employed to specify the range of tests to be conducted such that the presence of inertia can be systematically increased from the viscous flow base state to the inertia-dominated limit. The inertia dominated case for the wedge must be analyzed by a similar technique as presented previously for the parallel plate geometry, which in the end should be capable of analyzing all flow scenarios.

4 Justification for Extended Duration Microgravity Environment

4.1 Limitations of Terrestrial (1g laboratory) Testing

Ground-based experiments are limited by the hydrostatic pressure acting on the free surface. To obtain stability of the liquid in the channel, the hydrostatic pressure has to be sufficiently smaller than the capillary pressure. For this reason the Ohnesorge number Oh is limited. In case of a horizontal flow between parallel plates the following relation

$$\rho g_y a \approx \frac{2\sigma}{a} \tag{4.1}$$

is used to estimate the limits. Here $\rho g_y a$ is the maximal hydrostatic pressure in a channel of gap distance a. The term on the right hand side was derived from Eq. (2.13) neglecting the radius of curvature in flow direction x ($R_1 = -a/2$, $R_2 = \infty$). For the radius of curvature in the cross section plane half of the gap distance was assumed. This formulation is similar to a Bond number, as introduced in Eq. (2.11)

$$\mathrm{Bo}_y = \frac{\rho g_y a^2}{2\sigma}.$$

Since the stability limit is not known we require $\mathrm{Bo}_y < 0.01$. This yields an estimate of the maximal gap distance in a ground based experiment

$$a_{\max} = \sqrt{\frac{2\ Bo_y \sigma}{\rho g_y}} \tag{4.2}$$

as well as the minimal Ohnesorge number

$$\mathrm{Oh}_{\min} = \frac{\mu}{\sqrt{2 a_{\max} \rho \sigma}} \tag{4.3}$$

that is realizable. For the standard liquids we chose by virtue of their perfect wetting behavior, the limitations obtained from Eq. (4.2) and Eq. (4.3) are listed in Table 4.1. Thus, Ohnesorge numbers smaller than $\mathrm{Oh} \leq 5 \cdot 10^{-3}$ cannot be investigated on earth. The range to be investigated in this study will be $5 \cdot 10^{-3} > \mathrm{Oh} > 5 \cdot 10^{-4}$. Larger Oh numbers lead to a viscous dominated flow behavior and convective as well as inertia related effects cannot be studied.

	ρ	ν	σ	a_{max}	Oh_{min}
		10^{-6}	10^{-3}		10^{-3}
	[kg/m^3]	[m^2/s]	[N/m]	[mm]	[-]
Heptane	679	0.57	19.9	0.2	4.8
SF 0.65	761	0.65	15.6	0.2	7.2
SF 1.0	818	1.00	16.9	0.2	11
FC-77	1789	0.80	14.7	0.1	17

Table 4.1: Fluid properties at 25 °C. Maximal theoretical gap distance and minimal Ohnesorge number in a ground based experiment.

4.2 Limitations of Short Time Microgravity Facilities

The short experimental time in the drop tower essentially influences the choice of parameter and the accuracy of the determination of the critical flow rate and the critical velocity. As shown in section 3.1, the parameter field was limited to a certain range of Oh and Λ and moderate channel length to keep the rise time small compared to the remaining experiment time. To avoid the loss of time by the filling procedure, the channel was modified with a closure-mechanism. This modification enabled pre-filling the channel before the drop. However, opening the channel during the microgravity phase causes inertia effects which disturb the flow. Far away from the critical flow condition the disturbance is damped out during the remaining experiment time. Near the critical condition the inertia causes the surface to collapse. For this reason experiments in the drop tower yield the maximal flow rate with an accuracy that is sufficient for the design of technical applications. But for the investigation of the general physics of the flow rate limitation the accuracy of the drop tower experiment is insufficient. To prove whether the flow rate limitation occurs due to choking, a quasi-static increase of the flow rate is necessary, which is impossible in a drop tower.

Experiments in parabolic aircraft are unsuitable for a precise investigation since the level of the lateral acceleration in all three axes varies. The acceleration level in the aircraft is on the order of 0.01 g_0 with peaks as high as 0.1 g_0. If this acceleration is acting along the flow axis, the free surface in the capillary channel becomes unstable due to high hydrostatic pressures and the flow path is interrupted. We have experiences from two parabolic flight campaigns with the Airbus 300 Zero-g of the French space agency (CNES). We flew an experiment with the parallel plate channel geometry used for the TEXUS experiment. The surface was always strongly deformed and very often interrupted by high acceleration levels. Nevertheless, these experiments were essential to learn to operate a complex space experiment via telecommand in a very short mission duration.

The sounding rocket flight TEXUS-37 provided 360 s of microgravity and the possibility to interact with the experiment, i.e. video and data downlink and telecommand uplink. But this time was not sufficient to approach the critical velocity three times (one coarse, two fine approaches). The flow rate difference between the supply and the suction pump was higher than anticipated and the compensation tube was filled faster. This required some (trained) maneuvers to keep the meniscus within its margins. Nevertheless, the data could be used and some new findings were achieved. But a sounding rocket flight is always limited to one parameter point (Ohnesorge number, aspect ratio and channel length) and one approach (quasi steady). The investigation of the parameter space discussed in section 5 would require already 10 flights per channel for the investigation of the steady flow, not to mention the reproduction and the both modes transient and oscillatory. Concluding one can say that for this type of experiment a sounding rocket flight gives one data point only. Variations in the parameter space are not possible since one can expect a sounding rocket flight every 3-5 years.

4.3 Limitations of Modelling

Theoretical models are presented in the appendices to predict the critical flow rate and the free surface position. The theory is one-dimensional assuming all physical properties to be constant in the cross section plane. This model has to be validated by experiments.

In preparation for the sounding rocket experiment (TEXUS) we performed three-dimensional model computations concerning the flow inside the liquid reservoir, the nozzle and the open channel. The model computations were performed using the finite element code FIDAP (Fluent Inc.). It turned out that the computed critical flow rate was 17% too high and the predicted surface curvature was too small. The reason for this deviation from the results of the TEXUS experiment is the numerical diffusion, which is an inherent problem of the numerical algorithm. In addition, the calculation of moving contact lines, which occur when the liquid meniscus moves into the channel and is no longer pinned to the edges, is very difficult to solve numerically. Clearly the data from the proposed experiments may be used to validate numerical codes for problems with free surfaces or moving contact lines.

4.4 Need for Long Duration of Microgravity

The proposed experiment objectives cannot be obtained in short time facilities like drop towers, parabolic aircraft or sounding rockets. A study with different approaches to the critical value (quasi steady, transient or oscillatory) and with different channel geometries (parallel and tilted plates, wedge, and gapped wedge) can only be performed on a long term

microgravity facility with the possibility to interact with the experiment.

For the parallel plate channel and groove we assume that the curve of the speed index is sufficiently determined by 20 data points achieved by variation of the flow rate. Each speed index curve refers to a set of dimensionless parameter defined by the test matrix. For each channel the test matrix is arranged for 10 length, 7 modi (1 quasi-steady, 3 oscillatory, 3 transient) and 3 repetitions. In total this leads to 210 data points per channel. Assuming that the determination of the maximum flow rate and the related speed index curve (consisting of 20 data points) can be determined within 15 minutes, the total amount of pure experiment time (without fluid loop preparation) will be 53 h for each channel. This is only available on the space station.

We showed in the foregoing sections that

- the flow problem can not be investigated on earth in the desired parameter space,
- the parameter space is spanned by the independent dimensionless groups Ohnesorge number, aspect ratio, channel length, and the approach to the critical flow rate,
- the different geometries will enable us to investigate different features of the flow,
- open capillary channel flows have not been investigated thoroughly in the past except by the authors, and
- the experimental techniques as well as the theoretical modelling is mature enough to conduct a successful experiment in space.

4.5 Impact of two-phase bubbly flows

As currently envisioned for EU#2, the addition of bubbles to potentially all of liquid flows adds a significant dimension to the research. Especially for the wedge and gapped wedge geometries the various channels can act as passive phase separation devices that may be exploited in various fluid systems aboard spacecraft. The bubbles are excluded from the vertex region of these particular channels by a number of mechanisms that include volume ratios, developing boundary layers (shear gradients), and secondary flows normal to the free surface. The bubbles are passively forced to the interface where they coalesce and the fluid phases are separated. Such devices are useful for vapor bubble removal in cryogenic propellant tank vane structures, gas bubble removal in storable fuel tanks, noncondensible gas removal in thermal fluid systems such as Loop Heat Pipes, condensing heat exchangers, and water recycling systems. Such multi-phase flows can not be studied on the ground for all liquid fluid regimes due to the buoyancy force. Critical velocities below which the particular channels behave effectively as passive phase separators are one of many expected outcomes

of these studies as well as detailed data on bubble trajectories and coalescence rates for a variety of flow rates, bubble sizes, number densities, containers geometry, etc.

5 Experiment Plan

5.1 Experimental Apparatus

Similar to the TEXUS experiment (see §3.1.2) the experimental set-up will essentially consists of a test cell with the test channel and a main reservoir with compensation tube. The experiment observation requires two video cameras, one for the general view and one for the detail view of the test channel. The general view is necessary to monitor the flow system which should be transparent in its essential parts. The detail view provides the free surface data and should be designed to meet the optical resolution requirements. The flow through the test channel is maintained by a pump. The gas volume added to the fluid loop during the gas breakthroughs (collapsing surface) is accommodated by the compensation tube. An active control of the experiment should be possible via telecommand.

Fig. 5.1 shows the integration of the experiment set-up into the Microgravity Science

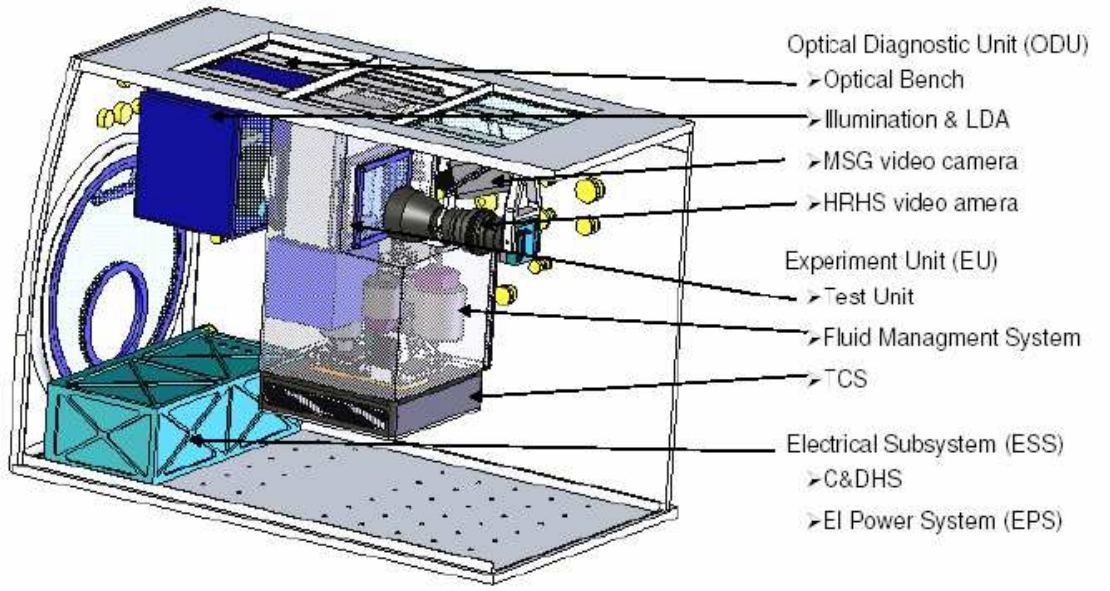

Figure 5.1: General view of the experimental setup integrated into the Glovebox.

Glovebox (MSG) as proposed by EADS Space Transportation (2005). The set-up is designed modularly and consist of the Experiment Unit (EU), the Optical Diagnostic Unit (ODU) and

the Electronical Subsystem (ESS). The EU contains the Test Unit (TU), the Fluid Management System (FMS) and the Temperature Control System (TCS). The video observations are performed with the ODU. It provides a background illumination with parallel light and enables a general view of the EU as well as a detail view of the channel. For the general a standard TV-camera (appurtenance of the MSG), for the detail view a high resolution, high speed camera is foreseen. The ESS contains the electrical power system (EPS) and the command and data handling system (C&DHS). The latter unit is used for the experiment control, the image processing and storage of the data.

Fig. 5.2 shows the schematic of the fluid loop. The operation principle is similar to

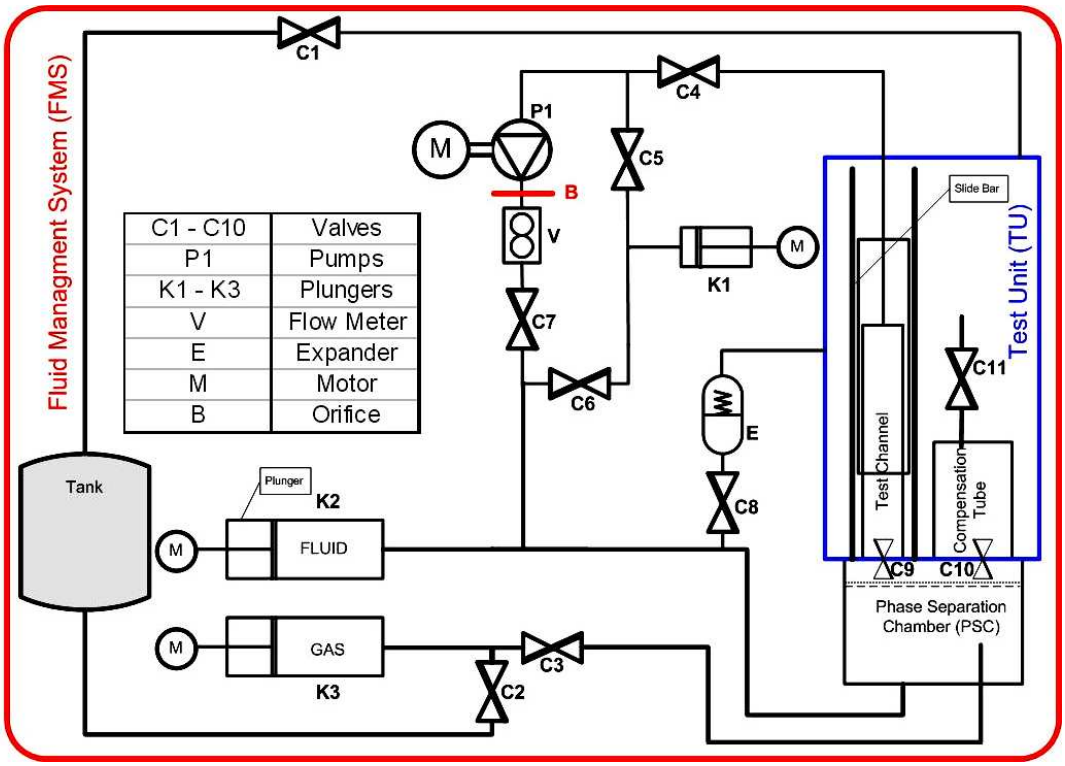

Figure 5.2: Schematic drawing of the fluid loop.

the hardware used for the TEXUS flight except that the system must be able to handle two-phase flows under microgravity conditions. The fluid cycle essentially consists of the test unit, pump P1, flow meter V, separator tank, plungers K1 - K3 and valves C1 - C11. The phase separation is achieved in the Phase Separation Chamber (PSC). In this device a master gas bubble is established with which the smaller gas bubbles of the entering two phase flow will coalesce. The bubble retainment is achieved by a screen. With help of the plungers K2 and K3 the gas and liquid volume inside the PSC and the compensation tube are controlled, respectively. Plunger K1 is necessary for the generation of transient flow modes. The separator tank contains a porous medium in the event that liquid enters the gas vent line.

Fig. 5.3 shows the test unit with the test channel and the compensation tube. The open length of the channel can be varied by two sidewise mounted slide bars. The compensation tube is very important; it accommodates the volume entered to the flow in case of the unsteady flow.

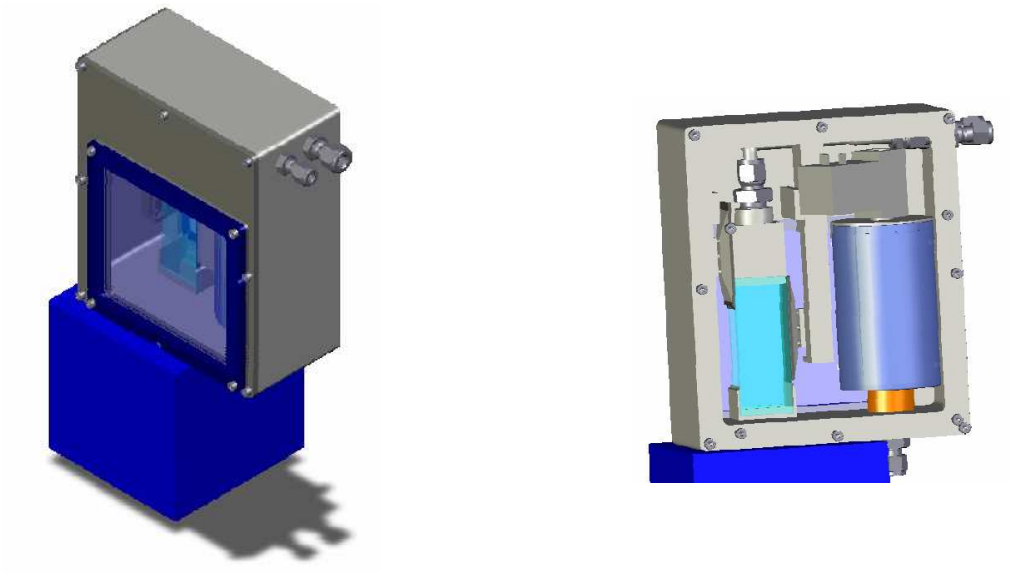

Figure 5.3: Test unit (TU) overview (left). Lid with observation window removed from TU (right).

5.2 Measurement Strategy

The primary aim of the experiment is to find the critical flow rates and the corresponding critical flow velocities for different capillary channels (EU# 1 parallel plates and groove and EU# 2 wedge, gapped wedge and tilted plates). The data should validate the prediction for the flow rate limitation. For stable flows the profiles of the free surfaces can be compared with the theoretical solutions of the governing time-independent equations. In general, but not for all test conditions, the critical flow velocity will be approached threefold employing:

1. Quasi-steady increases of the flow rate through the capillary channel
2. Transient changes of the flow rate
3. Sinusoidally modulated flow rate.

It has to be shown if and how the stability of the flow depends on the type of approach. In the quasi-steady approach the flow velocity is limited by the pressure losses in the channel and the inlet due to molecular (viscous friction) and convective (caused by convective acceleration)

momentum transport. In the transient approach the flow velocity is limited by the inertia of the system due to local accelerations. The modulated approach combines the possibility of changing the frequency and the amplitude of the modulation. It is known from complex chemical systems that the modulation of the main parameter may stabilize the system and thus increase the maximum flow rate. Secondly, the unstable flow regime should be observed. Up to now no theory is available to predict the bubble size and frequency at the outlet if the critical velocity is exceeded. The bubble size distribution at the outlet is important for fluid management in space.

5.3 Test Matrix

5.3.1 General Approach

In general, the test matrix is achieved from the range of non-dimensional numbers for each geometry. To convert the non-dimensional numbers into dimensional quantities liquid properties must be chosen. The properties of some adequate liquids are given in Table 5.1. The temperature range and most of the listed liquids have been taken from the Payload Accommodation Handbook of the MSG (DaimlerChrysler Aerospace, 1999). All liquids have a static contact angle of zero with the test channel material. The change of the temperature of the test liquid could be a method to change the dimensionless numbers of the experiment. In the meantime the test liquid for the space station experiment has been chosen (HFE-7500) and all previous calculations are updated. The achieved data is used for the first layout of the experimental set-up, in particular the field of observation and thus the resolution of the video pictures as well as the maximum volume rate for the layout of the tank system.

As seen in the previous sections the free liquid surface bends inwards between the plates. The optical system records the position of the surface profile k which is a measure of the curvature and thus for the pressure of the flow. The profile k varies in the range of half the plate distance $b/2 \leq k \lesssim (b/2 - a/2)$ (see Figure 3.10b). The required resolution for k is 1%. The range of plate distances to be investigated is 2.5 mm $< a <$ 65 mm. Capillary channels with $a <$ 0.25 mm can be investigated on earth. Larger channel widths lead to very high flow rates which may not be feasible in the space experiment. The required resolution for k follows from $k \approx a/2$ to

$$0.01\frac{a_{min}}{2}\frac{1}{\text{pixel}} \approx 0.0125\ \frac{\text{mm}}{\text{pixel}} < \Delta k < 0.325\frac{\text{mm}}{\text{pixel}} \approx 0.01\frac{a_{max}}{2}\frac{1}{\text{pixel}}.$$

We anticipate that at the time of the design of the experiment a camera system with a resolution of 1280 x 1024 pixel is available. We assume further that the cameras will be aligned such as shown in Figure 5.4, i.e. the larger pixel number $p_x = 1280$ is parallel to the

Fluid	T [^{o}C]	ρ [kg/m^3]	μ 10^{-3} [kg/(m s)]	σ 10^{-3} [N/m]	$\sqrt{\frac{\rho\nu^2}{2\sigma}}$ 10^{-4} [$\sqrt{m}$]
SF 0.65	15	771	0.546	16.3	1.089
SF 0.65	25	761	0.5	15.6	1.026
SF 0.65	45	741	0.393	13.8	0.869
SF 1.0	15	829	0.928	17.5	1.723
SF 1.0	25	818	0.818	16.9	1.556
SF 1.0	45	797	0.612	15.1	1.248
FC-77	15	1801	1.7	15.7	2.26
FC-77	25	1777	1.422	14.7	1.967
FC-77	45	1727	0.895	13.2	1.325
Ethanol C_2H_6O	15	794	1.315	23	2.17
Ethanol C_2H_6O	25	785	1.1	22.2	1.86
Ethanol C_2H_6O	45	768	0.76	20.4	1.36
Heptan C_7H_{16}	15	688	0.44	20.8	0.822
Heptan C_7H_{16}	25	679	0.39	19.9	0.75
Heptan C_7H_{16}	45	662	0.317	18	0.65
Butanol $C_4H_{10}O$	15	719	3.5	25.1	5.82
Butanol $C_4H_{10}O$	25	707	2.6	24.3	4.43
Butanol $C_4H_{10}O$	45	684	1.6	22.7	2.87
Decan $C_{10}H_{22}$	15	735	1.05	24.4	1.75
Decan $C_{10}H_{22}$	25	727	0.84	23.4	1.44
Decan $C_{10}H_{22}$	45	712	0.65	21.5	1.17
HFE 7500	15	1640	1.50	17.6	1.97
HFE 7500	25	1620	1.25	16.7	1.70
HFE 7500	45	1580	0.916	14.7	1.34

Table 5.1: Properties of possible test liquids for the MSG.

flow length l. Two cameras are necessary to observe the total flow length for large channels, one camera for the inlet region and one camera for the outlet region. The fields of view overlap in the middle of the channel. Then the maximal breadth b_{max} and the maximal length l_{max} can be defined as

$$\begin{aligned} 13 \text{ mm} &< b_{\max} < 256 \text{ mm} \\ 16 \text{ mm} &< l_{\max} < 320 \text{ mm} \end{aligned}$$

using the formulas

$$\Delta k \; p_z = b_{max}, \quad \Delta k \; p_x = l_{max}$$

with $p_x = 1280$ and $p_z = 1024$.

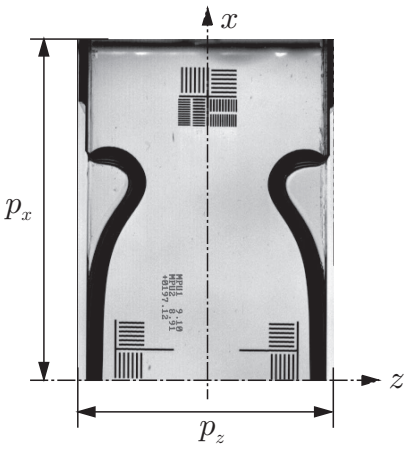

Figure 5.4: Alignment of the camera along the flow path. The picture has been taken from the upper view of the TEXUS experiment for supercritical flow.

We request that the flow length should be adjustable by covering the free surface at the side(s) or the circumference with a slider. To run the experiment without a free surface in a safety mode, the slider could cover the whole free surface. This procedure has been tested in parabolic flights for the parallel plate channel and was used for the release of the free surface in the liquid bridge experiment.

5.3.2 Parallel Plate Channel

The Tables 5.2 through 5.6 show the preliminary test matrices for the quasi-steady, transient and oscillatory modes, respectively. The symbols denote the flow rate Q, the critical flow rate Q_{crit}, the channel length l, the flow rate acceleration $q = \Delta Q/\Delta t$, the oscillator frequency ν, the stroke of the oscillator A, the frame rate of the camera f and recording time of the camera τ.

I. Quasi-steady mode: The quasi-steady mode is subdivided into two approaches: the determination of the critical flow state by variation of the flow rate Q (mode Ia) and the determination of the critical flow state by variation of the flow length l (mode Ib). The data achieved from the profiles of the surfaces are used to map the speed index S as function of Q and l respectively. A typical scenario of the first approach is displayed in Table 5.2. The flow length is kept constant and the flow rate is varied. It is assumed that twenty data points are sufficient for the determination of a S-Q-curve (repetitions not considered). Since the speed index varies strongly close to the critical flow state, a higher density of data points for the higher flow rates is required. After each change of Q the liquid surfaces will perform a damped harmonic oscillation. The oscillation will be damped out within 15 to 20 seconds. After that the flow is in steady state. The camera will be started directly before the change of Q. The typical recording time τ will be $\tau = 30$ s. For this purpose the frame rate is set to 100 Hz. The frame rate will be increased if the required time to observed the flow is shorter or if certain details shall be highlighted. In total mode Ia envisages the variation of Q for ten given length (see Table 5.3) and mode Ib the variation of the length l for ten given flow rates, $Q_1, \ldots, Q_{10}$ (see Table 5.4). The experiment strategy of mode Ib is analogous to Ia.

II. Transient mode: The procedure in mode II is analogous to mode Ia but the transition between two steady flow states (change of flow rate) is influenced by the parameter $q = \Delta Q/\Delta t$ (Table 5.5). For a given flow length l_i (ten in total) the S-Q-curve shall be determined for three different parameter q_{ij} with $i = 1, \ldots, 10$ and $j = 1, \ldots, 3$.

III. Oscillatory mode: The procedure in mode III is analogous to mode Ia but now the flow rate is superimposed by the flow rate of the oscillator (Table 5.6). For a given flow length l_i (ten in total) the S-Q-curve shall be determined for three given frequencies, ν_{ij} with $i = 1, \ldots, 10$ and $j = 1, \ldots, 3$. For each flow length the stroke of the oscillator A is kept constant but a variation form flow length to flow length is required.

No.	Mode	Q/Q_{crit}	l	$\Delta Q/\Delta t$	ν	f	τ
		[-]	[mm]	[-]	[s^{-1}]	[s^{-1}]	[s]
1	Ia	0.200	5	-	0	$100 \cdots 250$	$12 \cdots 30$
2	Ia	0.400	5	-	0	$100 \cdots 250$	$12 \cdots 30$
3	Ia	0.500	5	-	0	$100 \cdots 250$	$12 \cdots 30$
4	Ia	0.600	5	-	0	$100 \cdots 250$	$12 \cdots 30$
5	Ia	0.700	5	-	0	$100 \cdots 250$	$12 \cdots 30$
6	Ia	0.800	5	-	0	$100 \cdots 250$	$12 \cdots 30$
7	Ia	0.825	5	-	0	$100 \cdots 250$	$12 \cdots 30$
8	Ia	0.850	5	-	0	$100 \cdots 250$	$12 \cdots 30$
9	Ia	0.875	5	-	0	$100 \cdots 250$	$12 \cdots 30$
10	Ia	0.900	5	-	0	$100 \cdots 250$	$12 \cdots 30$
10	Ia	0.910	5	-	0	$100 \cdots 250$	$12 \cdots 30$
12	Ia	0.920	5	-	0	$100 \cdots 250$	$12 \cdots 30$
13	Ia	0.930	5	-	0	$100 \cdots 250$	$12 \cdots 30$
14	Ia	0.940	5	-	0	$100 \cdots 250$	$12 \cdots 30$
15	Ia	0.950	5	-	0	$100 \cdots 250$	$12 \cdots 30$
16	Ia	0.960	5	-	0	$100 \cdots 250$	$12 \cdots 30$
17	Ia	0.970	5	-	0	$100 \cdots 250$	$12 \cdots 30$
18	Ia	0.980	5	-	0	$100 \cdots 250$	$12 \cdots 30$
19	Ia	0.990	5	-	0	$100 \cdots 250$	$12 \cdots 30$
20	Ia	0.995	5	-	0	$100 \cdots 250$	$12 \cdots 30$

Table 5.2: Preliminary test matrix for the determination of the flow rate at a fixed channel length.

No.	Mode	Q/Q_{crit} [-]	l [mm]	$\Delta Q/\Delta t$ [-]	ν [s^{-1}]	f [s^{-1}]	τ [s]
1	Ia	0.200	5	-	0	$100 \cdots 250$	$12 \cdots 30$
⋮	⋮	⋮	⋮	⋮	⋮	⋮	
20	Ia	0.995	5	-	0	$100 \cdots 250$	$12 \cdots 30$
21	Ia	0.200	10	-	0	$100 \cdots 250$	$12 \cdots 30$
⋮	⋮	⋮	⋮	⋮	⋮	⋮	
40	Ia	0.995	10	-	0	$100 \cdots 250$	$12 \cdots 30$
41	Ia	0.200	15	-	0	$100 \cdots 250$	$12 \cdots 30$
⋮	⋮	⋮	⋮	⋮	⋮	⋮	
60	Ia	0.995	15	-	0	$100 \cdots 250$	$12 \cdots 30$
61	Ia	0.200	20	-	0	$100 \cdots 250$	$12 \cdots 30$
⋮	⋮	⋮	⋮	⋮	⋮	⋮	
80	Ia	0.995	20	-	0	$100 \cdots 250$	$12 \cdots 30$
81	Ia	0.200	25	-	0	$100 \cdots 250$	$12 \cdots 30$
⋮	⋮	⋮	⋮	⋮	⋮	⋮	
100	Ia	0.995	25	-	0	$100 \cdots 250$	$12 \cdots 30$
101	Ia	0.200	30	-	0	$100 \cdots 250$	$12 \cdots 30$
⋮	⋮	⋮	⋮	⋮	⋮	⋮	
120	Ia	0.995	30	-	0	$100 \cdots 250$	$12 \cdots 30$
121	Ia	0.200	35	-	0	$100 \cdots 250$	$12 \cdots 30$
⋮	⋮	⋮	⋮	⋮	⋮	⋮	
140	Ia	0.995	35	-	0	$100 \cdots 250$	$12 \cdots 30$
141	Ia	0.200	40	-	0	$100 \cdots 250$	$12 \cdots 30$
⋮	⋮	⋮	⋮	⋮	⋮	⋮	
160	Ia	0.995	40	-	0	$100 \cdots 250$	$12 \cdots 30$
161	Ia	0.200	45	-	0	$100 \cdots 250$	$12 \cdots 30$
⋮	⋮	⋮	⋮	⋮	⋮	⋮	
180	Ia	0.995	45	-	0	$100 \cdots 250$	$12 \cdots 30$
181	Ia	0.200	48	-	0	$100 \cdots 250$	$12 \cdots 30$
⋮	⋮	⋮	⋮	⋮	⋮	⋮	
200	Ia	0.995	48	-	0	$100 \cdots 250$	$12 \cdots 30$

Table 5.3: Preliminary test matrix for determination of the critical flow rate (quasi-steady mode).

No.	Mode	l/l_{crit} [-]	Q [cm^3 s^{-1}]	$\Delta Q/\Delta t$ [-]	ν [s^{-1}]	f [s^{-1}]	τ [s]
1	Ib	0.960	Q_1	-	0	$100 \cdots 250$	$12 \cdots 30$
⋮	⋮	⋮	⋮	⋮	⋮	⋮	
20	Ib	0.998	Q_1	-	0	$100 \cdots 250$	$12 \cdots 30$
21	Ib	0.960	Q_2	-	0	$100 \cdots 250$	$12 \cdots 30$
⋮	⋮	⋮	⋮	⋮	⋮	⋮	
40	Ib	0.998	Q_2	-	0	$100 \cdots 250$	$12 \cdots 30$
41	Ib	0.960	Q_3	-	0	$100 \cdots 250$	$12 \cdots 30$
⋮	⋮	⋮	⋮	⋮	⋮	⋮	
60	Ib	0.998	Q_3	-	0	$100 \cdots 250$	$12 \cdots 30$
61	Ib	0.960	Q_4	-	0	$100 \cdots 250$	$12 \cdots 30$
⋮	⋮	⋮	⋮	⋮	⋮	⋮	
80	Ib	0.998	Q_4	-	0	$100 \cdots 250$	$12 \cdots 30$
81	Ib	0.960	Q_5	-	0	$100 \cdots 250$	$12 \cdots 30$
⋮	⋮	⋮	⋮	⋮	⋮	⋮	
100	Ib	0.998	Q_5	-	0	$100 \cdots 250$	$12 \cdots 30$
101	Ib	0.960	Q_6	-	0	$100 \cdots 250$	$12 \cdots 30$
⋮	⋮	⋮	⋮	⋮	⋮	⋮	
120	Ib	0.998	Q_6	-	0	$100 \cdots 250$	$12 \cdots 30$
121	Ib	0.960	Q_7	-	0	$100 \cdots 250$	$12 \cdots 30$
⋮	⋮	⋮	⋮	⋮	⋮	⋮	
140	Ib	0.998	Q_7	-	0	$100 \cdots 250$	$12 \cdots 30$
141	Ib	0.960	Q_8	-	0	$100 \cdots 250$	$12 \cdots 30$
⋮	⋮	⋮	⋮	⋮	⋮	⋮	
160	Ib	0.998	Q_8	-	0	$100 \cdots 250$	$12 \cdots 30$
161	Ib	0.960	Q_9	-	0	$100 \cdots 250$	$12 \cdots 30$
⋮	⋮	⋮	⋮	⋮	⋮	⋮	
180	Ib	0.998	Q_9	-	0	$100 \cdots 250$	$12 \cdots 30$
181	Ib	0.960	Q_{10}	-	0	$100 \cdots 250$	$12 \cdots 30$
⋮	⋮	⋮	⋮	⋮	⋮	⋮	
200	Ib	0.998	Q_{10}	-	0	$100 \cdots 250$	$12 \cdots 30$

Table 5.4: Preliminary test matrix for determination of the critical flow length (quasi-steady mode).

No.	Mode	Q/Q_{crit}	l	$\Delta Q/\Delta t$	ν	f	τ
		[-]	[mm]	[-]	[s^{-1}]	[s^{-1}]	[s]
1	II	0.200	5	q_{1j}	0	$100 \cdots 250$	$12 \cdots 30$
⋮	⋮	⋮	⋮	⋮	⋮	⋮	
20	II	0.995	5	q_{1j}	0	$100 \cdots 250$	$12 \cdots 30$
21	II	0.200	10	q_{2j}	0	$100 \cdots 250$	$12 \cdots 30$
⋮	⋮	⋮	⋮	⋮	⋮	⋮	
40	II	0.995	10	q_{2j}	0	$100 \cdots 250$	$12 \cdots 30$
41	II	0.200	15	q_{3j}	0	$100 \cdots 250$	$12 \cdots 30$
⋮	⋮	⋮	⋮	⋮	⋮	⋮	
60	II	0.995	15	q_{3j}	0	$100 \cdots 250$	$12 \cdots 30$
61	II	0.200	20	q_{4j}	0	$100 \cdots 250$	$12 \cdots 30$
⋮	⋮	⋮	⋮	⋮	⋮	⋮	
80	II	0.995	20	q_{4j}	0	$100 \cdots 250$	$12 \cdots 30$
81	II	0.200	25	q_{5j}	0	$100 \cdots 250$	$12 \cdots 30$
⋮	⋮	⋮	⋮	⋮	⋮	⋮	
100	II	0.995	25	q_{5j}	0	$100 \cdots 250$	$12 \cdots 30$
101	II	0.200	30	q_{6j}	0	$100 \cdots 250$	$12 \cdots 30$
⋮	⋮	⋮	⋮	⋮	⋮	⋮	
120	II	0.995	30	q_{6j}	0	$100 \cdots 250$	$12 \cdots 30$
121	II	0.200	35	q_{7j}	0	$100 \cdots 250$	$12 \cdots 30$
⋮	⋮	⋮	⋮	⋮	⋮	⋮	
140	II	0.995	35	q_{7j}	0	$100 \cdots 250$	$12 \cdots 30$
141	II	0.200	40	q_{8j}	0	$100 \cdots 250$	$12 \cdots 30$
⋮	⋮	⋮	⋮	⋮	⋮	⋮	
160	II	0.995	40	q_{8j}	0	$100 \cdots 250$	$12 \cdots 30$
161	II	0.200	45	q_{9j}	0	$100 \cdots 250$	$12 \cdots 30$
⋮	⋮	⋮	⋮	⋮	⋮	⋮	
180	II	0.995	45	q_{9j}	0	$100 \cdots 250$	$12 \cdots 30$
181	II	0.200	48	q_{10j}	0	$100 \cdots 250$	$12 \cdots 30$
⋮	⋮	⋮	⋮	⋮	⋮	⋮	
200	II	0.995	48	q_{10j}	0	$100 \cdots 250$	$12 \cdots 30$

Table 5.5: Preliminary test matrix for determination of the critical flow rate (transient mode). For each flow length l_i the experiments are conducted at $j = 3$ different values of the flow rate acceleration, q_{i1}, q_{i2}, q_{i3}.

No.	Mode	Q/Q_{crit} [-]	l [mm]	$\Delta Q/\Delta t$ [-]	ν [s^{-1}]	A [$cm^3\ s^{-1}$]	f [s^{-1}]	τ [s]
1	III	0.200	5	-	ν_{1j}	A_1	$100 \cdots 250$	$12 \cdots 30$
⋮	⋮	⋮	⋮	⋮	⋮	⋮		
20	III	0.995	5	-	ν_{1j}	A_1	$100 \cdots 250$	$12 \cdots 30$
21	III	0.200	10	-	ν_{2j}	A_2	$100 \cdots 250$	$12 \cdots 30$
⋮	⋮	⋮	⋮	⋮	⋮	⋮		
40	III	0.995	10	-	ν_{2j}	A_2	$100 \cdots 250$	$12 \cdots 30$
41	III	0.200	15	-	ν_{3j}	A_3	$100 \cdots 250$	$12 \cdots 30$
⋮	⋮	⋮	⋮	⋮	⋮	⋮		
60	III	0.995	15	-	ν_{3j}	A_3	$100 \cdots 250$	$12 \cdots 30$
61	III	0.200	20	-	ν_{4j}	A_4	$100 \cdots 250$	$12 \cdots 30$
⋮	⋮	⋮	⋮	⋮	⋮	⋮		
80	III	0.995	20	-	ν_{4j}	A_4	$100 \cdots 250$	$12 \cdots 30$
81	III	0.200	25	-	ν_{5j}	A_5	$100 \cdots 250$	$12 \cdots 30$
⋮	⋮	⋮	⋮	⋮	⋮	⋮		
100	III	0.995	25	-	ν_{5j}	A_5	$100 \cdots 250$	$12 \cdots 30$
101	III	0.200	30	-	ν_{6j}	A_6	$100 \cdots 250$	$12 \cdots 30$
⋮	⋮	⋮	⋮	⋮	⋮	⋮		
120	III	0.995	30	-	ν_{6j}	A_6	$100 \cdots 250$	$12 \cdots 30$
121	III	0.200	35	-	ν_{7j}	A_7	$100 \cdots 250$	$12 \cdots 30$
⋮	⋮	⋮	⋮	⋮	⋮	⋮		
140	III	0.995	35	-	ν_{7j}	A_7	$100 \cdots 250$	$12 \cdots 30$
141	III	0.200	40	-	ν_{8j}	A_8	$100 \cdots 250$	$12 \cdots 30$
⋮	⋮	⋮	⋮	⋮	⋮	⋮		
160	III	0.995	40	-	ν_{8j}	A_8	$100 \cdots 250$	$12 \cdots 30$
161	III	0.200	45	-	ν_{9j}	A_9	$100 \cdots 250$	$12 \cdots 30$
⋮	⋮	⋮	⋮	⋮	⋮	⋮		
180	III	0.995	45	-	ν_{9j}	A_9	$100 \cdots 250$	$12 \cdots 30$
181	III	0.200	48	-	ν_{10j}	A_{10}	$100 \cdots 250$	$12 \cdots 30$
⋮	⋮	⋮	⋮	⋮	⋮	⋮		
200	III	0.995	48	-	ν_{10j}	A_{10}	$100 \cdots 250$	$12 \cdots 30$

Table 5.6: Preliminary test matrix for determination of the critical flow rate (oscillatory mode). For each flow length l_i the experiments are conducted at $j = 3$ different oscillator frequencies, ν_{i1}, ν_{i2}, ν_{i3}. For a given flow length the stroke A is kept constant.

Mode	n_l	n_Q	n_q	n_ν	n_r	n_{total}
Ia	10	-	-	-	3	30
Ib	-	10	-	-	3	30
II	10	-	3	-	3	90
III	10	-	-	3	3	90

Table 5.7: Number of parameters for the modes I to III (EU#1, parallel plates).

The number of parameter for each mode is summarized in Table 5.7. It denotes n_l the number of adjusted channel lengths, n_Q the number of adjusted flow rates, n_q the number of adjusted parameters $\Delta Q/\Delta t$, n_ν the number of adjusted oscillation frequencies and n_r the number of repetitions. In total the modes lead to $n_{total} = 240$ parameter. Assuming an average number of 20 variation of Q and l in order to determine the critical flow rate and critical flow length, respectively, for each given parameter set and mode, a number of 4800 data points regarding the speed index and the surface profiles is achieved for the comparison with the theoretical results.

The complete realization of the test matrix in terms of channel length, flow rates, flow rate changes and oscillator frequencies and test liquid is not the task of this document. This cannot be done before the complete design and the capabilities of the MSG data handling is available. Deviating from the first version of this document (SRD CCF Version 1.0) the channel properties a, b and l are now defined. The upper and lower critical flow rates using the test liquid HFE 7500 are displayed in Table 5.8.

Λ	Oh	$\mathcal{L}$	Q'_{crit}	a	b	l	Q_{crit}
[-]	[-]	[-]	[-]	[mm]	[mm]	[mm]	[cm^3 s^{-1}]
5	$2.47{\cdot}10^{-3}$	$6.19{\cdot}10^{-4}$	1.320	5	25	5	10.7
5	$2.47{\cdot}10^{-3}$	$6.19{\cdot}10^{-3}$	0.716	5	25	48	5.8

Table 5.8: Channel length-depending maximum (critical) flow rates for the parallel plates with HFE-7500 at $T = 23°$C and a compensation tube with diameter $D_c = 50$ mm. The inlet boundary conditions are $L = -24.0$, $K_1 = 1.39$, $K_2 = 312$ and $K_3 = 0.2$.

5.3.3 Groove Channel

The investigations of the groove channel will be performed in a similar way to that of the parallel plate channel. Three modes (mode I: quasi-static, mode II: transient, mode III:

Mode	n_l	n_Q	n_q	n_ν	n_r	n_{total}
Ia	10	-	-	-	3	30
Ib	-	10	-	-	3	30
II	10	-	3	-	3	90
III	10	-	-	3	3	90

Table 5.9: Number of parameters for the modes I to III (EU#1, groove).

oscillatory) as well as the variation of the flow rate and length are envisioned. Therefor the test matrices are similar to those for the parallel plates displayed in the Tables 5.2 through 5.6. The parameter to be varied are the flow rate Q, the channel length l, the flow rate acceleration $q = \Delta Q/\Delta t$, the oscillator frequency ν and the stroke of the oscillator A.

The number of parameter for each mode is summarized in Table 5.9. It denotes n_l the number of adjusted channel lengths, n_Q the number of adjusted flow rates, n_q the number of adjusted parameters $\Delta Q/\Delta t$, n_ν the number of adjusted oscillation frequencies and n_r the number of repetitions. In total the modes lead to $n_{total} = 240$ parameter. Assuming an average number of 20 variation of Q and l in order to determine the critical flow rate and critical flow length, respectively, for each given parameter set and mode, a number of 4800 data points regarding the speed index and the surface profiles is achieved for the comparison with the theoretical results.

The complete realization of the test matrix in terms of channel length, flow rates, flow rate changes and oscillator frequencies and test liquid is not the task of this document. This cannot be done before the complete design and the capabilities of the MSG data handling is available. Deviating from the first version of this document (SRD CCF Version 1.0) the channel properties a, b and l are now defined. The upper and lower critical flow rates using the test liquid HFE 7500 are shown in Table 5.10.

Λ	Oh	$\mathcal{L}$	Q'_{crit}	a	b	l	Q
[-]	[-]	[-]	[-]	[mm]	[mm]	[mm]	[ml/s]
5	$2.48{\cdot}10^{-3}$	$7.15{\cdot}10^{-4}$	1.287	5	25	5	10.7
5	$2.48{\cdot}10^{-3}$	$7.15{\cdot}10^{-3}$	0.811	5	25	48	6.8

Table 5.10: Channel length-depending maximum (critical) flow rates for the groove with HFE-7500 at $T = 23°C$ and a compensation tube with diameter $D_c = 50$ mm. The inlet boundary conditions are $L = -24.0$, $K_1 = 1.39$, $K_2 = 312$ and $K_3 = 0.2$.

5.3.4 Wedge Channel

For the TU#2 the investigation of three different channel channel geometries and tests are foreseen: Wedge without bubble injection (Ia), Wedge with bubble injection (Ib) and Gapped Wedge (II). The parameters to be varied are the wedge angle α, the gap distance G, the inlet height H_1, the bubble size D_b, the bubble injection frequency ν_b and location of bubble injection H_{in}. In the following, further details of the tests and a reduced form of test matrices are provided.

I. Wedge tests: The Wedge tests position the plates together at a vertex or virtual vertex if plates the plates must not touch each other. For the latter case, the plate gap must be on the order of 10 microns (see Fig. 5.5). The Wedge tests fix the wedge angle and interface

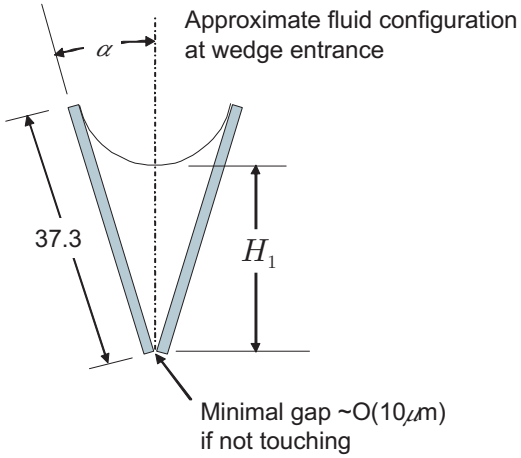

Figure 5.5: Sectional view of Wedge test cell geometry.

height H_1 (i.e. fixed upstream pressure) at the wedge entrance and increase the flow rate Q until air ingestion (Q_{crit}). The wedge angle α is then changed and processes repeated. H_1 is reduced by 50% and then 25% or 35% and the tests are repeated (i.e. upstream pressure reduced by 50%, 25%, or 35%). The resulting flows span the inertia and viscous dominated regimes and the majority of predicted maximum flow rates are in the range of 0.5 ml/s $\lesssim Q \lesssim$ 20 ml/s (effective Reynolds numbers $\sim$ 10 to $\sim$ 1000). The test matrix is shown in Table 5.11 (Note, 5 wedge angles are requested $\alpha = 5°$, $10°$, $15°$, $20°$, $25°$ but details here are provided only for $\alpha = 5°$, $10°$ and $20°$).

The experiments requesting a 'fixed height condition' H_1 at the test cell inlet require further clarification. The experiments are anticipated to run in a 'constant volume' mode, where the compensation chamber is valved off from the flow loop. The height of the interface H_1 is set by adjusting the volume in the system at quiescent conditions. Once the flow is initiated the interface will adjust in the test section resulting in a known small increase in

α [°]	H_1 [m]	Q_{crit} [ml/s]
5	0.034	4.0
5	0.017	0.5
5	0.012	0.2
10	0.031	11.0
10	0.015	1.4
10	0.011	0.5
20	0.026	20.3
20	0.013	2.5
20	0.009	0.9

Table 5.11: Sample test matrix for the Wedge tests ($\alpha = 5°$, $10°$ and $20°$ only). For a given wedge angle α and interface height H_1 the flow rate Q is increased up to the critical value Q_{crit}. The specified values for Q_{crit} are based on estimations.

the true height of the interface ($h = k$) at the entrance of the test cell. In this way the flow is more aptly defined as a 'known entrance height condition' as opposed to a 'fixed entrance height condition'. The video data provides the true inlet height conditions required of the theory. Estimations of fixed static height values verses dynamic height values are readily determined.

For flow rates less than the critical value, air bubbles introduced into the liquid supply can be used to study the passive phase separation capability of the wedge not possible on the ground. Single, multiple-timed, and arrays of bubbles can be introduced and Q_{crit} determined for which the device functions effectively as a phase separator. Controlling bubble size is a powerful variable and 0.5 mm up to 5 mm diameter bubbles are requested; the maximum size is determined by α and H. Only $\alpha = 5°$, $10°$, and $20°$ are considered for such tests ('spot' bubble tests would be conducted for gap wedge and tilted plate geometries). It is also expected that the position H_{in} (along x-direction as defined in Fig. 3.16) at which the bubbles are injected as well as the injection frequency ν_b has an impact of the flow. The test matrix for these investigations are shown in Table 5.12 through 5.14.

α [°]	H_1 [m]	D_b [m]	H_{in} [m]	ν_b [Hz]	Q_{crit} [ml/s]
5	0.034	0.005	0.01	0	4.0
			0.01	0.5	4.0
			0.005	0	4.0
			0.005	0.5	4.0
		0.002	0.01	0	4.0
			0.01	0.5	4.0
			0.005	0	4.0
			0.005	0.5	4.0
5	0.017	0.002	0.01	0	0.5
			0.01	0.5	0.5
			0.005	0	0.5
			0.005	0.5	0.5
		0.001	0.01	0	0.5
			0.01	0.5	0.5
			0.005	0	0.5
			0.005	0.5	0.5
5	0.012	0.001	0.005	0	0.2
			0.005	0.5	0.2

Table 5.12: Bubble tests for Wedge, $\alpha = 5°$. For a given interface height H_1, bubble diameter D_b, position of injection H_{in} and ν_b bubble injection frequency the flow rate Q is increased up to the critical value Q_{crit}. The specified values for Q_{crit} are based on estimations.

α [°]	H_1 [m]	D_b [m]	H_{in} [m]	ν_b [Hz]	Q_{crit} [ml/s]
10	0.031	0.005	0.01	0	11
			0.01	0.5	11
			0.005	0	11
			0.005	0.5	11
		0.002	0.01	0	11
			0.01	0.5	11
			0.005	0	11
			0.005	0.5	11
10	0.015	0.002	0.01	0	1.4
			0.01	0.5	1.4
			0.005	0	1.4
			0.005	0.5	1.4
		0.001	0.01	0	1.4
			0.01	0.5	1.4
			0.005	0	1.4
			0.005	0.5	1.4
10	0.011	0.002	0.005	0	0.5
			0.005	0.5	0.5
		0.001	0.005	0	0.5
			0.005	0.5	0.5

Table 5.13: Bubble tests for Wedge, $\alpha = 10°$. For a given interface height H_1, bubble diameter D_b, position of injection H_{in} and ν_b bubble injection frequency the flow rate Q is increased up to the critical value Q_{crit}. The specified values for Q_{crit} are based on estimations.

α [°]	H_1 [m]	D_b [m]	H_{in} [m]	ν_b [Hz]	Q_{crit} [ml/s]
20	0.026	0.005	0.01	0	20.3
			0.01	0.5	20.3
			0.005	0	20.3
			0.005	0.5	20.3
		0.002	0.01	0	20.3
			0.01	0.5	20.3
			0.005	0	20.3
			0.005	0.5	20.3
20	0.013	0.005	0.01	0	2.5
			0.01	0.5	2.5
			0.005	0	2.5
			0.005	0.5	2.5
		0.002	0.01	0	2.5
			0.01	0.5	2.5
			0.005	0	2.5
			0.005	0.5	2.5
20	0.009	0.002	0.005	0	0.9
			0.005	0.5	0.9
		0.001	0.005	0	0.9
			0.005	0.5	0.9

Table 5.14: Bubble tests for Wedge, $\alpha = 20°$. For a given interface height H_1, bubble diameter D_b, position of injection H_{in} and ν_b bubble injection frequency the flow rate Q is increased up to the critical value Q_{crit}. The specified values for Q_{crit} are based on estimations.

II. Gap Tests: The flow cross section of this test is shown in Fig. 5.6. For a given angle α, gap G and H_1, Q_{crit} is determined. A test matrix is provided in Table 5.15 for gaps of 1, 2 and 5 mm. Intermediate gaps of 1.5 mm and 3.5 mm are also requested but not listed in the tables. The requested angles are 5°, 10°, and 20°. A spot-check level of select bubble tests would be desirable.

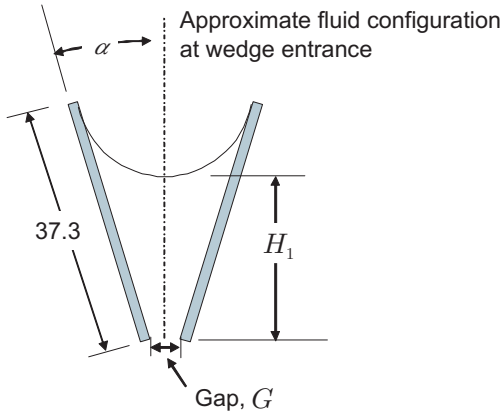

Figure 5.6: Cross section of the Gapped Wedge test cell geometry.

G [m]	α [°]	H_1 [m]	Q_{crit} [ml/s]
0.001	5	0.039	6.0
	10	0.034	13.6
	20	0.027	22.7
0.002	5	0.045	8.2
	10	0.036	16.4
	20	0.028	25.2
0.005	5	0.060	15.3
	10	0.043	25.20
	20	0.031	32.7
0.001	5	0.020	0.74
	10	0.017	1.7
	20	0.014	2.8
0.002	5	0.022	0.7
	10	0.018	1.8
	20	0.014	3.0
0.005	5	0.030	0.04
	10	0.022	1.5
	20	0.016	3.2
0.001	5	0.010	0.05
	10	0.008	0.2
	20	0.007	0.3
0.002	5	0.011	0.0005
	10	0.009	0.1
	20	0.007	0.3

Table 5.15: Test matrix for the Gapped Wedge tests (G = 1, 2, 5 mm only shown). For a given gap G, wedge angle α and interface height H_1 the flow rate Q is increased up to the critical value Q_{crit}. The specified values for Q_{crit} are based on estimations.

Test	n_α	n_{H_1}	n_{D_b}	$n_{H_{in}}$	n_{ν_b}	n_G	n_r	n_{total}
Ia	5	5	-	-	-	-	3	75
Ib	3	3	2	2	2	-	2	144
II	5	5	-	-	-	5	3	225

Table 5.16: Number of data parameters for the tests Ia, Ib and II (EU#2, wedge and gaped wedge).

The number of parameter is summarized in Table 5.16. It denotes n_α the number of adjusted wedge angles, n_{H_1} the number of adjusted inlet heights, n_{D_b} the number of adjusted bubble diameters, $n_{H_{in}}$ the number of locations for bubble injection, n_{ν_b} the number of adjusted bubble injection frequencies, n_G the number of adjusted gap distances and n_r the number of repetitions. In total the tests lead to $n_{total} = 444$ parameter. Assuming an average number of 20 variation of the flow rate Q and the liquid volume V inside the channel, respectively, a number of 8880 data points regarding the surface profiles and bubble traces is achieved for the comparison with the theoretical results.

5.4 Flight Experiment Procedure

1 insert test section (astronaut)

2 preparation of the experiment (via telescience / automated)

- 2.1 initializing the fluid loop (via telescience / automated)
  - i. withdraw liquid from compensation tube
  - ii. establish main gas bubble in phase separation chamber
  - iii. fill test channel
- 2.2 check filling ratio of system (via telescience)
- 2.3 gas-liquid distribution (via telescience)

3 choose channel parameter (via telescience)

- 3.1 TU#1: adjust channel length l
- 3.1 TU#2: adjust wedge angle α and gap distance G, and if in 2-phase mode: position of bubble injection H_{in}, bubble diameter D_b and injection frequency ν_b

4 choose operating mode (via telescience)

- 4.1 quasi-steady increase of flow rate (TU #1, TU#2)
- 4.2 transient increase (TU#1, for TU#2 spot check method only)
- 4.3 oscillatory mode (TU#1, for TU#2 spot check method only)
- 4.4 two phase mode (TU#2, for TU#1 spot check method only)

5 performance of the experiment (via telescience)

- 5.1 quasi-steady mode
  - i. start liquid flow far below critical flow rate
  - ii. observe free surface
  - iii. collect data
    - A. video mode high quality
    - B. flow sensor data
    - C. pressure sensor data
  - iv. increase flow rate with small increments (parameter Q, ΔQ)
  - v. repeat cycle

vi. critical flow velocity reached, gas ingestion at outlet

vii. decrease flow rate, change ΔQ

5.2 transient increase

i. start liquid flow far below critical flow rate

ii. observe free surface

iii. collect data

A. video mode high quality

B. flow sensor data

C. pressure sensor data

iv. increase flow rate with large increment (parameter Q, $q = \Delta Q/\Delta t$)

v. repeat cycle

vi. stop if critical flow velocity is reached, gas ingestion at outlet

vii. decrease flow rate, change ΔQ

5.3 oscillatory increase

i. start liquid flow far below critical flow rate

ii. observe free surface

iii. collect data

A. video mode high quality

B. flow sensor data

C. pressure sensor data

iv. start modulation of flow velocity (parameter Q, frequency, amplitude)

v. repeat cycle

vi. stop if critical flow velocity is reached, gas ingestion at outlet

5.4 unstable flow

i. start liquid flow slightly below critical flow rate

ii. observe free surface

iii. collect data

A. video mode high quality

B. flow sensor data

C. pressure sensor data

iv. increase quasi-steady to unstable flow with small increments (parameter Q, ΔQ)

v. repeat cycle

vi. observe different instabilities (asymmetric bubble ingestion, oscillatory bubble ingestion, frequency). Limiting factor is the gas-liquid separator

5.5 two phase mode

a) adjust flow rate

b) inject gas bubbles

c) observe bubble separation

d) collect data

i. video mode high quality

ii. flow sensor data

iii. pressure sensor data

e) increase flow rate with small increments (parameter Q, ΔQ)

f) repeat cycle until either ingestion of bubbles or normal ingestion at Q_{max}

6 emergency and malfunction (astronaut)

6.1 gas-liquids separator malfunction

6.2 unintended liquid discharge from the test section

During the experimentation a downlink video and an uplink telecommand is required. The video data may be supplied via the remote ISS video capability (information from Marshall Space Flight Center, FD43). During the run of an experiment, low resolution video data (25-30 fps, 200 x 200 pixel approx.) and the flow sensor data are required on ground. When the experiment is switched to collect data, the data could be grabbed on board and downlinked to the PI site at a later time (data format should be readable by the PI). It may be possible to run the approach to the critical flow rate without telescience, but this should be discussed in the preliminary design review. The experiment will be designed to run hours without surveillance by astronauts. If a malfunction occurs the flow can be stopped via telecommand or by some internal control loops and the experiment remains in a safe status until an astronaut is available to solve the problem.

5.5 Anticipated Results from Postflight Data

Data evaluation on ground consists of digital image processing to determine the contours of the free surface and to examine features of the flow (bubble size and frequency during unstable flow), examining the flow rate data as well as pressure and temperature to combine

them with the contour data. It is expected that these data are available during the run of the experiment (hours after each point in the test matrix). The test set-up and the test cells should be returned to the PI after the experiment period in orbit.

6 Experimental Requirements

This section summarizes the fundamental experiment requirements which directly result from the experimental and theoretical background of the experiment. More details – which are an outcome of the project phase B performed by industry – can be taken from the CCF System Specification attached to this document in appendix D.

6.1 Science Requirement Summary Table

Parameter	Section	Requirement
Observation Chamber	6.2	
Investigated Geometries	6.2.1	Parallel plates / groove, 1 test unit (EU#1) Wedge, 1 test unit (EU#2)
Channel Exchange	6.2.2	Test units should be exchanged
Channel (Material)	6.2.3	Quartz glass or comparable
Test Fluid	6.3	HFE 7500 or other

Parameter	Section	Requirement
Video Observation	6.4	
General view	6.4.1	
Video requirements		25-30 frames/s, black and white
Field of view		Test channel and compensation tube
Resolution		0.1 mm/Pixel
Data Insertion		Time, flow rate, temperature, pressure
Detail view	6.4.2	
Video requirements		250 frames/s, black and white
Field of View		Test channel and border areas 50 mm × 40 mm
Resolution		0.01 a/pixel
Data Insertion		Time, flow rate, temperature, pressure
Thermal System	6.5	
Temperature Measurement	6.5.1	2 for ambient temperature 1 for liquid inside plunger 1 for liquid inside PSC 1 for liquid at channel inlet 1 for liquid at channel outlet 1 for gas inside the test unit 1 for gas inside the vent line / tank
Temperature Control	6.5.2	maintain isothermal conditions within a range of 20 °C to 40 °C
Accuracy	6.5.3	±0.5 °C
Respond time	6.5.3	< 1 s
Sample rate	6.5.4	1 Hz

Parameter	Section	Requirement
Liquid Pressure Measurement and Control	6.6	
Pressure measurement	6.6.1	1 inside the PSC 1 at channel inlet 1 at channel outlet
Accuracy	6.6.2	10 hPa 0.1 Pa (special transducer)
Control	6.6.3	not requested
Gas Pressure Measurement and Control	6.7	
Pressure measurement	6.7.1	1 inside test unit 1 inside gas duct
Accuracy	6.7.2	10 hPa
Control	6.7.3	not requested
Flow Measurement and Control	6.8	
Measurement	6.8.1	$1 \leq Q \leq 20$ ml/s (EU#1) $0.5 \leq Q \leq 20$ ml/s (EU#2)
Accuracy	6.8.2	1% of actual Q
Control	6.8.3	$\Delta Q = 0.01$ ml/s (EU#1) $\Delta Q = 0.005$ ml/s (EU#2)

Parameter	Section	Requirement
Bubble injection (EU#2)	6.9	
Bubble diameter		$1 \text{ mm} \leq D_b \leq 5 \text{ mm}$
Accuracy of bubble diameter		$\Delta D_b / D_b \leq 20\%$
Repeatability of bubble diameter		$\leq 10\%$
Injection frequency		$0.5 \text{ Hz} \leq v_b \leq 2 \text{ Hz}$
Accuracy of injection frequency		$\Delta \nu_b / \nu_b \leq 10\%$
Acceleration	6.10	
Frequency range		$0.01 \text{ Hz} \leq \nu_{acc} \leq 400 \text{ Hz}$
Astronaut Involvement	6.11	exchange test unit
Telescience	6.12	during experiment operation
Post-flight Deliverables	6.13	Temperature, pressure, flow rate and house keeping data, evaluated surfaces profiles and video images of the general and the detail view

6.2 Observation Chamber

6.2.1 Investigated Geometries

Four different geometries are chosen for the investigation: (1) parallel plate, (2) groove, (3) wedge, and (4) gapped wedge. Two Experiment Units (EUs) are required to meet the test geometry requirements: EU#1 focuses on the parallel plate and the groove geometry. EU#2 focusses on the wedge and gapped wedge geometries. The variable geometrical property of EU#1 is the length l only. The gap distance a and the plates width b are kept constant. The variable geometrical properties of EU#2 are the wedge angle α and wedge gap G.

6.2.2 Channel Exchange

The channel exchange requires the exchange of the test unit. The optical system can be used for both units.

6.2.3 Channel Material

The test channels should be manufactured from quartz glass (or comparable material) to obtain optimal optical quality. The free liquid surface is observed through the channel walls. The channel walls should contain markers for the calibration and evaluation of the video data.

6.3 Test Fluid

The test liquid will be defined during the preliminary design of the experiment. From the list of acceptable liquid for the MSG we have chosen HFE-7500 due to its Ohnesorge number for a given hydraulic diameter (compare Table 5.1). During nominal operation no test liquid should escape from the test channel into the ambient. To maintain the correct ambient pressure, the test chamber is sealed and connected with the separator tank. This prevents leaking of liquid into the facility. A second sealing around the whole experimental set-up could be realized.

6.4 Video Observation

6.4.1 General View

One camera is needed to monitor the test section and the compensation tube. Usual video frequency (25 to 30 Hz) and number of picture elements (768 (h) × 494 (v)) is sufficient. The achieved resolution should be better than 0.1 mm/Pixel. Video downlink must be available during operation.

6.4.2 Detail View

For data acquisition one video camera is required. The resolution should better than 0.01 a/pixel. To achieve this, the number of picture elements of the image device should be at least 1280 (h) × 1024 (v) (for the discussion of the required resolution see section 5.3.1). The camera must provide a frame rate up to 250 fps. Video data at high resolution and frequency are required on demand and could be grabbed onboard and downlinked later (within minutes after the experiment run). The quality of the images should comply with digital video image standards.

6.5 Thermal System

6.5.1 Temperature Measurement

The temperature sensors are positioned inside the liquid plunger (1), inside the phase separation chamber close to the channel inlet (1) and inside the piping at the channel outlet (1). The two sensors in the fluid circulation should not disturb the liquid flow. Two sensors are required for the measurement of the ambient pressure. Two additional sensors shall measure the gas temperature inside the test unit and inside the vent line or separator tank.

6.5.2 Temperature Control

The temperature of the total set-up should be controllable to define the fluid properties and thus the Ohnesorge number of the experiment. The temperature range depends on the liquid which was not yet selected. The temperature inside the fluid reservoir and the storage tank has to be homogeneous to ± 0.5 °C to avoid changes in the liquid properties (less than 1%) and Marangoni convection along the free surface (velocities induced by surface tension gradients should not exceed 1% of the average velocity in the flow channel).

6.5.3 Accuracy and Response Time

The accuracy of the temperature measurement should be ±0.5°C, the response time $t_r < 1$ s.

6.5.4 Sample Rate

The sample rate shall be in the same range as the response time of the temperature sensors (1 Hz).

6.6 Liquid Pressure Measurement and Control

The system should operate at ambient pressure (1020 hPa ±50 hPa, hPa = 10^2·Pa).

6.6.1 Pressure measurements

The liquid pressures needs to be measured inside the phase separation chamber (PSC). Very low pressure changes occur along the flow path from the reservoir through the nozzle to the test section ($p \approx 1 \ldots 10$ Pa). If transducers with a small area for these small pressures are available, they should be positioned in the reservoir, at the channel inlet and at the channel outlet.

6.6.2 Accuracy

The required accuracy is 10 Pa of the liquid pressure inside the PSC. The accuracy of the pressure measurement along the channel should be better than 1% of the total pressure gradient between inlet and outlet.

6.6.3 Control

No active pressure control system is foreseen.

6.7 Gas Pressure Measurement and Control

6.7.1 Pressure measurements

The ambient pressure needs to be measured inside the test unit (TU) and inside the gas duct near the gas plunger.

6.7.2 Accuracy

The system operates at ambient pressure (1020 hPa ±50 hPa). No excess pressure inside the system is desired. The pressure above the compensation tube and beside the test channel should be the same within $\Delta p \leq 0.1$ Pa. The gas pressure should be measured with an accuracy of 10 hPa and a sampling rate of 1 Hz.

6.7.3 Control

No pressure control is foreseen.

6.8 Flow Measurement and Control

6.8.1 Measurement

A measurement of the volumetric flow rate by a flow meter is required. The flow meter shall be located at the channel outlet.

6.8.2 Accuracy

The accuracy of the flow meter should be 1% (of reading) of the actual value. 5% accuracy is acceptable for limiting cases of EU#2.

6.8.3 Control

Depending on the investigated channel geometries two ranges of flow rates are required: $1 \leq Q \leq 31$ ml/s (TU#1), $0.5 \leq Q \leq 20$ ml/s (TU#2). A variation of the flow rate by increments of $\Delta Q = 0.01$ ml/s and 0.005 ml/s, respectively, should be possible.

6.9 Gas bubble injection

The test matrix for EU#2 envisions the injection of gas bubbles in order to investigate the behavior of the gas-liquid separation at the liquid surface. The bubbles shall be injected at different locations of the inlet cross section. The bubble size as well as the bubble frequency are variable properties.

6.10 Acceleration

The frequency range of the experiment varies within the range from 0.1 Hz to 10 Hz (eigen-frequency of the fluid loop and oscillator frequency). The measurements of the acceleration which may interfere with the experiment should exceed this frequency range by one order of magnitude at the lower and upper end. Therefore the acceleration measurement within a frequency range from 0.01 Hz to 400 Hz are sufficient.

6.11 Astronaut Involvement

During nominal operation via telescience no astronaut involvement is required. The exchange of the test cell will require a crew member. For non-nominal operation a scenario will be provided. Experience is available from parabolic and sounding rocket flights.

6.12 Telescience

The experiment requires changing the flow rate manually in predefined steps. For an optimal approach to the critical flow condition, the step size and step direction (up or down) have to be controlled by telescience. The data to operate the experiment as specified above must be downlinked during the experiment run. The sample data of the experiment run (high resolution video data as well as flow rates) needs to be downlinked after each experiment run. An experiment run consists of a defined flow rate which will be recorded for tdb seconds. This time depends on oscillations which may occur in the whole liquid system. The frequency of this oscillation is not known a priori, thus the frame grabbing time should be adjusted after evaluation of the data (high resolution) on ground. For the transient and the oscillatory approach to the critical flow rate the data acquisition time is not known and should be adjustable.

6.13 Post-Flight Data Deliverables

All necessary data should be downlinked during or shortly after each experiment run. No post-flight data deliverables are required but the experiment set-up and the test cells should be returned to the PI after the end of the experiment.

During the flight the following data are requested for each experiment run:

- Time-synchronized record of all temperature sensors
- Time-synchronized record of all house keeping data

- Time-synchronized record of the set flow rate (uplinked value) of each pump generating the liquid flow
- Time-synchronized record of the measured flow rate (real value)
- Time-synchronized record of all gas pressures
- Time-synchronized record of all liquid pressures
- Time-synchronized digital video frames of the detail and the general camera with the required resolution
- Time-synchronized data of the evaluated surface profiles
- Time-synchronized three-axis acceleration data in the center of gravity in the observation chamber

6.14 Success Criteria

6.14.1 Minimal Success

The minimal success criteria is the determination of the critical flow velocity for the first data point. Data to be provided are the flow rate of the pump, the video information of the free surfaces, the compensation tube and the reservoir. With these data theoretical predictions can be compared. This would also show that the hardware was properly designed and was able to work under the planned conditions.

6.14.2 Significant Success

A significant success is achieved when the critical flow rates for all points of the test matrix and the quasi-steady approach can be measured. This requires long time periods of steady flow conditions (no gas ingestion at the outlet) and short time periods of unstable flow conditions (gas ingestion at the outlet). Thus the liquid-gas separation system should work with a low time-averaged gas void fraction. Data to be provided are the flow rates, the pressure and temperature data, the accelerometer data as well as all required video data.

6.14.3 Complete Success

A complete success is reached when the critical flow rates for all points of the test matrix with three different approaches (quasi-steady, transient and oscillatory) and the features of the unstable flow (bubble size and frequency) can be measured. In this case the liquid-gas

separation system should work long time periods with a high gas void fraction. Data to be provided are the flow rates, the pressure and temperature data, the accelerometer data as well as all required video data.

Bibliography

Allen, J. 2003 Observation of inertial capillary flows in microfluidic devices. Private communication.

Antar, B. N. & Nuotio-Antar, V. S. 1993 *Fundamentals of Low Gravity Fluid Dynamics and Heat Transfer*. CRC Press.

Ayyaswamy, P. S., Catton, I. & Edwards, D. K. 1974 Capillary flow in triangular grooves. *Trans. ASME: J. App. Mech.* **41**, 332–336.

Baumbach, V., Dreyer, M. E., Ohlhoff, A., Prengel, P., Rosendahl, U. & Stadtlander, M. 2003 Critical velocities in open capillary channel flows (CCF) – Phase A report. *Tech. Rep.*. ZARM, Universitt Bremen.

Bronstein, I. N. & Semendjajew, K. A. 1987 *Taschenbuch der Mathematik*, 23rd edn. Leipzig: Teubner Verlagsgesellschaft.

Chato, D. & Martin, T. 1997 Vented tank resupply experiment – flight test results. In *33rd Joint Propulsion Conference and Exhibit*, *AIAA Papers* 97–2815. American Institute of Aeronautics and Astronautics, Reston, Va.

Chen, Y. & Collicott, S. 2004 Investigation of the symmetric wetting of vane-wall gaps in propellant tanks. *AIAA J.* **42** (2), 305–314.

Chen, Y. & Collicott, S. H. 2002 Investigation of the wetting behavior of a vane-wall gap in propellant tanks. In *38th AIAA/ASME/SAE/ASEE Joint Propulsion Conference and Exhibit*, *AIAA Papers* 2002–3986, pp. 1–15. American Institute of Aeronautics and Astronautics, Reston, Va.

Chen, Y., Weislogel, M. M. & Nardin, C. 2006 Capillary-driven flows along rounded interior corners. *J. Fluid Mech.* **566**, 235–271.

Concus, P. & Finn, R. 1969 On the behaviour of capillary surfaces in a wedge. *P. Natl. Acad. Sci. USA* **63** (2), 292–299.

DaimlerChrysler Aerospace 1999 Microgravity science glovebox (MSG) payload handbook, MSG–RIBRE–RQ–0001, Rev. C. *Tech. Rep.*. DaimlerChrysler Aerospace.

Der, J. A. 1991 Linearized theory for unsteady surface tension driven flow along supercritical vane-formed fillets. In *27th AIAA/SAE/ASME/ASEE Joint Propulsion Conference*, *AIAA Papers* 91–2175. American Institute of Aeronautics and Astronautics, Washington, DC.

Dong, M. & Chatzis, I. 1995 The imbibition and flow of a wetting liquid along the corners of a square capillary tube. *J. Colloid Interf. Sci.* **172** (2), 278–288.

Dreyer, M. 1994 *Kapillarer Flüssigkeitsanstieg zwischen parallelen Platten unter kompensierter Gravitation. Fortschritt-Berichte VDI, Reihe 7: Strömungsmechanik* 241. Düsseldorf: VDI-Verlag.

Dreyer, M. 2006 *Free Surface Flows under Compensated Gravity Conditions*, *Springer Tracts in Modern Physics*, vol. 221. Berlin, Heidelberg, New York: Springer.

Dreyer, M. E., Delgado, A. & Rath, H. J. 1994 Capillary rise of liquid between parallel plates under microgravity. *J. Colloid Interf. Sci.* **163**, 158–168.

Dreyer, M. E., Rosendahl, U. & Rath, H. J. 1998 Experimental investigation on flow rate limitations in open capillary vanes. In *34th AIAA/SAE/ASME/ASEE Joint Propulsion Conference and Exhibit*, *AIAA Papers* 98–3165. American Institute of Aeronautics and Astronautics, Reston, Va.

EADS Space Transportation 2005 CCF Phase B Design Report, CCF–RP–EADS–1004. *Tech. Rep.*. EADS Friedrichshafen.

Faber, T. 1995 *Fluid Dynamics for Physicists*, 1st edn. Cambridge: Cambridge University Press.

J. A. Mann, J., Romero, L., Rye, R. R. & Yost, F. G. 1995 Flow of simple liquids down narrow V grooves. *Phys. Rev. E* **52** (4), 3967–3972.

Jaekle, D. E. 1991 Propellant management device conceptual design and analysis: Vanes. In *27th AIAA/SAE/ASME/ASEE Joint Propulsion Conference*, *AIAA Papers* 91–2172. American Institute of Aeronautics and Astronautics, Washington, DC.

Jaekle, D. E. 1997 Propellant management device conceptual design and analysis: Galleries. In *33rd AIAA/SAE/ASME/ASEE Joint Propulsion Conference and Exhibit*, *AIAA Papers* 97–2811. American Institute of Aeronautics and Astronautics, Reston, Va.

Klimek, R. & Wright, T. 2006 Spotlight-8 image analysis software. *Tech. Rep.* NASA TM–2006–214084. NASA Glenn Research Center, Washington, DC 20546-0001.

Klimek, R. B., Wright, T. W. & Sielken, R. S. 1996 Color image processing and object tracking system. *Tech. Rep.* NASA TM–107144. Lewis Research Center.

Landau, L. & Lifschitz, E. 1991 *Hydrodynamik*, 5th edn., *Lehrbuch der theoretischen Physik*, vol. VI. Berlin: Akademie Verlag.

Langbein, D. 1990 The shape and stability of liquid menisci at solid edges. *J. Fluid Mech.* **213**, 251–265.

Langbein, D. & Weislogel, M. 1998 Dynamics of liquids in edges and corners (DYLCO), IML-2 experiment for the BDPU. *Tech. Rep.*. NASA/TM–1998–207916.

de Lazzer, A., Langbein, D., Dreyer, M. E. & Rath, H. J. 1996 Mean curvature of liquid surfaces in cylindrical containers of arbitrary cross-section. *Microgravity Sci. Tec.* **4** (3), 208–219.

Lenormand, R. & Zarcone, C. 1984 Role of roughness and edges during imbibition in square capillaries. In *9th Annual Meeting of the SPE*.

Lighthill, J. 1978 *Waves in Fluids*. Cambridge: Cambridge University Press.

Mayer, F. J., McGrath, J. F. & Steele, J. W. 1983 A class of similarity solutions for the nonlinear thermal conduction problem. *J. Phys. A-Math. Gen.* **16** (14), 3393–3400.

Nardin, C. L. & Weislogel, M. M. 2005 Capillary driven flows along differentially wetted interior corners. *Tech. Rep.* NASA CR–2005–213799. National Aeronautics and Space Administration, Washington, DC 20546-0001.

Peterson, G. P. & Ha, J. M. 1998 Capillary performance of evaporating flow in micro grooves: An approximate analytical approach and experimental investigation. *J. Heat Transf.* **120**, 743–751.

Press, W. H., Teukolsky, S. A., Vetterling, W. T. & Flannery, B. P. 1992 *Numerical Recipes in C*. Cambridge: Cambridge University Press.

Quéré, D. 1997 Inertial capillarity. *Europhys. Lett.* **39**, 533.

Ransohoff, T. C., Gauglitz, P. A. & Radke, C. J. 1987 Snap-off of gas bubbles in smoothly constricted noncircular capillaries. *AICHE J.* **33** (5), 753–765.

Ransohoff, T. C. & Radke, C. J. 1988 Laminar flow of a wetting liquid along corners of a predominately gas-occupied noncircular pore. *J. Colloid Interf. Sci.* **121**, 392–401.

Romero, L. A. & Yost, F. G. 1996 Flow in an open capillary channel. *J. Fluid Mech.* **322**, 109–129.

Rosendahl, U. 2006 ber die Grenzen des stationären Flüssigkeitstransportes in offenen Kapillarkanälen. PhD thesis, University of Bremen, Bremen.

Rosendahl, U., Dreyer, M., Ohlhoff, A. & Prengel, P. 2004*a* Critical velocities in open capillary channel flows (CCF) – Phase B_0 report. *Tech. Rep.*. ZARM, University of Bremen.

Rosendahl, U., Motil, B., Ohlhoff, A., Dreyer, M. E. & Rath, H. J. 2001 Critical velocity in open capillary channel flows. In *Conference and Exhibit on International Space Station Utilization*, *AIAA Paper* 2001–5021. American Institute of Aeronautics and Astronautics, Reston, Va.

Rosendahl, U., Ohlhoff, A. & Dreyer, M. E. 2004*b* Choked flows in open capillary channels: theory, experiment and computations. *J. Fluid Mech.* **518**, 187–214.

Rosendahl, U., Ohlhoff, A., Dreyer, M. E. & Rath, H. J. 2002 Investigation of forced liquid flows in open capillary channels. *Microgravity Sci. Technol.* **XIII/4**, 53–59.

de Ryck, A. & Quéré, D. 1996 Inertial coating of a fibre. *J. Fluid Mech.* **311**.

Shapiro, A. H. 1953 *The Dynamics and Thermodynamics of Compressible Fluid Flow*, , vol. I. New York: The Ronald Press Company.

Sieber, H. 1982 *Mathematische Begriffe und Formeln*. Stuttgart: Klett Verlag.

Smits, A. J. 2000 *A Physical Introduction to Fluid Mechanics*. New York: John Wiley & Sons, Inc.

Sparrow, E. M. & Lin, S. H. 1964 Flow development in the hydrodynamic entrance region of tubes and ducts. *Phys. Fluids* **7** (3), 338–347.

Spurk, J. H. 1992 *Dimensionsanalyse*. Berlin: Springer Verlag.

Srinivasan, R. 2003 Estimating zero-g flow rates in open channels having capillary pumped vanes. *Int. J. Numer. Meth. Fluids* **41**, 389–417.

Verbist, G., Weaire, D. & Kraynik, A. 1996 The foam drainage equation. *J. Phys.: Condens. Matter* **8**, 3715–3731.

Weislogel, M. 1996 Capillary flow in an interior corner. PhD thesis, Northwestern University, Evanston, IL, UMI No. 9632810.

Weislogel, M. 2001*a* Capillary flow in containers of polygonal section. *AIAA J.* **39** (12), 2320–2326.

Weislogel, M. 2003*a* Some analytical tools for fluids management in space: Isothermal capillary flows along interior corners. *Adv. Space Res.* **32** (2), 163–170.

Weislogel, M. 2006 Steady capillary flow along interior corners. In preparation.

Weislogel, M. & Collicott, S. 2002 Analysis of tank pmd rewetting following thrust resettling with a post-analysis of the vented tank resupply experiment. *Tech. Rep.* NASA CR–2002–211974. National Aeronautics and Space Administration, Washington, DC 20546–0001.

Weislogel, M. & Collicott, S. 2004 Capillary re-wetting of vaned containers: Spacecraft tank rewetting following thrust resettling. *AIAA J.* **42** (12), 2551–2607.

Weislogel, M. M. 2001*b* Capillary flow in containers of polygonal section. *AIAA J.* **39** (12), 2320–2326.

Weislogel, M. M. 2003*b* Some analytical tools for fluids management in space: Isothermal capillary flows along interior corners. *Adv. Space Res.* **32** (2), 163–170.

Weislogel, M. M. & Lichter, S. 1996 A spreading drop in an interior corner: Theory and experiment. *Microgravity Sci. Tec.* **9** (3), 175–184.

Weislogel, M. M. & Lichter, S. 1998 Capillary flow in an interior corner. *J. Fluid Mech.* **373**, 349–378.

White, F. M. 1991 *Viscous Fluid Flow*, 2nd edn. New York: McGraw Hill.

White, F. M. 1994 *Fluid Mechanics*. New York: McGraw Hill.

7 Appendix A: Mathematical Model for the Flow between Parallel Plates

This appendix has been written to provide the referees with a more detailed description of the theoretical approach. The repetitions of section 2.4 are intended to make this appendix a comprehensive document in its own. In the course of this experiment some components of the theory may be improved, thus the appendix is subjected to change.

7.1 Model assumptions and basic equations

In our theoretical approach we consider the flow through a channel under reduced gravity conditions. As shown in Fig. 7.1(a) the channel consists of two parallel plates with gap distance a and plate width b. At the ends the plates are closed at the sides, and along the length l the flow path is bounded by two free surfaces. The origin of the coordinate system is located in the center of the cross section at the channel inlet. The liquid flows at a constant flow rate Q in positive x-direction. In case of a stable flow the differential pressure between the static liquid pressure p and the ambient pressure p_a is balanced by the capillary pressure of the free surface. For an internal pressure p lower than ambient pressure p_a the free liquid surfaces are concave at any cross section as shown in figure 7.1(b). The pressure decreases in flow direction, thus the curvature of the surfaces increases and the flow path constricts as indicated in 7.1(c). A steady flow is obtained only for a flow rate below a critical value ($Q < Q_{crit}$). For $Q > Q_{crit}$ the liquid surfaces collapse at the channel outlet, and the flow changes from steady single phase flow to unsteady two-phase flow.

The model assumptions are based on observations made during experiments on open capillary channel flow under microgravity conditions. The experiments show that the flow is essentially one-dimensional, and symmetries exist of the surfaces with respect to the planes $y = 0$ and $z = 0$. The assumptions are:

A1 The liquid is incompressible and isotherm, so that the density ρ, the viscosity ν and the surface tension σ may be considered as constant. The static contact angle of the liquid with the channel walls is $\gamma_s = 0$ (perfect wetting).

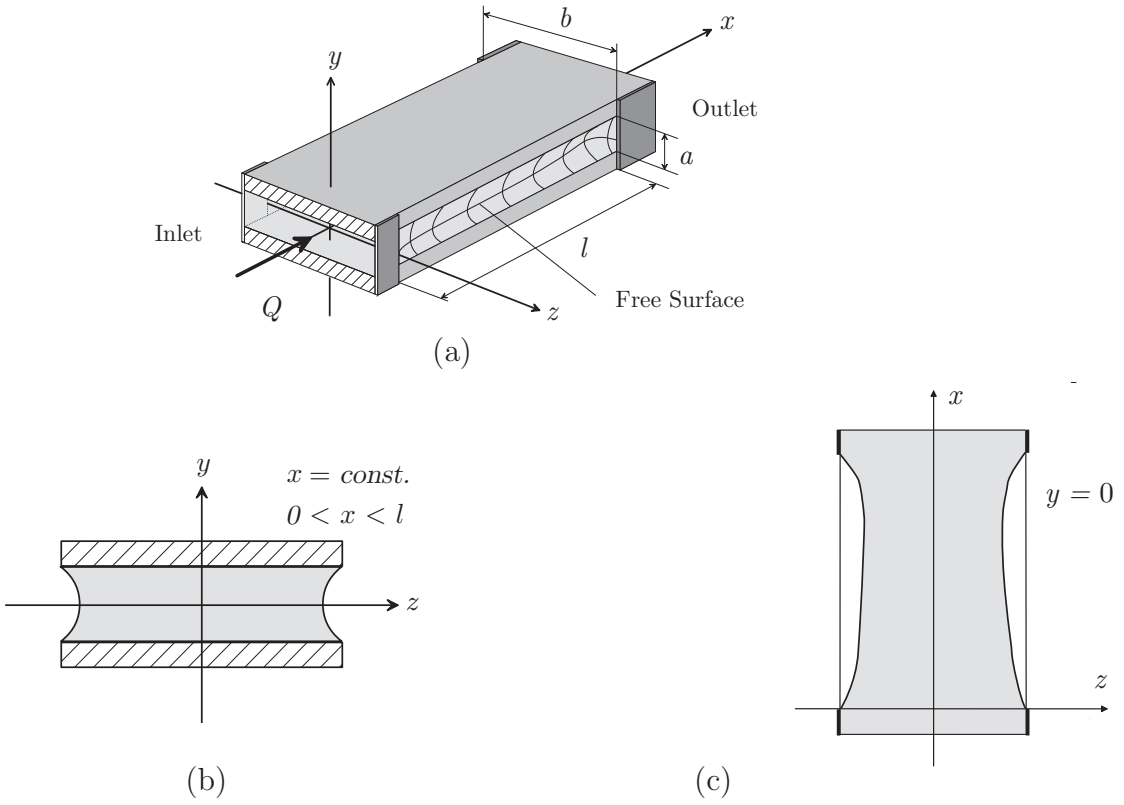

Figure 7.1: (a) Liquid flow through an open capillary channel consisting of two parallel plates. The free surfaces along the flow path x are bend inwards. (b) Cross sectional area for $x = const.$ (c) The symmetry plane $y = 0$.

A2 The flow is assumed to be laminar, one-dimensional and characterized by the static pressure p' and the mean velocity v.

A3 The flow is steady and limited to $Q \leq Q_{crit}$. Time-depending effects such as the collapse of the liquid surfaces are not considered.

A4 The shear stress at the gas-liquid interface (below named as liquid surface or surface) is negligible small, so that the gas phase may be considered as passive. Due to the constant surface tension the differential pressure at the liquid surface, $p - p_a$, is then determined by the GAUSS-LAPLACE equation

$$\frac{p - p_a}{\sigma} = -2H = -\left(\frac{1}{R_1} + \frac{1}{R_2}\right), \tag{7.1}$$

whereas the ambient pressure p_a is constant. Under these conditions the static pressure is proportional to twice the mean curvature $2H$, which is defined by the principal radii of curvature R_1 and R_2 in the corresponding principal normal planes $(y, \hat{z})$ and $(\hat{x}, \hat{z})$,

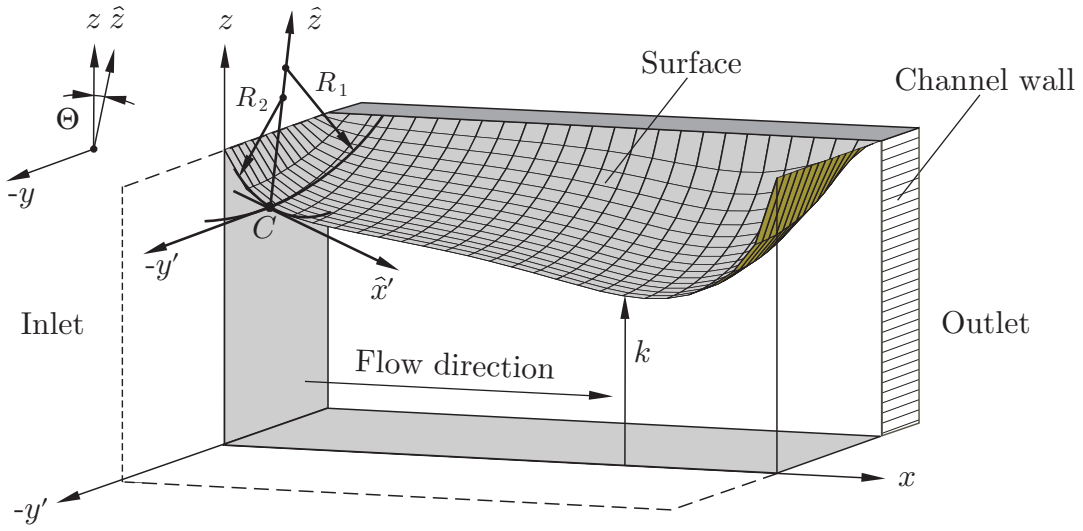

Figure 7.2: Schematic drawing of the right (in flow direction) liquid surface of the open capillary channel ($z > 0$). The curvature of the surface is defined by the principal radii of curvature R_1 and R_2 in the principal normal planes $(y, \hat{z})$ and $(\hat{x}, \hat{z})$, respectively.

respectively. For the point C of the surface the orientation of these planes are shown schematically in Fig. 7.2. The first plane is spanned by the coordinate axis y and the normal vector $\hat{z}$ of the surface in C and the second by $\hat{z}$ and the tangential vector of the surface $\hat{x}$.

A5 Hydrostatic pressures in terms of residual accelerations are negligible small compared to the capillary pressure at the liquid surface. Due to the assumed one-dimensionality of the flow, symmetries of the surfaces with respect to the planes $y = 0$ and $z = 0$ exist.

A6 For the determination of the cross sectional area of the flow A, it is assumed, that the liquid surface has a constant curvature in the (y, z)-planes. The radius of curvature in these planes is denoted with R, and it applies $1/R = const.$

A7 For the determination of H is assumed, that the curvature of the surface may be determined by the intersection line $k(x, y = 0)$ of the surface with the plane $y = 0$. Thereby the surface curvature in the principal normal plane, spanned by y and $\hat{z}$ in any point of the of the intersection line, is considered as constant, and it applies $1/R_1 = const.$

With the assumptions A1 through A5 the basic equations to be solved are the momentum equation

$$\underbrace{v\frac{\mathrm{d}v}{\mathrm{d}x}}_{\mathrm{I}} = \underbrace{-\frac{1}{\rho}\frac{\mathrm{d}p}{\mathrm{d}x}}_{\mathrm{II}} \underbrace{-\frac{4\tau_w}{\rho D_h}}_{\mathrm{III}} \tag{7.2}$$

and the equation of continuity

$$\frac{\mathrm{d}Q}{Q} = \frac{\mathrm{d}A}{A} + \frac{\mathrm{d}v}{v} = 0. \tag{7.3}$$

Here $Q = Av$ is the constant volumetric flow rate passing the cross sectional area A of the flow in the planes $x = const.$ The terms in the momentum equation result from the convective momentum transport (I), the gradient od the static pressure (II) and the viscous or molecular momentum transport (III). The irreversible pressure gradient due to viscous forces,

$$\frac{\mathrm{d}p_v}{\mathrm{d}x} = -\frac{4\tau_w}{D_h}, \tag{7.4}$$

is approached by the generalized form for non-circular cross sections based on the mean wall shear stress τ_w and the hydraulic diameter

$$D_h = \frac{4A_0}{U} \tag{7.5}$$

according to White (1991). With the cross section area of the channel $A_0 = ab$ and the wetted perimeter $U = 2b$ Eq. (7.5) yields $D_h = 2a$.

According to A4 the static pressure p is related to mean surface curvature H by Eq. (7.1). For the further considerations we introduce the variable $h = 2H$ (below named as "curvature" to simplify matters). Since the ambient pressure p_a is constant the pressure gradient then becomes

$$\mathrm{d}p = -\sigma \mathrm{d}h, \tag{7.6}$$

and Eq. (7.2) may be rewritten as

$$\sigma\frac{\mathrm{d}h}{\mathrm{d}x} - \rho v\frac{\mathrm{d}v}{\mathrm{d}x} - \frac{4\tau_w}{D_h} = 0. \tag{7.7}$$

7.2 Modelling of the free liquid surface

In order to solve Eq. (7.3) and Eq. (7.7) a functional correlation between the curvature and and the cross section area is required. In general the mean curvature H of the surface is calculated by

$$h(x,y) = 2H(x,y) = \frac{(1+z_x^2)\,z_{yy} - 2z_x z_y z_{xy} + (1+z_y^2)z_{xx}}{(1+z_x^2+z_y^2)^{3/2}} \tag{7.8}$$

(see Bronstein & Semendjajew, 1987), where here $z = f(x,y)$ is the position of the liquid surface over the area of the open channel with $x \in [0,l]$ and $y \in [-a/2, a/2]$. The indices in Eq. (7.8) denote partial derivatives: $z_i = \partial z/\partial i$, $z_{ij} = \partial^2 z/\partial i \partial j$, with $i,j \in \{x,y\}$. Eq. (7.8) may be simplified since due to the assumed one-dimensionality the surfaces are

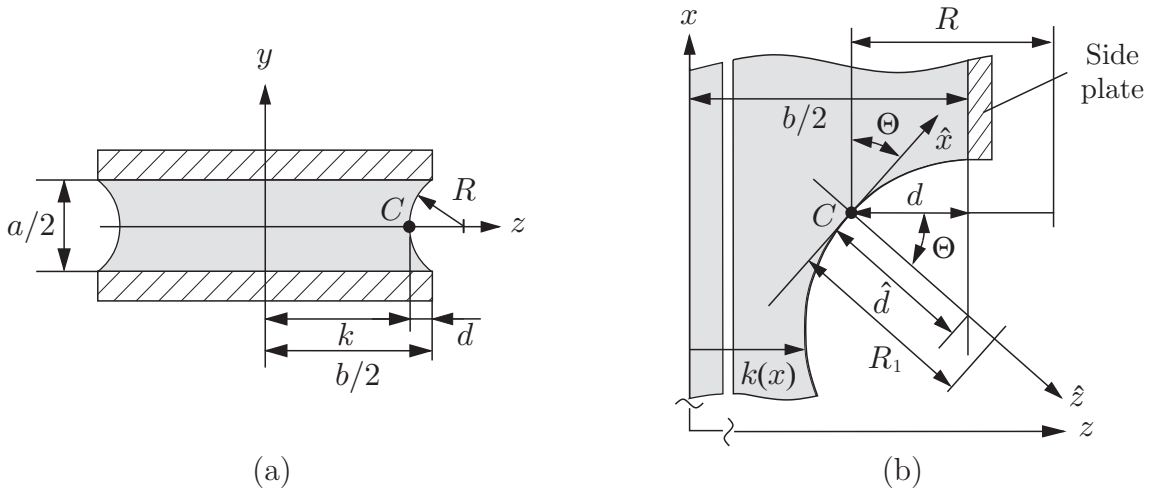

Figure 7.3: (a) Cross section of the channel in the plane $x = const$. The position k defines the profile of the liquid surface. For slight variation of the cross section along the flow path the surface curvature may be approximated by the radius of curvature R. (b) Section through the liquid in the (x, z)-plane at $y = 0$. The coordinate axes x, $\hat{x}$ and z, $\hat{z}$ are pairwise rotated about the angle Θ.

symmetrical with respect to the planes $y = 0$ and $z = 0$. Therefor it is sufficient to restrict the considerations to the profile of the surface

$$z(x, y = 0) \equiv k(x) \tag{7.9}$$

with $0 \leq z \leq b/2$. The profile is defined by the intersection line of the surface with the plane $y = 0$, and it identifies the innermost position of the liquid surface in the cross sectional planes $x = const$, as shown in Fig. 7.3a[1]. The simplification of Eq. (7.8) occurs since k defines the minimum of $z = z(x = const, y)$ in each cross section plane. Since $z_y(x, y = const) = 0$, Eq. (7.8) reduces to

$$h(x, y = 0) = \frac{1}{R_1} + \underbrace{\frac{\mathrm{d}_{xx}k}{(1 + (\mathrm{d}_x k)^2)^{3/2}}}_{R_2^{-1}} \tag{7.10}$$

with the derivatives $\mathrm{d}_x k = \mathrm{d}k/\mathrm{d}x$ and $\mathrm{d}_{xx}k = \mathrm{d}^2k/\mathrm{d}x^2$. For the point C of the profile the second term in Eq. (7.10) defines the potion of the curvature in the principal normal plane $(\hat{x}, \hat{z})$, which is give by the inverse principal radius of curvature $1/R_2$ (curvature in flow direction). The principal normal plane is spanned by the normal vector $\hat{x}$ and the tangent vector $\hat{z}$ of the surface in C, and it is congruent to the (x, z)-plane (see Fig. 7.2). The first

[1]The term 'profile' results form the experimental observations in which the distance $d = b/2 - k$ appears as dark area due to the orientation of the camera in negative y-direction. After evaluation of the video images only the edge of this area which is faced to the liquid – the contour or profile – is available for the comparison with the theoretical results.

term gives the portion of the curvature in the principal normal plane $(y, \hat{z})$ defined by the inverse principal radius of curvature $1/R_1$.

In general the principal normal plane $(y, \hat{z})$ is rotated by the angle Θ compared to the cross sectional plane (y, z). To demonstrate the geometrical relations, a section of the surface at the channel outlet in the plane $y = 0$ is shown in Fig. 7.3b. In this plane $\hat{d}$ and the $\hat{x}$-axis as well as d and the x-axis form a right angle. The rotation angle Θ between the coordinate axes appears therefor also between $\hat{d}$ and d, it applies

$$\cos\Theta = \frac{d}{\hat{d}}. \tag{7.11}$$

With the slope of the profile $\tan\Theta = \mathrm{d}_x k$ and the trigonometrical relation $\cos\Theta = 1/\sqrt{1+\tan^2\Theta}$ the Eq. (7.11) can be transferred into

$$\frac{d}{\hat{d}} = \frac{1}{\sqrt{1+\Gamma^{-2}(\mathrm{d}_x k)^2}}. \tag{7.12}$$

From this equation it follows, that $\hat{d}$ may be approximated by d, if the profile varies only slightly in flow direction ($\mathrm{d}_x k \ll \Gamma$). Since according to Eq. (7.11) for $\hat{d} \simeq d$ the angle Θ is small, the planes $(y, \hat{z})$ and (y, z) are practical congruent. The principal radius of curvature R_1 is then in good approximation determined by the radius R. This radius defines the curvature of the surface in the cross sectional plane in C (see Fig. 7.3a).

This circumstance is given for a one-dimensional flow, since the cross section for these flows varies by definition slightly. Under these conditions also the surface curvature in flow direction is negligible small ($\mathrm{d}_{xx} k \ll \Gamma^2$), and because of $R_1 \simeq R$ the Eq. (7.10) may be approximated by

$$h_R = \frac{1}{R}. \tag{7.13}$$

Since for one-dimensional flows the pressure does not vary over the cross sectional area A, Eq. (7.13) not only holds for C but in any point of the surface in the cross section plane. This follows for $p - p_a = const$ from Eq. (7.1). For flows with small variation of A the surface curvature in any cross section plane is therefor approximately constant and may be approximated by the inverse radius of $1/R$. Within this approximation the radius R defines always segments of circle and may be therefor expressed as function of k. Consequently, the curvature from Eq. (7.13) as well as cross section area of the flow (channel cross sectional area minus the both areas of the segments of circle) are defined unique by the surface profile.

According to Fig. 7.3a applies $R^2 = a^2/4 + (R-d)^2$, so that between R and k the dependency

$$R = \frac{a^2 + 4d^2}{8d} \quad \text{and} \quad d = b/2 - k \tag{7.14}$$

are derived. This relation holds for $d \leq a/2$ as long as the liquid is attached to the edges of the plates, which is for $k \geq (b-a)/2$ the case. In the experiment also states were observed,

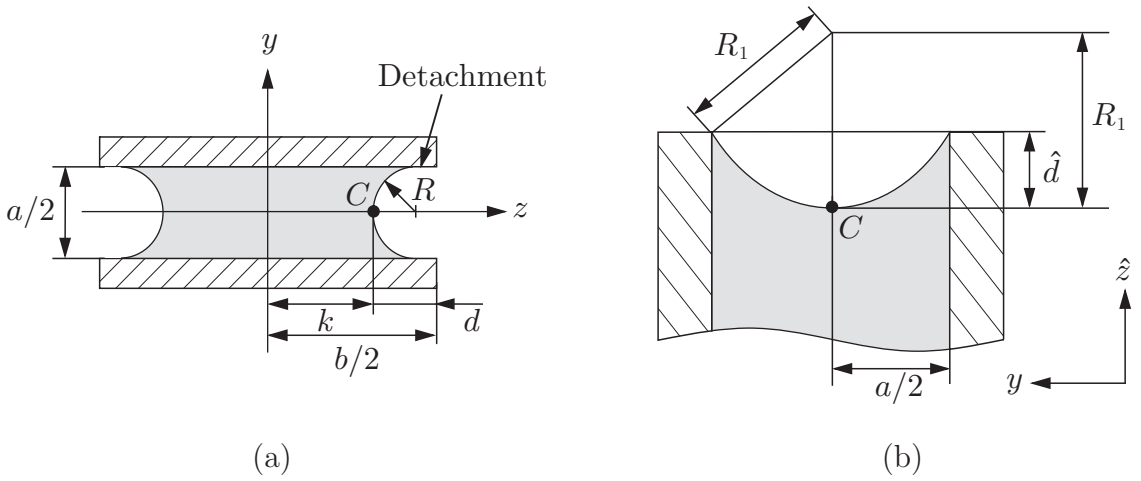

Figure 7.4: (a) Cross sectional plane of the flow at detachment of the contact line from the edges of the plates. (b) Cut in the principal normal plane $(y, \hat{z})$.

for which the contact line of the liquid is detached form the edges $(k < (b-a)/2)$. The radius R then remains constant independent of the position of the profile, and since for perfectly wetting liquid the static contact angle with the wall is $\gamma_s = 0°$, the surface must form a semicircle with $R = 1/2$ (see Fig. 7.4a). Both cases are summarized by

$$R = \begin{cases} \dfrac{a^2 + (b-2k)^2}{4(b-2k)} & \text{for} \quad k \geq \left(\dfrac{b}{2} - \dfrac{a}{2}\right) \\ \dfrac{a}{2} & \text{for} \quad k < \left(\dfrac{b}{2} - \dfrac{a}{2}\right). \end{cases} \tag{7.15}$$

Using the geometrical relations for the by R defined segments of circle (see Sieber, 1982) one gain the cross section area of the flow

$$A = \begin{cases} ab - 2R^2 \arcsin\left(\dfrac{a}{2R}\right) + a\left(R - \dfrac{b}{2} + k\right) & \text{for} \quad k \geq \left(\dfrac{b}{2} - \dfrac{a}{2}\right), \\ a^2 + 2ka - \dfrac{\pi}{4}a^2 & \text{for} \quad k < \left(\dfrac{b}{2} - \dfrac{a}{2}\right). \end{cases} \tag{7.16}$$

This approximation is satisfied sufficiently when the flow cross section area varies slightly. This is the case for the predominant part of the flow path except for the regions close to the inlet and outlet. Here the rotation angle Θ is no longer negligible small, and strictly speaking the curvature in the cross section planes cannot be considered as constant. However, for the considered channel properties this effect is small, so that Eq. (7.16) holds in good approximation for the overall flow path.

If Eq. (7.15) is applied to Eq. (7.13), it follows that for $k < (b-a)/2$ the curvature is constant while the cross section from Eq. (7.16) still varies. This leads to a contradiction since a variation of h implies a variation of A. Herefrom it follows, that Eq. (7.15) is not

the adequate approximation of the curvature and the curvature portion in flow direction must not be neglected. In order to include this portion into the model we assume – different from the assumption for the determination of the cross section area – that the liquid surface shows a constant curvature in the principal normal plane $(y, \hat{z})$. With this assumption the surface defines in the $(y, \hat{z})$-plane segments of circle with radius R_1 (see Fig. 7.4b). With $R_1^2 = a^2/4 + (R_1 - \hat{d})^2$ the corresponding radius may be determined by

$$R_1 = \frac{a^2 + \hat{d}^2}{8\hat{d}}, \quad \hat{d} = d\sqrt{a^2 + 4(\mathrm{d}_x k)^2}/2 \quad \text{and} \quad d = b/2 - k, \tag{7.17}$$

whereas the second correlation follows from Eq. (7.12). These correlation hold for $\hat{d} \leq a/2$, as long as the liquid is attached to the edges of the plates. For $k < \{b - [a^2 + 4(\mathrm{d}_x k)^2]^{-1/2}\}/2$ the radius corresponds to the half the plates distance, and the curvature $1/R_1$ becomes maximum in the $(y, \hat{z})$-plane. Both cases may be summarized by

$$R_1 = \begin{cases} \dfrac{a^2 + (b-2k)^2\left[a^2 + 4(\mathrm{d}_x k)^2\right]}{8(b-2k)\left[a^2 + 4(\mathrm{d}_x k)^2\right]^{1/2}} & \text{for} \quad k \geq \{b - [a^2 + 4(\mathrm{d}_x k)^2]^{-1/2}\}/2 \\ a/2 & \text{for} \quad k < \{b - [a^2 + 4(\mathrm{d}_x k)^2]^{-1/2}\}/2. \end{cases} \tag{7.18}$$

7.3 Modelling of the irreversible pressure loss

The gradient of the irreversible pressure loss due to viscous forces $4\tau_w/D_h$ in Gl. (7.34), consists of two parts, the pressure loss $4\tau_{wl}/D_h$ of the fully developed laminar flow with parabolic velocity distribution (POISEUILLE-flow) and the additional pressure loss $4\tau_{we}/D_h$ of the entrance flow. The latter pressure loss results from the change of the velocity distribution at the channel inlet to the parabolic velocity distribution at the end of the entrance length.

For the fully developed laminar liquid flow between two infinite wide parallel plates an analytic solution of the two-dimensional NAVIER-STOKES exists. From this solution the wall shear stress

$$\tau_{wl} = \frac{K_{pl}}{\mathrm{Re}_h}\frac{\rho v^2}{8} \quad \text{with} \quad \mathrm{Re}_h = \frac{D_h v}{\nu} \tag{7.19}$$

may be derived (see White, 1991), where $K_{pl} = 96$ is a friction constant and Re_h the REYNOLDS number based on the hydraulic diameter D_h. Since the flow velocity varies along the flow path due to the changing cross section area, Eq. (7.19) is applied locally (vgl. Spurk, 1992), so that

$$\tau_{wl}(x) = \frac{\mu K_{pl}}{8D_h} v(x) = \frac{\mu K_{pl}}{8D_h}\frac{Q}{A(x)} \tag{7.20}$$

is achieved. The determination of the pressure loss of the inlet flow is based on the work of Sparrow & Lin (1964). Herein the momentum equation of a flow between two infinite

wide parallel plates are solved by an approach, in which the difference between the local flow velocity and the parabolic distribution of the fully developed flow is approximated by a superposition of certain eigenfunctions. After determination of the velocity distribution the pressure loss may be derived, for which Sparrow & Lin quote

$$p_e(x) = K(\check{x})\frac{\rho v^2}{2} \tag{7.21}$$

with the loss factor

$$K(\check{x}) = 0,4 + \sum_i \frac{4}{\alpha_i^2}\{e^{-\alpha_i^2\check{x}^*} - 2\}e^{-\alpha_i^2\check{x}^*} - 2\int_0^{\check{x}^*} \epsilon(\check{x}^*)\left(\frac{\partial\check{u}^*}{\partial\check{y}}\right)_{\check{y}=1} d\check{x}^*. \tag{7.22}$$

Here α_i are the solutions of the Eigenvalue equation $\tan\alpha_i = \alpha_i$, $\check{u}(\check{x}^*, \check{y})$ the velocity distribution and $\check{x}^*$ a stretched property which is coupled by the factor $\epsilon(\check{x}^*)$ to the dimensionless coordinate $\check{x} = 16x'/(\mathrm{Re}_h D_h)$.

From the definition $\mathrm{d}p/\mathrm{d}x = -4\tau_w/D_h$ and Eq. (7.21) it arises the mean wall shear stress

$$\tau_{we} = \frac{D_h}{4}\frac{\mathrm{d}p_e}{\mathrm{d}x} = \frac{D_h}{4}\frac{\mathrm{d}p_e}{\mathrm{d}\check{x}}\frac{\mathrm{d}\check{x}}{\mathrm{d}x} = 2\frac{\mathrm{d}K}{\mathrm{d}\check{x}}\frac{\rho v'^2}{\mathrm{Re}_h} \tag{7.23}$$

for constant cross sections. For variable cross sections Eq. (7.23) is applied locally, and

$$\tau_{wl}(x) = \frac{2\mu K_{pe}}{D_h}v(x) = \frac{2\mu K_{pe}}{D_h}\frac{Q}{A(x)} \tag{7.24}$$

with

$$K_{pe}(\check{x}) = \frac{\mathrm{d}K(\check{x})}{\mathrm{d}\check{x}} \tag{7.25}$$

is achieved. Eq. (7.22) is based on the assumption of a homogenous velocity distribution at the channel inlet. Since the flow enters the channel with a certain thickness of the boundary layer, the wall shear stress needs to be adapted to these boundary conditions. The adaption is achieved by the transformation of Eq. (7.25) using

$$\check{x}_S = \check{x} + (1 - \beta_0)\check{x}_e, \quad \text{with} \quad 0 \le \beta_0 \le 1. \tag{7.26}$$

Here the parameter β_0 gives the rate of profile development, and

$$\check{x}_e = \frac{16x'_e}{\mathrm{Re}_h D_h} \quad \text{with} \quad x_e = 0,01639\mathrm{Re}_h D_h \tag{7.27}$$

is the the entrance length for which the parabolic velocity profile is quasi fully developed (White, 1991). This is the case for $\beta_0 = 0$ and then entrance pressure loss does not contribute to the total pressure loss. In the opposite case $\beta = 1$ the flow at the inlet is fully homogeneous and entrance pressure loss enters to the full extent in the pressure balance. With Eq. (7.20) and Eq. (7.24) the gradient of the irreversible pressure loss reads

$$\frac{4\tau_w}{D_h} = \frac{4(\tau_{wl} + \tau_{we})}{D_h} = \frac{\mu(K_{pl} + 16K_{pe})}{4D_h^2}\frac{Q}{A(x)}. \tag{7.28}$$

Length	Velocities	Other	Characteristic properties
$x' = x/\tilde{x}$	$v' = v/\tilde{v}_c$	$p' = p/\tilde{p}$	$\tilde{x} = l$
$y' = y/\tilde{y}$	$v'_c = v_c/\tilde{v}_c$	$A' = A/\tilde{A}$	$\tilde{y} = a/2$
$z' = z/\tilde{y}$		$Q' = Q/(\tilde{A}\tilde{v}_c)$	$\tilde{v}_c = \sqrt{2\sigma/(\rho a)}$
$k' = k/\tilde{y}$		$\tau'_w = \tau_w/\tilde{\tau_w}$	$\tilde{p} = 2\sigma/a$
$R' = R/\tilde{y}$			$\tilde{A} = ab$
$R'_{1,2} = R_{1,2}/\tilde{y}$			$\tilde{\tau_w} = 4\mu\tilde{v}_c/D_h$
$1/h' = 1/(h\tilde{y})$			

Table 7.1: Dimensionless variables and characteristic properties.

7.4 Scaling and dimensionless numbers

For the non-dimensionalisation of Eq. (7.7) and Eq. (7.3) all length perpendicular to the flow direction are scaled by $a/2$. The cross sectional area is non-dimensionalized with $A_0 = ab$ and the x-axis with the channel length l. From the scaling of the Gauss-Laplace equation (7.1) the characteristic pressure $\tilde{p} = 2\sigma/a$ is achieved which yields the characteristic velocity $\tilde{v}_c = \sqrt{\tilde{p}/\rho} = \sqrt{4\sigma/\rho D_h}$. This velocity is already known as characteristic property from experiments of the capillary rise of liquids between parallel plates (see Dreyer, 1994). For the wall shear stress we find $\tilde{\tau_w} = 4\mu\tilde{v}_c/D_h$. The applied scaling and the characteristic properties are summarized in table 7.1. Non-dimensional variables are denoted with $'$.

Four dimensionless numbers are determining this flow problem. They are the aspect ratio

$$\Lambda = b/a, \tag{7.29}$$

the Ohnesorge number

$$\mathrm{Oh} = \sqrt{\frac{\rho\nu^2}{\sigma D_h}}, \tag{7.30}$$

the dimensionless length

$$\mathcal{L} = \frac{\mathrm{Oh}\, l}{2D_h} \tag{7.31}$$

and the volumetric flow rate

$$Q' = \frac{Av}{abv_c}. \tag{7.32}$$

The Ohnesorge number defines the influence of the friction. If we introduce the viscous velocity $\tilde{v}_v = 2\nu/D_h$ at which the molecular momentum is transported, the Ohnesorge number is defined by $\mathrm{Oh} = \tilde{v}_v/\tilde{v}_c$. The influence of friction forces is low for $\tilde{v}_v \ll \tilde{v}_c$ and vice versa. Thus, the Ohnesorge number is inversely proportional to a Reynolds number based on the capillary velocity $\tilde{v}_c$, $\mathrm{Oh} = 2/\mathrm{Re}_c = 2\nu/(D_h\tilde{v}_c)$. Eq. (7.31) may also be

achieved by the multiplication of Eq. (7.30) with the aspect ratio $l/(2D_h)$. For this reason the dimensionless length may be interpreted as the ratio between the characteristic time scales of both momentum transports, $\mathcal{L} = \tilde{t}_c/\tilde{t}_v$. Consequently we find $\mathcal{L} = l/(\mathrm{Re}_c D_h)$ which is similar to the usual scaling of viscous duct flows.

As further characteristic numbers the BOND numbers

$$\mathrm{Bo}_i = \frac{\rho g_i a L_i}{2\sigma} \tag{7.33}$$

need to be introduced. They are required for each axes $i = x, y, z$ with the characteristic lengths $L_i = a, b, l$, respectively, and define the ratio between the hydrostatic pressure caused by the acceleration g_i and the capillary pressure. Eq. (7.33) needs to be sufficiently small to enable the capillary flow between the plates. In addition $\mathrm{Bo}_y \ll 1$ and $\mathrm{Bo}_z \ll 1$ are required in order to achieve surface symmetry as assumed in A5.

With the introduced scaling and the dimensionless numbers the momentum equation (7.7) and the equation of continuity (7.3) may be rewritten as

$$\frac{\mathrm{d}h'}{\mathrm{d}x'} - v'\frac{\mathrm{d}v'}{\mathrm{d}x'} - 16\tau_w\mathcal{L} = 0, \tag{7.34}$$

and

$$\frac{\mathrm{d}Q'}{Q'} = \frac{\mathrm{d}A'}{A'} + \frac{\mathrm{d}v'}{v'} = 0, \tag{7.35}$$

respectively. For the cross sectional area we get

$$A'(k') = \begin{cases} 1 - \dfrac{R'^2}{2\Lambda}\arcsin\dfrac{1}{R'} + \dfrac{1}{2\Lambda}(R' - \Lambda + k') & \text{for} \quad k' \geq \Lambda - 1 \\ \dfrac{1}{\Lambda}(k' + 1 - \dfrac{\pi}{4}) & \text{for} \quad k' < \Lambda - 1 \end{cases} \tag{7.36}$$

with the dimensionless radius

$$R' = \begin{cases} \dfrac{1 + (\Lambda - k')^2}{2(\Lambda - k')} & \text{for} \quad k' \geq \Lambda - 1 \\ 1 & \text{for} \quad k' < \Lambda - 1. \end{cases} \tag{7.37}$$

In dimensionless form the surface curvature form Eq. (7.10) reads

$$h'(x', y' = 0) = \frac{1}{R'_1} + \frac{\Gamma^{-2}\mathrm{d}_{xx}k'}{(1 + \Gamma^{-2}(\mathrm{d}_x k')^2)^{3/2}} \tag{7.38}$$

where the dimensionless principal radius of curvature R_1 is defined by

$$R'_1 = \begin{cases} \dfrac{1 + (\Lambda - k')^2\left[1 + \Gamma^{-2}(\mathrm{d}_x k')^2\right]}{2(\Lambda - k')\left[1 + \Gamma^{-2}(\mathrm{d}_x k')^2\right]^{1/2}} & \text{for} \quad k' \geq \Lambda - \left[1 + \Gamma^{-2}(\mathrm{d}_x k')^2\right]^{-1/2} \\ 1 & \text{for} \quad k' < \Lambda - \left[1 + \Gamma^{-2}(\mathrm{d}_x k')^2\right]^{-1/2}. \end{cases} \tag{7.39}$$

7.5 Model equations and numerical method of solution

Due to the relation $A' = A'(k')$ corresponding Eq. (7.36), the second term in Eq. (7.34) may be rewritten under usage of the continuity equation (7.35) to

$$v' \frac{\mathrm{d}v'}{\mathrm{d}x'} = -\frac{Q'^2}{A'^3} \frac{\mathrm{d}A'}{\mathrm{d}k'} \frac{\mathrm{d}k'}{\mathrm{d}x'}. \tag{7.40}$$

If this term together with Eq. (7.28) is applied to Eq. (7.34) the momentum equation

$$\frac{\mathrm{d}h'}{\mathrm{d}x'} + \frac{Q'^2}{A'^3} \frac{\mathrm{d}A'}{\mathrm{d}k'} \frac{\mathrm{d}k'}{\mathrm{d}x'} - \left[K_{pl} + 16K_{pe}(\check{x}_S)\right] \frac{\mathcal{L}Q'}{2A'} = 0 \equiv \mathcal{F} \tag{7.41}$$

is gained. The reformulation of Eq. (7.38) yields

$$\Gamma^{-2} \frac{\mathrm{d}^2 k'}{\mathrm{d}x'^2} + \left(\frac{1}{R_1'} - h'\right) \left[1 + \Gamma^{-2} \left(\frac{\mathrm{d}k'}{\mathrm{d}x'}\right)^2\right]^{3/2} = 0 \equiv \mathcal{G}. \tag{7.42}$$

These equations are coupled ordinary differential equations of first order in h' and second order in k' and require three boundary conditions. These are given by the fixed liquid surface at the channel inlet and outlet,

$$k_0' = k'(x' = 0)\,, \tag{7.43}$$

$$k_1' = k'(x' = 1), \tag{7.44}$$

and the surface curvature at the channel inlet

$$h_0' = h'(x' = 0). \tag{7.45}$$

Additionally the rate of of profile development,

$$\beta_0 = \beta(x' = 0), \tag{7.46}$$

need to be defined.

For solving Eq. (7.41) and (7.42) the range of solutions $0 \leq x' \leq 1$ is discretized into N grid point $x_i' = (i-1)\Delta x'$, $i = 1, \ldots, N$, with $\Delta x' = 1/(N-1)$, and the derivatives are approximated by difference quotients. For the derivatives $\mathrm{d}k'/\mathrm{d}x'$ and $\mathrm{d}^2k'/\mathrm{d}x'^2$ central differences of second order are suited. The derivative $\mathrm{d}h'/\mathrm{d}x'$ is replaced by a backwards difference of first order, to achieve higher numerical stability. Consequently a nonlinear system of equations of dimension $2N$ is obtained, which can be solved by Newton-Raphson method

$$\boldsymbol{X}^{m+1} = \boldsymbol{X}^{m} - \mathbf{A}^{-1} \boldsymbol{F}(\boldsymbol{X}^{m}) \tag{7.47}$$

(Press *et al.*, 1992). Here $\boldsymbol{X} = (k_1', \ldots, k_N', h_1', \ldots, h_N')^{\mathrm{T}}$ is the vector of solution with $k_i' = k(x_i)$ and $h_i' = h'(x_i')$, $\mathbf{A}$ the Jacobian matrix, $\boldsymbol{F} = (\mathcal{F}_1, \ldots, \mathcal{F}_N, \mathcal{G}_1, \ldots, \mathcal{G}_N)^{\mathrm{T}}$ the vector of function and m the iteration step.

No.	K_1	K_2	K_3	L	Q'
TE-35a	1.4	374	0.222	-24	$0.44 < Q' < 0.88$
DT-29	2.7	168	0	-5.5	$0.06 < Q' < 0.4$
DT-32	2.2	91	0	-4.2	$0.07 < Q' < 0.5$
DT-33	2.2	138	0	-6.6	$0.19 < Q' < 0.57$
DT-34	2.3	215	0	-9.7	$0.19 < Q' < 0.57$
DT-35/35a	2.0	180	0	-5.8	$0.44 < Q' < 0.88$

Table 7.2: Coefficients for the entrance pressure drop at the inlet of the channel and for the velocity profile formula. The calculations have been performed with the flow rates indicated in the table to cover the region of the experiment data.

For the standard routines for the calculation of the inverse matrix $\mathbf{A}^{-1}$ and for the iteration of Eq. (7.47). As initial solution for $\boldsymbol{X}^0$ the values $k_i'^0 = \Lambda$ and $h_i'^0 = h_0'$ are forced. The iteration is considered as sufficient accurate, when the criterion $|\boldsymbol{X}^{m+1} - \boldsymbol{X}^m|/2N \leq 10^{-7}$ is fulfilled.

7.6 Boundary conditions

Due to the complex geometry no analytical data for the determination of the boundary condition h_0' and s_0' from (7.45, 7.46) are not available in sufficient accuracy and a direct measurement was not possible. For this reason we performed three-dimensional model computations using the finite element code FIDAP (Version 8.0, Fluent Inc.).

The capillary pressure at the channel inlet $h_0' = p_a' - p_0'$ is defined by the capillary pressure of the meniscus in the compensation tube $(p_a' - p_1')$ plus convective and frictional flow losses inside the liquid reservoir and the nozzle (see figure 3.9). The pressure loss nondimensionalized with $\rho/2v_0^2$, $v_0 = v(x = 0)$, is linear versus $1/\mathrm{Re}_0$ with $\mathrm{Re}_0 = 2av_0/\nu$ (White (1991)). The regression of the numerical data yields the relation

$$h_0' = \frac{K_1 Q^2}{2} + \frac{K_2 \mathrm{Oh}\, Q'}{4} + K_3, \quad K_3 = \frac{a(p_a' - p_1')}{2\sigma}. \tag{7.48}$$

The values of $K_{1,2,3}$ are given in Table 7.2. Note that for the drop tower experiments the capillary pressure of the bulk surface is negligible small compared to h_0' and therefore $K_3 = 0$.

To adapt the analytic entrance pressure loss proposed by Sparrow & Lin (1964) to the condition of the experiment, the velocity profiles at the channel inlet are compared between the three-dimensional model computations and the solution from Sparrow & Lin (1964),

which gives values for β_0 from Eq. (7.26) in dependence of Q. It is remarkable that for all experiment configurations β_0 is nearly a linear function of $1/\mathrm{Re}_0$

$$\beta_0 = \frac{L}{\mathrm{Re}_0} = \frac{L\mathrm{Oh}}{2Q'}, \tag{7.49}$$

where the fitted values for L are given in Table 7.2.

To obtain the best approximation to the one-dimensional model assumption, the flow path before the open channel of the TEXUS experiment was optimized. The model computations led to a nozzle with 25 mm by 30 mm rectangular inlet cross section that converges to the channel cross section. The nozzle has an elliptical shape in the (x, y)-plane but no constriction in the (x, z)-plane. With this form the lateral velocity components in the entrance cross section of the open channel were minimized to 2% of the longitudinal component. Concerning the x-component of the velocity the flow is characterized by a constant core flow with small boundary layers along the walls.

7.7 Numerical results

7.7.1 Influence of the viscous losses on the flow.

The dimensionless length $\mathcal{L}$ may be understand as a measure for the ratio between the convective and the viscous term of the momentum equation (7.41). Therefor two distinct cases may be identified depending on the dimensionless length $\mathcal{L}$. For sufficiently small $\mathcal{L}$ the viscous pressure loss vanishes and the flow is influenced by the convective term. In the opposite case for sufficiently large $\mathcal{L}$ the irreversible viscous losses dominate the flow.

In order to investigate the influence of $\mathcal{L}$ on the solution of Eq. (7.41) and Eq. (7.42), a parametric study was performed. For each $\mathcal{L}$ the maximum flow rate Q'^{num}_{crit} and the corresponding mean curvature difference between the channel inlet and outlet, $\Delta h' = h'(x' = 1) - h'(x' = 0)$, were determined. Since the reversible convective momentum transport does not affect a net decrease of pressure between the inlet and outlet, $\Delta h'$ is a direct measure for the influence of the frictional pressure loss. The calculations were performed under assumption of a fully developed parabolic velocity profile along the channel. The inlet pressure boundary condition h'_0 was taken from the formula (7.48) with the coefficients $K_1 = 1.4$, $K_2 = 374$ and $K_3 = 0$. Fig. 7.5 shows a plot for $\Delta h'$ as a function of $\mathcal{L}$. The curve was computed for $\mathrm{Oh} = 10^{-4}$ and $\Lambda = 5$, but can be seen to represent the general behavior. The labels of the single squares refer to the experiments listed in Table 3.1 (black squares) and three numerical cases discussed, which will be discussed below (white squares). Note that due to the different values of Λ and Oh the experiment values of $\Delta h'$ deviate slightly from those given in Fig. 7.5 (deviation stays within the squares). The curve may be divided

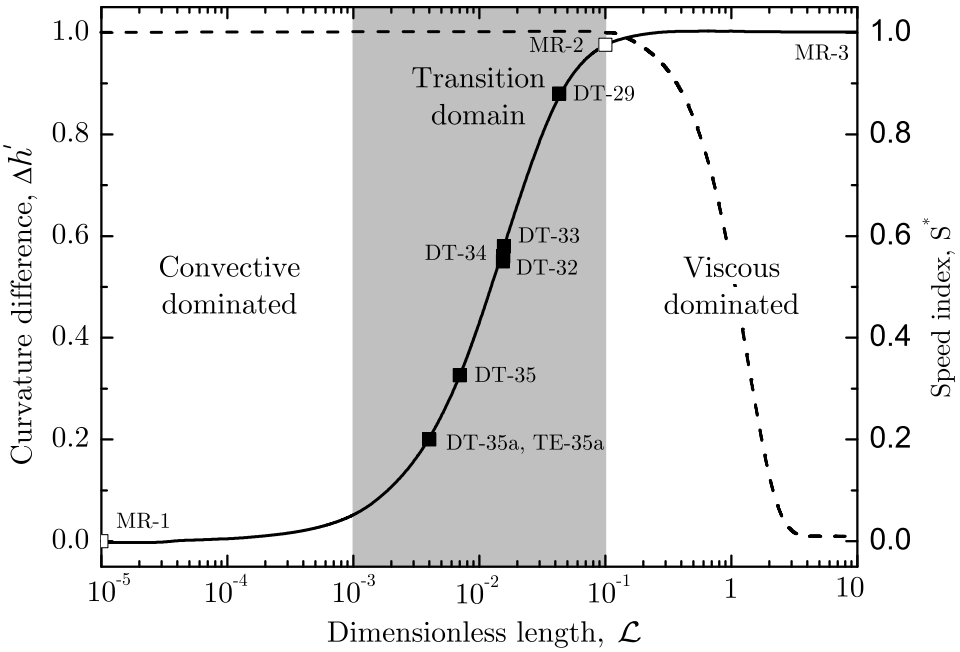

Figure 7.5: Curvature difference between the inlet and outlet of the capillary channel $\Delta h^{'}$ (——) and maximum speed index S^* (– – –) as function of $\mathcal{L}$ at Q'^{num}_{krit}. The symbols denote the experiment parameter (■) from table 3.1 and the parameter of the numerical model computations MR-1, MR-2, and MR-3 (□).

in three regions. For small flow lengths, ($\mathcal{L} \lesssim 10^{-3}$), the irreversible pressure loss $\Delta h'$ is small, and the flow is dominated by convective momentum transport. In the limit of a very short length the curvature difference $\Delta h'$ tends to zero. For that case the pressure loss along the flow path is fully reversible. For the other extreme of a very long channel, ($\mathcal{L} \geq 10^{-1}$), the flow is dominated by viscous momentum transport (convection contributes $< 1\%$). In the limit $\mathcal{L} \to \infty$ the curvature difference $\Delta h'$ tends towards unity yielding a pure Stokes flow. Between these two extremes, denoted as the transition domain, the flow is controlled by both convective and frictional pressure losses.

The influence of the domains on the nature of the flow is demonstrated by the numerical examples MR-1 ($\mathrm{Oh} = 10^{-5}$, $\Lambda = 5$, $\mathcal{L} = 10^{-5}$, $Q'^{num}_{crit} = 1.123$) and MR-02 ($\mathrm{Oh} = 10^{-3}$, $\Lambda = 5$, $\mathcal{L} = 0.1$, $Q'^{num}_{crit} = 0.1927$). For the first example the flow the properties k', v' and h' at the maximum flow rate Q'^{num}_{crit} are shown in Fig. 7.6(a). Since the pressure loss due to convective momentum transport is reversible, the minimum cross section appears at half the channel length $l^{*'} = l/2$. The pressure loss along $0 < x' < l^{*'}$ is recovered along the

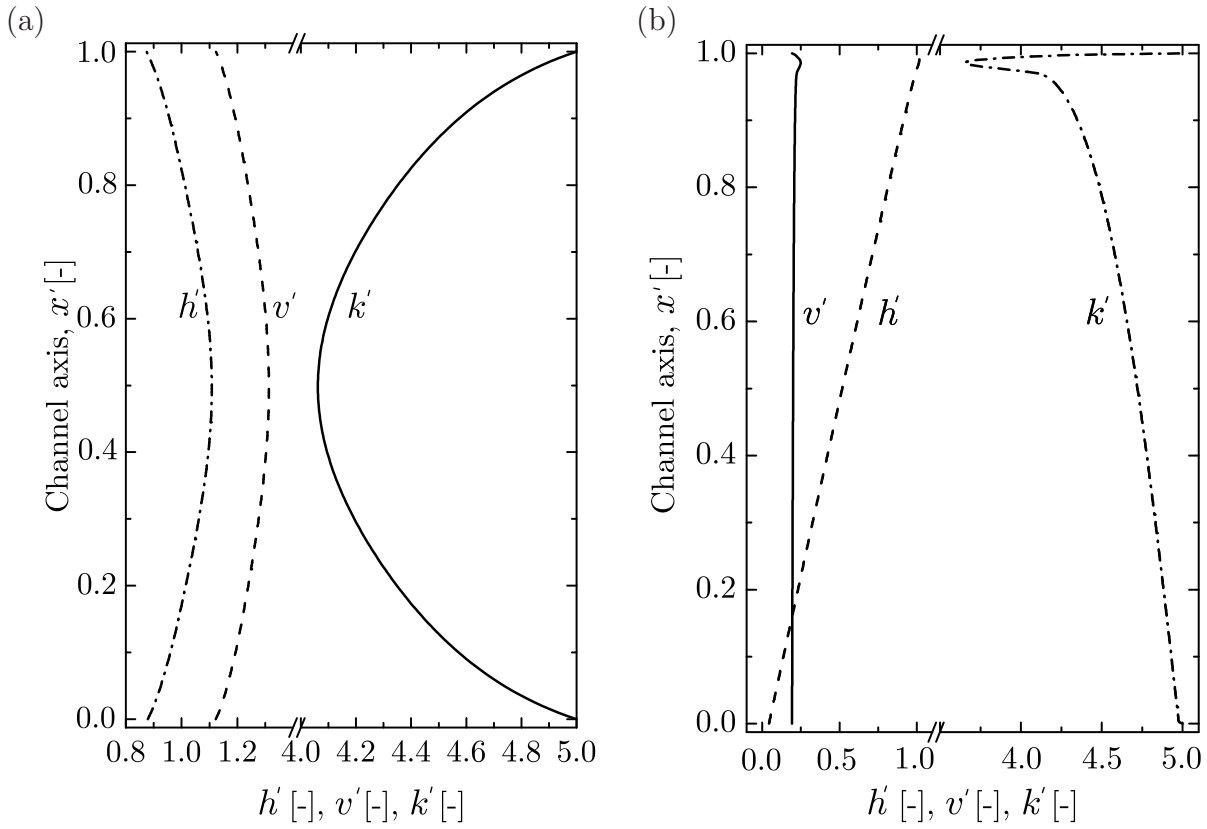

Figure 7.6: Numerical solution for the profile k' (solid line), the velocity v' (dashed line) and the curvature h' (dash-dot line) at Q'^{num}_{crit}. (a) Example MR-1, Oh $= 10^{-5}$, $\Lambda = 5$, $\mathcal{L} = 10^{-5}$, $Q'^{num}_{crit} = 1.123$, (b) Example MR-2, Oh $= 10^{-3}$, $\Lambda = 5$, $\mathcal{L} = 0.1$, $Q'^{num}_{crit} = 0.1927$.

distance $l^{*'} < x < 1$. With increasing $\mathcal{L}$ the frictional loss $\Delta h'$ increases, and the position of the minimal cross section l'^{*} moves towards the outlet. The influence of the convective term vanishes. In the extreme example MR-2 (Fig. 7.6(b)) the local importance of the convective term is reduced to a small zone at $x = l^{*'}$ leading to the distinct constriction of the flow path at the channel outlet. As a result the total frictional loss increases approximately linearly with x' as indicated by the nearly linear increase h'.

The drop tower experiments which cover a wide range of the transitional domain ($10^{-3} < \tilde{l} < 10^{-1}$) confirm these findings. The experiment DT-35a (Fig. 3.7a) at the lower range of the transitional domain is essentially dominated by the convective acceleration. Thus the shape is similar to example MR-1. Experiment DT-29 (Fig. 3.7b) is dominated by friction characterized by the sharp distinct minimum of the cross section as in the example MR-2.

The appearance of the flow for ($\mathcal{L} \geq 10^{-1}$) does not deviate significantly from Fig. 7.6(b) but it turned out, that speed index S no longer tends towards unity for the critical flow

rate. Fig. 7.5 shows that for ($\mathcal{L} \geq 10^{-1}$) the maximum achievable value for S (dashed line) decreases with increasing $\mathcal{L}$. This is plausible since the choking mechanism bases on an interaction between the static and the dynamic pressure. Sine for large $\mathcal{L}$ the convective term is small compared to the viscous term in Eq. (7.41), the choking effect loses its impact. Therefor the speed index is practically zero in case of example MR-3 (Oh $= 10^{-2}$, $\Lambda = 5$, $\mathcal{L} = 10$, $Q'^{num}_{crit} = 0.0020$) in Fig. 7.5.

7.7.2 Approximations solutions

In order to provide a larger database, the critical flow rate of the model equations (7.41) and (7.42) was determined numerically over several orders of magnitude of the characteristic numbers Oh and $\mathcal{L}$. Thereby Eq. (7.48) with the parameter $K_1 = 1.4$, $K_2 = 374$ and $K_3 = 0$ served as curvature boundary condition. The flow was assumed to be laminar with fully developed flow profile.

For the aspect ratios $\Lambda = 5$ and $\Lambda = 50$, the isolines of the critical flow rate are plotted as function of Oh and $\mathcal{L}$ is Fig. 7.7. The graphic shows that for $\mathcal{L} = const < 10^{-3}$ the flow rate increases with increasing Ohnesorge number. This is plausible since (i) for this case Oh $\sim l^{-1}$ applies, and (ii) the flow is convective dominated. The decrease of length causes an increase of the convective dominated pressure drop, which cannot be exclusively compensated by the frictional losses due to the increase of the Ohnesorge number. According to this the flow rate increases for Oh $= const$ with increasing length $\mathcal{L}$. The independency of Q from the Ohnesorge number for $\mathcal{L} > 0.1$ results from the effect, that the choking mechanism loses its impact in strong frictional flows. Since Oh $= \tilde{v}_v/\tilde{v}_c$, the Ohnesorge number is a measure for the ratio of the characteristic propagation speeds of the viscous and convective momentum, $\tilde{v}_v$ and $\tilde{v}_c$, respectively. Consequently the dimensionless length $\mathcal{L} = \mathrm{Oh}l/(2D_h)$ defines the ratio of the characteristic time scales of both momentum transports. For $\mathcal{L} = \tau_c/\tau_v < 1$ it may assumed, that the convective momentum transport along the channel takes place faster than the lateral viscous momentum transport. The flow rate is then limited due to choking. The limitation due to viscous forces occurs in the opposite case for $\mathcal{L} > 1$, since the viscous time scale then is short compared to the convective one. The fact that the transition between both effects occurs at $\mathcal{L} \simeq 1$, results among others from the unsatisfactory definition of $\tilde{v}_c$ in which the dependency of the surface curvature is not considered. For this value the viscous time scale is already short that a variation of the Ohnesorge number has no impact. Consequently, the convective momentum transport is negligible small, and the limitation of the flow rate is no longer caused by choking but only by viscous forces.

For this viscous dominated range, which is highlighted grey in Fig. 7.7, the approximation

$$Q'_{crit} = \left(1 - \frac{1}{5\Lambda}\right) \frac{2}{K_{pl}\mathcal{L}}. \tag{7.50}$$

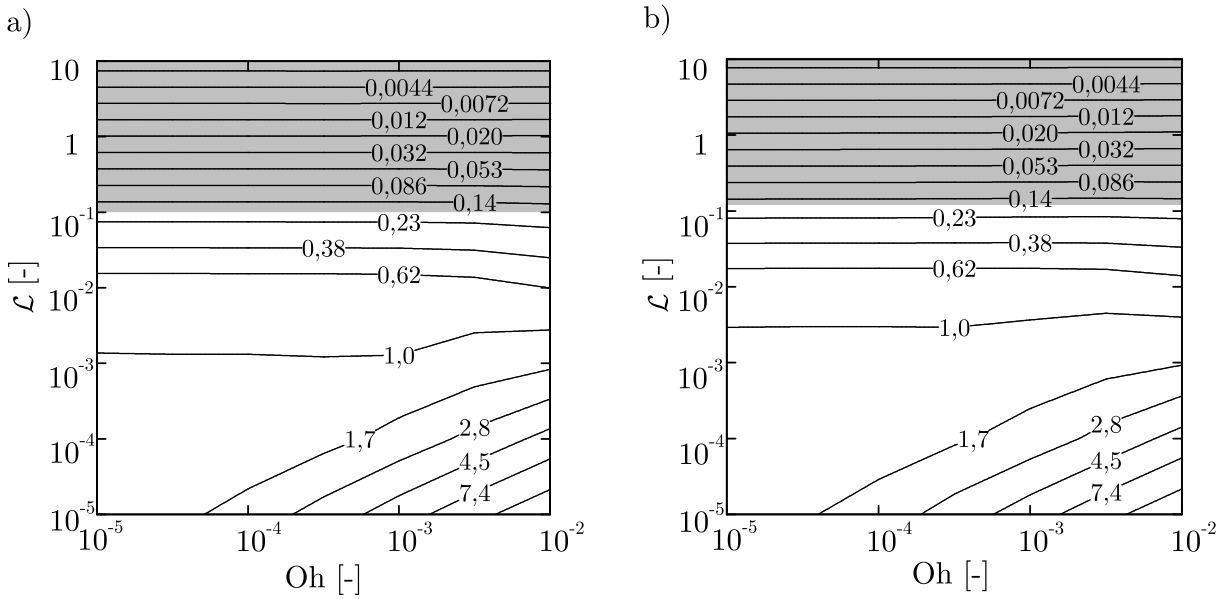

Figure 7.7: Numerically determined isolines of the critical flow rate as function of Oh and $\mathcal{L}$. (a) $\Lambda = 5$. (b) $\Lambda = 50$.

applies. The marginal influence of the aspect ratio, which the isolines shifts towards larger $\mathcal{L}$, is considered by the factor $1 - (5\Lambda)^{-1}$. For $\Lambda \to \infty$ it merges to

$$Q'_{crit} = \frac{2}{K_{pl}\mathcal{L}}. \tag{7.51}$$

This function may be also achieved by the integration of (7.41) within the limits $x' = 0$, $h'_0 = 0$ and $x' = 1$, $h'(x' = 1) = 1$ under neglecting of the convective term. It defines the flow rate of the classical Poiseuille flow between two parallel plates with capillary pressure gradient $\mathrm{d}p'/\mathrm{d}x' = 1$.

8 Appendix B: Mathematical Model for the Flow in a Groove (Confidential)

This appendix has been written to provide the referees with a more detailed description of the theoretical approach. The repetitions of section 2.4 are intended to make this appendix a comprehensive document in its own. Since some of the findings have not been published yet, the appendix is considered to be confidential and not a part of the SRD. In the course of this experiment some components of the theory may be improved, thus the appendix is subjected to change.

8.1 Mathematical Approach

In our theoretical approach we consider the flow through a capillary groove. The flow enters the groove via the inlet and leaves the groove at the outlet. The flow is sustained by an external pump at the outlet. The inlet is connected to a reservoir which provides the necessary liquid volume. For the analysis we follow the steady state approach introduced by Jaekle (1997) for the flow rate limitation in different capillary vanes. We assume a one-dimensional flow along the channel axis x characterized by the mean velocity v and the liquid pressure p (see Fig. 8.1). The origin of the system of coordinates is located in the center of the cross section at the channel inlet.

The basic equations to be solved are the momentum equation

$$\mathrm{d}p + \rho v \mathrm{d}v - \mathrm{d}w_f = 0 \tag{8.1}$$

and the continuity equation

$$\mathrm{d}(Av) = 0, \tag{8.2}$$

both given in differential form. The symbol A denotes the cross section of the flow path perpendicular to the longitudinal axis x. The term $\mathrm{d}w_f$ of Eq. (8.1) takes into account irreversible pressure losses of the flow due to friction. The hydrostatic pressure has not been considered due to vanishing body forces under microgravity conditions.

For the first term of Eq. (8.1) we need a relation between the liquid pressure and the position of the free surface z. The liquid pressure p is related to the curvature of the free

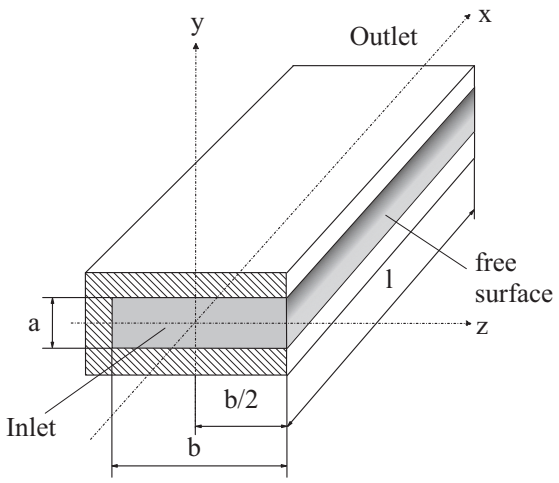

Figure 8.1: Schematic drawing of the flow through a groove with width b, gap distance a and length l.

surface and can be written with the GAUSS-LAPLACE equation

$$\frac{p - p_a}{\sigma} = -2H = -\left(\frac{1}{R_1} + \frac{1}{R_2}\right). \tag{8.3}$$

Here p_a is the ambient pressure and H is the mean curvature of the surface. R_1 and R_2 are the corresponding principal radii of curvature. Since the ambient pressure p_a is constant the pressure gradient becomes

$$\mathrm{d}p = -2\sigma \mathrm{d}H. \tag{8.4}$$

In general the mean curvature H of the surface is defined by

$$H(x,y) = \frac{1}{2}\frac{(1+z_x^2)\, z_{yy} - 2z_x z_y z_{xy} + (1+z_y^2) z_{xx}}{(1+z_x^2+z_y^2)^{3/2}} \tag{8.5}$$

(see Bronstein & Semendjajew, 1987) if the surface is given as $z = f(x,y)$. As shown in Fig. 8.2 z is the position of the surface defined by a function $z = f(x,y)$ with $x \in [0,l]$ and $y \in [-a/2, a/2]$. The indices in Eq. (8.5) denote the partial derivatives: $z_i = \partial z/\partial i$, $z_{ij} = \partial^2 z/\partial i \partial j$, with $i,j \in \{x,y\}$.

Analogous to the flow between two parallel plates (see Appendix A), Eq. (8.5) can be simplified by

$$h = 2H = \frac{1}{R_1} + \underbrace{\frac{\frac{\mathrm{d}^2 k}{\mathrm{d}x^2}}{\left[1 + \left(\frac{\mathrm{d}k}{\mathrm{d}x}\right)^2\right]^{3/2}}}_{= R_2^{-1}}. \tag{8.6}$$

Herein variable $k(x) = z(x, y=0)$ defines the position of the free surface in the plane $y = 0$. The terms on the right side define the portion of the surface curvature in lateral to the flow

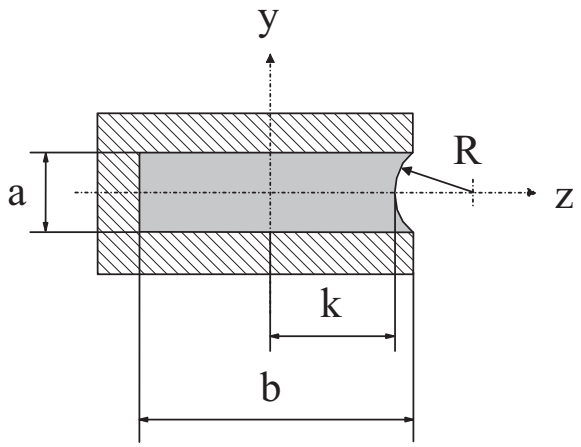

Figure 8.2: Cross section area of the groove.

and in flow direction, respectively. Thereby the principal radius of curvature R_1 is defined by

$$R_1(k) = \begin{cases} \dfrac{a^2}{4(b-2k)\Omega} + \dfrac{(b-2k)\Omega}{4} & \text{for} \quad k \geq \dfrac{b}{2} - \dfrac{a}{2\Omega} \\ \dfrac{a}{2} & \text{for} \quad k < \dfrac{b}{2} - \dfrac{a}{2\Omega} \end{cases}, \tag{8.7}$$

where the coefficient Ω is given by

$$\Omega = \sqrt{1 + \left(\frac{\mathrm{d}k}{\mathrm{d}x}\right)^2}. \tag{8.8}$$

In the first case of Eq. (8.7) the surface is assumed to be pinned at the edges of the groove. The radius of curvature may vary from $R = a/2 \ldots \infty$. The second case allows the free surfaces to move into the groove. The radius of curvature which appears inside the channel depends on the wetting property of the liquid on the solid. Since the investigated liquids are perfectly wetting the contact angle between the liquid and the solid is zero degree and the radius of curvature is half the plates distance $R = a/2$.

From the geometrical relations in Fig. 8.2, the cross section area may be determined by

$$A(k) = \begin{cases} ab - R^2 \arcsin\left(\dfrac{a}{2R}\right) + \dfrac{a}{2}\left(R - \dfrac{b}{2} + k\right) & \text{for} \quad k \geq \dfrac{b-a}{2} \\ \dfrac{1}{2}\left[ab + 2ka + \left(1 - \dfrac{\pi}{4}\right)a^2\right] & \text{for} \quad k < \dfrac{b-a}{2}. \end{cases} \tag{8.9}$$

Herein R is the radius of curvature in the cross section plane. It is defined by

$$R(k) = \begin{cases} \dfrac{a^2 + (b-2k)^2}{4(b-2k)} & \text{for} \quad k \geq \dfrac{b-a}{2} \\ \dfrac{a}{2} & \text{for} \quad k < \dfrac{b-a}{2}. \end{cases} \tag{8.10}$$

Assuming a constant flow rate through the channel,

$$Q = Av = const, \tag{8.11}$$

the second term of Eq. (8.1) can be rewritten as

$$\rho v \mathrm{d}v = -\rho \frac{Q^2}{A^3} \mathrm{d}A. \tag{8.12}$$

The loss of energy per unit volume $\mathrm{d}w_f$ due to friction consists of two parts, the laminar viscous pressure loss and the additional entrance pressure loss which is a result of the change of the velocity profile from the entrance profile to the parabolic velocity distribution (Poiseuille flow). The laminar pressure loss for the groove is obtained from an analytical solution of the Navier-Stokes equation

$$\frac{\mathrm{dp_l}}{\mathrm{d}x} = -\frac{K_{pf}}{D_h \mathrm{Re}_h} \frac{\rho}{2} v^2, \tag{8.13}$$

with the factor $K_{pf} = K_{pf}(\Lambda)$ (interpolation of the values given by White (1991), Table 6.4), the aspect ratio $\Lambda = b/a$, the hydraulic diameter $D_h = 4b/(2\Lambda + a)$ and the Reynolds number

$$\mathrm{Re}_h = \frac{D_h v}{\nu} \ . \tag{8.14}$$

The additional pressure loss due to the transformation of the entrance velocity profile to the laminar parabolic velocity distribution has to be considered for the comparison of the mathematical model with experimental results. An analytical relation proposed by Sparrow & Lin (1964) might be applied to the groove geometry even though it was derived for a tube and a parallel plate channel. The application of this relation requires the knowledge of the velocity distribution and the pressure gradient in flow direction at the inlet of the capillary channel. This can be achieved only by numerical calculations for the respective geometry of the channel entrance section (nozzle between the reservoir and the inlet). For the calculation of the parameter space to be investigated in this experiment this contribution to the pressure drop has been omitted. The critical volume fluxes derived by this method are slightly higher than the expected ones and thus give the upper limit for the flow velocities required for the experimental setup.

The total irreversible pressure loss dw_f is determined by

$$\mathrm{d}w_f = -\frac{\rho}{2} \frac{K_{pf}}{D_h \mathrm{Re}_h} \frac{Q^2}{A^2} \mathrm{d}x \tag{8.15}$$

with $K_{pf} = K_{pf}(\Lambda)$.

Substituting Eq. (8.1) by Eq. (8.4), Eq. (8.12) and Eq. (8.15) the final differential equation

$$\frac{\sigma}{\rho} \frac{\mathrm{d}h}{\mathrm{d}x} + \frac{Q^2}{A^3} \frac{\mathrm{d}A}{\mathrm{d}x} - \frac{1}{2} \frac{K_{pf}}{D_h \mathrm{Re}_h} \frac{Q^2}{A^2} = 0 \tag{8.16}$$

for the change of pressure along the channel axis is obtained. Note that $2H = h$. The boundary conditions are

$$k(x \ = \ 0) = \frac{b}{2}$$

$$\begin{aligned} k(x &= l) = \frac{b}{2} \\ h(x &= 0) = h_0. \end{aligned}$$

As discussed in section 7.6, the boundary condition h_0 depends on the flow path stream upwards the channel inlet. For its determination three-dimensional computations with commercial software are required.

8.2 Non-dimensional Equation

The x-axis is scaled by l, all lengths and areas are scaled by $D_h/4$ and A_0, respectively. The liquid velocity is scaled by the characteristic velocity $v_0 = \sqrt{4\sigma/\rho D_h}$ (derived from Dreyer Dreyer *et al.* (1994)). This yields the following dimensionless properties

$$x' = \frac{x}{l};\ k' = \frac{4k}{D_h};\ l' = \frac{4l}{D_h};\ R' = \frac{4R}{D_h};\ h' = \frac{D_h}{4}h;\quad A' = \frac{A}{ab}; \tag{8.17}$$

$$v' = \frac{v}{v_0};\ Q' = \frac{Q}{v_0 A_0} = \frac{D_h Oh}{2\nu A_0}Q; \mathrm{Oh} = \sqrt{\frac{\rho\nu^2}{\sigma D_h}}; \Lambda = \frac{b}{a}\ . \tag{8.18}$$

The dimensionless form of Eq. (8.16) reads

$$\frac{dh'}{dx'} + \frac{Q'^2}{2A'^3}\frac{dA'}{dx'} - \frac{K_{pf}}{32}\frac{Q'\mathrm{Oh}l}{A'} = 0, \tag{8.19}$$

and from Eq. (8.6) the form

$$\Gamma^2 \frac{\mathrm{d}^2 k'}{\mathrm{d}x'^2} + \left(\frac{1}{R_1'} - h'\right)\left[1 + \Gamma^2\left(\frac{\mathrm{d}k'}{\mathrm{d}x'}\right)^2\right]^{3/2} = 0 \tag{8.20}$$

with $\Gamma = D_h/4l$ is achieved,

Eqs. (8.19) and (8.20) need to be integrated numerically with the boundary conditions which are the (i) position of the surface at the inlet and outlet of the channel and (ii) the surface curvature at the channel inlet

$$\begin{aligned} k'(x' &= 0) = k'(x' = l) = \frac{2\Lambda + 1}{2} \\ h'(x' &= 0) = h_0'. \end{aligned}$$

The numerical solution yields the position of the liquid surface

$$k' = f(\Lambda, \mathrm{Oh}, l', Q').$$

For each set of Λ, Oh, and l' several computations with different Q' have to be performed. To identify the critical volume flux we assume that the maximum volume flux is reached when the numerical integration does not converge for $Q' > Q'_{crit}$. As the maximum theoretical volume flux Q'_{crit} we define the maximum flow rate Q' leading to the convergence of the numerical algorithm.

9 Appendix C: Mathematical Model for the Critical Velocity due to Choking

In Section 7 Eq. (7.41) and Eq. (7.42) were set up to calculate the pressure change in flow direction. Theses equations were solved numerically for fixed flow rate Q. To find the limitation of flow rate, several calculations at different flow rate Q have been performed. The maximum stable flow rate Q_{crit} is exceeded if the integration of Eq. (7.34) together with Eq. (7.35) diverges and no solution is obtained.

As mentioned in Section 2.4.1 we expect that the limitation of flow rate occurs due to choking. The effect of choking is known from compressible gas flow and open channel flow under normal gravity. Choking occurs if the flow locally runs at the characteristic wave speed at which physical information propagates in the flow. The theory of choking predicts a limit of mass flow if the ratio of the fluid velocity and the characteristic signal speed becomes unity. In compressible gas duct flows the limiting speed is defined by the speed of sound. The characteristic number is the MACH number Ma, and the maximal flow passes through the duct when Ma = 1 is reached. In open channel flow the speed of shallow water waves defines the limiting velocity (FROUDE number problem). The following subsection gives a brief introduction to the mechanism of choking. Since this effect is mostly discussed in gas dynamics we summarize the main findings obtained from compressible gas flow. As it turns out later, most relations can be transferred to open channel flow, since there is a close analogy between both flow types based on the basic equations. As a consequence, the characteristic wave speed in compressible gases and open channels, which has a key role in this phenomena, can be derived from a single universal form.

9.1 Introduction

Choking is characterized by the fact that the mass flow per unit area w of an arbitrary flow has a maximum. In case of a compressible flow the mass flow is related to the MACH number

$$\mathrm{Ma} = \frac{v_g}{c_s} \tag{9.1}$$

and in case of isentropic flow the maximum flow rate per unit area w is reached when the local MACH number becomes unity Shapiro (1953). In other words, choking occurs if the

gas velocity v_g locally reaches the speed of sound c_s.

For a frictionless flow along a streamline this limitation can be derived analytically ((see e.g. Landau & Lifschitz, 1991)). From the momentum equation

$$\mathrm{d}p = -\rho v dv \tag{9.2}$$

and the definition of the sound speed

$$c_s^2 = \left.\frac{\mathrm{d}p}{d\rho}\right|_{S=const} \tag{9.3}$$

the relation

$$\frac{\mathrm{d}\rho}{\mathrm{d}v} = -\frac{\rho v}{c_s^2}$$

is obtained. ρ is the density, p the pressure and S the entropy, which is kept constant. Applying the differential form of the flow rate per unit area $\mathrm{d}w = \mathrm{d}(\rho v) = \rho \mathrm{d}v + v\mathrm{d}\rho$ we find:

$$\frac{\mathrm{d}w}{\mathrm{d}v} = \rho(1 - \mathrm{Ma}^2). \tag{9.4}$$

As long as the flow is subsonic the mass flow per unit area w increases with increasing velocity ($\mathrm{d}w/\mathrm{d}v > 0$). For supersonic flow the mass flow decreases with increasing flow velocity v ($\mathrm{d}w/\mathrm{d}v < 0$). At $\mathrm{Ma} = 1$ the flow runs at its maximum flow rate.

Eq. (9.4) has fundamental consequences for duct flows. First we consider a frictionless flow through a smooth constriction with changing cross section area A. With Eq. (9.2), Eq. (9.3) and the equation of continuity in the differential form

$$\frac{\mathrm{d}\rho}{\rho} + \frac{\mathrm{d}v}{v} + \frac{\mathrm{d}A}{A} = 0$$

the equation

$$\frac{\mathrm{d}v}{v} = -\frac{\mathrm{d}A}{A}\frac{1}{1 - \mathrm{Ma}^2} = -\frac{\mathrm{d}p}{\rho v^2} \tag{9.5}$$

is derived, which relates the relative change of the flow properties v and p to the change of cross section $\mathrm{d}A/A$ forced by the geometry of the duct. Obviously the change of properties are of opposite sign for subsonic or supersonic flow. The following four combinations of area change and Mach number exist:

Duct geometry	Subsonic flow			Supersonic flow		
$\mathrm{d}A/A > 0$	$\mathrm{d}v/v$	$<$	0	$\mathrm{d}v/v$	$>$	0
	$\mathrm{d}p/\rho v^2$	$>$	0	$\mathrm{d}p/\rho v^2$	$<$	0
$\mathrm{d}A/A < 0$	$\mathrm{d}v/v$	$>$	0	$\mathrm{d}v/v$	$<$	0
	$\mathrm{d}p/\rho v^2$	$<$	0	$\mathrm{d}p/\rho v^2$	$>$	0

When a subsonic flow passes through a duct with increasing cross section the flow velocity decreases and the pressure increases. But in case of supersonic flow the flow velocity decreases leading to an increase of pressure. The opposite behavior occurs for an area decrease, which speeds up a subsonic flow and slows down a supersonic flow. At the sonic point Ma = 1 a singularity occurs in Eq. (9.5) caused by the expression $1 - \mathrm{Ma}^2$ in the denominator. Since infinite acceleration is physically impossible the change in cross section $\mathrm{d}A/A$ has to vanish at the sonic point (White, 1994). $\mathrm{d}A/A = 0$ is related to the minimal cross section and maximal cross section area of the duct. But it can be shown that critical flow conditions only occur in minimal cross section like at the outlet of a nozzle or the throat of a converging / diverging nozzle.

The mechanisms of choking can be discussed for a flow through a nozzle. We consider a nozzle with constant entrance pressure p_0 which discharges into a region where the back pressure p_b is controllable. At a constant pressure ratio $p_b/p_0 < 1$ a steady subsonic flow at a certain exit MACH number appears. If the pressure ratio is increased the flow accelerates associated with an increased ratio $\mathrm{d}v/v$. As Eq. (9.5) indicates increased ratios of $\mathrm{d}v/v$ lead to higher values of the MACH number since the local ratio $\mathrm{d}A/A$ does not change. At a certain pressure ratio p_b^*/p_0 the exit MACH number is unity. A further increase of the MACH number is impossible since Eq. (9.5) requires a change of sign of $\mathrm{d}A/A$. The pressure drop $\Delta p = p_0 - p_b^*$ along the nozzle is maximal at this state, just as the mass flow per unit area w given by Eq. (9.4). Even if the back pressure p_b is reduced strongly below the value p_b^* no additional pressure drop and mass flux are achieved in the nozzle. This effect, that the mass flux becomes maximal if MACH number is unity, is called choking.

To understand the fundamental significance of the MACH number the problem strictly has to be considered as time-dependent. Eq. (9.5) is derived from steady state assumptions which are valid after a certain relaxation time of the flow. In practice the change of the back pressure does not change the pressure conditions along the duct instantaneously. Each change of pressure p_b induces a density wave traveling upstream, which reaches the duct entrance with a time delay. The velocity v_w of the traveling wave related to the flow speed v is defined as

$$v_w = v - c_s. \tag{9.6}$$

Eq. (9.6) shows that the wave speed v_w vanishes if the velocity of the flow reaches the speed of sound. This is the case if the MACH number is unity at the nozzle exit. Since the wave speed tends down to zero in the smallest cross section of the channel, pressure reduction will not reach the inlet section of the nozzle. For that reason the pressure drop along the nozzle remains unchanged.

In the case discussed above the nozzle the flow was assumed to be frictionless and choking occurred due to the change of cross section. But gas flow in a pipe of constant cross section also can be choked. The reason for that is the friction which causes the pressure drop and

accelerates the gas. To explain the effect we choose the following three working relations Shapiro (1953)for adiabatic flow

$$\frac{\mathrm{d}p}{p} = -\frac{\kappa \mathrm{Ma}^2[1+(\kappa-1)\mathrm{Ma}^2]}{2(1-\mathrm{Ma}^2)}\frac{4f}{D_h}\mathrm{d}x \tag{9.7}$$

$$\frac{\mathrm{d}\rho}{\rho} = -\frac{\kappa \mathrm{Ma}^2}{2(1-\mathrm{Ma}^2)}\frac{4f}{D_h}\mathrm{d}x = -\frac{\mathrm{d}v}{v} \tag{9.8}$$

$$\frac{\mathrm{dMa}^2}{\mathrm{Ma}^2} = -\frac{\kappa \mathrm{Ma}^2(1+\frac{\kappa-1}{2}\mathrm{Ma}^2)}{1-\mathrm{Ma}^2}\frac{4f}{D_h}\mathrm{d}x \tag{9.9}$$

where f is the friction factor defined as

$$f = \frac{2\tau_w}{\rho v^2}. \tag{9.10}$$

Eq. (9.7) to Eq. (9.9) depend on wether the MACH number is larger or smaller than unity, since the term $(1-\mathrm{Ma}^2)$ appears in the denominator of each of these equations. Eq. (9.9) shows that with increasing duct length the MACH number tends down toward unity.

9.2 Characteristic Velocity

The liquid flow in the capillary channel is treated as longitudinal motion although transversal velocity components occur due to the change of cross section. This assumption is valid since the liquid acceleration in z-direction is sufficiently smaller than the acceleration in the main direction. For that reason lateral pressure gradients can be neglected and the motion of liquid is essentially caused by longitudinal gradients.

The characteristic wave speed at which physical information in the flow propagates is of the same flow type. The basic assumption in the theory of longitudinal wave motion is that the variation of the driving pressure

$$p^* = p - p_0.$$

over the cross section is negligible. p is pressure at position x when the wave passes and p_0 is the undisturbed pressure of the fluid in the channel[1]. If transversal components of the driving pressure p^* are negligible the wave motion is forced by longitudinal gradients of p^*.

For the derivation of the wave speed, the channel is supposed to be uniform and the fluid at rest. With this the flow through cross section area A does not depend explicitly on the x-axis, and it related only to the driving pressure

$$A = A(p^*). \tag{9.11}$$

[1]Note that in the following all variables are dimensionless. To simplify matters the index ' is omitted.

In order to obtain a universal formulation including waves in gases, compressibility is included. If the entropy S is kept constant the density is related to the driving pressure

$$\rho = \rho(p^*). \tag{9.12}$$

The equations of the one-dimensional motion to be solved are the momentum equation

$$\rho \frac{\partial v}{\partial t} = -\frac{\partial p}{\partial x} - \rho v \frac{\partial v}{\partial x} \tag{9.13}$$

and the equation of continuity,

$$\frac{\partial(\rho A)}{\partial t} = -\frac{\partial(\rho A v)}{\partial x}. \tag{9.14}$$

Using the following approach of linearization

$$p = p_0 + p^*,\ v = v^*,\ A = A_0 + A^*,\ \rho = \rho_0 + \rho^* \tag{9.15}$$

Eq. (9.13) and Eq.(9.14) are linearized. The basic idea of Eq. (9.15) is that driving pressure p^* is small compared to the fluid pressure at rest p_0. In response to p^* all other physical quantities will change within the same order of magnitude. Thus the solution for each quantity can be taken as a superposition of the fundamental solution indicated by index zero and a small disturbance indicated by the asterisk in Eq. (9.15). Applying the linearization, Eq. (9.13) and Eq. (9.14) read

$$\rho_0 \frac{\partial v^*}{\partial t} = -\frac{\partial p^*}{\partial x} \tag{9.16}$$

$$\frac{\partial}{\partial t}\left[\rho_0 A^* + \rho^* A_0\right] = -\rho_0 A_0 \frac{\partial v^*}{\partial x}. \tag{9.17}$$

Differentiating with respect to x and t both equations can be combined

$$\frac{1}{\rho_0 A_0}\frac{\partial^2}{\partial t^2}\left[\rho_0 A^* + \rho^* A_0\right] = \frac{1}{\rho_0}\frac{\partial^2 p^*}{\partial x^2}, \tag{9.18}$$

which already has the structure of a wave equation. To introduce the pressure p^* in the left hand side of Eq. (9.18) A^* and ρ^* are expanded in Taylor series of first order about $p^* = 0$. Since the partial derivative with respect to t does not act on the Taylor series Eq. (9.18) can be written as

$$\frac{1}{A_0}\left[\rho_0 \left.\frac{\partial A^*}{\partial p^*}\right|_{p^*=0} + A_0 \left.\frac{\partial \rho^*}{\partial p^*}\right|_{p^*=0}\right]\frac{\partial^2 p^*}{\partial t^2} = \frac{\partial^2 p^*}{\partial x^2} \tag{9.19}$$

or

$$\frac{\partial^2 p^*}{\partial t^2} = A_0 \left.\frac{\partial p}{\partial(\rho A)}\right|_{p^*=0}\frac{\partial^2 p^*}{\partial x^2}. \tag{9.20}$$

Eq. (9.20) has the structure of the well know linear wave equation

$$\frac{\partial^2 p^*}{\partial t^2} = v_l^2 \frac{\partial^2 p^*}{\partial x^2} \tag{9.21}$$

in which the factor v_l^2 with

$$c = \sqrt{A_0 \left.\frac{dp}{d(\rho A)}\right|_{p^*=0}} \tag{9.22}$$

is the wave speed of longitudinal waves in flows in which the density and the cross section are related to the fluid pressure Lighthill (1978). Examples are compressible constant-area duct flows, free surface flows in channel with uniform walls or flows in flexible tubes.

For the physical interpretation Eq. (9.22) is rewritten as:

$$\frac{1}{\rho_0 v_l^2} = \left[\frac{1}{\rho}\frac{\mathrm{d}\rho}{\mathrm{d}p}\right]_{p^*=0} + \left[\frac{1}{A}\frac{\mathrm{d}A}{\mathrm{d}p}\right]_{p^*=0} = K + D \tag{9.23}$$

If the second term on the right hand side is not considered, Eq. (9.23) yields the definition of the compressibility K of the gas. Obviously the relative change of cross section per unit change of pressure, which is the second term, acts like the compressibility. It is called the distensibility D and Eq. (9.23) can be interpreted as the effective compressibility of compressible fluid flow in a channel with variable cross section. This is one indication for the above mentioned close analogy between compressible gas flow and open channel flow. Both the motion of longitudinal waves in compressible gases and in open channel are given by the solution of the same wave equation Eq. (9.21). As a consequence the wave speeds in both different flow types are calculated from Eq. (9.22), and finally Eq. (9.23) shows that the variable cross section A in open channel flows acts like the density ρ in compressible duct flows and vice versa. With this correlation many effects known from gas dynamics can be transferred qualitatively to open channel flows just by replacing ρ by A.

In the following, two special cases of Eq. (9.22) are derived where the cross section and density are kept constant respectively. The first case considers a gas flow at constant cross section area $A = A_0$, and Eq. (9.22) reduces to the well known speed of sound

$$v_s = \left.\sqrt{\frac{\mathrm{d}p}{\mathrm{d}\rho}}\right|_{p^*=0,\ S=const} . \tag{9.24}$$

Scaling the velocity of the gas v_g by Eq. (9.24) the definition of the MACH number Eq. (9.1) is obtained. Note that the constancy of entropy S was assumed in Eq. (9.12).

The second case considers a liquid flow through an open channel at constant density $\rho = \rho_0$. Here the cross section A is variable and the wave speed is obtained from

$$v_{ch} = \left.\sqrt{\frac{A_0}{\rho_0}\frac{\mathrm{d}p}{\mathrm{d}A}}\right|_{p^*=0} . \tag{9.25}$$

If a flow under gravity is considered, the driving pressure p is given by the hydrostatic pressure $p = \rho_0 g h$. h is the fill level of an uniform rectangular channel of breadth b. With

hydrostatic pressure and the cross section $A = bh$ Eq. (9.25) yields

$$v_{sw} = \sqrt{gh} \tag{9.26}$$

which is the wave speed of water waves in the shallow water approximation. Scaling the liquid flow velocity v_f by Eq. (9.26) the definition of the FROUDE number

$$\mathrm{Fr} = \frac{v_f}{c_{sw}}$$

is obtained. If capillary forces are dominant, the pressure in Eq. (9.25) has to be replaced by the capillary pressure defined by Eq. (7.6) which yields

$$v_c = \sqrt{\frac{A}{\rho}\frac{\mathrm{d}h}{\mathrm{d}A}}, \tag{9.27}$$

the longitudinal wave speed in an open capillary channel. Concerning the application of this equation a problem occurs since the term $\mathrm{d}h/\mathrm{d}A$ is not determined analytically. For the first approach we solve this problem by neglecting the surface curvature in flow direction x. Applying Eq. (7.13) to Eq. (9.27) we obtain

$$v_c = \sqrt{\frac{\sigma}{\rho}\frac{A}{R^2}\frac{\mathrm{d}R}{\mathrm{d}A}}. \tag{9.28}$$

Scaling the mean liquid velocity $v = Q/A$ by Eq. (9.28) the dimensionless speed index

$$\mathrm{S} = Q/(Av_c) = v/v_c \tag{9.29}$$

is defined.

In the following, a set differential equations is derived to show the behavior of the capillary free surface channel flow. Using the definition of the speed number Eq. (7.41) can be rewritten and the following formulas

$$\mathrm{d}h = \frac{K_{pg}\mathcal{L}Q}{2A(1-\mathrm{S}^2)}\mathrm{d}x = -\mathrm{d}p, \tag{9.30}$$

$$\frac{\mathrm{d}A}{A} = -\frac{\mathrm{S}^2 A K_{pg}\mathcal{L}}{2Q(1-\mathrm{S}^2)}\mathrm{d}x = -\frac{\mathrm{d}v}{v}, \tag{9.31}$$

$$\frac{\mathrm{dS}^2}{\mathrm{S}^2} = \frac{(2+M)\mathrm{S}^2 A K_{pg}\mathcal{L}}{2Q(1-\mathrm{S}^2)}\mathrm{d}x, \tag{9.32}$$

with

$$M = 1 + A\frac{\mathrm{d}^2h/\mathrm{d}A^2}{\mathrm{d}h/\mathrm{d}A} \tag{9.33}$$

are obtained where as $K_{pg} = K_{pl} + 16K_{pe}$. Eq. (9.30) through Eq. (9.32) defined the gradient of properties p, A, v and S along the flow path. The sign of the gradient depends

on whether the speed index is larger or smaller than unity, since the term $(1-S^2)$ appears in the denominator. Note that the structure of the equations is similar to Eq. 9.7 through Eq. 9.9. From the model assumptions it is known that the cross section A and the pressure p both decrease along the channel axis while the liquid accelerates. Eq. (9.30) and Eq. (9.31) state that the investigated flow must be subcritical ($S < 1$). Accordingly the speed index increases in flow direction as given by Eq. (9.32), leading to the maximum speed index at the channel outlet. With increasing flow rate in the channel, the outlet speed index increases. For the supercritical flow ($S > 1$) the opposite behavior occurs and p, A and S decreases along the flow path. On each flow branch $S = 1$ defines the flow limit, since for this value a singularity occurs in Eq. (9.30) through Eq. (9.32). At that state choking is present, and the flow rate is maximum. A flow rate above this critical value leads to collapse of the liquid surface, and the time dependent form of Eq. (7.41) must be solved to predict the flow.

10 Appendix D: CCF system specification

CAPILLARY CHANNEL FLOW

Titel:
Title: CCF EU#1 System Specification

Dokumenten Typ: Document Type:	Specification	**Konfigurations-Nr.:** Configuration Item No.:	Issue 2
Referenz- Nr.: Reference No.:	CCF-SP-AST-1001	**Klassifikations-Nr.:** Classification No.:	
Lieferbedingungs-Nr.: DRL/DRD No.:		**Freigabe Nr.:** Release No.:	
Gruppierung (Dok.): Group (Doc.-related):		**Gruppierung (Version):** Group (Version-related):	
Thema: Subject:			
Kurzbeschreibung: Abstract:			

Autor: Prepared by:	Dr. Jürgen Held Author	**Org. Einh.:** Organ. Unit:	TO62	**Unternehmen:** Company:	Astrium ST
Geprüft: Agreed by:	Bernd Hummelsberger System Engineering	**Org. Einh.:** Organ. Unit:	TO62	**Unternehmen:** Company:	Astrium ST
Genehmigt: Approved by:	Gabriele Danzer Product Assurance	**Org. Einh.:** Organ. Unit:	TOQ5	**Unternehmen:** Company:	Astrium ST
Genehmigt: Approved by:	Bernd Hummelsberger Configuration Control	**Org. Einh.:** Organ. Unit:	TO62	**Unternehmen:** Company:	Astrium ST
Genehmigt: Approved by:	Bernd Hummelsberger Project Manager	**Org. Einh.:** Organ. Unit:	TO62	**Unternehmen:** Company:	Astrium ST

Copyright by Astrium ST - All Rights Reserved

(This Page Intentionally Blank)

Copyright by Astrium ST - All Rights Reserved

Daten/Dokument-Änderungsnachweis/*Data/Document Change Record (DCR)*

Ausgabe *Issue*	**Datum** *Date*	**Betroffener Abschnitt/Paragraph/Seite** *Affected Section/Paragraph/Page*	**Änderungsgrund/Kurze Änderungsbeschreibung** *Reason for Change/Brief Description of Change*
1	2006-12-11	all	

Copyright by Astrium ST - All Rights Reserved

Interner Verteiler/*Internal Distribution List*

Name *Name*	**Abteilung** *Organisation*	**Anzahl d. Kopien** *Number of Copies*	**Zustimmung** *Approval*	**Genehmigung** *Acceptance*	**Information** *Information*
Bernd Hummelsberger	TO62	1 (electronic)			
Roman Gmünder	TO62	1 (electronic)			
Gabriele Danzer	TOQ5	1 (electronic)			

Externer Verteiler/*External Distribution List*

Name *Name*	**Abteilung** *Organisation*	**Anzahl d. Kopien** *Number of Copies*	**Zustimmung** *Approval*	**Genehmigung** *Acceptance*	**Information** *Information*
Michael Dreyer	ZARM	1 (electronic)			
Mark Weislogel	CECS	1 (electronic)			
Uwe Rosendahl	ZARM	1 (electronic)			

Copyright by Astrium ST - All Rights Reserved

Table of Contents

8.4 Verification Matrix

1. Introduction

2 *3829 73*

Verification Method: Description

1.1. Purpose

2 *3829 217*

Verification Method: Description

The Critical Velocity in Open Capillary Cannel Flows Experiment Facility (CCF) will provide the capability of operating different open capillary channel geometries at variable fluid flow rates on board the International Space Station (ISS) inside the Microgravity Science Glovebox (MSG) Working Volume (WV).

The project was launched in the frame of DLR-NASA compensation agreement. The specification is written in course of the CCF phase B and updated during Phase DeltaB.

1.2. Scope

2 *3829 218*

Verification Method: Description

This specification establishes the requirements for the function, properties, performance, design, development, testing, verification and preparation for delivery of the CCF assembly. This specification is the baseline for the CCF design.

1.3. General Explanations

2 *3829 219*

Verification Method: Description

A numbering system has been introduced in order to improve the identification and tracking of each individual requirement.

Explanatory or descriptive parts of the specification are marked by
- the verification method "Not To Be Tracked" or
- the word "Comment:" at the beginning.

The Verification Methods for the requirements are listed below the headers. The Verification Method(s) for an individual requirement is marked within this document below the requirement header.

The science requirements are derived from AD01, AD11, RD01 and RD02. The logic behind this source documents is as following: AD11 overwrites AD01 and RD02 overwrites RD01 in case that to the same requirement different definitions or values are provided. In case of later agreements, fixed in minutes of meeting, such MoMs overwrite AD11.

1.4. Abbrevations

2 3829 74

Verification Method: Description

C&DH Command & Data Handling
CCF Cpillary Channel Flow
CDHS Command and Data Handling System
COTS Commercial Off-The-Shelf
CT Compensation Tube
EADS European Aeronautic Defense Space Company
EM Engineering Model
ESS Electronic SubSystem
EU Electronics Unit
FM Flight Model
FMC Front Mounted Camera
FMS Fluid Management System
FPC Flow Preparation Chamber
HSHRC High Speed High Resolution Camera
I/F Interface
ISS International Space Station
KHB KSC Handbook
LDA Laser Doppler Anemometry
MOM MinutesOf Meeting
MSFC Marshall Space Flight Center
MSG Microgravity Science Glovebox
MTR Mid Term Review
NASA National Aeronautics and Space Administration
NSTS National Space Transportation System
OB Optical Bench
ODU Optical Diagnostic Unit
PA Product Assurance
PFE Portable Fire Extinguisher
PI Principal Investigator
PLS Parallel Light Source
PSC Phase Separation chamber
QD Quick Disconnect
RD Reference Document
S/W Software
SAMS Space Acceleration Measurement System
SPLC Standard Payload Computer
TC Test Channel
TCU Thermal Control Unit
TO Training Objective
TU Test Unit
WV Work Volume
ZARM Zentrum für Angewandte Raumfahrttechnologie und Mikrogravitation

2. Applicable and Reference Documents

2 3829 75

Verification Method: Description

2.1. Applicable Documents 2 *3829 76*

Verification Method: Description

AD1.: Science Requirement Document for the proposal Critical Velocities in Open Capillary Channel Flows (CCF), Dreyer et al; 2002-101-11
AD2.: Microgravity Science Glovebox (MSG) Investigation Interface requirements document, MSFC-RQMT-2888, rev. F, 2006-06-08
AD3.: MSG Capabilities Manual,MSFC-HDBK 3051, 2002-09-01
AD4.: Protective Finishes for Space Vehicles Structures, MSFC-SPEC-250, Rev. A, 1977-10-01
AD5.: Design Criteria for Controlling Stress Corrosion Cracking, MSFC-SPEC-522, Rev. B, 1987-07-01
AD6.: Interface Control Document MSG Data Handling System, MSG-ORIGIN-IC-0001
AD7.: Safety Policy and Requirements For Payloads Using the Space Transportation System, NSTS1700.7B, 1989-01-01, NSTS 1700.7_1_B_ ISS Addendum, 01.12.1995
AD8.: Interpretations of NSTS/ISS Payload Safety Requirements, NSTS 18798, Rev. 1B, 1997-09-01
AD9.: Payload Safety Review and Data Submittal Requirements, NSTS 13830, Rev. C, 1998-07-01
AD10.: Product Assurance & Safety Requirements For CCF, CCF-RD-QP-DLR-169/N, 2004-06-18
AD11.: MOM requirements clarification, CCF-MN-EADS-1002, 2004-11-08
AD12.: MOM requirements clarification, CCF-MN-EADS-1003, 2004-11-08
AD13.: MOM progress meeting 1, CCF-MN-EADS-1004, 2004-12-15
AD14.: MOM MTR / System Requirements Review, CCF-MN-EADS-1005, 2005-01-26
AD15.: CCF work package ZARM + follow on clarifications, CCF-EM-ZARM-1010, 2005-03-02, CCF-EM-EADS-1009, 2005-03-08, CCF-EM-EADS-1011, 2005-03-09

2.2. Reference Documents 2 *3829 77*

Verification Method: Description

RD1: CCF: Critical Velocities in Open Capillary Channel Flows (CCF); Phase A Report, Baumbach et al., 2003-03-31
RD2: Critical Velocities in Open Capillary Channel Flows (CCF); Phase B0 Report, Rosendahl et al, 2004-07-21

3. SYSTEM Definition 2 *3829 79*

Verification Method: Description

3.1. Physical Description 2 *3829 80*

Verification Method: Description

The CCF assembly provides the possibility to investigate the critical velocity in open capillary channel flows for different channel shapes and channel geometry parameters as well as for different mass flow rates under low / zero g environment. The investigation will be performed by flow parameter measurement, flow video observation and video data processing.

The CCF assembly consist of the following main components:
- The Experiment Unit (EU) which contains
  - the Fluid Management System (FMS),
  - the Thermal Control Unit (TCU) and
  - the Test Unit (TU).
    - the Test Channel (TC),
    - the Compensation Tube (CT)

- The Optical Diagnostic Unit (ODU) which contains
  - the Optical Bench OB,
  - the High Speed, High Resolution video camera (HSHRC) and
  - the Telecentric Objective,
  - the Parallel Light Source (PLS)

- The Electrical Subsystem (ESS) which contains
  - the Command and Data Handling System (C&DHS) including the functions of the board computer and
  - the image processing, Soft Ware (S/W) and
  - the Electrical Power Supply
- In addition parts of the MSG provided Video System is used.

3.2. Mission Profile 2 *3829 81*

Verification Method: Description

a) The CCF facility will be launched once with the space shuttle.
b) The CCF shall be operated inside the MSG WV.

4 Functional Science Requirements 2 *3829 847*

Verification Method: Description

Comment: The test channel (TC) is that part of the CCF assembly which will be observed via video camera(s) to detect the resulting contour line of the fluid free surface(s) for the different test channel shapes and geometries as well as for the different flow parameters, Figure 1. The test channels have different shapes like parallel plate, groove channel, wedge, gapped wedge, and tilted plate. Each shape may have different geometry parameters, like (e.g. for TC shape: parallel plate) length l, width b, and height a.

4.1. Test Channel Types 2 *3829 88*

Verification Method: Description

4.1.1	**Test Channel Types: Parallel Plate**	2	*3829 89*

Verification Method: Description

It shall be possible to investigate test channel shapes of Parallel Plates

4.1.2	**Test Channel Types: Groove Channel**	2	*3829 90*

Verification Method: Description

It shall be possible to investigate test channel shapes of Groove Channel.

4.1.3	**Test Channel Types: Wedge Channel**	2	*3829 845*

Verification Method: Description

Experiment Unit 2 shall include the possibility to investigate test channel shapes of wedge, gapped wedge, and tilted plates

4.1.4	**Test Channel Types: Exchange**	2	*3829 510*

Verification Method: Inspection

The Test channel (TC) exchange shall be realised on orbit by complete Experiment Unit exchange.

4.2	**Test Channel Shape**	2	*3829 93*

Verification Method: Description

4.2.1	**Test Channel Shape: Parallel Plate Geometry (Experiment Unit 1)**	2	*3829 94*

Verification Method: Inspection

It shall be possible to investigate different test channel geometry parameter (l, b, a) of the TC Shape Parallel Plate.
For test channel shape and parameter definition see figure 1.

4.2.1.1	**Test Channel Shape: Parallel Plate Geometry: Parameter l**	2	*3829 95*

Verification Method: Test

The geometry parameter l shall be 0.0 mm < l <= 48mm, tolerance +/- 0.05mm

Comment: This means that the parameter l can be changed (on orbit) within this range thanks to the use of slide bars.

4.2.1.2 **Test Channel Shape: Parallel Plate Geometry: Parameter l** 2 *3829 509*

Verification Method: Test

The geometry parameter l shall be adjustable independently for each open side.

Comment: This feature allows to investigate parallel channel geometries as well as groove channel geometries.

4.2.1.3 **Test Channel Shape: Parallel Plate Geometry: Parameter b** 2 *3829 826*

Verification Method: Test

The test channel of Experiment Unit #1 shall have a geometry parameter b = 25mm, +/- 0.05mm.

4.2.1.4 **Test Channel Shape: Parallel Plate Geometry: Parameter a** 2 *3829 827*

Verification Method: Test

The test channel of Experiment Unit #1 shall have a geometry parameter a = 5 mm, +/-0.05mm.

4.2.1.5 **Test Channel Shape: Parallel Plate Geometry: Sharp Edges** 2 *3829 499*

Verification Method: Test

The TC shall have sharp edges according to the following definition: precision grind with chunking <0.02 mm at the glass plate edges.

4.2.2 **Test Channel Shape: Parallel Plate: Inlet** 2 *3829 500*

Verification Method: Description

The test unit shall ensure a homogeneous flow into the test channel.

4.2.2.1 **Test Channel Shape: Parallel Plate: Inlet: Nozzle** 2 *3829 502*

Verification Method: Inspection

Upstream of the test channel the test unit shall have an inlet nozzle with a length of 30 mm and a constant (flow) cross section channel with parameters a and b and the length 20 mm, Figure 2.

Fig. 2 **Location, Shape, and Dimension of the Axial Markers**

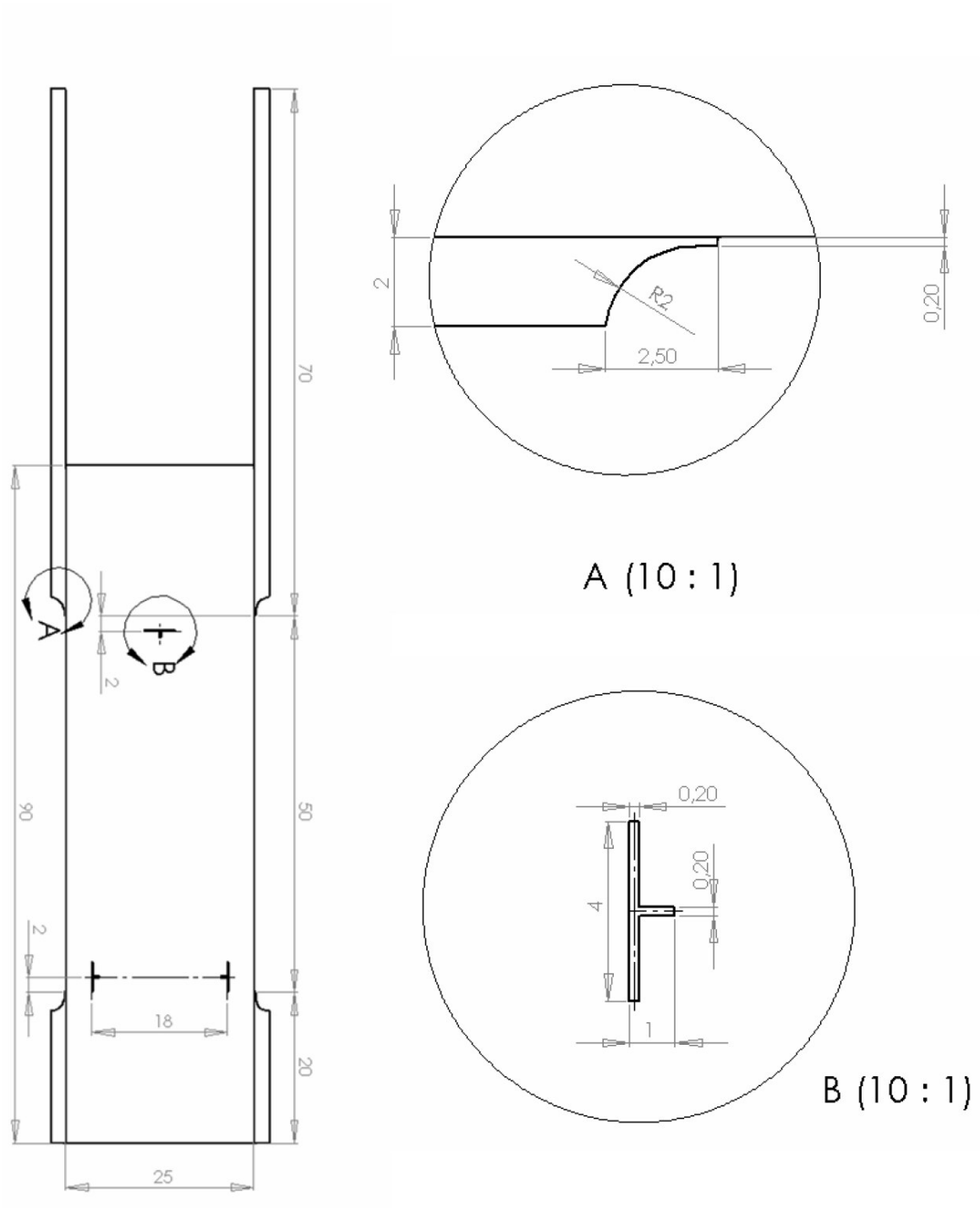

4.2.2.2 **Test Channel Shape: Parallel Plate: Inlet: Sharp Edges** 2 *3829 503*

Verification Method: Inspection

The test unit inlet into the test channel shall have sharp edges with h < 0.2 mm at the beginning of the free surface area, Figure 2, Detail A.

4.2.3 **Test Channel Shape: Parallel Plate: Outlet** 2 *3829 504*

Verification Method: Description

The test unit shall ensure a homogeneous undisturbed flow out of the test channel.

4.2.3.1 **Test Channel Shape: Parallel Plate: Outlet: Channel Geometry** 2 *3829 505*

Verification Method: Inspection

Downstream of the test channel the test unit shall have a constant (flow) cross section channel with parameters a and b for a length 20mm, Figure 2.

4.2.3.2 **Test Channel Shape: Parallel Plate: Outlet: Sharp Edges** 2 *3829 508*

Verification Method: Inspection

The test unit outlet from the test channel shall have sharp edges with h < 0.2 mm at the end of the free surface area, Figure 2, Detail A.

4.3 **Liquid Loop (Experiment Unit 1)** 2 *3829 512*

Verification Method: Description Inspection

4.3.1 **Liquid Loop: Test Liquid** 2 *3829 511*

Verification Method: Inspection

3M Engineering Fluid HFE-7500 shall be used as test liquid.

4.3.2 **Liquid Loop: Liquid Flow Rate** 2 *3829 513*

Verification Method: Description

Comment: "Flow" is used in this content as a synonym for "Volume Flow Rate"

4.3.2.1 **Liquid Loop: Liquid Flow Rate: Range** 2 *3829 828*

Verification Method: Test

The test liquid flow Q shall be controllable in a range of 1 ml/s <= Q <= 20 ml/s for Experiment Unit 1

4.3.2.2.1 **Liquid Loop: Liquid Flow Rate: Steps** 2 *3829 877*

Verification Method: Test

The test fluid flow rate Q shall be controllable in the range defined above in steps of <= 0.25 ml/s.

4.3.2.2.2 **Liquid Loop: Liquid Flow Rate: Steps** 2 *3829 841*

Verification Method: Test

The test fluid flow rate Q shall be controllable every 0.1 s.

4.3.2.2.3 **Liquid Loop: Liquid Flow Rate: Transient** 2 *3829 878*

Verification Method: Test

The test fluid flow rate q = dQ/dt shall be in the range 0.083 ml/s^2 <= q <= 25 ml/s^2

4.3.2.3 **Liquid Loop: Liquid Flow Rate: Measurement Accuracy** 2 *3829 858*

Verification Method: Test

The test liquid Flow Rate Q shall be measured with an accuracy of +/-1% of the maximum specified flow rate.

Comment: Flow sensor calibration with the working liquid is required. Temperature sensivity shall be taken into account.

4.3.2.4 **Liquid Loop: Liquid Flow Rate: Measurement Location** 2 *3829 517*

Verification Method: Inspection

The test fluid Flow Rate Q shall be measured between pump and first junction.

4.3.2.5 **Liquid Loop: Liquid Flow Rate: Oszillation** 2 *3829 518*

Verification Method: Demonstration

When required, an oszillation flow shall be superimposed over the predefined test liquid flow.

4.3.2.5.1 **Liquid Loop: Liquid Flow Rate: Oscillation: Frequency Range** 2 *3829 859*

Verification Method: Test

The superimposed oscillation flow shall have a frequency range of 0.2 Hz <= f_Qosc <= 10 Hz.

4.3.2.5.2 **Liquid Loop: Liquid Flow Rate: Oscillation: Frequency Accuracy** 2 *3829 520*

Verification Method: Test

The frequency range of the superimposed oscillation flow f_Qosc shall remain within df_Qosc = +/-10%.

4.3.2.5.3 **Liquid Loop: Liquid Flow Rate: Oscillation: Amplitude** 2 *3829 876*

Verification Method: Test

The superimposed oscillation flow shall have a volume of less than or equal 1 ml (tbc)

4.3.3 **Liquid Loop: Gas / Liquid Phase Separation** 2 *3829 570*

Verification Method: Description

Comment: During the experiment run in the critical mode the test fluid free surface line will become instable and gas will be sucked into the fluid loop. This gas has to be removed from the test fluid loop prior the test fluid enters the test channel again.

4.3.3.1 **Liquid Loop: Gas / Liquid Phase Separation Feature** 2 *3829 571*

Verification Method: Test

The CCF liquid loop shall provide gas removal / separation from the liquid.

4.3.3.2 **Liquid Loop: Gas / Liquid Phase Separation: Phase Separation Chamber (PSC) Dimensions** 2 *3829 572*

Verification Method: Inspection

The Phase Separation Chamber shall have
a) an internal diameter of 130 mm
b) an internal height of 72 mm below the separation mesh (screen).
and further internal dimensions as given in figure 3.

Please note: the liquid outlet of the phase separation chamber has changed and is not valid any more.

Fig. 3 **Phase Separation Chamber**

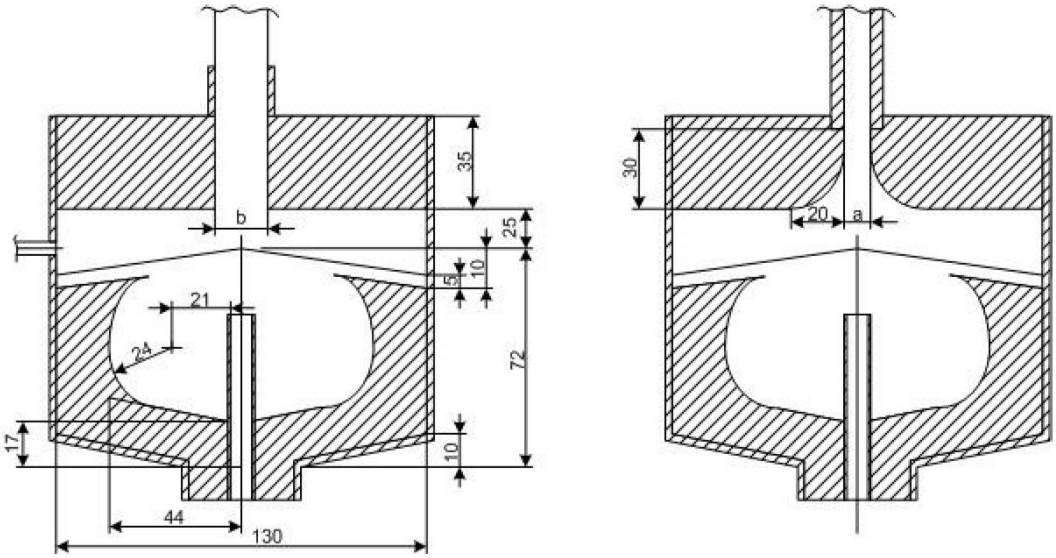

4.3.3.3 **Liquid Loop: Gas / Liquid Phase Separation: Phase Separation Chamber Mesh Size** 2 *3829 879*

Verification Method: Inspection

The Phase Separation Chamber mesh shall have a mesh size less or equal 15 µm to retain the gas bubbles.

4.3.3.4 **Liquid Loop: Gas / Liquid Phase Separation: Phase Separation Chamber Inlay** 2 *3829 574*

Verification Method: Inspection

The PSC shall include a bubble shape inlay to hold the gas volume/bubble in the centre of the PSC.

4.3.3.5	**Liquid Loop: Gas / Liquid Phase Separation: Phase Separation Chamber Rebounding Plate**	2	*3829 860*

Verification Method: Inspection

The PSC shall have a velocity plate at the bottom above the fluid inlet.

4.3.3.6	**Liquid Loop: Gas / Liquid Phase Separation: Gas Injection / Removal**	2	*3829 575*

Verification Method: Test

It shall be possible to inject / remove gas to / from the centre of the PSC.

4.3.4	**Liquid Loop: Flow Preparation Chamber**	2	*3829 577*

Verification Method: Description

4.3.4.1	**Liquid Loop: Flow Preparation Chamber: Location**	2	*3829 581*

Verification Method: Inspection

The Flow Preparation Chamber shall be located downstream of the phase separation chamber.

4.3.4.2	**Liquid Loop: Flow Preparation Chamber: Valve**	2	*3829 578*

Verification Method: Test

The Flow Preparation Chamber shall include a valve to open/close the connection to the test channel inlet nozzle.

4.3.4.3	**Liquid Loop: Flow Preparation Chamber: Port to CT**	2	*3829 579*

Verification Method: Inspection

The Flow Preparation Chamber shall include a port to be connected to the compensation tube inlet.

4.3.4.4	**Liquid Loop: Flow Preparation Chamber: TC Inlet**	2	*3829 861*

Verification Method: Inspection

The Flow Preparation Chamber shall include a rectangular test channel inlet.

4.3.5 Compensation Tube 2 *3829 583*

Verification Method: Description

Comment: The CCF facility will provide a compensation tube (CT) connected to the fluid loop (at the FPC) and open to the TU atmosphere. The CT is necessary to allow/ensure pressure equalization between fluid loop pressure and TU atmosphere pressure prior to slide bar(s) opening as well as during experiment run (especially during critical flow mode). In addition during a flow above critical velocity the fluid volume expansion, induced by the air bubble suction, will be compensated by the CT volume.

4.3.5.1 Compensation Tube: Connection 2 *3829 584*

Verification Method: Inspection

The compensation tube (CT) shall be connected to the fluid loop at the FPC port.

4.3.5.2 **Compensation Tube: Dimension** 2 *3829 862*

Verification Method: Inspection

The compensation tube, Figure 4, shall have
a) an internal diameter of 60 mm +/- 0.1mm
b) a height of 100 mm +/- 1mm.

Fig. 4 **Compensation Tube Dimensions**

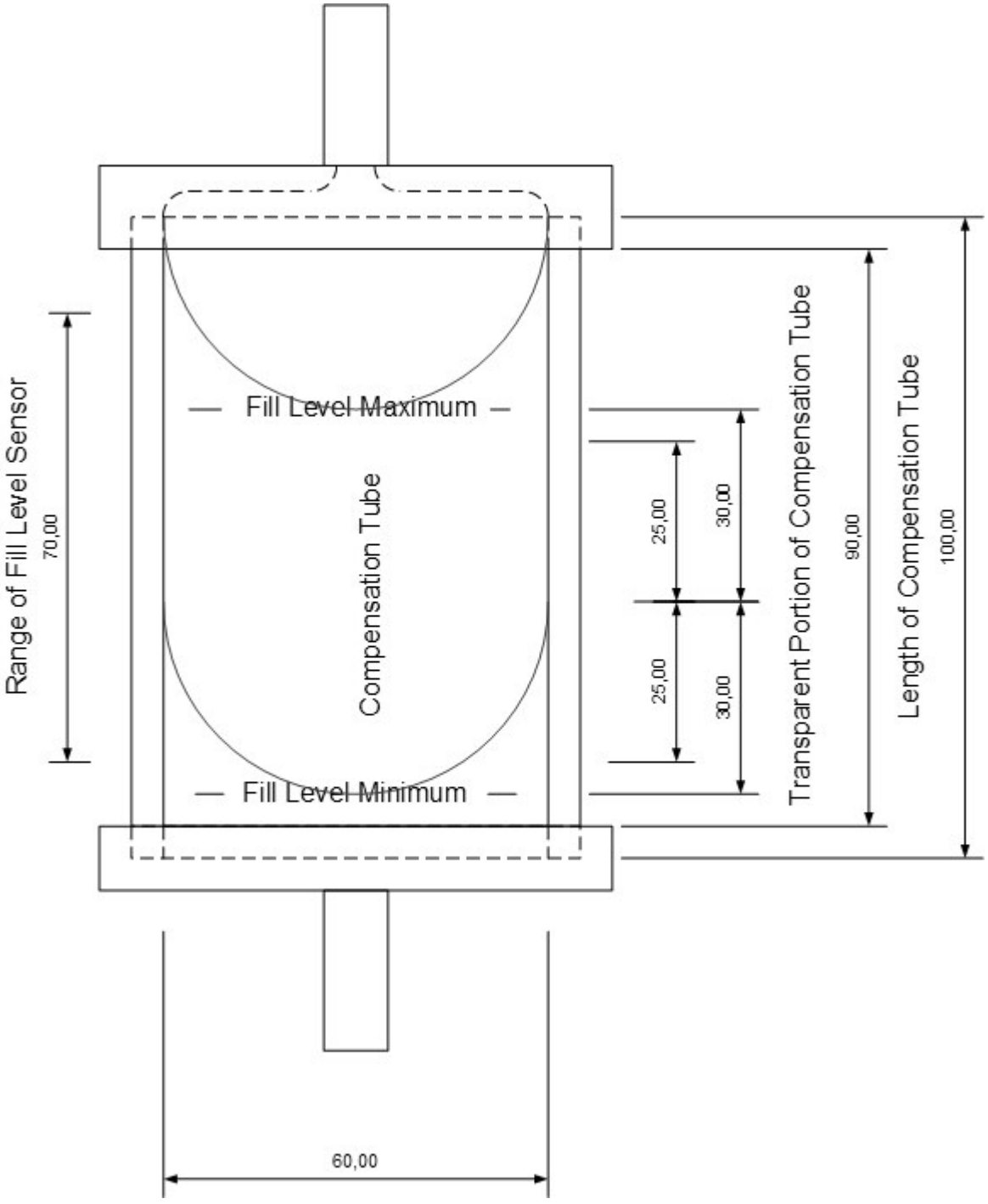

4.3.5.3	**Compensation Tube: Fill Level Range**	2	*3829 591*

Verification Method: Test

The C&DHS shall measure the compensation tube fill level over a range of +/- 35 mm at a tolerance of tbd mm, Figure 4.

4.3.5.4	**Compensation Tube: Fill Level Observation**	2	*3829 592*

Verification Method: Inspection

The compensation tube fill level shall be observable by General Video over the entire range of at least +/- 45 mm, Figure 4.

4.3.5.5	**Compensation Tube: Fill Level Extremata**	2	*3829 593*

Verification Method: Test

The C&DHS shall indicate fill levels "minimum" and "maximum" by dedicated sensors, Figure 4.

4.3.5.6	**Compensation Tube: Fill Level Minimum**	2	*3829 831*

Verification Method: Inspection

The minimum indicated fill level shall be at -30 mm, +/- 0.5 mm, Fig. 4.

4.3.5.7	**Compensation Tube: Fill Level Maximum**	2	*3829 832*

Verification Method: Inspection

The minimum indicated fill level shall be at +30 mm, +/- 0.5 mm, Fig. 4.

4.3.5.8	**Compensation Tube: Isolation from TU Atmosphere**	2	*3829 596*

Verification Method: Test

During stowage, transportation, and installation the compensation tube inner volume shall be separated from the test unit atmosphere.

4.3.5.9	**Compensation Tube: Pressure Difference to Test Unit Atmosphere**	2	*3829 597*

Verification Method: Analyses

During experiment execution the gas pressure above the liquid in the compensations tube shall be equal to the test unit atmosphere.

4.3.5.10 **Compensation Tube: Liquid Plug to Test Unit Atmosphere** 2 *3829 833*

Verification Method: Analyses

During experiment execution no liquid plug shall hamper the pressure equalization between compensation tube and the test unit atmosphere.

4.3.5.11 **Compensation Tube: Tube to Flow Preparation Chamber** 2 *3829 600*

Verification Method: Review of Design

The compensation tube and the flow preparation chamber shall be connected by a tube as straight as possible. No inserts inside the tube shall influence any flow pattern.

4.3.5.11.1 **Compensation Tube: Tube to Flow Preparation Chamber: Diameter** 2 *3829 834*

Verification Method: Inspection Review of Design

The tube, which connects the Compensation Tube and the Flow Preparation Chamber, shall have a constant inner diameter of 8 mm +/- 0.3 mm.

4.3.5.11.2 **Compensation Tube: Tube to Flow Preparation Chamber: Length** 2 *3829 602*

Verification Method: Inspection Review of Design

The tube, which connects the Compensation Tube and the Flow Preparation Chamber, shall have as a design goal the length according to

D*D / l = 1 mm

l length of tube in mm
D inner diameter of tube in mm

4.3.5.11.3 **Compensation Tube: Tube to Flow Preparation Chamber: Port at CT** 2 *3829 603*

Verification Method: Inspection Review of Design

The tube, which connects the Compensation Tube and the Flow Preparation Chamber, shall enter the compensation tube centrically at the bottom.

4.3.5.11.4 **Compensation Tube: Tube to Flow Preparation Chamber: Port at FPC** 2 *3829 604*

Verification Method: Inspection Review of Design

The tube, which connects the Compensation Tube and the Flow Preparation Chamber, shall enter the flow preparation chamber in an area of low flow velocity, i.e. appart from the core flow.

4.3.6	**Liquid Recovery**	2	*3829 598*

Verification Method: Analyses

Liquid, splashed out of the test channel or out of the compensation tube, shall be recovered such that it does not impact the experiment observation.

4.4	**Gas Atmosphere**	2	*3829 582*

Verification Method: Inspection

The gas in the test unit shall be GN2.

5	**Environment**	2	*3829 528*

Verification Method: Description

5.1	**Environment: Temperature Control**	2	*3829 529*

Verification Method: Description

5.1.1	**Environment: Temperature Control: Range**	2	*3829 530*

Verification Method: Test

The thermal control of the test liquid temperature shall ensure that the liquid temperature will be in a range of 20°C <= T_liq <= 40°C.

5.1.2	**Environment: Temperature Control: Accuracy**	2	*3829 531*

Verification Method: Test

The test liquid temperature shall be controlled prior to experiment start and during experiment run such that the measured test liquid temperature difference inside the liquid loop between PSC inlet and TC outlet shall be less than 1.0°C.

5.2	**Environment: Pressure Control**	2	*3829 532*

Verification Method: Description

Comment: Very low pressure changes along the test channel are expected (dp ~ 10 Pa range).
The absolute pressure of the system has less influence on the test results.

5.2.1	**Environment: Pressure Control: Percipitation**	2	*3829 835*

Verification Method: Analyses

The pressure between test channel outlet and pump inlet shall not drop below 987 hPa.

Comment: Cavitation and/or precipitation shall not occur in the duct between test channel and flow sensor.

5.3	**Liquid and Gas Compensation**	2	*3829 610*

Verification Method: Description

Comment: Due to the fact that the open test channel walls may suck air from the test unit atmosphere in over-critical flow condition the volume inside the fluid loop changes; e.g. the gas bubble inside the PSC increases and the filling level in the CT rises. At latest the maximum gas bubble volume inside the PSC is reached a compensation has to be performed. That means that gas has to be removed from the PSC. Also prior to the start of an experiment run a minimum gas bubble volume has to be injected into the PSC.

5.3.1	**Liquid Volume Compensation**	2	*3829 611*

Verification Method: Description

5.3.1.1	**Liquid Volume Compensation: Thermal Expansion**	2	*3829 612*

Verification Method: Test

The Fluid Managmenet Subsystem shall provide means for thermal liquid volume expansion compensation for the temperature range between 5°C and 48°C.

5.3.1.2	**Liquid Volume Compensation: Thermal Expansion Starting Pressure**	2	*3829 613*

Verification Method: Test

Under worst case conditions the means for thermal liquid volume expansion compensation shall not be activated at liquid pressure below 2 bar abs.

5.3.1.3	**Liquid Volume Compensation: Thermal Expansion Final Pressure**	2	*3829 614*

Verification Method: Test

Under worst case conditions the means for thermal liquid volume expansion compensation shall not generate a liquid pressure above 4 bar abs (tbc).

5.3.1.4	**Liquid Volume Compensation: Operational Volume**	2	*3829 615*

Verification Method: Test

The FMS shall compensate the operational liquid volume changes from liquid volume in start configuration to liquid volume in experiment running configuration.

5.3.1.5	**Liquid Volume Compensation: Operational Volume Control**	2	*3829 616*

Verification Method: Test

The FMS shall control the operational liquid volume fill level with an accuracy of 1 ml or less.

5.3.2	**Gas Volume Compensation**	2	*3829 617*

Verification Method: Description

5.3.2.1	**Gas Volume Compensation: Operational Volume**	2	*3829 619*

Verification Method: Test

The FMS shall compensate the operational gas volume changes from liquid volume in start configuration to gas volume in experiment running configuration without change of the atmopheric pressure.

5.3.2.2	**Gas Volume Compensation: Fill Level Control**	2	*3829 618*

Verification Method: Test

The FMC shall control the gas fill level volume at an accuracy of 1 ml or less.

6	**Data Acquisition**	2	*3829 522*

Verification Method: Description

6.1	**Data Acquisition: Temperatures**	2	*3829 523*

Verification Method: Description

6.1.1 **Data Acquisition: Temperatures: Sensor Locations** 2 *3829 836*

Verification Method: Inspection

Temperature sensors shall be located at least at:
a) inside / close to the outlet of the liquid plunger (measuring the liquid temperature)
b) inside / close to the PSC inlet (measuring the liquid temperature)
c) inside the test flow preparation chamber close to the test channel inlet nozzle (measuring the liquid temperature)
d) inside the test liquid ducting close to the test channel outlet (measuring the liquid temperature)
e) inside the test unit atmosphere (measuring the gas temperature inside the TU)
f) inside the ducting close to the flow sensor outlet (measuring the liquid temperature)
g) near the outlet of the gas plunger (measuring gas temperature)

The sensor inside the fluid loop at location c) and d) shall not disturb the flow, as far as possible.

6.1.2 **Data Acquisition: Temperatures: Sensor Accuracy Absolut** 2 *3829 525*

Verification Method: Test

The absolute accuracy of the temperature measurement shall be +/- 0.5°C or better.

6.1.3 **Data Acquisition: Temperatures: Sensor Accuracy Relative** 2 *3829 526*

Verification Method: Test

The relative accuracy of each temperature sensor to each other shall be +/- 0.2°C.

6.1.4 **Data Acquisition: Temperatures: Sensor Time constant** 2 *3829 837*

Verification Method: Inspection

The temperature sensor time constant shall be less than 1 s on a metal surface.

6.2 **Data Acquisition: Pressures** 2 *3829 536*

Verification Method: Description

6.2.1 **Data Acquisition: Pressure Control: Sensor Locations** 2 *3829 533*

Verification Method: Inspection

The total Pressure shall be measured at:
a) inside the phase separation chamber (to measure the test fluid total pressure)
b) inside the test unit gas atmosphere (to measure the atmosphere total pressure)
c) inside the gas duct near the plunger (measuring the gas total pressure)

6.2.2 **Data Acquisition: Pressure Control: Sensor Range** 2 *3829 534*

Verification Method: Test

The total pressure sensor shall include the measurement range of 920 hPa <= p <= 1120 hPa

---

6.2.3 **Data Acquisition: Pressure Control: Sensor Accuracy** 2 *3829 535*

Verification Method: Inspection

The total pressure sensor shall have a measurement accuracy of 0,5% full scale reading.

6.3 **Video Observation** 2 *3829 539*

Verification Method: Description

Comment: The test channel and the compensation tube shall be observed via video camera during the experiment run especially during the supercritical operation mode; that means that this video data have to be down linked to the PI to enable the PI for online decision to change the flow rate and/or the free surface length. This kind of video observation will be called Experiment General Observation.

Comment: In addition the test channel area (l x b) shall be observed via a high speed, high resolution video camera for test result data acquisition (free surface behavior). These video data shall be processed on board and the evaluation/process results (reduced data amount) shall be down linked for detailed evaluation. This kind of video observation will be called Experiment Detailed Observation.

6.3.1 **Experiment General Video Observation** 2 *3829 541*

Verification Method: Inspection

a) The CCF General Video equipment shall observe the test channel (TC) during experiment run.
b) The CCF General Video equipment shall observe the compensation tube (CT) during experiment run.
c) The CCF transparent wall parts shall have a comparable optical quality as defined for the TC

6.3.1.1 **Experiment General Video Observation: Camera** 2 *3829 542*

Verification Method: Inspection

The CCF facility shall use one of the MSG provided video camera to observe the test channel and the compensation tube or use video pictures (low data amount) resulting from the video camera(s) for detailed observation.

6.3.1.2 **Experiment General Video Observation: Frequency** 2 *3829 543*

Verification Method: Inspection

The flow in the test channel and the liquid in the compensation tube shall be observed by video frequency of more or equal 24 fps (frames per second).

6.3.1.3 **Experiment General Video Observation: Resolution** 2 *3829 863*

Verification Method: Inspection

Deleted.

Comment: The MSG video camera is used. Therefore no requirement to CCF.

6.3.1.4 **Experiment General Video Observation: Video Data Down Link** 2 *3829 545*

Verification Method: Inspection

The CCF facility shall use the MSG provided "data handling system" for the above defined video data online down link.

6.3.2 **Experiment Detailed Video Observation** 2 *3829 546*

Verification Method: Description

6.3.2.1 **Experiment Detailed Video Observation** 2 *3829 547*

Verification Method: Test

The CCF facility shall observe the the channel area (as a maximum (1mm + l_testchannel + 1mm) x b) during the experiment run.

6.3.2.2 **Experiment Detailed Video Observation: Resolution** 2 *3829 548*

Verification Method: Test

The flow in the test channel shall be recorded by video with an optical resolution in the test channel plane (l x b) of 0.05 mm/pixel or better.

6.3.2.3 **Experiment Detailed Video Observation: Frequency** 2 *3829 549*

Verification Method: Test

The CCF detailed video data acquisition shall operate up to a frequency of 250 fps at least.

6.3.2.4 **Experiment Detailed Video Observation: Intermediate Stowage** 2 *3829 838*

Verification Method: Test

The CCF detailed video data acquisition shall intermediately store the contineous high speed video data stream. The duration shall be selectable from 0 s < record duration to the maximimum capability of the HSHRC, which shall be not less than 5 s.

6.3.2.5 **Experiment Detailed Video Observation: Observation Direction** 2 *3829 551*

Verification Method: Inspection

The flow in the test channel shall be recorded by video perpendicular to the test channel l x b plane.

6.3.2.6 **Experiment Detailed Video Observation: Gray Scale** 2 *3829 552*

Verification Method: Test

The flow in the test channel shall be recorded by video in black and white with a 8 bit gray scale resolution for each pixel.

6.3.3 **Experiment Detailed Video Observation: On Board Data Storage and Processing** 2 *3829 553*

Verification Method: Description

Comment: The test result data acquisitioned by the high speed, high resolution video camera shall be processed on board after each individual experiment run (= offline) to extract the relevant surface details (detection of the contour lines k(x)). Contour line data will be down linked together with reference frames.

6.3.3.1 **Experiment Detailed Video Observation: On Board Data Storage** 2 *3829 555*

Verification Method: Description

The C&DHS does NOT store any video data after provision of the reference images to the MSG downlink.

6.3.3.2 **Experiment Detailed Video Observation: Reference Frame Extraction** 2 *3829 556*

Verification Method: Test

The C&DHS extract offline the reference images from the raw video data according to a frequency of 1 fps.

6.3.3.3 **Experiment Detailed Video Observation: Contour Line Detection** 2 *3829 557*

Verification Method: Test

The CDHS shall detect offline from each recorded video frame the contour lines k(x).

6.3.3.4 **Experiment Detailed Video Observation: Coordinate Transfer and Optical Corrections** 2 *3829 864*

Verification Method: Test

DELETED.

6.3.3.5 Experiment Detailed Video Observation: Downlink

2 *3829 559*

Verification Method: Test

The CDHS shall provide preprocessed (reduced) data to the downlink via the MSG provided data handling interface, i.e. the counter lines k(x) and the reference video frames.

6.3.3.6 Experiment Detailed Video Observation: Full Frame Transmission

2 *3829 880*

Verification Method: Test

On request the C&DHS shall offline provide predefined single images or sequences of the last experiment run for documentation to the MSG downlink:

resolution: full (1280 x 1024) or video (full frame reseized to 576 x 720)
frame rate: as recorded or video 25 fps
frame: progressiv
compression: quality factor of compression selectable by parameter

6.3.4 Optical Requirements

2 *3829 586*

Verification Method: Description

Comment: To be able to observe the fluid behavior inside the test channel and inside the compensation tube via video camera(s) that part of the walls which will be observed by video camera(s) for liquid free surface(s) will be made out of transparent material.

Comment: The illumination of the test channel (TC) and the compensation tube (CT) have to be performed such that the illumination is compatible with Video Camera(s) with which the TC and the CT will be observed (different cameras may be used for TC and for CT observation).
Video camera and illumination have to be defined/chosen such that they fit together. Therefore below the illumination parameters will be listed, but no dedicated values will be defined. That means illumination and cameras have to be verified/tested together.

6.3.4.1 Optical Requirements: Tansparency TC

2 *3829 85*

AD01	*Issue 1*	*Rev. 0*	*06.02.03*	*(Req. ID: AD01-CCF/744)*	
KHB 1700.7	*Issue 1*	*Rev. 0*	*01.*	*(Req. ID: AD11-CCF/804)*	

Verification Method: Inspection

The test channel walls to be observed by video camera(s) shall be made out of a transparent material.

6.3.4.2 Optical Requirements: Tansparency CT

2 *3829 587*

Verification Method: Inspection

The compensation tube walls to be observed by video camera(s) shall be made out of transparent material.

6.3.4.3 Optical Requirements: Wettability TC

2 *3829 497*

Verification Method: Test

The test channel transparent walls shall be perfect wettable by the test fluid.

6.3.4.4 Optical Requirements: Wettability CT

2 *3829 588*

Verification Method: Test

The compensation tube transparent walls shall be perfect wettable by the test fluid.

6.3.4.5 Optical Requirements: Surface TC

3829 589

Verification Method: Test

The test channel wall surfaces to be observed by video camera(s) shall have a surface quality 5/4x0.16 according to ISO10110 (DIN 3140).

Comment: 5 is the indicator for surface errors, N ,here 4, is the indicator for the numbers of errors, A ,here 0.16, is the area of the error.

6.3.4.6 Optical Requirements: Surface CT

2 *3829 86*

Verification Method: Test

The compensation tube wall surfaces to be observed by video camera(s) shall have a surface quality 5/N(tbd)xA(tbd) according to ISO10110 (DIN 3140).

Comment: 5 is the indicator for surface errors, N is the indicator for the numbers of errors, A is the area of the error.

6.3.4.7 **Optical Requirements: Test Channel Markers** 2 *3829 840*

Verification Method: Inspection

The test channel wall outer surface to be observed by video camera shall have:
a) three marker as defined in figure 2
b) location and tolerances on the upper plate outer surface (close to the camera wall surfaces outer side) for video data calibration and evaluation as defined in figure 2.

Fig. 2 **Location, Shape, and Dimension of the Axial Markers**

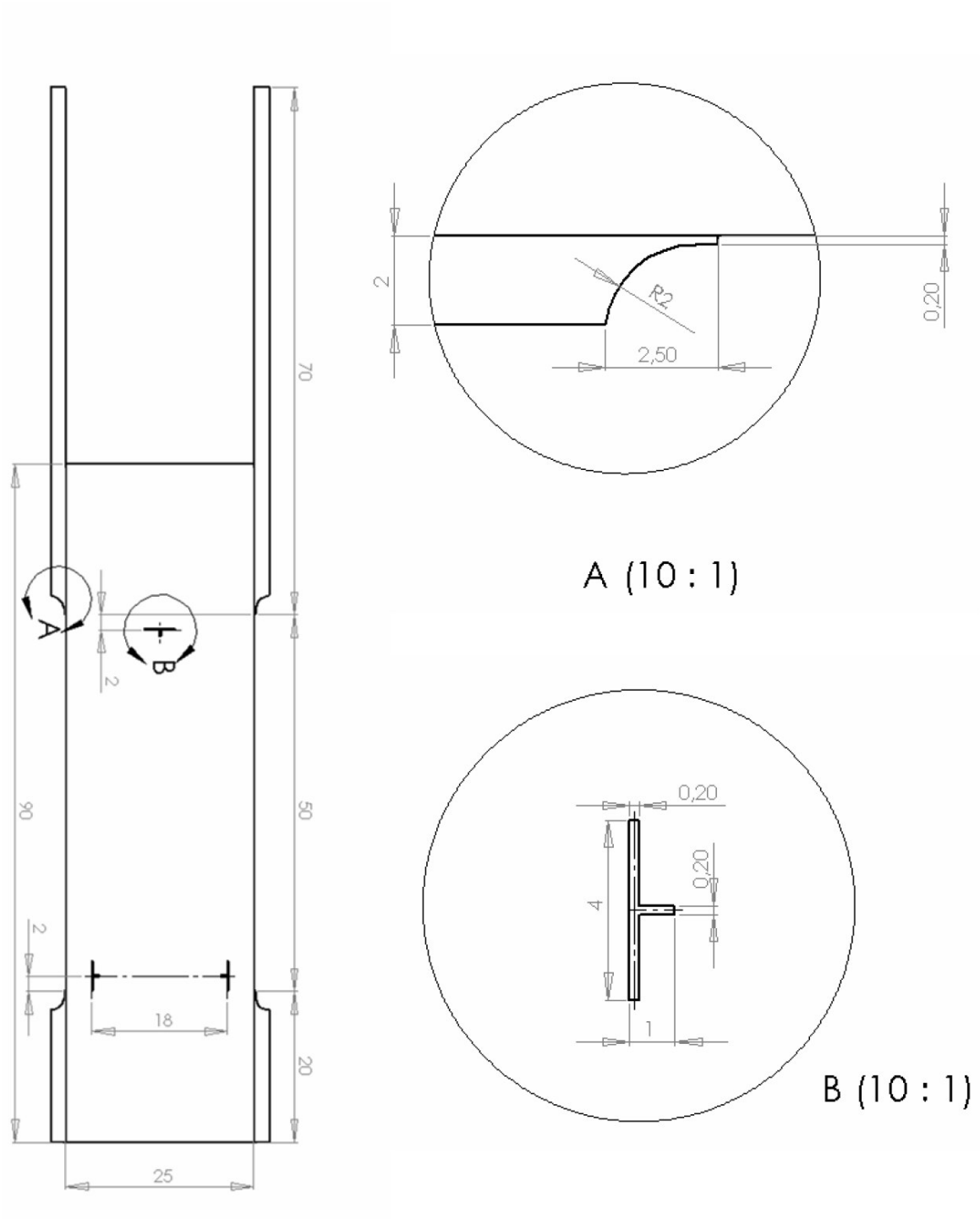

6.3.4.8 Illumination Brightness

2 *3829 606*

Verification Method: Test

The Optical diagnostic Unit (ODU) shall provide

a) a test channel illumination
b) a compensation tube illumination

with a brightness which is compatible with the camera and the set up.

6.3.4.9 Illumination Type

2 *3829 607*

Verification Method: Test

The ODU provided illumination for

a) the test channel
b) the compensation tube

shall be backlight illumination.

6.3.4.10 Illumination Homogeneity

2 *3829 608*

Verification Method: Test

The ODU shall provide a test channel illumination with a light intensity homogeneity which is compatible with the edge detection technique and the set up.

6.3.4.11 Illumination Light Wave Length

2 *3829 609*

Verification Method: Test

The ODU shall provide a illuminations with a wave lengths which are compatible with the video cameras observing
a) the test channel
b) the compensation tube

6.3.5 Experiment Control

2 *3829 843*

Verification Method: Description

Comment: The experiment control data like the temperature data, the pressure data, the mass flow data, the geometrical parameter data (e.g. l and a) will be stored according to the defined sample rate. All this data have to be correlated between each other as well as to the video data via the time stamp (absolute time or relative experiment time).

Due to several reasons, e.g. driver availability for the high speed high resolution camera, the selected operating system of the CCF controller is Windows XP Embedded. This is NOT a realtime system. The frequencies and durations given below are therfore statistical and average values. With Windows XP it is not possible to grant timelines due to system activities which cannot be interrupted.

6.3.5.1 **Experiment Control: Telecommand Receipt** 2 *3829 561*

Verification Method: Test

The C&DHS shall receive telecommands from ground via MSG.

6.3.5.2 **Experiment Control: Telecommand Execution** 2 *3829 562*

Verification Method: Test

The C&DHS shall initiate and control the relevant actions according to the telecommands from ground.

6.3.5.3 **Experiment Control: Telecommand Acknowledgement** 2 *3829 564*

Verification Method: Test

The C&DHS shall acknowledge telecommands in the housekeeping data stream.

6.3.5.4 **Experiment Control: Downlink Provision Rate** 2 *3829 565*

Verification Method: Test

The C&DHS shall provide for downlink via MSG the entire set of housekeeping data during the experiment run with a frequency of at least 1Hz.

6.3.5.5 **Experiment Control: Housekeeping Data Set** 2 *3829 865*

Verification Method: Test

The C&DHS housekeeping data set shall consist of at least:
a) time stamp (absolute or relative)
b) CCF health status summary
c temperatures
d) pressures
e) volume flow rate
f) rotation speed of pump drive
g) superimposed oscillation frequency and amplitude
h) all valve positions (open/closed) (actual value)
i) position of plunger K1 (plunger for oscillation modes) (actual value)
j) position of plunger K2 (liquid volume) (actual value)
k) position of plunger K3 (gas volume) (actual value)
l) position of left and right slide bar (actual value)
m) position of liquid level in CT (based on fill level sensor signal)
n) signal of the photo sensors (e.g. light barriers) of the CT (minimum/maximum level)
o) status report of the image processing
p) all commands from the PI site to CCF (telecommand acknowledgement)

Comment: micro-g level data are recorded and transferred by SAMS separately.

6.3.5.6	**Experiment Control: Time Correlation**	2	*3829 567*

Verification Method: Test

The C&DHS shall ensure the time correlation between experiment housekeeping data and video data.

6.3.5.7	**Experiment Control: Automatic Experiment Execution**	2	*3829 821*

Verification Method: Test

The C&DHS shall be able to execute experiment runs with predefined parameter sets, in particular liquid flow rate, oscillation frequency, open channel length l, duration of experiment, etc., automatically.

6.3.5.8	**Experiment Control: Choking Detection**	2	*3829 568*

Verification Method: Test

The C&DHS shall detect choking from the available sensor data automatically.

6.3.5.9	**Experiment Control: Automatic Flow Stop**	2	*3829 866*

Verification Method: Test

In full automatic mode the C&DHS shall adjust the liquid flow automatically to a predefined value in the parameter set when choking is detected.

7	**Interfaces**	2	*3829 622*

Verification Method: Description

Comment: The CCF facility I/F requirements are defined in AD02. These requirements are not repeated in this specification. Only reference will be provided. The requirement verification has to be done as requested in AD02.

7.1	**CCF Mass**	2	*3829 206*

Verification Method: Test

The CCF facility total mass (including the MSG provided equipment in the Working Volume (WV)) shall not exceed 200 kg.

7.2	**CCF Volume**	2	*3829 207*

Verification Method: Test

The CCF facility total volume (including the MSG provided equipment in the WV) shall be noticeable below the MSG WV which is in total 255 l.

7.3 **CCF Envelope** 2 *3829 208*

Verification Method: Description

7.3.1 **CCF Subsystems / Components Transfer Envelope** 2 *3829 209*

Verification Method: Test

The CCF facility subsystems / components have to be designed such that they can be transferred into the MSG WV via the two loading ports, one located on each side of the WV.

Comment: Loading ports max. diameter D = 406mm.

7.3.2 **CCF Subsystems / Components Envelope** 2 *3829 210*

Verification Method: Demonstration

The CCF facility subsystems / components have to be designed such that they can be handled (integrated) inside the MSG WV.

Comment: The MSG WV max. dimensions are: Width = 906mm, Depth (bottom) = 500mm, Depth (top) = 385mm, Height = 638mm. Adequate space from windows, gloveports, ... and for QD and connector handling have to be taken into account.

7.3.3 **CCF Subsystems / Components Storage Constraints** 2 *3829 211*

Verification Method: Analyses Demonstration

The CCF facility subsystems / components have to be designed such that they can be handled (integrated) and stored during transport and on ISS.

7.4 **CCF Thermal Dissipation** 2 *3829 212*

Verification Method: Description

7.4.1 **CCF Total Thermal Dissipation** 2 *3829 213*

Verification Method: Test Analyses

The CCF facility total thermal dissipation (including the MSG provided equipment in the WV) shall be less than 1000 W.

7.4.2	**CCF Thermal Dissipation to WV Air**	2	*3829 214*

Verification Method: Analyses

The CCF facility total thermal dissipation (including the MSG provided equipment in the WV) to the WV air flow shall be less than 200 W.

7.4.3	**CCF Thermal Dissipation to WV Coldplate**	2	*3829 215*

Verification Method: Test Analyses

The CCF facility total thermal dissipation (including the MSG provided equipment in the WV) to the WV coldplate shall be less than 800 W.

7.4.4	**Loss of Cooling**	2	*3829 216*

Verification Method: Test

The CCF facility shall be designed not to create hazards in case of sudden loss or temporary interruption of MSG coolant loop.

7.5	**CCF Micro Gravity Environment Disturbances**	2	*3829 222*

Verification Method: Test

The CCF facility micro gravity disturbances introduced into the MSG shall be less than that defined in AD12 para. 3.1.2.

7.6	**Depress- / Repress Rates**	2	*3829 223*

Verification Method: Test

The CCF facility shall be designed to withstand the depress rate of 878 Pa/sec and the repress rate of 800 Pa/sec.

7.7	**Exposure to PFE Discharge**	2	*3829 224*

Verification Method: Analyses

The CCF facility shall be designed not to create a hazard when exposed to Portable Fire Extinguisher (PFE) discharge.

7.8	**Mechanical / Structural Interface Requirements**	2	*3829 226*

Verification Method: Test Inspection Analyses

The CCF facility shall comply with requirements defined in AD02

7.9 **Electrical Interface Requirements** 2 *3829 227*

Verification Method: Test Inspection Analyses

The CCF facility shall comply with requirements defined in AD02

7.10 **Command and Data Handling Interface Requirements** 2 *3829 228*

Verification Method: Test Analyses

The CCF facility shall comply with requirements defined in AD02

7.11 **Thermal Control Interface Requirements** 2 *3829 229*

Verification Method: Test Analyses

The CCF facility shall comply with requirements defined in AD02

7.12 **Vacuum System Interface Requirements** 2 *3829 230*

Verification Method: Analyses

The CCF facility shall comply with requirements defined in AD02

7.13 **Pressurized Gas Interface Requirements** 2 *3829 231*

Verification Method: Analyses

The CCF facility shall comply with requirements defined in AD02

7.14 **Environmental Interface Requirements** 2 *3829 232*

Verification Method: Analyses

The CCF facility shall comply with requirements defined in AD02

7.15 **Fire Protection Interface Requirements** 2 *3829 233*

Verification Method: Analyses

The CCF facility shall comply with requirements defined in AD02

7.16 **Material and Parts Interface Requirements** 2 *3829 234*

Verification Method: Test Inspection Analyses

The CCF facility shall comply with requirements defined in AD02

7.17	**Human Factors Interface Requirements**	2	*3829 235*

Verification Method: Test Inspection Demonstration

The CCF facility shall comply with requirements defined in AD02

7.18	**PA AND SAFETY REQUIREMENTS**	2	*3829 236*

Verification Method: Description

7.18.1	**PA and Safety Requirements**	2	*3829 237*

Verification Method: Test Inspection Analyses

The CCF facility shall comply with the safety requirements defined in AD02

7.18.2	**PA and Safety Requirements**	2	*3829 238*

Verification Method: Test Inspection Analyses

The CCF facility shall comply with the safety requirements defined in AD07

7.18.3	**PA and Safety Requirements**	2	*3829 239*

Verification Method: Test Inspection Analyses

The CCF facility shall comply with the safety requirements defined in AD07

7.18.5	**PA and Safety Requirements**	2	*3829 241*

Verification Method: Test Inspection Analyses

The CCF facility shall comply with the safety requirements defined in AD08 and AD09.

7.19	**LABELING**	2	*3829 243*

Verification Method: Inspection

The CCF shall comply with the labeling requirements defined in AD02

8	**VERIFICATION**	2	*3829 242*

Verification Method: Inspection

The CCF shall comply with the verification requirements defined in AD02

8.1 Verification Requirement Sources and Breakdown Strategy 2 *3829 266*

Verification Method: Description

This CCF System Specification defines the science / functional performance requirements in detail In addition to the science / functional performance requirements some other requirements have to be fulfilled to be allowed to fly and integrate the CCF into MSG and to operate the CCF.
Such requirements have been made applicable in this CCF System Specification via some applicable documents like AD02, the MSG Investigation Interface Requirements Document from NASA.

It should be mentioned that Safety Requirements Verification are not addressed in detail here because it is assumed that Safety Requirements Verification will be covered by the Safety Data Package.

Further on it has to be mentioned that all the CCF Command and Data Handling activities are foreseen to be part of the ESS which was not part of the phase B. Therefore for CCF ESS development there may be also software requirements to be verified depending on the ESS software. This is not reflected here because the ESS was excluded from phase B.

8.2 Models 2 *3829 875*

Verification Method: Description

DELETED.

8.3 Verification Methods 2 *3829 268*

Verification Method: Description

8.3.1 Analysis 2 *3829 269*

Verification Method: Description

Analysis is a technical evaluation that relates equipment design and use parameters for prediction of actual design and operation. Analysis may be used to verify requirements, provided established techniques used are adequate to yield confidence, or where testing is impractical. Included in this category is analysis of similarity to items previously verified to the same criteria or more stringent criteria. Verification accomplished by analysis shall be evidenced by an analysis report.

8.3.2 Test 2 *3829 270*

Verification Method: Description

Test is actual operation of equipment under simulated conditions or the subjection of equipment to specified environments to measure responses. When analysis or inspection is specified as the method of verification, testing may be used to satisfy the requirement if preferred by the hardware developer, if it is cost effective, and if the Microgravity Science Glovebox Integration Manager agrees. Verification accomplished by test shall be evidenced by a test report.

8.3.3 Inspection

2 *3829 271*

Verification Method: Description

Inspection is a physical evaluation of equipment and associated documentation.
Inspection may be used to verify construction features, drawing compliance, workmanship, and physical condition. It includes determination of physical dimensions.
Verification accomplished by inspection shall be evidenced by an inspection report.

8.3.4 Demonstration

2 *3829 272*

Verification Method: Description

Demonstration is the qualitative determination of compliance with requirements by observation during actual operation or simulation under preplanned conditions and guidelines. Some human factor requirements were the method of closure is a demonstration requires the investigation to be set up in its on-orbit configuration in the MSG Engineering Unit to verify that the requirement is satisfied.

8.3.5 Review of Design

2 *3829 273*

Verification Method: Description

Review of design means verification compliance to requirement by evidence from documents and drawings. (only be used in Verification matrix…..

8.4 Verification Matrix

2 *3829 274*

Verification Method: Description

Legend:
EU = Experiment Unit, ESS = Electrical Subsystem, FM = Flight Model (complete CCF System) T = Test, A = Analysis,
I = Inspection, R = Review of Design, *+* = according to applicable doc.

CAPILLARY CHANNEL FLOW

Titel:
Title: CCF EU#2 System Specification

Dokumenten Typ:
Document Type: Specification

Konfigurations-Nr.:
Configuration Item No.: Issue 2

Referenz- Nr.:
Reference No.: CCF-SP-AST-1002

Klassifikations-Nr.:
Classification No.:

Lieferbedingungs-Nr.:
DRL/DRD No.:

Freigabe Nr.:
Release No.:

Gruppierung (Dok.):
Group (Doc.-related):

Gruppierung (Version):
Group (Version-related):

Thema:
Subject:

Kurzbeschreibung:
Abstract:

Autor: Prepared by:	Dr. Jürgen Held Author	**Org. Einh.:** Organ. Unit:	TO62	**Unternehmen:** Company:	Astrium ST
Geprüft: Agreed by:	Bernd Hummelsberger System Engineering	**Org. Einh.:** Organ. Unit:	TO62	**Unternehmen:** Company:	Astrium ST
Genehmigt: Approved by:	Gabriele Danzer Product Assurance	**Org. Einh.:** Organ. Unit:	TOQ5	**Unternehmen:** Company:	Astrium ST
Genehmigt: Approved by:	Bernd Hummelsberger Configuration Control	**Org. Einh.:** Organ. Unit:	TO62	**Unternehmen:** Company:	Astrium ST
Genehmigt: Approved by:	Bernd Hummelsberger Project Manager	**Org. Einh.:** Organ. Unit:	TO62	**Unternehmen:** Company:	Astrium ST

Copyright by Astrium ST - All Rights Reserved

(This Page Intentionally Blank)

Copyright by Astrium ST - All Rights Reserved

Daten/Dokument-Änderungsnachweis/*Data/Document Change Record (DCR)*

Ausgabe *Issue*	**Datum** *Date*	**Betroffener Abschnitt/Paragraph/Seite** *Affected Section/Paragraph/Page*	**Änderungsgrund/Kurze Änderungsbeschreibung** *Reason for Change/Brief Description of Change*
1	2006-12-11	all	
2	2006-01-16	paragraph 4, 4.1.3, 4.2.1, 4.1.1.9 to 4.1.1.11	removal of taper angle phi requirements

Copyright by Astrium ST - All Rights Reserved

Interner Verteiler/*Internal Distribution List*

Name *Name*	**Abteilung** *Organisation*	**Anzahl d. Kopien** *Number of Copies*	**Zustimmung** *Approval*	**Genehmigung** *Acceptance*	**Information** *Information*
Bernd Hummelsberger	TO62	1 (electronic)			
Roman Gmünder	TO62	1 (electronic)			
Gabriele Danzer	TOQ5	1 (electronic)			

Externer Verteiler/*External Distribution List*

Name *Name*	**Abteilung** *Organisation*	**Anzahl d. Kopien** *Number of Copies*	**Zustimmung** *Approval*	**Genehmigung** *Acceptance*	**Information** *Information*
Michael Dreyer	ZARM	1 (electronic)			
Mark Weislogel	CECS	1 (electronic)			
Uwe Rosendahl	ZARM	1 (electronic)			

Copyright by Astrium ST - All Rights Reserved

1. Introduction 1 *3831 625*

Verification Method: Description

1.1. Purpose 1 *3831 626*

Verification Method: Description

The Critical Velocity in Open Capillary Cannel Flows Experiment Facility (CCF) will provide the capability of operating different open capillary channel geometries at variable fluid flow rates on board the International Space Station (ISS) inside the Microgravity Science Glovebox (MSG) Working Volume (WV).

The project was launched in the frame of DLR-NASA compensation agreement. The specification is written in course of the CCF phase B and updated during Phase DeltaB.

1.2. Scope 1 *3831 627*

Verification Method: Description

This specification establishes the requirements for the function, properties, performance, design, development, testing, verification and preparation for delivery of the CCF assembly. This specification is the baseline for the CCF design.

1.3. General Explanations 1 *3831 882*

Verification Method: Description

A numbering system has been introduced in order to improve the identification and tracking of each individual requirement.

Explanatory or descriptive parts of the specification are marked by
- the verification method "Not To Be Tracked" or
- the word "Comment:" at the beginning.

The Verification Methods for the requirements are listed below the headers. The Verification Method(s) for an individual requirement is marked within this document below the requirement header.

The science requirements are derived from AD01, AD11, RD01 and RD02. The logic behind this source documents is as following: AD11 overwrites AD01 and RD02 overwrites RD01 in case that to the same requirement different definitions or values are provided. In case of later agreements, fixed in minutes of meeting, such MoMs overwrite AD11.

1.4. Abbrevations

1 *3831 883*

Verification Method: Description

C&DH	Command & Data Handling
CCF	Cpillary Channel Flow
CDHS	Command and Data Handling System
COTS	Commercial Off-The-Shelf
CT	Compensation Tube
EADS	European Aeronautic Defense Space Company
EM	Engineering Model
ESS	Electronic SubSystem
EU	Electronics Unit
FM	Flight Model
FMC	Front Mounted Camera
FMS	Fluid Management System
FPC	Flow Preparation Chamber
HSHRC	High Speed High Resolution Camera
I/F	Interface
ISS	International Space Station
KHB	KSC Handbook
LDA	Laser Doppler Anemometry
MOM	MinutesOf Meeting
MSFC	Marshall Space Flight Center
MSG	Microgravity Science Glovebox
MTR	Mid Term Review
NASA	National Aeronautics and Space Administration
NSTS	National Space Transportation System
OB	Optical Bench
ODU	Optical Diagnostic Unit
PA	Product Assurance
PFE	Portable Fire Extinguisher
PI	Principal Investigator
PLS	Parallel Light Source
PSC	Phase Separation chamber
QD	Quick Disconnect
RD	Reference Document
S/W	Software
SAMS	Space Acceleration Measurement System
SPLC	Standard Payload Computer
TC	Test Channel
TCU	Thermal Control Unit
TO	Training Objective
TU	Test Unit
WV	Work Volume
ZARM	Zentrum für Angewandte Raumfahrttechnologie und Mikrogravitation

2. Applicable and Reference Documents

3831 630

Verification Method: Description

2.1. Applicable Documents 1 *3831 884*

Verification Method: Description

AD1.: Science Requirement Document for the proposal Critical Velocities in Open Capillary Channel Flows (CCF), Dreyer et al; 2002-101-11
AD2.: Microgravity Science Glovebox (MSG) Investigation Interface requirements document, MSFC-RQMT-2888, rev. F, 2006-06-08
AD3.: MSG Capabilities Manual,MSFC-HDBK 3051, 2002-09-01
AD4.: Protective Finishes for Space Vehicles Structures, MSFC-SPEC-250, Rev. A, 1977-10-01
AD5.: Design Criteria for Controlling Stress Corrosion Cracking, MSFC-SPEC-522, Rev. B, 1987-07-01
AD6.: Interface Control Document MSG Data Handling System, MSG-ORIGIN-IC-0001
AD7.: Safety Policy and Requirements For Payloads Using the Space Transportation System, NSTS1700.7B, 1989-01-01, NSTS 1700.7_1_B_ ISS Addendum, 01.12.1995
AD8.: Interpretations of NSTS/ISS Payload Safety Requirements, NSTS 18798, Rev. 1B, 1997-09-01
AD9.: Payload Safety Review and Data Submittal Requirements, NSTS 13830, Rev. C, 1998-07-01
AD10.: Product Assurance & Safety Requirements For CCF, CCF-RD-QP-DLR-169/N, 2004-06-18
AD11.: MOM requirements clarification, CCF-MN-EADS-1002, 2004-11-08
AD12.: MOM requirements clarification, CCF-MN-EADS-1003, 2004-11-08
AD13.: MOM progress meeting 1, CCF-MN-EADS-1004, 2004-12-15
AD14.: MOM MTR / System Requirements Review, CCF-MN-EADS-1005, 2005-01-26
AD15.: CCF work package ZARM + follow on clarifications, CCF-EM-ZARM-1010, 2005-03-02, CCF-EM-EADS-1009, 2005-03-08, CCF-EM-EADS-1011, 2005-03-09

2.2. Reference Documents 1 *3831 885*

Verification Method: Description

RD1: CCF: Critical Velocities in Open Capillary Channel Flows (CCF); Phase A Report, Baumbach et al., 2003-03-31
RD2: Critical Velocities in Open Capillary Channel Flows (CCF); Phase B0 Report, Rosendahl et al, 2004-07-21

3. SYSTEM Definition 1 *3831 633*

Verification Method: Description

3.1. Physical Description 1 *3831 634*

Verification Method: Description

The CCF assembly provides the possibility to investigate the critical velocity in open capillary channel flows for different channel shapes and channel geometry parameters as well as for different mass flow rates under low / zero g environment. The investigation will be performed by flow parameter measurement, flow video observation and video data processing.

The CCF assembly consist of the following main components:
- The Experiment Unit (EU) which contains
  - the Fluid Management System (FMS),
  - the Thermal Control Unit (TCU) and
  - the Test Unit (TU).
    - the Test Channel (TC),

- The Optical Diagnostic Unit (ODU) which contains
  - the Optical Bench OB,
  - the High Speed, High Resolution video camera (HSHR) and
  - the Telecentric Objective,
  - the Parallel Light Source (PLS)

- The Electrical Subsystem (ESS) which contains
  - the Command and Data Handling System (C&DHS) including the functions of the board computer and
  - the image processing, Soft Ware (S/W) and
  - the Electrical Power Supply (EPS).
- In addition parts of the MSG provided Video System is used.

3.2. Mission Profile 1 *3831 635*

Verification Method: Description

a) The CCF facility will be launched once with the space shuttle.
b) The CCF shall be operated inside the MSG WV.

4 Functional Science Requirements 1 3831 844

Verification Method: Description

Comment: The test channel (TC) is that part of the CCF assembly which will be observed via video camera(s) to detect the resulting contour line of the fluid free surface(s) for the different test channel shapes and geometries as well as for the different flow parameters, Figure 1. The test channels have different shapes like parallel plate, groove channel, wedge, gapped wedge, and tilted plate. Each shape may have different geometry parameters: like (e.g. for TC shape: parallel plate) length l, width b, and height a.

Fig. 1 Channel Geometries

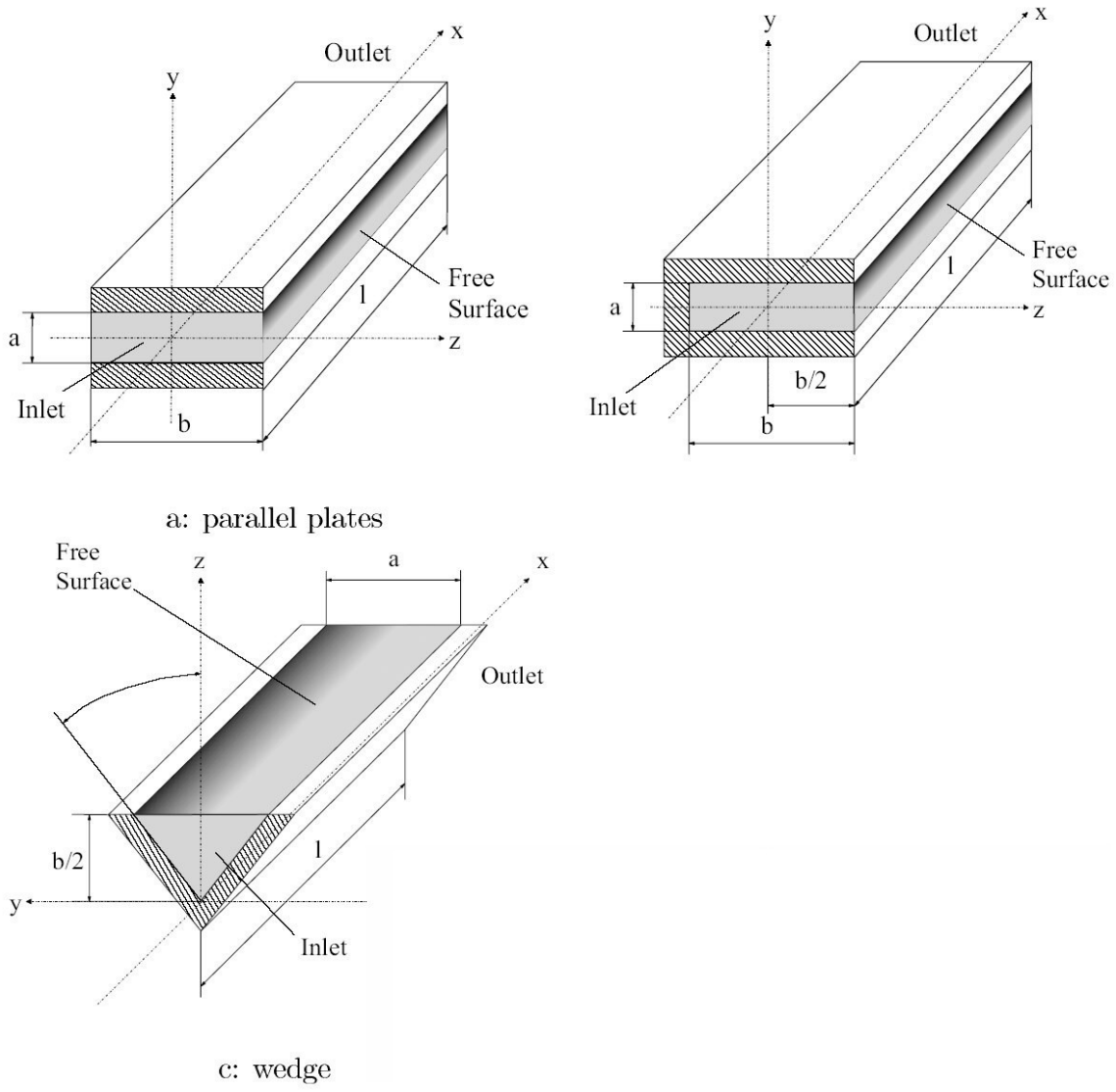

4.1. Test Channel Types 1 3831 637

Verification Method: Description

4.1.1	**Test Channel Types: Parallel Plate**	1	*3831 638*

Verification Method: Description

It shall be possible to investigate test channel shapes of Parallel Plates

4.1.2	**Test Channel Types: Groove Channel**	1	*3831 639*

Verification Method: Description

It shall be possible to investigate test channel shapes of Groove Channel

4.1.3	**Test Channel Types: Wedge Channel**	2	*3924 890*

Verification Method: Description

Experiment Unit 2 shall include the possibility to investigate test channel shapes of wedge and gapped wedge.

4.1.4	**Test Channel Types: Exchange**	1	*3831 641*

Verification Method: Inspection

The Test channel (TC) exchange shall be realised on orbit by complete Experiment Unit exchange.

4.2	**Test Channel Shape**	1	*3831 642*

Verification Method: Description

4.2.1 **Test Channel Shape: Wedge Geometry (Experiment Unit #2)** 2 *3924 891*

Verification Method: Inspection

It shall be possible to investigate different test channel geometry parameter (a, H, alpha,) of the TC Shape Wedge.
For test channel shape and parameter definition see figure 2.

Fig. 2 **Open Capillary Channel**

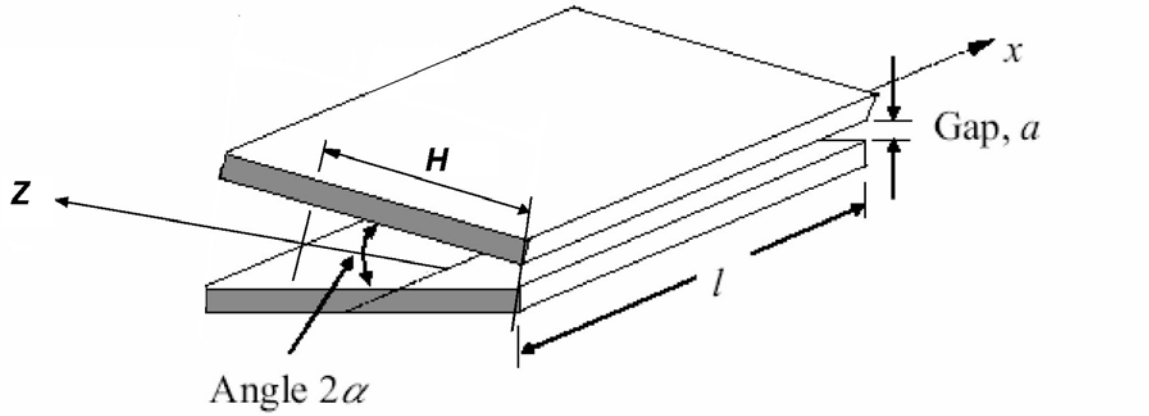

4.2.1.1 **Test Channel Shape: Wedge Geometry: Parameter l** 1 *3831 853*

Verification Method: Test

The geometry parameter l shall be l = 50 mm, tolerance +/- 1 mm.

4.2.1.2 **Test Channel Shape: Wedge Geometry: Parameter b** 1 *3831 849*

Verification Method: Inspection

The geometry parameter b shall be b = 35 mm, tolerance +2/-0 mm.

4.2.1.3 **Test Channel Shape: Wedge Geometry: Parameter a: Commanding** 1 *3831 805*

Verification Method: Test

The parameter a shall be adjustable on orbit by telecommand.

4.2.1.4 **Test Channel Shape: Wedge Geometry: Parameter a: Range** 1 *3831 647*

Verification Method: Test

The geometry parameter a shall be 0.01 mm (i.e. closed as far as possible) <= a <= 15 mm.

4.2.1.5	**Test Channel Shape: Wedge Geometry: Parameter a: Accuracy**	1	*3831 806*

Verification Method: Test

The parameter a shall be adjustable on orbit with an accuracy of 0.2 mm or less.

4.2.1.6	**Test Channel Shape: Wedge Geometry: Parameter alpha: Commanding**	1	*3831 807*

Verification Method: Test

The parameter alpha shall be adjustable on orbit by telecommand.

4.2.1.7	**Test Channel Shape: Wedge Geometry: Parameter alpha: Range**	1	*3831 808*

Verification Method: Test

The geometry parameter alpha shall be 0° <= alpha <= 30°.

4.2.1.8	**Test Channel Shape: Wedge Geometry: Parameter alpha: Accuracy**	1	*3831 809*

Verification Method: Test

The parameter alpha shall be adjustable on orbit with an accuracy of 0.5° or less.

4.2.1.9	**Deleted**	2	*3924 892*

Verification Method: Description

4.2.1.10	**Deleted**	2	*3924 893*

Verification Method: Description

4.2.1.11	**Deleted**	2	*3924 894*

Verification Method: Description

4.2.1.12	**Test Channel Shape: Wedge Geometry: Parameter H: Commanding**	1	*3831 813*

Verification Method: Test

The parameter H, fill level of wedge, shall be adjustable on orbit by telecommand.

4.2.1.13	**Test Channel Shape: Wedge Geometry: Parameter H: Range**	1	*3831 851*

Verification Method: Test

The geometry parameter H at the wedge entrance shall be b*1/5 <= H <= b*2/3.

4.2.1.14	**Test Channel Shape: Wedge Geometry: Parameter H: Accuracy**	1	*3831 815*

Verification Method: Test

The parameter H shall be adjustable on orbit with an accuracy of b/5 or less (b2/15 tbc).

4.2.1.15	**Test Channel Shape: Wedge Geometry: Sharp Edges**	1	*3831 855*

Verification Method: Test

The TC shall have sharp edges according to the following definition: precision grind with chunking <= 0.02 mm

4.2.2	**Test Channel Shape: Wedge: Inlet**	1	*3831 649*

Verification Method: Description

The test unit shall ensure a homogeneous flow into the test channel.

4.2.2.1	**Test Channel Shape: Wedge: Inlet: Nozzle**	1	*3831 650*

Verification Method: Inspection

Upstream of the test channel the test unit shall have an inlet nozzle with a length of 30 mm.

4.2.3	**Test Channel Shape: Wedge: Outlet**	1	*3831 652*

Verification Method: Description

The test unit shall ensure a homogeneous undisturbed flow out of the test channel.

4.2.3.1 **Test Channel Shape: Wedge: Outlet: Channel Geometry** 1 *3831 653*

Verification Method: Inspection

Downstream of the test channel the test unit shall have a constant (flow) cross section channel similar to the inlet nozzel outlet.

4.2.3.2 **Test Channel Shape: Wedge: Outlet: Sharp Edges** 1 *3831 857*

Verification Method: Inspection

The test unit outlet from the test channel shall have sharp edges at the end of the free surface area.

4.2.4 **Two Phase Flow** 1 *3831 816*

Verification Method: Inspection

The test unit inlet into the test channel shall be prepared to inject gas bubbles.

4.2.4.1 **Two Phase Flow** 1 *3831 818*

Verification Method: Inspection

The test unit inlet injection device shall not disturb the liquid flow pattern as far as possible.

4.2.4.2 **Two Phase Flow: Bubble Injection: Frequency** 1 *3831 817*

Verification Method: Test

The bubble injection frequency f_bi should vary within 0.1Hz < f_bi <10 Hz.

4.2.4.3 **Two Phase Flow: Bubble Injection: Size** 1 *3831 819*

Verification Method: Test

The bubble diameter shall be 1 mm <= d_bi <= 4 mm.

4.3 **Liquid Loop (Experiment Unit #2)** 1 *3831 655*

Verification Method: Description Inspection

4.3.1 **Liquid Loop: Test Liquid** 1 *3831 656*

Verification Method: Inspection

3M Engineering Fluid HFE-7500 shall be used as test liquid.

4.3.2 **Liquid Loop: Liquid Flow Rate** 1 *3831 657*

Verification Method: Description

Comment: "Flow" is used in this content as a synonym for "Volume Flow Rate"

4.3.2.1 **Liquid Loop: Liquid Flow Rate: Range** 1 *3831 868*

Verification Method: Test

The test liquid flow Q shall be controllable in a range of 0.5 ml/s <= Q <= 15 ml/s for Experiment Unit #2.

4.3.2.2 **Liquid Loop: Liquid Flow Rate: Steps** 1 *3831 659*

Verification Method: Test

The test fluid flow rate Q shall be controllable in the range defined above in steps of <= 0.01 ml/s.

4.3.2.3 **Liquid Loop: Liquid Flow Rate: Measurement Accuracy** 1 *3831 870*

Verification Method: Inspection

The test liquid Flow Rate Q shall be measured with an accuracy of +/-1% of the maximum specified flow rate (see §4.3.2.1).

Comment: Flow sensor calibration with the working liquid is required. Temperature sensivity shall be taken into account.

4.3.2.4 **Liquid Loop: Liquid Flow Rate: Measurement Location** 1 *3831 661*

Verification Method: Inspection

The test fluid Flow Rate Q shall be measured between pump and first junction.

4.3.3 **Liquid Loop: Gas / Liquid Phase Separation** 1 *3831 666*

Verification Method: Description

Comment: During the experiment run in the critical mode the test fluid free surface line will become instable and gas will be sucked into the fluid loop. This gas has to be removed from the test fluid loop prior the test fluid enters the test channel again.

4.3.3.1 **Liquid Loop: Gas / Liquid Phase Separation Feature** 1 *3831 667*

Verification Method: Test

The CCF liquid loop shall provide gas removal / separation from the liquid.

4.3.3.2 **Liquid Loop: Gas / Liquid Phase Separation: Phase Separation Chamber (PSC) Dimensions** 1 *3831 668*

Verification Method: Inspection

The Phase Separation Chamber shall have
a) an internal diameter of 130 mm
b) an internal height of 72 mm below the separation mesh (screen).
and further internal dimensions as given in figure 3.

Please note: the liquid outlet of the phase separation chamber has changed and is not valid any more.

Fig. 3 **Phase Separation Chamber**

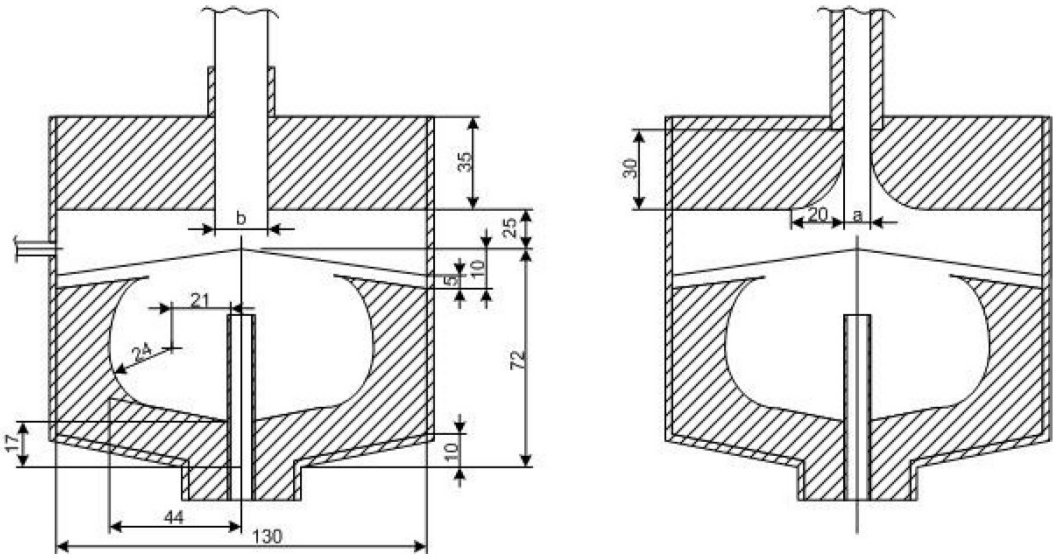

4.3.3.3 **Liquid Loop: Gas / Liquid Phase Separation: Phase Separation Chamber Mesh Size** 1 *3831 886*

Verification Method: Inspection

The Phase Separation Chamber mesh shall have a mesh size less or equal 15 µm to retain the gas bubbles.

4.3.3.4 **Liquid Loop: Gas / Liquid Phase Separation: Phase Separation Chamber Inlay** 1 *3831 670*

Verification Method: Inspection

The PSC shall include a bubble shape inlay to hold the gas volume/bubble in the centre of the PSC.

4.3.3.5	**Liquid Loop: Gas / Liquid Phase Separation: Phase Separation Chamber Rebounding Plate**	1	*3831 671*

Verification Method: Inspection

The PSC shall have a velocity plate at the bottom above the fluid inlet.

4.3.3.6	**Liquid Loop: Gas / Liquid Phase Separation: Gas Injection / Removal**	1	*3831 672*

Verification Method: Test

It shall be possible to inject / remove gas to / from the centre of the PSC.

4.3.4	**Liquid Loop: Flow Preparation Chamber**	1	*3831 673*

Verification Method: Description

4.3.4.1	**Liquid Loop: Flow Preparation Chamber: Location**	1	*3831 674*

Verification Method:

The Flow Preparation Chamber shall be located downstream of the phase separation chamber.

4.3.4.2	**Liquid Loop: Flow Preparation Chamber: Valve**	1	*3831 675*

Verification Method: Inspection

The Flow Preparation Chamber shall include a valve to open/close the connection to the test channel inlet.

4.3.4.3	**Liquid Loop: Flow Preparation Chamber: TC Inlet**	1	*3831 854*

Verification Method: Inspection

The Flow Preparation Chamber shall include a test channel inlet.

4.3.4.5	**Liquid Loop: Flow Preparation Chamber: Valve**	1	*3831 871*

Verification Method: Analyses

The valve shall not disturb the flow.

Comment: Therefore the valve shall be removed sufficiently far from the nozzle.

4.3.5	**Liquid Recovery**	1	*3831 694*

Verification Method: Analyses

Liquid, splashed out of the test channel, shall be recovered such that it does not impact the experiment observation.

4.4	**Gas Atmosphere**	1	*3831 695*

Verification Method: Inspection

The gas in the test unit shall be GN2.

5	**Environment**	1	*3831 696*

Verification Method: Description

5.1	**Environment: Temperature Control**	1	*3831 697*

Verification Method: Description

5.1.1	**Environment: Temperature Control: Range**	1	*3831 698*

Verification Method: Test

The thermal control of the test liquid temperature shall ensure that the liquid temperature will be in a range of 20°C <= T_liq <= 40°C.

5.1.2	**Environment: Temperature Control: Accuracy**	1	*3831 699*

Verification Method: Test

The test liquid temperature shall be controlled prior to experiment start and during experiment run such that the measured test liquid temperature difference inside the liquid loop between PSC inlet and TC outlet shall be less than 1.0°C.

5.2	**Environment: Pressure Control**	1	*3831 700*

Verification Method: Description

Comment: Very low pressure changes along the test channel are expected (dp ~ 10 Pa range).
The absolute pressure of the system has less influence on the test results.

5.2.1	**Environment: Pressure Control: Percipitation**	1	*3831 872*

Verification Method: Analyses

The pressure between test channel outlet and pump inlet shall not drop below 987 hPa.

Comment: Cavitation and/or precipitation shall not occur in the duct between test channel and flow sensor.

5.3	**Liquid and Gas Compensation**	1	*3831 702*

Verification Method: Description

Comment: Due to the fact that the open test channel walls may suck air from the test unit atmosphere in over-critical flow condition the volume inside the fluid loop changes; e.g. the gas bubble inside the PSC increases and the filling level in the test channel rises. At latest the maximum gas bubble volume inside the PSC is reached a compensation has to be performed. That means that gas has to be removed from the PSC. Also prior to the start of an experiment run a minimum gas bubble volume has to be injected into the PSC.

5.3.1	**Liquid Volume Compensation**	1	*3831 703*

Verification Method: Description

5.3.1.1	**Liquid Volume Compensation: Thermal Expansion**	1	*3831 704*

Verification Method: Test

The Fluid Managmenet Subsystem shall provide means for thermal liquid volume expansion compensation for the temperature range between 5°C and 48°C.

5.3.1.2	**Liquid Volume Compensation: Thermal Expansion Starting Pressure**	1	*3831 705*

Verification Method: Test

Under worst case conditions the means for thermal liquid volume expansion compensation shall not be activated at liquid pressure below 2 bar abs.

5.3.1.3	**Liquid Volume Compensation: Thermal Expansion Final Pressure**	1	*3831 706*

Verification Method: Test

Under worst case conditions the means for thermal liquid volume expansion compensation shall not generate a liquid pressure above 4 bar abs (tbc).

5.3.1.4	**Liquid Volume Compensation: Operational Volume**	1	*3831 707*

Verification Method: Test

The FMS shall compensate the operational liquid volume changes from liquid volume in start configuration to liquid volume in experiment running configuration.

5.3.2	**Gas Volume Compensation**	1	*3831 709*

Verification Method: Description

5.3.2.1	**Gas Volume Compensation: Operational Volume**	1	*3831 710*

Verification Method: Test

The FMS shall compensate the operational gas volume changes from liquid volume in start configuration to gas volume in experiment running configuration without change of the atmopheric pressure.

5.3.2.2	**Gas Volume Compensation: Fill Level Control**	1	*3831 711*

Verification Method: Test

The FMC shall control the gas fill level volume at an accuracy of 1 ml or less.

5.4.1	**Micro Gravity Level Measurement**	1	*3831 712*

Verification Method: Description

Comment:
At the time being the availability of a MSG or ISS provided micro gravity level measurement dedicated to MSG experiments is tbd.
The accommodation of the SAMS-II sensor head shall be considered in the CCF design.

6	**Data Acquisition**	1	*3831 713*

Verification Method: Description

6.1	**Data Acquisition: Temperatures**	1	*3831 714*

Verification Method: Description

6.1.1 **Data Acquisition: Temperatures: Sensor Locations** 1 *3831 715*

Verification Method: Inspection

Temperature sensors shall be located at least at:
a) inside / close to the outlet of the liquid plunger (measuring the liquid temperature)
b) inside / close to the PSC inlet (measuring the liquid temperature)
c) inside the test flow preparation chamber close to the test channel inlet nozzle (measuring the liquid temperature)
d) inside the test liquid ducting close to the test channel outlet (measuring the liquid temperature)
e) inside the test unit atmosphere (measuring the gas temperature inside the TU)
f) inside the ducting close to the flow sensor outlet (measuring the liquid temperature)
g) near the outlet of the gas plunger (measuring gas temperature)

The sensor inside the fluid loop at location c) and d) shall not disturb the flow, as far as possible.

6.1.2 **Data Acquisition: Temperatures: Sensor Accuracy Absolut** 1 *3831 716*

Verification Method: Test

The absolute accuracy of the temperature measurement shall be +/- 0.5°C or better.

6.1.3 **Data Acquisition: Temperatures: Sensor Accuracy Relative** 1 *3831 717*

Verification Method: Test

The relative accuracy of each temperature sensor to each other shall be +/- 0.2°C.

6.1.4 **Data Acquisition: Temperatures: Sensor Time constant** 1 *3831 718*

Verification Method: Inspection

The temperature sensor time constant sahll be less than 1 s on a metal surface.

6.2 **Data Acquisition: Pressures** 1 *3831 719*

Verification Method: Description

6.2.1 **Data Acquisition: Pressure Control: Sensor Locations** 1 *3831 720*

Verification Method: Inspection

The total Pressure shall be measured at:
a) inside the phase separation chamber (to measure the test fluid total pressure)
b) inside the test unit gas atmosphere (to measure the atmosphere total pressure)
c) inside the gas duct near the plunger (measuring the gas total pressure)

6.2.2 **Data Acquisition: Pressure Control: Sensor Range** 1 *3831 721*

Verification Method: Test

The total pressure sensor shall include the measurement range of 920 hPa <= p <= 1120 hPa

---

6.2.3 **Data Acquisition: Pressure Control: Sensor Accuracy** 1 *3831 722*

Verification Method: Inspection

The total pressure sensor shall have a measurement accuracy of 0,5% full scale reading.

6.3 **Video Observation** 1 *3831 723*

Verification Method: Description

Comment: The test channel shall be observed via video camera during the experiment run; that means that this video data have to be down linked to the PI to enable the PI for online decision to change the flow rate and/or the free surface parameter. This kind of video observation will be called Experiment General Observation.

Comment: In addition the test channel area (l x b) shall be observed via a high speed, high resolution video camera for test result data acquisition (free surface behavior). These video data shall be processed on board and the evaluation/process results (reduced data amount) shall be down linked for detailed evaluation. This kind of video observation will be called Experiment Detailed Observation.

6.3.1 **Experiment General Video Observation** 1 *3831 724*

Verification Method: Inspection

a) The CCF General Video equipment shall observe the test channel (TC) during experiment run.
b) The CCF transparent wall parts shall have a comparable optical quality as defined for the TC.

6.3.1.1 **Experiment General Video Observation: Camera** 1 *3831 725*

Verification Method: Inspection

The CCF facility shall use one of the MSG provided video camera to observe the test channel or use video pictures (low data amount) resulting from the video camera(s) for detailed observation.

6.3.1.2 **Experiment General Video Observation: Frequency** 1 *3831 726*

Verification Method: Inspection

The flow in the test channel shall be observed by video frequency of more or equal 24 fps (frames per second).

6.3.1.3 **Experiment General Video Observation: Resolution** 1 *3831 887*

Verification Method: Inspection

DELETED

6.3.1.4 **Experiment General Video Observation: Video Data Down Link** 1 *3831 728*

Verification Method: Inspection

The CCF facility shall use the MSG provided "data handling system" for the above defined video data online down link.

6.3.2 **Experiment Detailed Video Observation** 1 *3831 729*

Verification Method: Description

6.3.2.1 **Experiment Detailed Video Observation** 1 *3831 730*

Verification Method: Test

The CCF facility shall observe the the test channel area ((l_testchannel x b) during the experiment run.

6.3.2.2 **Experiment Detailed Video Observation: Resolution** 1 *3831 731*

Verification Method: Test

The flow in the test channel shall be recorded by video with an optical resolution in the test channel plane (l x b) of 0.05 mm/pixel or better.

6.3.2.3 **Experiment Detailed Video Observation: Intermediate Stowage** 1 *3831 869*

Verification Method: Test

The CCF detailed video data acquisition shall intermediately store the contineous high speed video data stream. The duration shall be selectable from 0 s < record duration to the maximimum capability of the HSHRC, which shall be not less than 5 s.

6.3.2.4 **Experiment Detailed Video Observation: Frequency** 1 *3831 733*

Verification Method: Test

The CCF detailed video data acquisition shall operate up to a frequency of 250 fps at least.

6.3.2.5 **Experiment Detailed Video Observation: Observation Direction** 1 *3831 734*

Verification Method: Inspection

The flow in the test channel shall be recorded by video perpendicular to the test channel l x b plane of the non-rotating glass plate during wedge / gapped wedge configuration.

Comment:
This is to reduce the maximum optical distortation.

6.3.2.6 **Experiment Detailed Video Observation: Gray Scale** 1 *3831 735*

Verification Method: Test

The flow in the test channel shall be recorded by video in black and white with a 8 bit gray scale resolution for each pixel.

6.3.3 **Experiment Detailed Video Observation: On Board Data Storage and Processing** 1 *3831 736*

Verification Method: Description

Comment: The test result data acquisitioned by the high speed, high resolution video camera shall be processed on board after each individual experiment run (= offline) to extract the relevant surface details (detection of the contour lines k(x)). Contour line data will be down linked together with reference frames.

6.3.3.1 **Experiment Detailed Video Observation: On Board Data Storage** 1 *3831 737*

Verification Method: Description

The C&DHS does NOT store any video data after provision of the reference images to the MSG downlink.

6.3.3.2 **Experiment Detailed Video Observation: Reference Frame Extraction** 1 *3831 738*

Verification Method: Test

The C&DHS extract offline the reference images from the raw video data according to a frequency of 1 fps.

6.3.3.3 **Experiment Detailed Video Observation: Contour Line Detection** 1 *3831 739*

Verification Method: Test

The CDHS shall detect offline from each recorded video frame the contour lines k(x).

6.3.3.4 **Experiment Detailed Video Observation: Contour Line Detection** 1 *3831 820*

Verification Method: Test

The CDHS shall detect offline from each recorded video frame the contour lines of the injected gas bubbles, if any.

6.3.3.5 **Experiment Detailed Video Observation: Coordinate Transfer and Optical Corrections** 1 *3831 873*

Verification Method: Test

DELETED

6.3.3.6 **Experiment Detailed Video Observation: Downlink** 1 *3831 741*

Verification Method: Test

The CDHS shall provide preprocessed (reduced) data to the downlink via the MSG provided data handling interface, i.e. the counter lines k(x) and the reference video frames.

6.3.3.7 **Experiment Detailed Video Observation: Full Frame Transmission** 1 *3831 888*

Verification Method: Test

On request the C&DHS shall offline provide predefined single images or sequences of the last experiment run for documentation to the MSG downlink:

resolution: full (1280 x 1024) or video (full frame reseized to 576 x 720)
frame rate: as recorded or video 25 fps
frame: progressiv
compression: quality factor of compression selectable by parameter

---

6.3.4 **Optical Requirements** 1 *3831 742*

Verification Method: Description

Comment: To be able to observe the fluid behavior inside the test channel via video camera(s) that part of the walls which will be observed by video camera(s) for liquid free surface(s) will be made out of transparent material.

Comment: The illumination of the test channel (TC) have to be performed such that the illumination is compatible with Video Camera(s) with which the TC will be observed.
Video camera and illumination have to be defined/chosen such that they fit together. Therefore below the illumination parameters will be listed, but no dedicated values will be defined. That means illumination and cameras have to be verified/tested together.

6.3.4.1 **Optical Requirements: Tansparency TC** 1 *3831 743*

Verification Method: Inspection

The test channel walls to be observed by video camera(s) shall be made out of a transparent material.

6.3.4.2 **Optical Requirements: Wettability TC** 1 *3831 745*

Verification Method: Test

The test channel transparent walls shall be perfect wettable by the test fluid.

6.3.4.3 **Optical Requirements: Surface TC** 1 *3831 889*

Verification Method: Test

The test channel wall surfaces to be observed by video camera(s) shall have a surface quality 5/4x0.16 according to ISO10110 (DIN 3140).

Comment: 5 is the indicator for surface errors, N ,here 4, is the indicator for the numbers of errors, A ,here 0.16, is the area of the error."

6.3.4.4 **Illumination Brightness** 1 *3831 750*

Verification Method: Test

The Optical diagnostic Unit (ODU) shall provide a test channel illumination with a brightness which is compatible with the camera and the set up.

6.3.4.5 **Illumination Type** 1 *3831 751*

Verification Method: Test

The ODU provided illumination for the test channel shall be backlight illumination.

6.3.4.6 **Illumination Homogeneity** 1 *3831 752*

Verification Method: Test

The ODU shall provide a test channel illumination with a light intensity homogeneity which is compatible with the edge detection technique and the set up.

6.3.4.7 **Illumination Light Wave Length** 1 *3831 753*

Verification Method: Test

The ODU shall provide a illuminations with a wave lengths which are compatible with the video cameras observing the test channel

---

6.3.5 Experiment Control 1 *3831 754*

Verification Method: Description

Comment: The experiment control data like the temperature data, the pressure data, the mass flow data, the geometrical parameter data (e.g. l and a) will be stored according to the defined sample rate. All this data have to be correlated between each other as well as to the video data via the time stamp (absolute time or relative experiment time).

Due to several reasons, e.g. driver availability for the high speed high resolution camera, the selected operating system of the CCF controller is Windows XP Embedded. This is NOT a realtime system. The frequencies and durations given below are therfore statistical and average values. With Windows XP it is not possible to grant timelines due to system activities which cannot be interrupted.

6.3.5.1 Experiment Control: Telecommand Receipt 1 *3831 755*

Verification Method: Test

The C&DHS shall receive telecommands from ground via MSG.

6.3.5.2 Experiment Control: Telecommand Execution 1 *3831 756*

Verification Method: Test

The C&DHS shall initiate and control the relevant actions according to the telecommands from ground.

6.3.5.3 Experiment Control: Telecommand Acknowledgement 1 *3831 757*

Verification Method: Test

The C&DHS shall acknowledge telecommands in the housekeeping data stream.

6.3.5.4 Experiment Control: Downlink Provision Rate 1 *3831 758*

Verification Method: Test

The C&DHS shall provide for downlink via MSG the entire set of housekeeping data during the experiment run with a frequency of at least 1Hz.

6.3.5.5 **Experiment Control: Housekeeping Data Set** 1 *3831 759*

Verification Method: Test

The C&DHS housekeeping data set shall consist of at least:
a) time stamp (absolute or relative)
b) CCF health status summary
c temperatures
d) pressures
e) volume flow rate
f) rotation speed of pump drive
g) geometric parameter set
h) all valve positions (open/closed) (actual value)

j) position of plunger K2 (liquid volume) (actual value)
k) position of plunger K3 (gas volume) (actual value)

o) status report of the image processing
p) micro-g level
q) all commands from the PI site to CCF (telecommand acknowledgement)

6.3.5.6 **Experiment Control: Time Correlation** 1 *3831 760*

Verification Method: Test

The C&DHS shall ensure the time correlation between experiment housekeeping data and video data.

6.3.5.7 **Experiment Control: Automatic Experiment Execution** 1 *3831 822*

Verification Method: Test

The C&DHS shall be able to execute experiment runs with predefined parameter sets, in particular liquid flow rate, geometric parameters, duration of experiment, etc., automatically.

6.3.5.8 **Experiment Control: Choking Detection** 1 *3831 761*

Verification Method: Test

The C&DHS shall detect choking from the available sensor data automatically.

6.3.5.9 **Experiment Control: Automatic Flow Stop** 1 *3831 762*

Verification Method: Test

The C&DHS shall stop the liquid flow automatically when choking is detected.

---

7 Interfaces

1 *3831 763*

Verification Method: Description

Comment: The CCF facility I/F requirements are defined in AD02. These requirements are not repeated in this specification. Only reference will be provided. The requirement verification has to be done as requested in AD02

7.1 CCF Mass

1 *3831 764*

Verification Method: Test

The CCF facility total mass (including the MSG provided equipment in the Working Volume (WV)) shall not exceed 200 kg.

7.2 CCF Volume

1 *3831 765*

Verification Method: Test

The CCF facility total volume (including the MSG provided equipment in the WV) shall be noticeable below the MSG WV which is in total 255 l.

7.3 CCF Envelope

1 *3831 766*

Verification Method: Description

7.3.1 CCF Subsystems / Components Transfer Envelope

1 *3831 767*

Verification Method: Test

The CCF facility subsystems / components have to be designed such that they can be transferred into the MSG WV via the two loading ports, one located on each side of the WV.

Comment: Loading ports max. diameter D = 406mm.

7.3.2 CCF Subsystems / Components Envelope

1 *3831 768*

Verification Method: Demonstration

The CCF facility subsystems / components have to be designed such that they can be handled (integrated) inside the MSG WV.

Comment: The MSG WV max. dimensions are: Width = 906mm, Depth (bottom) = 500mm, Depth (top) = 385mm, Height = 638mm. Adequate space from windows, gloveports, ... and for QD and connector handling have to be taken into account.

7.3.3 **CCF Subsystems / Components Storage Constraints** 1 *3831 769*

Verification Method: Analyses Demonstration

The CCF facility subsystems / components have to be designed such that they can be handled (integrated) and stored during transport and on ISS.

7.4 **CCF Thermal Dissipation** 1 *3831 770*

Verification Method: Description

7.4.1 **CCF Total Thermal Dissipation** 1 *3831 771*

Verification Method: Test Analyses

The CCF facility total thermal dissipation (including the MSG provided equipment in the WV) shall be less than 1000 W.

7.4.2 **CCF Thermal Dissipation to WV Air** 1 *3831 772*

Verification Method: Analyses

The CCF facility total thermal dissipation (including the MSG provided equipment in the WV) to the WV air flow shall be less than 200 W.

7.4.3 **CCF Thermal Dissipation to WV Coldplate** 1 *3831 773*

Verification Method: Test Analyses

The CCF facility total thermal dissipation (including the MSG provided equipment in the WV) to the WV coldplate shall be less than 800 W.

7.4.4 **Loss of Cooling** 1 *3831 774*

Verification Method: Test

The CCF facility shall be designed not to create hazards in case of sudden loss or temporary interruption of MSG coolant loop.

7.5 **CCF Micro Gravity Environment Disturbances** 1 *3831 775*

Verification Method: Test

The CCF facility micro gravity disturbances introduced into the MSG shall be less than that defined in AD12 para. 3.1.2.

7.6 **Depress- / Repress Rates** 1 *3831 776*

Verification Method: Test

The CCF facility shall be designed to withstand the depress rate of 878 Pa/sec and the repress rate of 800 Pa/sec.

7.7 **Exposure to PFE Discharge** 1 *3831 777*

Verification Method: Analyses

The CCF facility shall be designed not to create a hazard when exposed to Portable Fire Extinguisher (PFE) discharge.

7.8 **Mechanical / Structural Interface Requirements** 1 *3831 778*

Verification Method: Test Inspection Analyses

The CCF facility shall comply with requirements defined in AD02

7.9 **Electrical Interface Requirements** 1 *3831 779*

Verification Method: Test Inspection Analyses

The CCF facility shall comply with requirements defined in AD02

7.10 **Command and Data Handling Interface Requirements** 1 *3831 780*

Verification Method: Test Analyses

The CCF facility shall comply with requirements defined in AD02

7.11 **Thermal Control Interface Requirements** 1 *3831 781*

Verification Method: Test Analyses

The CCF facility shall comply with requirements defined in AD02

7.12 **Vacuum System Interface Requirements** 1 *3831 782*

Verification Method: Analyses

The CCF facility shall comply with requirements defined in AD02

7.13	**Pressurized Gas Interface Requirements**	1	*3831 783*

Verification Method: Analyses

The CCF facility shall comply with requirements defined in AD02

7.14	**Environmental Interface Requirements**	1	*3831 784*

Verification Method: Analyses

The CCF facility shall comply with requirements defined in AD02

7.15	**Fire Protection Interface Requirements**	1	*3831 785*

Verification Method: Analyses

The CCF facility shall comply with requirements defined in AD02

7.16	**Material and Parts Interface Requirements**	1	*3831 786*

Verification Method: Test Inspection Analyses

The CCF facility shall comply with requirements defined in AD02

7.17	**Human Factors Interface Requirements**	1	*3831 787*

Verification Method: Test Inspection Demonstration

The CCF facility shall comply with requirements defined in AD02

7.18	**PA AND SAFETY REQUIREMENTS**		*3831 788*

Verification Method: Description

7.18.1	**PA and Safety Requirements**	1	*3831 789*

Verification Method: Test Inspection Analyses

The CCF facility shall comply with the safety requirements defined in AD02 and AD10

7.18.2	**PA and Safety Requirements**	1	*3831 790*

Verification Method: Test Inspection Analyses

The CCF facility shall comply with the safety requirements defined in AD07

7.18.4 **PA and Safety Requirements** *3831 792*

Verification Method: Test Inspection Analyses

The CCF facility shall comply with the safety requirements defined in AD09

7.18.5 **PA and Safety Requirements** 1 *3831 793*

Verification Method: Test Inspection Analyses

The CCF facility shall comply with the safety requirements defined in AD08 and AD09.

7.19 **LABELING** 1 *3831 794*

Verification Method: Inspection

The CCF shall comply with the labeling requirements defined in AD02

---

8 **VERIFICATION** 1 *3831 795*

Verification Method: Inspection

The CCF shall comply with the verification requirements defined in AD02

8.1 **Verification Requirement Sources and Breakdown Strategy** 1 *3831 796*

Verification Method: Description

This CCF System Specification defines the science / functional performance requirements in detail In addition to the science / functional performance requirements some other requirements have to be fulfilled to be allowed to fly and integrate the CCF into MSG and to operate the CCF.
Such requirements have been made applicable in this CCF System Specification via some applicable documents like AD02, the MSG Investigation Interface Requirements Document from NASA.

It should be mentioned that Safety Requirements Verification are not addressed in detail here because it is assumed that Safety Requirements Verification will be covered by the Safety Data Package.

Further on it has to be mentioned that all the CCF Command and Data Handling activities are foreseen to be part of the ESS which was not part of the phase B. Therefore for CCF ESS development there may be also software requirements to be verified depending on the ESS software. This is not reflected here because the ESS was excluded from phase B.

8.3 **Verification Methods** 1 *3831 798*

Verification Method: Description

8.3.1 Analysis 1 *3831 799*

Verification Method: Description

Analysis is a technical evaluation that relates equipment design and use parameters for prediction of actual design and operation. Analysis may be used to verify requirements, provided established techniques used are adequate to yield confidence, or where testing is impractical. Included in this category is analysis of similarity to items previously verified to the same criteria or more stringent criteria. Verification accomplished by analysis shall be evidenced by an analysis report.

8.3.2 Test 1 *3831 800*

Verification Method: Description

Test is actual operation of equipment under simulated conditions or the subjection of equipment to specified environments to measure responses. When analysis or inspection is specified as the method of verification, testing may be used to satisfy the requirement if preferred by the hardware developer, if it is cost effective, and if the Microgravity Science Glovebox Integration Manager agrees. Verification accomplished by test shall be evidenced by a test report.

8.3.3 Inspection 1 *3831 801*

Verification Method: Description

Inspection is a physical evaluation of equipment and associated documentation.
Inspection may be used to verify construction features, drawing compliance, workmanship, and physical condition. It includes determination of physical dimensions.
Verification accomplished by inspection shall be evidenced by an inspection report.

8.3.4 Demonstration 1 *3831 802*

Verification Method: Description

Demonstration is the qualitative determination of compliance with requirements by observation during actual operation or simulation under preplanned conditions and guidelines. Some human factor requirements were the method of closure is a demonstration requires the investigation to be set up in its on-orbit configuration in the MSG Engineering Unit to verify that the requirement is satisfied.

8.3.5 Review of Design 1 *3831 803*

Verification Method: Description

Review of design means verification compliance to requirement by evidence from documents and drawings. (only be used in Verification matrix…..

8.4 Verification Matrix

1 *3831 804*

Verification Method: Description

Legend:
EU = Experiment Unit, ESS = Electrical Subsystem, FM = Flight Model (complete CCF System) T = Test, A = Analysis,
I = Inspection, R = Review of Design, *+* = according to applicable doc.